creative commons
COMMONS DEED

저작자표시-비영리-변경금지 2.0 대한민국

이용자는 아래의 조건을 따르는 경우에 한하여 자유롭게

- 이 저작물을 복제, 배포, 전송, 전시, 공연 및 방송할 수 있습니다.

다음과 같은 조건을 따라야 합니다:

저작자표시. 귀하는 원저작자를 표시하여야 합니다.

비영리. 귀하는 이 저작물을 영리 목적으로 이용할 수 없습니다.

변경금지. 귀하는 이 저작물을 개작, 변형 또는 가공할 수 없습니다.

- 귀하는, 이 저작물의 재이용이나 배포의 경우, 이 저작물에 적용된 이용허락조건을 명확하게 나타내어야 합니다.
- 저작권자로부터 별도의 허가를 받으면 이러한 조건들은 적용되지 않습니다.

저작권법에 따른 이용자의 권리는 위의 내용에 의하여 영향을 받지 않습니다.

이것은 이용허락규약(Legal Code)을 이해하기 쉽게 요약한 것입니다.

Disclaimer

dCollection

이학박사 학위논문

The Globular Cluster Systems in Virgo and M85

처녀자리은하단과 M85의 구상성단계

2017년 8월

서울대학교 대학원
물리·천문학부 천문학전공
고 유 경

To my loved ones...

ABSTRACT

This thesis presents a study of the globular clusters (GCs) in the Virgo cluster and M85 based on the comprehensive photometric and spectroscopic surveys. The GCs are of great use to trace the formation and evolution history of their host environments. We investigate the origin of intracluster GCs (IGCs) in the Virgo cluster as well as the GCs in the merger remnant galaxy M85.

We present the results of a wide-field spectroscopic survey of GCs in the Virgo cluster. We obtain spectra for 201 GCs and 55 ultracompact dwarfs (UCDs) using Hectospec on the Multiple-Mirror Telescope and derive their radial velocities. We identify 46 genuine IGCs, not associated with any Virgo galaxies, using the 3D GMM test on the spatial and radial velocity distribution. They are located at a projected distance 200 kpc $< R <$ 500 kpc from the center of M87. The radial velocity distribution of these IGCs shows two peaks, one at $v_{\rm r}$ =1023 km s^{-1}, associated with the Virgo main body, and another at $v_{\rm r}$ = 36 km s^{-1}, associated with the infalling structure. The velocity dispersion of the IGCs in the Virgo main body is $\sigma_{\rm IGC} \sim 314$ km s^{-1}, which is smoothly connected to the velocity dispersion profile of M87 GCs but is much lower than that of dwarf galaxies in the same survey field, $\sigma_{\rm dwarf} \sim 608$ km s^{-1}. The UCDs are more centrally concentrated on massive galaxies–M87, M86, and M84. The radial velocity dispersion of the UCD system is much smaller than that of dwarf galaxies. Our results confirm the large-scale distribution of Virgo IGCs indicated by previous photometric surveys. The color distribution of the confirmed IGCs shows a bimodality similar to that of M87 GCs. This indicates that most IGCs are stripped off dwarf galaxies and some off massive galaxies in the Virgo.

M85 is one of nearby merger remnant galaxies that underwent merging events a few Gyrs ago. The GCs in M85 are surveyed with the MegaCam attached at 3.6m Canada-French-Hawaii telescope. We obtain *ugi*-band images of 1°$\times$ 1° field around

M85. We identify 1318 GC candidates among point sources in the survey region using color and magnitude criteria. The GC candidates are well concentrated on M85 but show more extended spatial distribution than the galaxy light. The effective radius of the entire GC system is about 5.′54, corresponding to 29 kpc. The color distribution of the GC candidates shows two peaks of $(g-i)_0 = 0.65$ and 0.87. We detect the green GC population in the inner region $R < 2'$ in addition to blue and red GC populations. The radial number density profile and the surface number density map of the blue GC system show more extended features than those of red GC system. The effective radii of the blue and red GC systems are 7.′41 and 2.′31, respectively. The spatial distributions of both blue and red GC systems are elongated, which are similar to galaxy light. This feature differs from that shown in typical early-type galaxies. We suggest that the presence of the green GCs and the elongated spatial distribution of the blue and red GC systems are merger-induced features.

We present the first spectroscopic study of GCs in the merger remnant galaxy M85 using two instruments: Gemini Multi-Object Spectrograph (GMOS) attached at the 8.1m Gemini-North telescope and Hectospec on the 6.5m Multiple-Mirror Telescope. We obtain the spectra for 20 GCs as well as the nucleus of M85 using the Gemini/GMOS. The radial velocities of the GCs range from 396 km s^{-1} to 1127 km s^{-1}, which is consistent with that of the M85 nucleus ($v_r = 743 \pm 8$ km s^{-1}). We find a signal of rotation of M85 GC system, and estimate their rotation-corrected radial velocity dispersion as 154 km s^{-1}. The ages and metallicities of the GCs are derived from Lick indices and full spectrum fitting. We detect the intermediate-age population of which mean age is 4.0 ± 2.0 Gyr with solar metallicities ([Fe/H] $\sim$ –0.19), comprising 50% of the observed GCs, as well as old population. This suggests that M85 experienced a wet merging event about 4 Gyrs ago.

In addition, we obtain the spectra for 53 GCs including 11 IGCs using the MMT/Hectospec. The radial velocities of the GCs range from $\sim$ 400 km s^{-1} to

$\sim$ 1600km s^{-1}. We classify the GC sample into three categories, blue and red GCs in M85, and IGCs. We select the GCs that belong to M85 with two criteria: $v_{\rm r} <$ 1200 km s^{-1} and $R < 20'$, and the other GCs are considered as IGCs. The color criterion $(g-i)_0 = 0.8$ is used to divide the M85 GCs into blue and red ones. All red GCs are located within $R < 6'$, while the blue ones are distributed to $R \sim 20'$. We investigate the kinematics of the GC system of M85. The entire M85 GC system shows overall rotation as shown in the GC sample of GMOS observation. The red GC system shows more clear rotation feature than the blue GC system despite the small sample. The rotation axis of the GC system of M85 is clearly different from that of the central galaxy light. We derive the rotation-corrected radial velocity dispersion of two GC systems: $\sigma_{\rm r} = 149 \pm 20$ km s^{-1} for blue GCs and σr $= 51 \pm 14$ km s^{-1} for red GCs. The rotation-corrected velocity dispersion of red GC system is much lower than that of blue GC system. The strong rotation feature of the GC system and kinematically decoupled GC system from the stellar light are suspected to be caused by merging events. The kinematics of the M85 GCs and IGCs are clearly different from each other. The mean radial velocities of M85 GCs and IGCs are 765 $\pm$ 27 km s^{-1} and 1012 $\pm$ 108 km s^{-1}, respectively. The radial velocity dispersion of the IGCs is 354 $\pm$ 78 km s^{-1}, which is higher than that of the M85 GCs and similar to that of dwarf galaxies in the survey region ($\sigma = 330 \pm 95$ km s^{-1}). This indicates that the IGCs are governed by the gravitational potential of the galaxy cluster.

Keywords: galaxy clusters; galaxy clusters:Virgo; galaxies; galaxies:individual (M85); galaxies:formation; globular clusters; survey; photometry; spectroscopy

Student Number: 2010-20386

Contents

List of Figures

List of Tables

Chapter 1

Introduction

1.1 Globular Clusters

Globular clusters (GCs) are aggregates of 10^3–10^6 stars and one of the oldest populations in the Universe. In the past, they have been categorized as stars by observation with naked eye, but after the 17^{th} century they have been classified as non-stellar objects like nebulae by observation with modern telescopes (see a review by Meylan 2003). Since Herschel (1847) identified ω Cen and 47 Tuc as GCs, numerous studies have investigated the GCs in various types of galaxies as well as Milky Way.

Generally, they are 10–13 Gyrs old, and the member stars in a GC are believed to form at the same epoch. However, various studies found the GCs with multiple stellar populations, ω Cen (Freeman & Rodgers 1975; Cohen 1981; Lee et al. 1999; Bedin et al. 2004; Norris 2004; Piotto et al. 2005), NGC 1846 in the Large Magellanic Cloud (Mackey & Broby Nielsen 2007), and NGC 1851 (Lee et al. 2009), NGC 5824 (Da Costa et al. 2014) (see a review by Gratton, Carretta & Bragaglia 2012). Typical GCs have the absolute magnitude range of $-1.7 < M_V < -10.2$ and a total mass range of $10^3 M_\odot < M < 10^6 M_\odot$. They are found ubiquitously in various kinds of galaxies from low-mass dwarf to massive early-type galaxies. Recently, the GCs have been

also found in ultra-diffuse galaxies, one of the new types of galaxies characterized by low surface brightness but L^* galaxy size (Beasley & Trujillo 2016; Peng & Lim 2016; van Dokkum et al. 2016). This indicates that the formation of GCs must happen in the primordial stage of the galaxy formation. The ubiquitous GC system is a great tool to study the formation and evolution of various types of galaxies.

1.2 GCs in Early-type Galaxies

Since Hubble (1932) first identified and investigated the GCs in M31, there have been numerous studies about the GCs in galaxies (Brodie & Strader 2006 and references therein). Especially, massive elliptical galaxies host a plenty of GCs (10^3–10^4). For example, there are about 6000 and 12000 GCs in M49 and M87 (Rhode & Zepf 2001; Tamura et al. 2006), massive elliptical galaxies in the Virgo cluster, respectively, compared to Milky Way's 200 and M31's 600 GCs (Harris 1996; Barmby & Huchra 2001; Huxor et al. 2014). In addition, the GCs are detected in the faint stellar halo because they are much brighter than individual stars. Therefore, they are a good tracer to investigate the halo structure and dynamics of their host galaxies.

One of the salient features of GCs in early-type galaxies is their bimodal color distribution. The color bimodality for the extragalactic GCs was first proposed by Zepf & Ashman (1993) (NGC 4472 and NGC 5128) and Ostrov et al. (1993) (NGC 1399). Subsequent studies investigated the origin of this bimodality by comparing the physical properties of GC subpopulations, blue and red GCs. The color of old GCs can be a proxy for the metallicity: blue and red GCs are metal-poor and metal-rich populations, respectively. Some studies investigated the radial density profile of blue and red GCs in several early-type galaxies, and concluded that blue GCs are more extended to the outer region of galaxies, as compared to the red ones (Kissler-Patig et al. 1997; Lee et al. 1998; Strader et al. 2011; Forbes et al. 2012). Wang et al. (2013) and Park & Lee (2013) studied the two-dimensional structure of

GC systems in early-type galaxies of the Virgo cluster. They found that red GCs are more elongated along the galaxy stellar light than blue ones, although both GC systems are well-aligned with the major axis of their host galaxies. The different shapes of these two kinds of GC populations imply that early-type galaxies have dual halos.

Kinematics of both GC populations provides a clue to reveal their own formation mechanism as well as that of their host galaxy. There have been large spectroscopic surveys of GCs in early-type galaxies, from which it is found that the kinematics features of blue and red GCs in early-type galaxies are diverse (Brodie & Strader 2006, and references therein). Recently, Pota et al. (2013) presented a homogenoues spectroscopic survey of GCs in 12 early-type galaxies. They found that red GCs exhibit kinematic features similar to those of their host galaxy light and blue GCs show random motions in most sample galaxies. However, since there are still some exceptions, it is difficult to argue strongly that there exist a clear difference in kinematics between blue and red GCs, corresponding to color bimodality.

To explain above observation results, several scenarios have been proposed so far (see a review by West et al. 2004). Ashman & Zepf (1992) and Zepf & Ashman (1993) suggested that elliptical galaxies are formed by gas-rich major mergers between disk galaxies. Consequently, in this model, metal-poor GCs originated from the progenitor spirals and metal-rich GCs were formed during merging epoch. Forbes et al. (1997) suggested a multiphase collapse scenario that metal-poor GCs were formed during the early stage of galaxy formation at high redshift and metal-rich GCs were during second collapse phase after a few Gyr. Côté et al. (1998) suggested an accretion scenario that metal-rich GCs were formed in a massive seed galaxy and metal-poor GCs were accreted from nearby low-mass galaxies. Lee et al. (2010b) proposed a mixture model that includes key ingredients of the previous models described above. Metal-poor GCs were mainly formed in low-mass dwarf galaxies and

metal-rich GCs were formed in massive galaxies in-situ or dissipative merging galaxies later than metal-poor GCs. Massive galaxies grows via dissipationless mergers with surrounding dwarf galaxies. Consequently, metal-poor GCs in massive galaxies originated from dwarf galaxies via accretion. From these scenarios to explain the origin of GC subpopulations, we extend our understanding of the formation process of their host galaxy as well.

1.3 GCs in Interesting Environments

1.3.1 Wandering GCs

White (1987) predicted "galaxy cluster-wide population of globulars", which are called intracluster GCs (IGCs). They are controlled by the gravitational potential of their host galaxy cluster, not that of any single galaxy. Muzzio (1987) and West et al. (1995) also addressed the presence of the IGCs. Consequent observational studies detected the IGCs in various galaxy clusters: Virgo (Tamura et al. 2006; Williams et al. 2007; Lee et al. 2010a, 2011; Durrell et al. 2014), Fornax (Bassino et al. 2003; Bergond et al. 2007; Schuberth et al. 2008, 2010; D'Abrusco et al. 2016), Coma (Peng et al. 2011), A1185 (Jordán et al. 2003; West et al. 2011), A1689 (Alamo-Martínez et al. 2013), and A2744 (Lee & Jang 2016).

These studies discussed the origin of the IGCs by investigating their photometric and spectroscopic properties. They found that most IGCs have bluish color, which indicates that they are metal-poor populations. According to the GC formation scenarios described in Section 1.2, they might originate from low-mass dwarf galaxies and be tidally stripped to galaxy cluster region. Bekki & Yahagi (2006) also supported this scenario based on high resolution cosmological simulations. They assumed that the GCs were formed at high redshift ($z > 6$) and that galaxies and clusters grow via dissipationless merging.

In addition, the kinematics of the IGCs is also expected to be clearly distinct from the galactic GCs. The IGCs are governed by the gravitational potential of their host galaxy cluster, so that they might have larger peculiar motion than the GCs in the individual galaxy potential. However, there have been no extensive kinematic studies of IGCs in any galaxy cluster so far.

1.3.2 GCs in Merger Remnant Galaxies

According to ΛCDM hierarchical galaxy formation model, massive early-type galaxies form by continuous mergers of small galaxies (Toomre & Toomre 1972; Toomre 1977). Merger remnant galaxies show snap shots of the transition phase to massive elliptical galaxies. They have various merging features produced by major or minor merging a few Gyrs ago. Schweizer et al. (1990) defined the fine structure index Σ as a quantitative parameter about the amount of fine structures in galaxies as follows.

$$\Sigma = S + log(1 + n) + J + B + X, \tag{1.1}$$

where S is the strength of the most prominent ripples, n is the number of detected ripples, J is the number of jets, B is the maximum boxiness of isophotes, and X is the existence of an X structure. They found that there is a correlation between fine structure indices and Hβ absorption strengths of elliptical galaxies. It indicates that ellipticals with more merging features like merger remnant galaxies have more intermediate-age (2-7 Gyr) populations. There are several studies about the GCs in merger remnant galaxies to understand the formation history of the galaxies based on the second-generation GCs formed by merger-induced star formation: e.g. NGC 3610 (Strader et al. 2003, 2004; Bassino & Caso 2017), NGC 1316 (Goudfrooij et al. 2001a,b, 2004), NGC 1700, NGC 2865, NGC 4382, and NGC 7727 (Trancho et al. 2014).

1.4 IGCs in the Virgo

The Virgo Cluster is the nearest galaxy cluster at 16.5 Mpc (Mei et al. 2007), consisting of on the order of 2000 galaxies. It is a dynamically young galaxy cluster with several subclusters (Binggeli et al. 1985, 1987, 1993): the main cluster A centered on M87; the cluster B centered on M49; three small clouds named M, W, and W′ clouds (de Vaucouleurs 1961); the NGC 4636 group; and so on.

Several studies reported the presence of IGCs in the Virgo cluster, especially around M87. M87 is the most massive elliptical galaxy in the Virgo cluster, classified as a cD galaxy. Tamura et al. (2006) found the marginal signal of the presence of IGCs at $R > 450$ kpc from M87. After, Lee et al. (2010a) constructed the surface number density map of the GCs in the entire region of the Virgo cluster. They found a diffuse large scale distribution of GCs extending out to the boundary of Virgo. It also shows that GCs are concentrated on several substructures centered on massive galaxies but much larger than galaxies. Recently, Durrell et al. (2014) showed a number density map of the Virgo GCs of which scale is finer than that of Lee et al. (2010a), using the Next Generation Virgo Cluster Survey (Ferrarese et al. 2012). The IGCs appears to be mostly blue and are probably dominated by the potential of the galaxy cluster or substructures in Virgo, rather than by that of a single galaxy.

1.5 GCs in M85

M85 is one of the most famous merger remnant galaxies located at the northernmost region of the Virgo cluster. It is classified as S0pec, and several studies reported that it has some signatures resulting from the consequence of merging events. M85 has the second highest fine structure index, $\Sigma = 6.85$ in the list of elliptical and S0 galaxies presented in Schweizer & Seitzer (1992). It shows the distorted isophotes due to its neighbor galaxies (Burstein 1979), a dozen of irregular ripples Schweizer &

Table 1.1. Basic Information of M85

Parameter	Value	References
R.A. (J2000)	12:25:24.1	1
Decl. (J2000)	+18:11:29	1
Morphological type	$S0_1(3)$pec	2
Blue total magnitude, B_T	10.09	2
V-band total magnitude, V_T	8.82	3
Distance	17.86 Mpc	4
Distance modulus, $(m-M)_0$	31.26 ± 0.05	4
Foreground reddening, $E(B-V)$	0.0239	5
Effective radius from Sérsic fit, $R_{\rm eff}$	$128\farcs89^{+10.2}_{-8.8}$	3
Radial velocity, $v_{\rm r}$	729 ± 2 km s^{-1}	6

Reference. – (1) NASA/IPAC Extragalactic Database, (2) Binggeli et al. (1985), (3) Kormendy et al. (2009), (4) Mei et al. (2007), (5) Schlafly & Finkbeiner (2011), (6) Smith et al. (2000)

Seitzer (1988), bluish core (Fisher et al. 1996), two brightness peak in the core region (Lauer et al. 2005). Kormendy et al. (2009) found that the surface brightness profile of M85 is highly distorted and different from that of typical S0 galaxies. Based on this feature, they suggested that M85 is not yet relaxed because of recent merger events. The basic information of M85 is listed in Table 1.1.

Despite its interesting morphology mentioned above, the GCs in M85 have been rarely studied. Peng et al. (2006) suggested that the color distribution of M85 GCs is not bimodal but trimodal, indicative of the presence of intermediate-age (1–3

Gyr) GCs based on photometry of the *Hubble space telescope/ACS* Virgo Cluster Survey (Côté et al. 2004; Jordán et al. 2009). In addition, Trancho et al. (2014) also detected some intermediate-age GCs using Gemini/NIRI K_s-band photometry combined with HST optical photometry. However, these previous studies covered only a small ($2' \times 2'$, corresponding to 8 kpc $\times$ 8 kpc) region of M85.

1.6 Purpose and Outline of the Thesis

In this thesis, we perform an extensive survey of GC systems in two examples of the interesting environments: Virgo and M85. We identify the genuine IGCs in the central region of the Virgo cluster covering $2^\circ \times 2^\circ$ field near M87. We analyze the kinematics of the IGCs in the Virgo for the first time and discuss the origin of the IGCs. In addition, we carry out a comprehensive GC survey over 1° diameter field around M85 covering the widest extent to date. We investigate the physical properties of GC subpopulations in M85. Based on spectroscopic data, the ages and metallicities of the GCs are measured as well as their kinematics. We discuss their own origins of the GCs as well as their host environments.

This thesis is organized as follows. In Chapter 2, we present the results of a wide-field spectroscopic survey of GCs in the Virgo cluster. The survey covers the central region of the Virgo including M84, M86, and a part of M87. We identify IGCs in the Virgo, and investigate their photometric and kinematic properties. The origins of Virgo IGCs are discussed in this chapter. In Chapter 3, 4, and 5, we present the results of photometric and spectroscopic survey of GCs in the merger remnant galaxy M85. The photometric properties of the GC candidates in M85 are described in Chapter 3. We perform first spectroscopic surveys for these GC candidates in M85, and confirm the genuine GCs that belong to M85. The ages and metallicities of the M85 GCs are presented in Chapter 4. We investigate the kinematics of the GC system of M85 in Chapter 5. Based on the photometric and spectroscopic properties

of the GCs, we discuss the merging history of M85. We summarize our main results of the thesis in Chapter 6.

Chapter 2

To the Edge of M87 and Beyond: Spectroscopy of IGCs and Ultra Compact Dwarfs in the Virgo Cluster

2.1 Introduction

[a] The central regions of galaxy clusters provide a dense environment where galaxies interact frequently. This results in the abundant tidal debris in the intergalactic region. The intracluster light of galaxy clusters is understood to be the tidal debris stripped from cluster galaxies, and it is commonly detected not only in nearby galaxy clusters but also in z $\sim$ 1 galaxy clusters (Adami et al. 2005; Gonzalez et al. 2005; Mihos et al. 2005; Zibetti et al. 2005; Krick et al. 2006; Krick & Bernstein 2007; Burke et al. 2012; Mihos 2015). It is also expected that the GCs stripped

[a]This chapter is published in the Astrophysical Journal (Ko, Y. et al. 2017, ApJ, 835, 212).

from cluster galaxies populate the intergalactic region. They are called IGCs, the existence of which has been proposed by various studies (Muzzio 1987; White 1987; West et al. 1995). They do not belong to any individual galaxies but wander between galaxies. There have been several attempts to identify these IGCs in several galaxy clusters, including Fornax (Bassino et al. 2003; Bergond et al. 2007; Schuberth et al. 2008, 2010; D'Abrusco et al. 2016), Coma (Peng et al. 2011), A1185 (Jordán et al. 2003; West et al. 2011), A1689 (Alamo-Martínez et al. 2013), and A2744 (Lee & Jang 2016).

The Virgo cluster is an excellent target to investigate IGCs because of its proximity. Several studies have reported the presence of IGCs based on wide-field imaging surveys of GCs in the Virgo. Tamura et al. (2006) performed a wide-field photometric survey of GCs up to a galactocentric radius of $\sim$ 500 kpc from the most massive galaxy of the Virgo, M87. They detected a marginal excess of the surface number density of GCs compared with model predictions, which indicates the presence of IGCs. Lee et al. (2010a) presented a large-scale map of GCs covering the entire Virgo cluster using SDSS photometric data and suggested that there are a significant number of IGCs in the Virgo ($N \sim$ 11,900). Recently, Durrell et al. (2014) used the Next Generation Virgo Cluster Survey (NGVS; Ferrarese et al. 2012) data, showing a number density map of Virgo GCs with a finer scale than that of Lee et al. (2010a). Most of these studies found that IGCs have bluish colors, consistent with the idea that they originate from low-mass dwarf galaxies. This scenario is supported by *Hubble Space Telescope (HST)/ACS* photometry of resolved stars in four IGC candidates in the Virgo (Williams et al. 2007); these IGC candidates contain metal-poor stars with [M/H] $<$ -1.

Spectroscopy is very efficient in removing foreground and background contamination in the photometric candidates of IGCs, because the radial velocities of the targets can be derived. However, there is only one spectroscopic observation of IGCs

in the Virgo in the literature. Firth et al. (2008) obtained spectra of IGC candidates in the Virgo and confirmed only three IGCs at $\sim$ 750–850 kpc from M87. In the central region of the Virgo, it is also important to distinguish the IGCs from the GCs bound to M87.

M87 is the most massive elliptical galaxy located in the central region of the Virgo, and it is known as a marginal cD galaxy, of which the cD halo begins to emerge at $R = 3' - 7'$, corresponding to 15 – 35 kpc (Liu et al. 2005; Kormendy et al. 2009). Mihos et al. (2005) found that the cD halo of M87 is stretched to about 200 kpc. M87 hosts a significant number of GCs up to $\sim$ 200 kpc (Lee et al. 2010a). Côté et al. (2001), Strader et al. (2011), and Zhu et al. (2014) have performed spectroscopic surveys of GCs around M87, but their radial coverage is only at $R < 150$ kpc, which is not large enough to find IGCs.

The velocity dispersion of IGCs is expected to be larger than that of GCs bound to individual galaxies because IGCs are governed by the gravitational potential of their host cluster. Strader et al. (2011) quantitatively discussed the presence of IGCs with extreme radial velocities higher than 1000 km s^{-1} relative to the system velocity of M87. These IGCs with extreme velocities can increase the velocity dispersion of IGCs. Based on the number density of GCs beyond 40 kpc from M87 estimated by Tamura et al. (2006), Strader et al. (2011) expected that there might exist 17-87 IGCs in their survey field. Then they suggested that 16-67% of the IGCs in their survey field may have extreme radial velocities, similar to the fractions of intracluster planetary nebulae (ICPNe) and Virgo galaxies with extreme velocities. However, Strader et al. (2011) could not identify individual IGCs, because their survey field covered only the M87 region at $R < 150$ kpc. On the other hand, Caldwell et al. (2014) reported a hypervelocity GC with $v_r \sim -1025$ km s^{-1}. However, they concluded that it is not a Virgo IGC, but an object ejected from the Virgo.

In this chapter, we present a wide-field ($2^\circ \times 2^\circ$) spectroscopic survey of Virgo

IGCs and ultracompact dwarfs (UCDs) with MMT/Hectospec. This chapter is organized as follows. We briefly describe the spectroscopic observation and data reduction in Section 2.2. In Section 2.3, we select the genuine GCs in the Virgo, distinguishing them from contaminants such as foreground stars and background galaxies. We identify IGCs using spatial and kinematic information and compare their kinematics with those of other tracers, including UCDs, dwarf galaxies, and M87 GCs. We discuss and summarize the results in Sections 2.4 and 2.5, respectively. We adopted a distance to M87 of 16.5 Mpc (Blakeslee et al. 2009). One arcminute corresponds to 4.80 kpc at the distance to M87. The heliocentric radial velocity of M87 is 1260 km s^{-1} (Kim et al. 2014).

2.2 Observation and Data Reduction

2.2.1 Target Selection for Spectroscopy

We selected GC candidates using the NGVS archival images covering the central region of the Virgo cluster. The NGVS is a wide-field imaging survey of the Virgo cluster using MegaCam with a field of view of $1^\circ \times 1^\circ$ attached at the Canada–French–Hawaii Telescope (Ferrarese et al. 2012). The calibrated images were retrieved, covering an about $3^\circ \times 2^\circ$ field, which includes M86, M84, and part of M87, shown in Figure 2.1. We performed astrometry for these images using SCAMP (Bertin 2006) and combined them using SWarp (Bertin et al. 2002) to make mosaic images in each filter.

We used SExtractor (Bertin & Arnouts 1996) to detect sources with a threshold of 3σ and performed aperture photometry with an aperture radius of $1''$. Because most of the GCs at the distance of the Virgo cluster appear as point sources in the NGVS images, we selected point sources as GC candidates using the "CLASS_STAR" (stellarity index) parameter of SExtractor. The stellarity index ranges from 0 to 1,

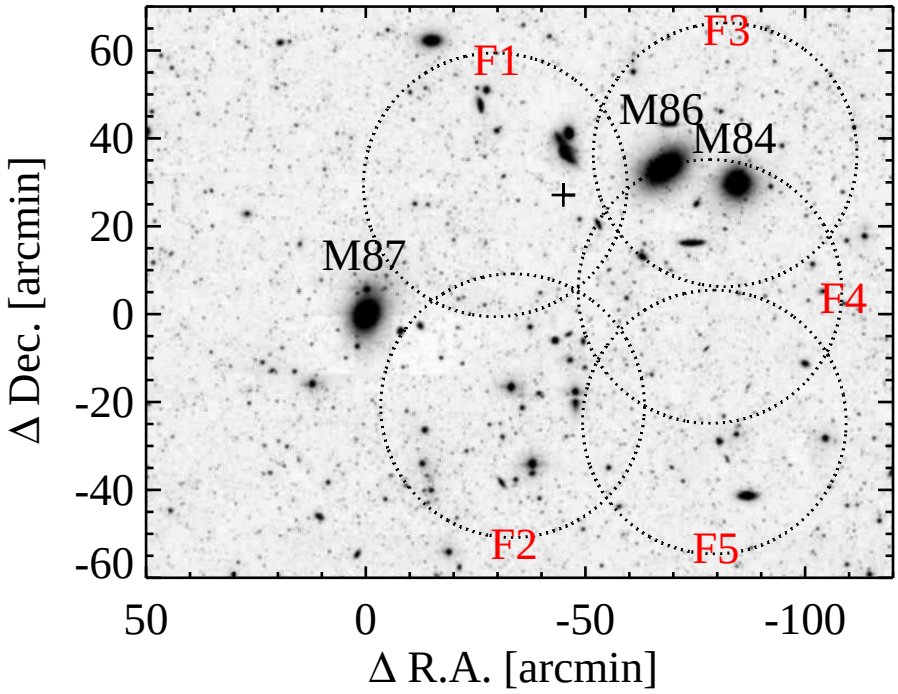

Figure 2.1: Field configuration for the MMT/Hectospec observation overlaid on the gray-scale map of the SDSS. A dotted-line circle represents a field of view of MMT/Hectospec with a 1° diameter. The cross indicates the center of the Virgo cluster derived from the number density map of dwarf galaxies in the Virgo (Binggeli et al. 1985).

based on a comparison between the FWHM of each source and a given seeing size. If this value of a given source is close to 1, the source is thought to be a point source. We used a generous criterion to select many spectroscopic targets: stellarity index $\geq$ 0.35 in *gri* filters. For these point sources, we performed standard calibration using SDSS DR12 *gri* PSF photometry (Alam et al. 2015) after transforming the SDSS to

the CFHT/Megacam filter system.[b] We used the foreground galactic extinction values for the Virgo derived by Schlafly & Finkbeiner (2011). Hereafter, all photometry results are based on the AB magnitude and CFHT/MegaCam filter system.

Figure 2.2 shows the $i_0 - (g-i)_0$ color-magnitude diagram (CMD) and $(g-r)_0 - (r-i)_0$ color-color diagram (CCD) for the point sources in the field of $3^\circ \times 2^\circ$ around the central region of the Virgo. Typical GCs in the Virgo have a color range of $0.6 < g - i < 1.25$ (Durrell et al. 2014). We used a color range, $0.6 < (g-i)_0 < 1.6$, for target GC selection. We adopted a redder color limit ($(g-i)_0 = 1.6$) to include more spectroscopic GC targets for filling the available fibers. We also used the $(g-r)_0 - (r-i)_0$ CCD to select GC candidates following the color criteria used for selecting M31 GCs in Peacock et al. (2010). Peacock et al. (2010) provided SDSS photometry of the M31 GCs in the AB magnitude system, so we transformed it to the system in this paper. The selection color criteria are as follows:

$$(g-r)_0 < 1.33 \times ((r-i)_0 - 0.39) + 0.82, \text{ and}$$

$$(g-r)_0 > 1.33 \times ((r-i)_0 - 0.63) + 0.72.$$

We also set the magnitude limit ($17.0 < i_0 < 20.9$) to remove possible contamination by bright foreground stars and to avoid too faint targets. We then visually inspected all the targets to remove background galaxies. We included 11 additional GC candidates that have resolved HST/ACS photometric data (Lee et al. 2011). In total, we selected 910 GC candidates for spectroscopic observations.

2.2.2 Spectroscopic Observation

We carried out spectroscopic observation of GC candidates in the Virgo using the Hectospec (Fabricant et al. 2005) mounted on the 6.5m Multiple-Mirror Telescope in queue mode under the program ID 2014A-UAO-G18 (PI: Myung Gyoon Lee)

[b] http://www.cadc-ccda.hia-iha.nrc-cnrc.gc.ca/en/megapipe/docs/filt.html

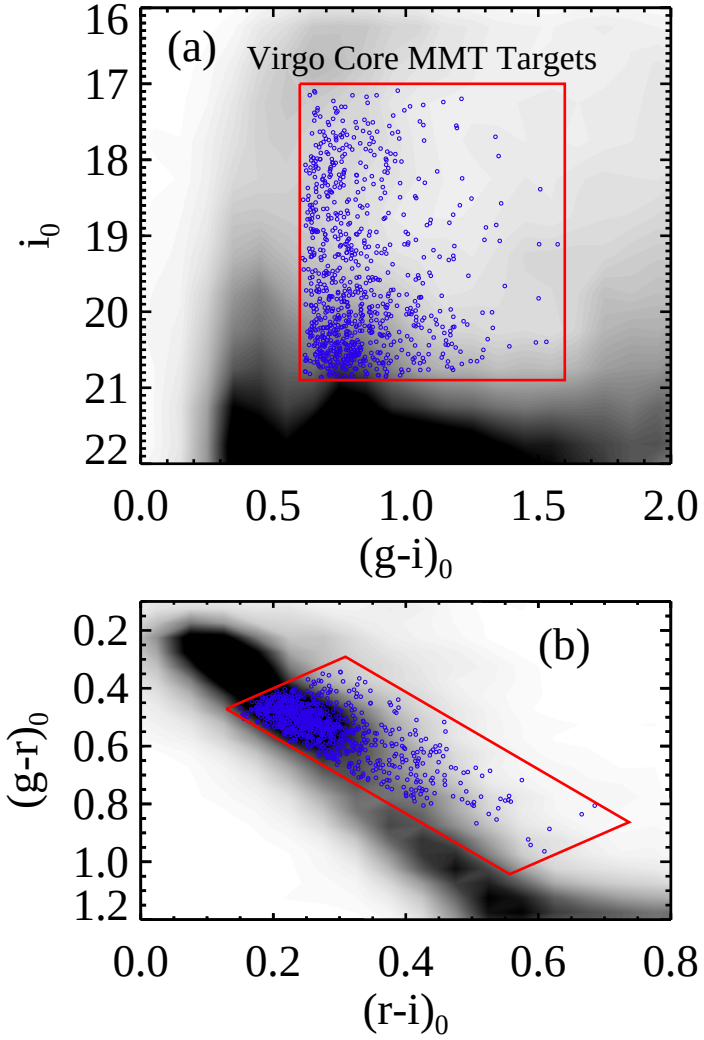

Figure 2.2: Target selection for spectroscopy. (a) $i_0 - (g-i)_0$ CMD and (b) $(g-r)_0 - (r-i)_0$ CCD of the point sources in the $3^\circ \times 2^\circ$ field around the center of the Virgo derived from the NGVS data. The blue circles inside the red-line boxes represent the spectroscopic targets observed in this study. The gray scale represents the Hess diagram.

Table 2.1. Observation Log for the MMT/Hectospec Run

Mask Name	α (J2000)	δ (J2000)	N^a	Exp. Time	Date (UT)
Virgo-F1	12:25:13.66	+12:59:43.8	258	5 × 1440 s	2014 Feb 25
Virgo-F2	12:25:25.00	+11:58:55.3	255	5 × 1440 s	2014 Feb 26
Virgo-F3	12:25:28.50	+12:28:38.1	255	5 × 1440 s	2014 Feb 27
Virgo-F4	12:28:32:69	+12:02:38.3	258	5 × 1440 s	2014 Mar 24
Virgo-F5	12:28:48.44	+12:52:53.6	258	5 × 1440 s	2014 Mar 25

Note. — [a] Number of object fibers among 300 fibers in each field. The remaining fibers are assigned to sky regions.

between 2014 February and March. The Hectospec is a 300-fiber-fed optical spectrograph with a circular field of view of 1° in diameter. We selected a 270 mm^{-1} grating with a dispersion of 1.2 Å $pixel^{-1}$, covering the wavelength range of 3650 Å to 9200 Å. We made five different configurations, covering the central region of the Virgo, as shown in Figure 2.1. The field coordinates and exposure times are given in Table 2.1. We used 5 × 24 minute exposures for each field.

2.2.3 Data Reduction and Radial Velocity Measurement

We used version 2.0 of the HSRED reduction pipeline[c] for data reduction. The pipeline includes bias and dark correction, flat-fielding, aperture extraction of spectra, and wavelength calibration. Flux calibration was done following the steps in

[c]This is an updated reduction pipeline originally developed by Richard Cool, and more details can be found at http://www.mmto.org/node/536.

Fabricant et al. (2008), which include atmospheric extinction correction, Hectospec relative throughput correction, and absolute flux normalization with SDSS r photometry. The spectral resolution is ~ 6 Å. The median signal-to-noise ratios of the spectra of GC candidates at 3700 Å – 7000 Å range from 4 to 72. We derived the heliocentric radial velocities of GC candidates using the xcsao task in the IRAF RVSAO package (Kurtz & Mink 1998). We used 10 templates, including the spectra of an A star, three M31 GCs, an SDSS QSO, and elliptical and spiral galaxies in the RVSAO package. To apply the cross-correlation method (Tonry & Davis 1979), we used the absorption features of the target spectra and templates over the wavelength range of 3800–5400 Å where there are no strong sky emission lines–only prominent absorption lines. We adopted the radial velocities of targets with the highest correlation coefficient and visually inspected all spectra with the absorption lines shifted as their derived radial velocities. We matched the targets with $v_{\rm r} > 3000$ km s^{-1} with galaxy spectra and the others with GC spectra. The radial velocity uncertainties were derived by the correlation error, and their mean value is 28 km s^{-1}. For 19 out of the 910 targets, we could not determine the radial velocities because of low signal-to-noise ratios (< 5). The radial velocities of targets derived in this study agree well with those from the literature (see Section 2.3.1).

2.3 Results

2.3.1 Construction of GC and UCD samples

Identification of GCs and UCDs from the spectroscopic sample

We distinguish GCs from contaminants using several criteria among the spectroscopic targets. The possible contaminants and their classification criteria are (1) background galaxies with $v_{\rm r} > 3000$ km s^{-1}, (2) UCDs with $v_{\rm r} < 3000$ km s^{-1} and $r_{\rm h} > 9.5$ pc, and (3) foreground stars with $v_{\rm r} < 500$ km s^{-1} and their marked spectral

features. The detailed classification procedure of each step is described as follows.

First, we classify targets with $v_{\rm r} > 3000$ km s^{-1} as background galaxies. Kim et al. (2014) presented the Extended Virgo Cluster Catalog (EVCC) and showed that there is a dip at $v_{\rm r} \sim 3000$ km s^{-1} in the velocity distribution of the galaxies in the EVCC, separating galaxies in the Virgo cluster from background galaxies. Among the spectroscopic targets, there are 93 background galaxies. They have radial velocities of 23,427 km s^{-1} $< v_{\rm r} <$ 240,257 km s^{-1}.

Second, we use the NGVS i band images to measure the sizes of 798 GC candidates at $v_{\rm r} < 3000$ km s^{-1} with the ISHAPE (Larsen 1999) to distinguish GCs from UCDs. The PSF FWHMs of the NGVS images we used are in the range of 2.3-4.8 pixels, which correspond to $0\farcs4$-$0\farcs9$. The ISHAPE manual suggests that the size estimates are reliable only when the FWHMs are greater than $\sim 0.1 \times {\rm FWHM_{PSF}}$. We estimate the FWHM of 106 GC candidates using the KING30 function. The half-light radii ($r_{\rm h}$) are derived by multiplying the FWHM by 1.48 following the ISHAPE manual. They range from 5.3 pc to 33.7 pc, assuming that the distance to the Virgo is 16.5 Mpc. These are larger than the mean half-light radius of the GCs in Virgo galaxies (2.9 $\pm$ 1.2 pc) derived from HST/ACS images (Jordán et al. 2009), because we cannot derive the half-light radii of GCs smaller than 4.9 pc from ground-based images, which have limited resolution. Figure 2.3 shows a comparison of the half-light radii of GCs and UCDs derived in this study with those from the literature (Jordán et al. 2009; Liu et al. 2015; Zhang et al. 2015). The size measurements of two GCs show a difference between this study and Jordán et al. (2009). We use ISHAPE on the NGVS images for the size measurement, while Jordán et al. (2009) used KINGPHOT on the HST/ACS images. Thus, this difference for the GCs is mainly due to the difference in image resolution and size-measuring software. However, for most of the UCDs, the sizes are well consistent with those from Liu et al. (2015) and Zhang et al. (2015), who used KINGPHOT on the NGVS images.

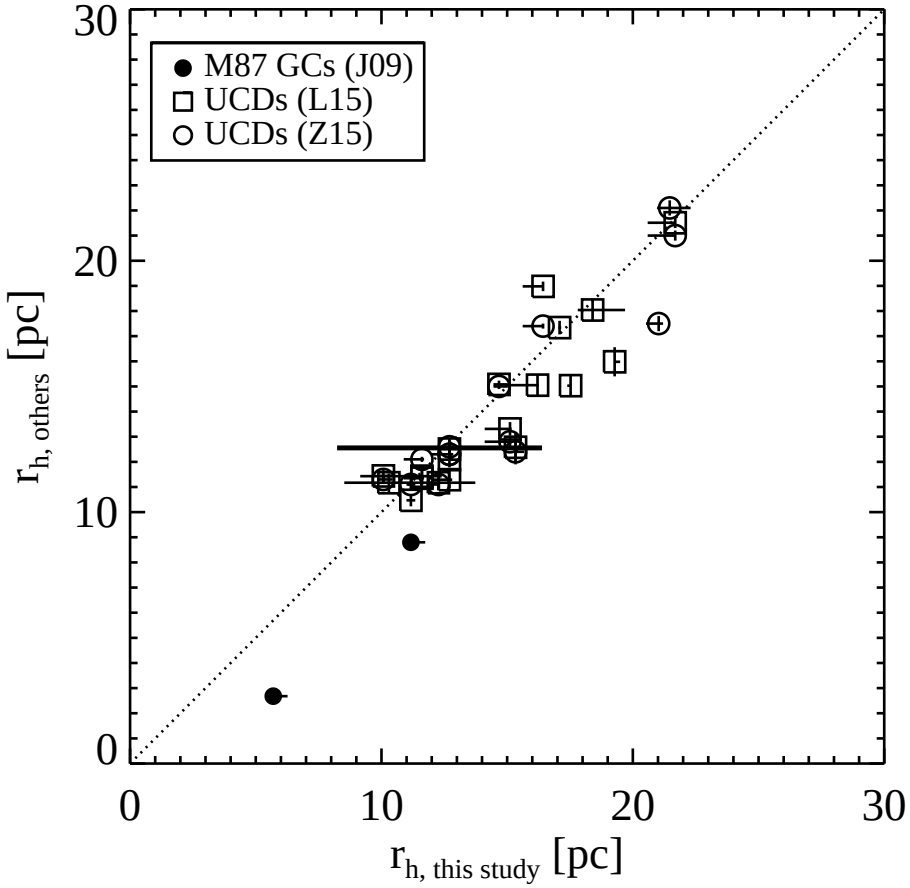

Figure 2.3: Comparison of the half-light radii derived in this study with those derived in previous studies. The filled circles, open circles, and open squares represent the GCs in M87 (Jordán et al. 2009), the UCDs in M87 (Zhang et al. 2015), and the UCDs in M87 (Liu et al. 2015), respectively. The dotted line denotes the one-to-one relation.

Some outliers of the UCDs are due to the difference in the size-measuring software between this study and other studies. Following the criterion in Strader et al. (2011), we classify targets with $r_{\rm h} > 9.5$ pc as UCDs. We find 55 UCDs in our sample.

Third, we remove foreground stars using size estimates, radial velocities, and spectral features. Among 743 GC candidates, we classify 51 objects that have half-light radii of 5.3 pc $< r_{\rm h} <$ 9.5 pc as GCs in the Virgo because they are more significantly extended than the PSF. Among the rest of the GC candidates, we select 95 with 500 km s^{-1} $< v_{\rm r} <$ 3000 km s^{-1} as genuine GCs in the Virgo. Galactic stars rarely have radial velocities greater than 500 km s^{-1}. In addition, three of the authors independently conduct visual inspection of the spectra of the remaining 597 objects with $v_{\rm r} <$ 500 km s^{-1}. We compare the features of the target spectra with those of template spectra. We use the spectra of the GCs with 500 km s^{-1} $< v_{\rm r} <$ 3000 km s^{-1} in this study and those of Galactic stars in Santos et al. (2001) as templates. Figure 2.4 shows the spectra of the GCs and Galactic stars classified in this study. For the GC spectra, the continuum slope between 4000 Å and 7000 Å differs depending on the GC color. Compared with that in the GC spectra, the Mgb absorption line is generally broader and stronger in the spectra of the stars, especially of the dwarf stars. The visual inspection results in a sample of 55 GCs with $v_{\rm r} <$ 500 km s^{-1}. Finally, we obtain 201 GCs, 55 UCDs, 542 foreground stars, and 93 galaxies from 910 spectroscopic targets. Table 2.2 lists the foreground stars and background galaxies observed in this study, and Tables 2.3 and 2.4 list the photometric and spectroscopic parameters of the GCs and UCDs.

Figure 2.5 shows the $i_0 - (g-i)_0$ CMD of GCs, UCDs, foreground stars, and galaxies in the spectroscopic targets. The majority of the GCs and UCDs have a color range of $0.6 < (g-i)_0 < 1.0$. Most of the red objects with $(g-i)_0 > 1.0$ turn out to be foreground stars or background galaxies. We discuss in detail the color distribution of GCs in Section 2.4.2. The i_0 magnitudes of most of the GCs, UCDs,

Table 2.2. Spectroscopic and photometric properties of foreground stars and background galaxies

ID	α (J2000) (deg)	δ (J2000) (deg)	i (mag)	$g-r$ (mag)	$g-i$ (mag)	$v_{\rm r}$ (km s^{-1})
STAR001	185.848618	12.998183	19.515 ± 0.002	0.456 ± 0.002	0.685 ± 0.002	–33 ± 15
STAR002	185.851730	13.125706	18.030 ± 0.001	0.533 ± 0.001	0.759 ± 0.001	18 ± 5
STAR003	185.853333	13.100986	19.770 ± 0.002	0.465 ± 0.003	0.703 ± 0.002	–33 ± 20
STAR004	185.857193	12.048497	17.782 ± 0.001	0.502 ± 0.001	0.776 ± 0.001	–95 ± 9
STAR005	185.866241	12.020297	20.861 ± 0.006	0.551 ± 0.006	0.835 ± 0.008	68 ± 25
GAL01	185.852463	12.890166	20.032 ± 0.002	0.724 ± 0.004	1.167 ± 0.003	58978 ± 7
GAL02	185.852768	12.977111	19.596 ± 0.002	0.621 ± 0.003	1.087 ± 0.002	61396 ± 10
GAL03	185.866852	12.093072	20.669 ± 0.005	0.605 ± 0.005	0.920 ± 0.007	240245 ± 186
GAL04	185.875107	12.850986	20.750 ± 0.004	0.575 ± 0.005	0.827 ± 0.005	76235 ± 4
GAL05	185.988205	13.227654	20.826 ± 0.004	0.537 ± 0.006	0.886 ± 0.006	69472 ± 4

Note. — The five sample foreground stars and background galaxies are shown here as guidance for the table's form and content. This table is available in its entirety in machine-readable form from Ko et al. (2017).

Table 2.3. Spectroscopic and photometric properties of the combined GC sample

ID	α (J2000) (deg)	δ (J2000) (deg)	i (mag)	$g-r$ (mag)	$g-i$ (mag)	Phot. Src.[a]	v_r (km s^{-1})	v_r Src.	r_h (pc)	r_h Src.	Host MCLUST[b]	Host Rv cut
GC001	185.872772	13.161441	19.751 ± 0.002	0.557 ± 0.003	0.869 ± 0.002	K16	1137 ± 22	K16	$8.3^{+1.0}_{-0.2}$	K16	IGC (H)	IGC
GC002	185.945038	12.503950	20.254 ± 0.003	0.488 ± 0.004	0.727 ± 0.003	K16	840 ± 51	K16	$6.8^{+0.1}_{-0.2}$	K16	IGC (H)	IGC
GC003	185.950409	13.076539	20.675 ± 0.004	0.546 ± 0.005	0.820 ± 0.005	K16	124 ± 26	K16	-	-	IGC (H)	IGC
GC004	185.970627	12.773033	19.651 ± 0.002	0.552 ± 0.003	0.828 ± 0.002	K16	1167 ± 28	K16	$7.0^{+0.3}_{-0.2}$	K16	M84 (F)	IGC
GC005	185.975204	12.940945	20.595 ± 0.004	0.532 ± 0.005	0.829 ± 0.004	K16	796 ± 47	K16	$6.6^{+1.2}_{-<0.1}$	K16	M84 (F)	IGC
H52724	187.299957	12.466810	20.75	0.52	0.83	S11	1124 ± 15	S11	-	-	M87 (C)	-
H46835	187.313446	12.411310	21.32	0.62	0.80	S11	1253 ± 17	S11	-	-	M87 (C)	-
H57011	187.331863	12.510560	20.54	0.68	0.90	S11	1409 ± 11	S11	-	-	M87 (C)	-
H44278	187.377747	12.390920	21.14	0.54	0.83	S11	1511 ± 27	S11	-	-	M87 (C)	-
H58443	187.411087	12.526390	21.46	0.67	0.73	S11	441 ± 24	S11	-	-	IGC (H)	-

Note. — The five sample GCs confirmed in this study and five sample GCs from Strader et al. (2011) are shown here as guidance for the table's form and content. This table is available in its entirety in machine-readable form from Ko et al. (2017).

[a]The magnitudes in this study and in Strader et al. (2011) are CFHT/MegaCam AB and dereddened SDSS AB magnitudes, respectively.

[b]The MCLUST subgroup that a given GC belongs to (see Table 2.5) is in the parentheses.

Table 2.4. Spectroscopic and photometric properties of the combined UCD sample

ID	α (J2000) (deg)	δ (J2000) (deg)	i (mag)	$g-r$ (mag)	$g-i$ (mag)	Phot. Src.[a]	$v_{\rm r}$ (km s^{-1})	$v_{\rm r}$ Src.	$r_{\rm h}$ (pc)	$r_{\rm h}$ Src.	Mclust Group[b]
UCD01	185.919037	12.211850	20.379 ± 0.004	0.680 ± 0.005	1.143 ± 0.006	K16	867 ± 17	K16	$11.4^{+0.1}_{-0.1}$	K16	C
UCD02	186.069351	13.008061	20.727 ± 0.004	0.503 ± 0.005	0.819 ± 0.005	K16	719 ± 39	K16	$9.9^{+0.6}_{-<0.1}$	K16	C
UCD03	186.190231	13.049951	19.961 ± 0.002	0.622 ± 0.003	1.005 ± 0.003	K16	952 ± 22	K16	$20.8^{+1.6}_{-0.1}$	K16	C
UCD04	186.192642	12.341794	19.766 ± 0.003	0.503 ± 0.003	0.808 ± 0.003	K16	955 ± 19	K16	$10.7^{+0.1}_{-0.4}$	K16	C
UCD05	186.242004	12.895044	20.096 ± 0.002	0.621 ± 0.004	0.983 ± 0.003	K16	1219 ± 23	K16	$18.4^{+0.8}_{-0.9}$	K16	C
M87UCD-29	187.027588	12.410120	20.21	0.52	0.73	Z15	599 ± 33	Z15	12.6 ± 0.3	Z15	A
M87UCD-34	187.311966	11.895510	19.40	0.54	0.79	Z15	905 ± 19	Z15	11.7 ± 0.3	Z15	A
M87UCD-20	187.422165	12.664570	19.45	0.52	0.80	Z15	1754 ± 105	Z15	16.7 ± 0.3	Z15	A
M87UCD-22	187.467834	12.627160	19.92	0.59	0.88	Z15	905 ± 20	Z15	11.7± 0.2	Z15	A
M87UCD-10	187.508118	12.707470	19.17	0.45	0.69	Z15	1178 ± 30	Z15	21.9 ± 0.3	Z15	A

Note. — The five sample UCDs confirmed in this study and five sample UCDs from Zhang et al. (2015) are shown here as guidance for the table's form and content. This table is available in its entirety in machine-readable form from Ko et al. (2017).

[a]The magnitudes in this study and in Strader et al. (2011) are CFHT/MegaCam AB and dereddened SDSS AB magnitudes, respectively.

[b]The Mclust subgroup that a given UCD belongs to (see Table 2.5) is in the parentheses.

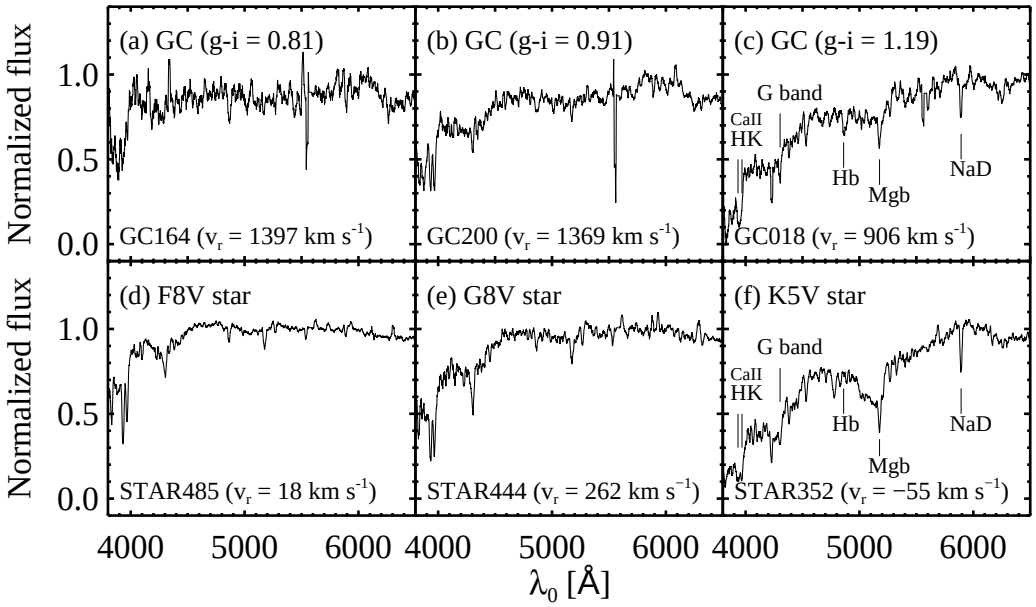

Figure 2.4: Sample spectra of GCs and foreground stars. (a) a GC (ID: GC164) with $i = 20.459$ mag and $(g - i) = 0.81$; (b) a GC (ID: GC200) with $i = 19.371$ mag and $(g - i) = 0.91$; (c) a GC (ID: GC018) with $i = 20.471$ mag and $(g - i) = 1.19$; and (d)–(f) stars with $i = 19.481$, 20.041 and 18.427 mag classified as F8V (ID: STAR485), G8V (ID: STAR444), and K5V (ID: STAR352) stars by the HSRED package, respectively. All flux-calibrated spectra are plotted in the rest frame, smoothed using a boxcar filter with a size of 12 Å, and normalized at 5800 – 5850 Å.

and background galaxies are in the range of $18.7 < i_0 < 20.8$, but those of the stars are in the range of $17.0 < i_0 < 20.8$. One GC with $i_0 = 17.8$ (ID: GC068) is 1.5 mag brighter than other GCs, while it has a half-light radius similar to those of other GCs confirmed in this study ($r_{\rm h} \sim 6$ pc). Consequently, its luminosity density is $\sim 5 \times 10^4 L_{i,\odot}$ pc^{-2}, which is higher than those of other GCs and UCDs (around a few thousand $L_{i,\odot}$ pc^{-2}). Misgeld et al. (2011) and Sandoval et al. (2015) reported

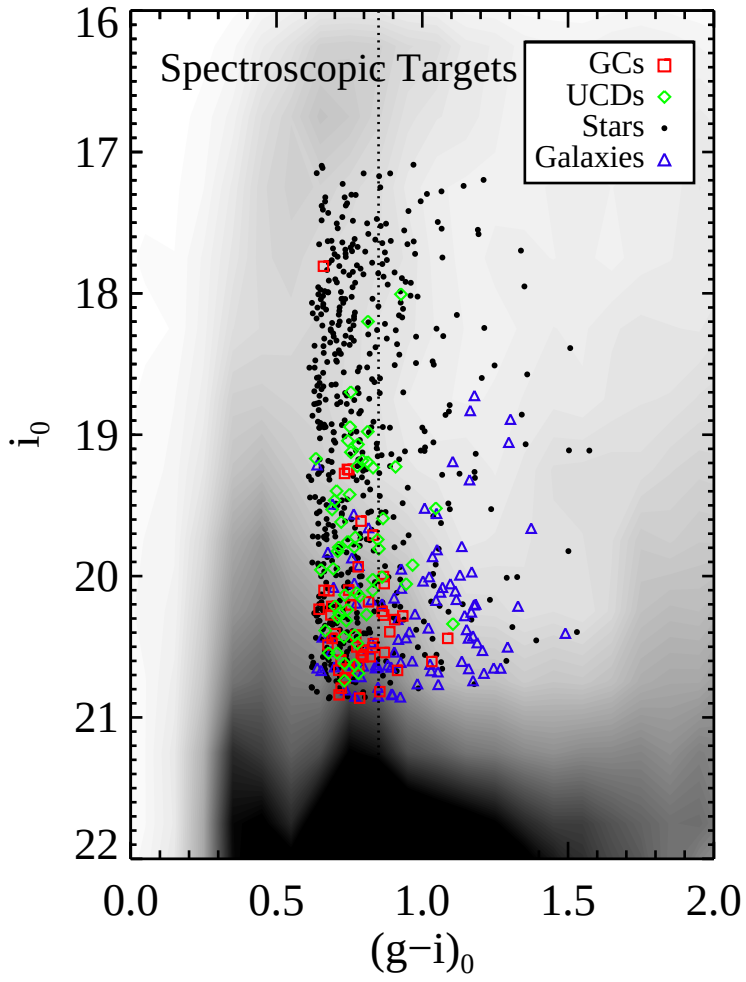

Figure 2.5: $i_0 - (g-i)_0$ CMD of the spectroscopic targets classified in this study. The gray scales are the same as in Figure 2.2(a). The squares, diamonds, circles, and triangles represent GCs, UCDs, foreground stars, and galaxies, respectively. The dotted line is $(g-i)_0 = 0.8$, which is a criterion to divide GCs into blue and red ones.

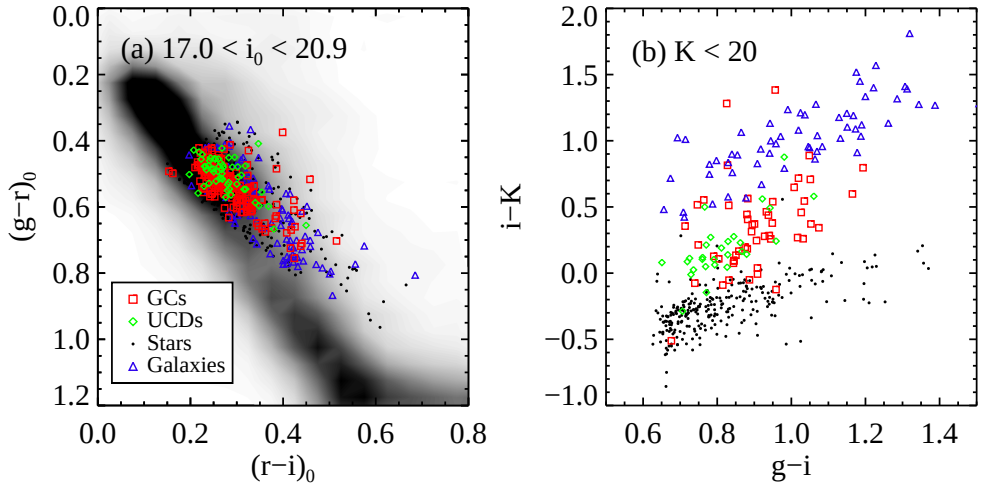

Figure 2.6: (a) $(g-r)_0-(r-i)_0$ CCD of the spectroscopic targets classified in this study. The gray scale is the same as in Figure 2.2(b). (b) $(i-K)-(g-i)$ CCD of the spectroscopic targets with $K<20$. The Petrosian magnitudes are used in this plot. The symbols are the same as in Figure 2.5.

the existence of some dense stellar systems in UCD and compact cluster samples. The luminosity densities of HUCD1 in Hydra I (Misgeld et al. 2011), M59-UCD3, and M85-HCC1 (Sandoval et al. 2015) are $\sim 4.8\times10^3 L_{V,\odot}$ pc^{-2}, $\sim 2.7\times10^4 L_{r,\odot}$ pc^{-2}, and $\sim 4\times10^5 L_{r,\odot}$ pc^{-2}, respectively. The luminosity density of GC068 in this study is comparable with that of M59-UCD3, five times as high as that of HUCD1, and one tenth that of M85-HCC1.

Figure 2.6 shows the $(g-r)_0-(r-i)_0$ and $(i-K)-(g-i)$ CCDs for the spectroscopic targets. Many GCs and UCDs are in the color ranges of $0.4<(g-r)_0<0.65$ and $0.2<(r-i)_0<0.35$. The colors of different populations are significantly distinct in the optical to near-infrared CCD (Muñoz et al. 2014). We derive photometry for the point sources in the K-band images taken from UKIRT/WFCAM and use the Petrosian AB magnitudes to construct the CCD. The GCs and UCDs occupy

a similar color domain, but the foreground stars and galaxies are clearly separated from the GCs and UCDs in the $(i-K)-(g-i)$ CCD. There are two GCs in the stellar sequence (ID: GC041 and GC068). They are classified as GCs because GC068 is an extended source ($r_{\rm h}$ = 6 pc) and GC041 has a radial velocity of $v_{\rm r}$ = 812 km s^{-1}.

The radial velocity distributions of the GCs and UCDs are shown in Figure 2.7(a). The GCs and the UCDs have the radial velocities of –800 km s^{-1} to 2600 km s^{-1}. The radial velocity distribution of the GCs shows two peaks at –200 km s^{-1} and 1100 km s^{-1}, which are similar to the radial velocities of M86 and M84, respectively. The UCDs show a similar radial velocity distribution to that of the GCs. The radial velocity distribution of GCs with $v_{\rm r} > 400$ km s^{-1} consists of at least two components, M87 and M84 GCs. The peak at the radial velocity of M87 is not more prominent than that at the radial velocity of M84 because our survey region does not include the main body of M87. These radial velocity distributions are distinct from that of the foreground stars, which show a strong concentration at $v_{\rm r} \sim 53 \pm 5$ km s^{-1} with a dispersion of 105 km s^{-1} (see Figure 2.7(b)).

Compilation of Velocity Data of GCs and UCDs

We compile the velocity data of GCs and UCDs from this study and from the literature to study the kinematics of GCs and UCDs in the central region of the Virgo. Prior to the compilation, we compare the radial velocities of the GCs, UCDs, and foreground stars derived in this study with the measurements from the literature (see Figure 2.8). Strader et al. (2011) presented the radial velocities of M87 GCs, UCDs, and foreground stars in the M87 field. Zhang et al. (2015) presented the radial velocities of M87 UCDs, including all UCDs confirmed in Strader et al. (2011). In addition, Park et al. (2012a) presented those of M86 GCs. The numbers of GCs and foreground stars common to this study and Strader et al. (2011) are 15 and

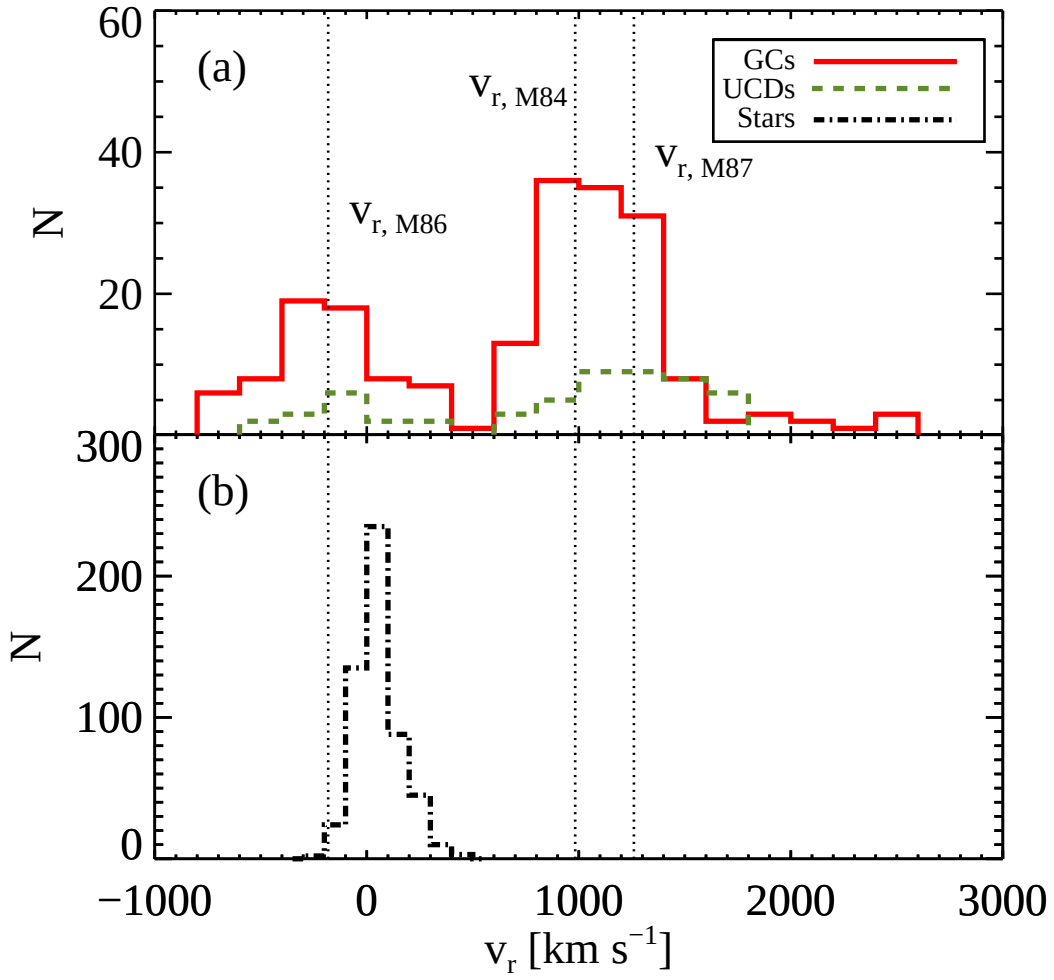

Figure 2.7: (a) Radial velocity distribution of the GCs (red solid line) and the UCDs (dashed line) observed in this study. (b) Radial velocity distribution of the foreground stars classified in this study. The dotted lines in the two panels represent the systemic radial velocity of M86 (–182 km s^{-1}), M84 (983 km s^{-1}), and M87 (1260 km s^{-1}) (Kim et al. 2014).

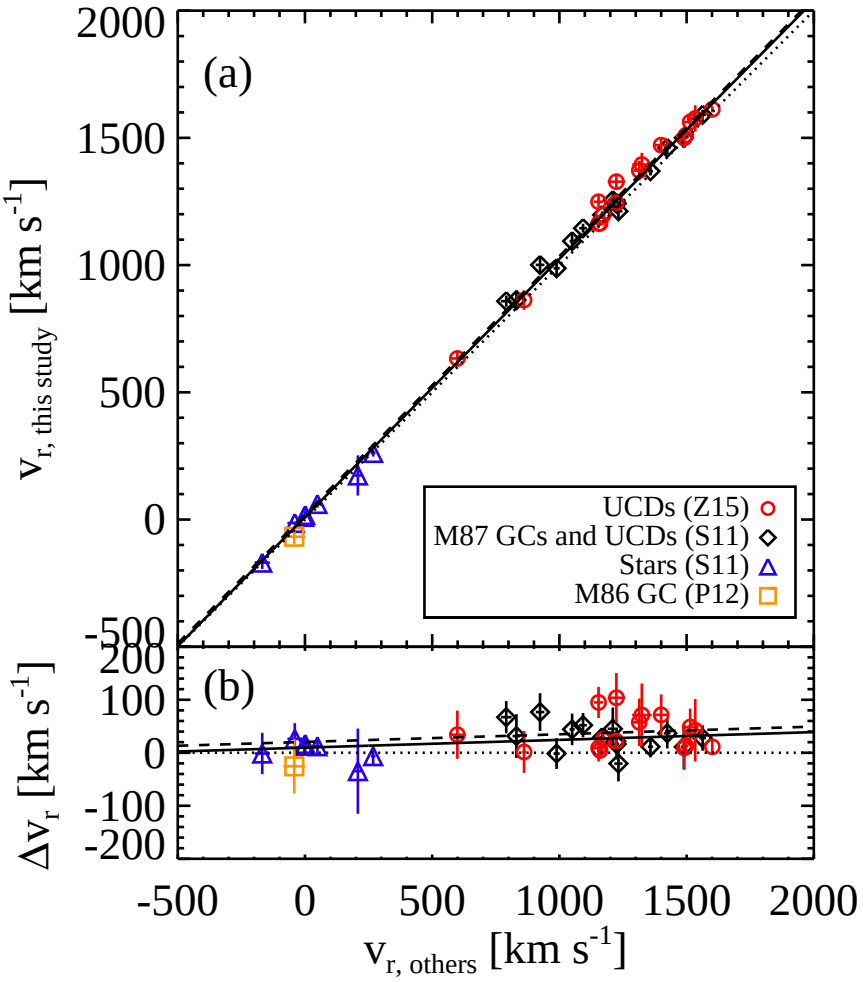

Figure 2.8: (a) Comparison of radial velocities of the objects measured in this study with those in Strader et al. (2011), Park et al. (2012a), and Zhang et al. (2015). The circles, diamonds, triangles, and a square represent M87 UCDs (Zhang et al. 2015), M87 GCs/UCDs, foreground stars near M87 (Strader et al. 2011), and an M86 GC (Park et al. 2012a), respectively. The dotted line denotes the one-to-one relation. The solid lines and dashed lines represent the least-squares fit with the velocity data of Strader et al. (2011) and that of Zhang et al. (2015), respectively. The horizontal and vertical error bars represent the measurement uncertainties of the radial velocities. (b) Radial velocity difference ($v_{others} - v_{this\ study}$). The symbols are the same as in (a).

7, respectively, and the number of UCDs common to this study and Zhang et al. (2015) is 16. For M86 GCs, there is only one common to both this study and Park et al. (2012a). Figure 2.8 shows that our measurements agree well with previous measurements.

We fit to the data and derive a transformation relation between the measurements of this study and those of Strader et al. (2011),

$$\mathrm{v_{r,\ this\ study}} = 1.01\ (\pm\ 0.007) \times \mathrm{v_{r,\ str11}} + 9.69\ (\pm\ 7.39)\ \mathrm{km\ s^{-1}}.$$

Similarly, the transformation relation between the measurements of this study and those of Zhang et al. (2015) is

$$\mathrm{v_{r,\ this\ study}} = 1.01\ (\pm\ 0.02) \times \mathrm{v_{r,\ Zhang15}} + 20.45\ (\pm\ 27.53)\ \mathrm{km\ s^{-1}}.$$

The root mean square errors of the above two relations are about 25 and 32 km $\mathrm{s^{-1}}$, respectively, which are comparable with the mean error of the radial velocity estimates in this study (28 km $\mathrm{s^{-1}}$). We transform the radial velocities of the GCs and UCDs in Strader et al. (2011) and Zhang et al. (2015) using the above relations and produce a master catalog of radial velocities for the GCs and UCDs in the central region of the Virgo.

Figure 2.9(a) and (b) show the radial velocity distributions for 633 GCs and 138 UCDs in the Virgo central region, respectively. The radial velocity distributions of the GCs and UCDs show two groups with peak positions of $v_\mathrm{r} \sim 1300$ and –180 km $\mathrm{s^{-1}}$. The peak positions are consistent with the radial velocities of M87 and M86 ($v_\mathrm{r} = 1260$ km $\mathrm{s^{-1}}$ and –182 km $\mathrm{s^{-1}}$). The GCs and UCDs with $v_\mathrm{r} > 400$ km $\mathrm{s^{-1}}$ are expected to consist of at least two components: M87 and M84 populations.

To decompose spatially and kinematically different groups in the GCs, we perform three-dimensional Gaussian mixture modeling for ΔR.A., Δdecl., and radial velocities using the MCLUST package in the R statistical computing language (Fraley

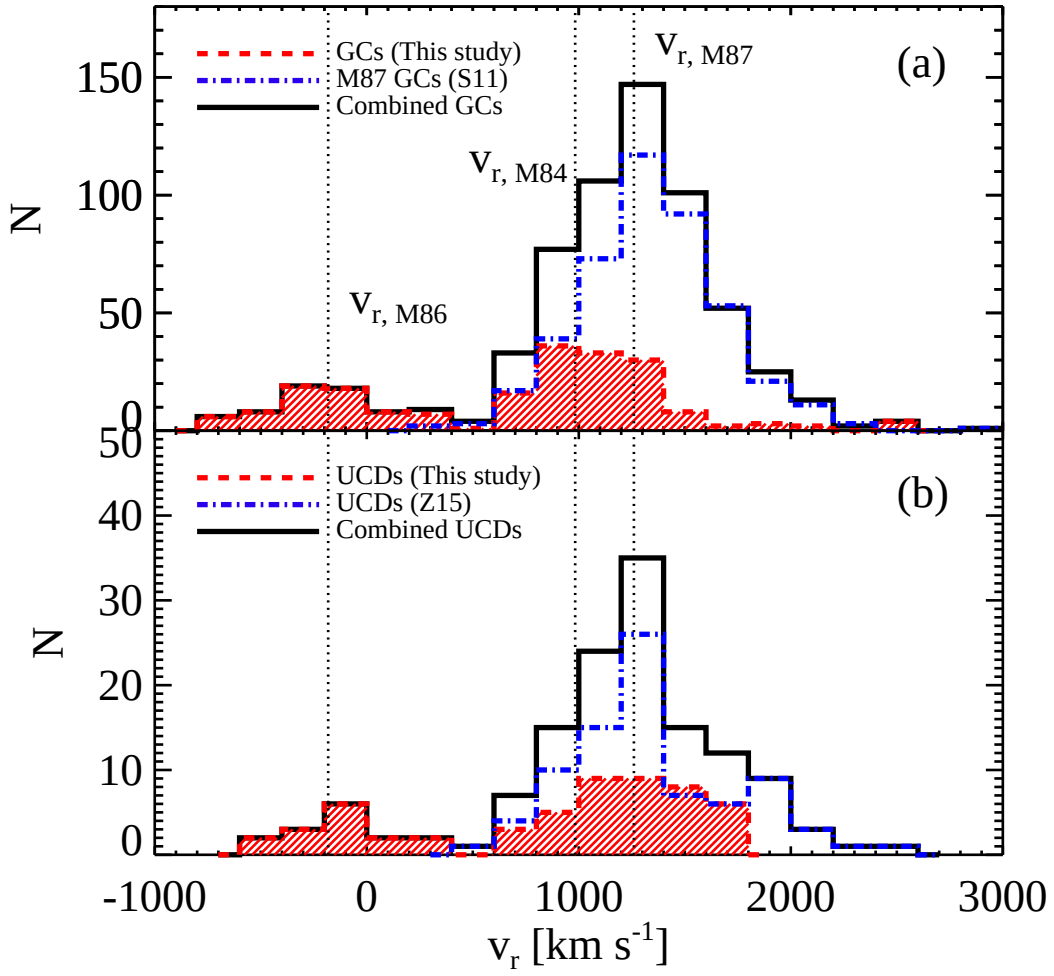

Figure 2.9: (a) Radial velocity distribution of the GCs in the central region of the Virgo confirmed in this study (hatched histogram) and in Strader et al. (2011) (dotted-dashed histogram). The solid histogram indicates the radial velocity distribution for the combined GC sample. (b) Same as (a), but for the UCDs. The dotted-dashed histogram represents the UCDs presented in Zhang et al. (2015).

& Raftery 2002; Fraley et al. 2012). MCLUST finds the optimal number of components in a given sample set by calculating the Bayesian information criterion (BIC; Schwarz 1978) based on 13 different mixture models for multivariate data. It detects eight and three different groups in the master GC and UCD catalogs, respectively. The model at which the optimal BIC occurs for the GC and UCD samples is the VVI (diagonal, varying volume and shape) model.

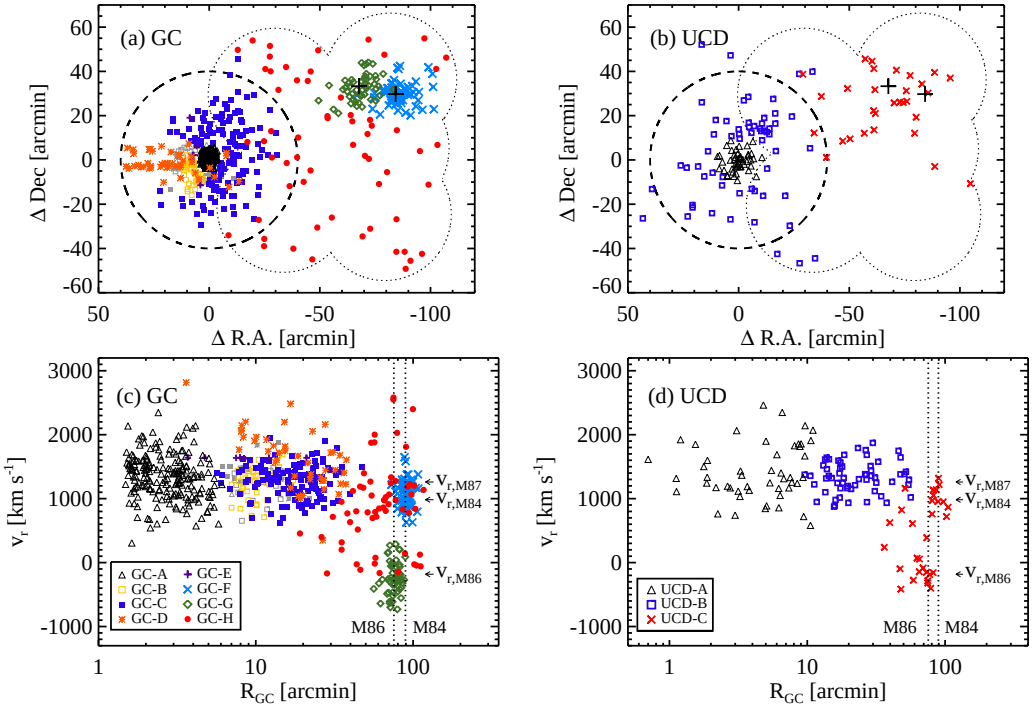

Figure 2.10: (a) Spatial distribution of the master GC sample (this study and Strader et al. 2011). (0,0) indicates the center of M87. The dashed-line open circle centered on M87 has a radius of 40 arcmin, where the slope of the GC number density profile starts to change (Lee et al. 2010a). The dotted outlines show the survey region of this study. The two large pluses represent the position of M86 and M84. (b) Spatial distribution of the master UCD sample (this study and Zhang et al. 2015). The lines and pluses represent the same locations in (a). (c) Radial velocity vs. galactocentric distance from M87 of the master GC sample. The two dotted vertical lines represent the position of M86 and M84. (d) Radial velocity vs. galactocentric distance from M87 of the master UCD sample. The lines represent the same positions in (c). The symbols in four panels show different GCs belonging to different components as found by MCLUST.

Figure 2.10 shows the spatial distribution and the radial velocity as a function of galactocentric distance from M87 for the master GC and UCD samples. The GCs are divided into eight different groups: GC-A, B, C, D, E, F, G, and H. Most of the GC-A, B, C, D, and E groups are located within $R_{\rm GC} = 40'$ (see Figure 2.10(a)), where a break is shown in the radial number density profile of the GCs (Lee et al. 2010a). We consider 460 GCs in these five groups as the GCs that belong to M87. The relatively large number of groups for M87 GCs might be due to the substructures in M87 (Strader et al. 2011; Romanowsky et al. 2012) and to the non-uniform spatial coverage of the observed data. The GC-F and G groups are well concentrated, both spatially and kinematically, on the position of M84 and M86, respectively (see Figures 2.10(a) and (c)). Therefore, the GC-F and G groups are considered as M84 and M86 GCs, respectively. The GC-H group spreads out on the entire survey region and is not associated with M84, M86, or M87. They could be IGC candidates. The selection method for IGCs in the Virgo is described in following section.

The UCDs are divided into three different groups: UCD-A, B, and C (see Figure 2.10(b) and (d)). Most of the UCD-A and B groups are located within the M87 region. The UCD-C group shows a weaker concentration on M86 and M84. Unlike the GC sample, the UCDs around M84 and M86 are not clearly distinguished from those in the intracluster region, because the UCD sample is much smaller than the GC sample. We divide the UCDs into two groups, M87 UCDs (UCD-A and B groups) and others (UCD-C group), for the following analysis. The 3D GMM results derived by MCLUST are summarized in Table 2.5.

Identification of Intracluster GCs

We select the intracluster population from our GC sample based on the MCLUST results presented in the previous section. The GC-H group is considered to be the

Table 2.5. Summary of MCLUST Results[a] for ΔR.A., ΔDec. and radial velocities of the master GC and UCD Sample

Group	N	$\text{Mean}_{\Delta\text{R.A.}}$ [arcmin]	$\sigma_{\Delta\text{R.A.}}$ [arcmin]	$\text{Mean}_{\Delta\text{Dec.}}$ [arcmin]	$\sigma_{\Delta\text{Dec.}}$ [arcmin]	Mean_{v_r} [km s^{-1}]	σ_{v_r} [km s^{-1}]	Fraction	Comment
GC-A	202	0.0	1.8	0.9	2.4	1350	350	0.28	M87 GCs
GC-B	62	7.0	5.2	–3.7	6.2	1281	259	0.09	M87 GCs
GC-C	138	–4.1	11.2	3.2	14.6	1267	268	0.23	M87 GCs
GC-D	51	12.0	13.4	–1.9	4.5	1481	411	0.11	M87 GCs
GC-E	7	5.5	2.4	3.3	8.5	1637	4	0.01	M87 GCs
GC-F	62	–85.8	6.3	29.9	5.0	1067	202	0.09	M84 GCs
GC-G	51	–68.5	6.0	32.8	5.5	–247	252	0.08	M86 GCs
GC-H	60	–54.3	29.0	6.8	30.2	916	680	0.11	IGC candidates
UCD-A	49	0.3	4.6	–0.4	4.8	1424	440	0.32	UCDs in the M87 region
UCD-B	59	–2.4	16.8	2.6	21.1	1328	257	0.46	UCDs in the M87 region
UCD-C	30	–66.7	18.2	24.6	14.3	416	584	0.21	

[a]Based on the VVI (diagonal, varying volume and shape) models for both GC and UCD sample, respectively.

IGC candidates not associated with M87, M86, or M84. There are 60 IGC candidates in the GC-H group: 59 GCs from this study and one GC (ID: H58443) from Strader et al. (2011).

In addition, we try a different method to select the IGCs in the GC sample confirmed in this study using three criteria. First, IGCs are not located within $R_{\rm GC} < 40'$. Lee et al. (2010a) found a break in the radial number density profile of GCs at the galactocentric radius of $40'$ from M87. We therefore use $R = 40'$ to distinguish M87 GCs from IGCs. Second, IGCs are not located in any galaxy region defined by $R \sim 2D_{25}$. This is a stricter criterion for selecting IGCs than the one used for the Fornax Cluster ($R > 1.5D_{25}$; Bergond et al. 2007). Third, when the GCs are located at $R < 2D_{25}$ of individual galaxies but have radial velocities significantly different from those of the galaxies (i.e. $\Delta v_{\rm r} > 600$ km s^{-1}), we consider them as IGCs. These criteria result in 47 IGCs.

We compare the IGCs selected by the two different methods described above. We call the first method, based on 3D GMM results, the 3D GMM method and the second method, based on spatial and kinematic information, the Rv cut method. Thirty-eight IGCs satisfy both selection methods. These are about 63% and 83% of the IGCs selected by the 3D GMM and Rv cut methods, respectively. Figure 2.11 shows the spatial distribution of these IGC candidates overlaid on the region of Virgo galaxies in the survey region. The most prominent differences between the IGCs from the two methods occur at $R_{\rm GC} < 40'$ and the western part of M84. With the 3D GMM method, eight IGCs within $40'$ of M87 are statistically well distinguished from M87 GCs. Some IGCs around M84 selected by the Rv cut method are excluded from the IGCs from the 3D GMM method.

We adopt both methods to select the IGCs in the Virgo. The 3D GMM method is more objective than the Rv method but is not efficient for the decomposition of the group containing a small sample. We apply the same spatial and radial velocity

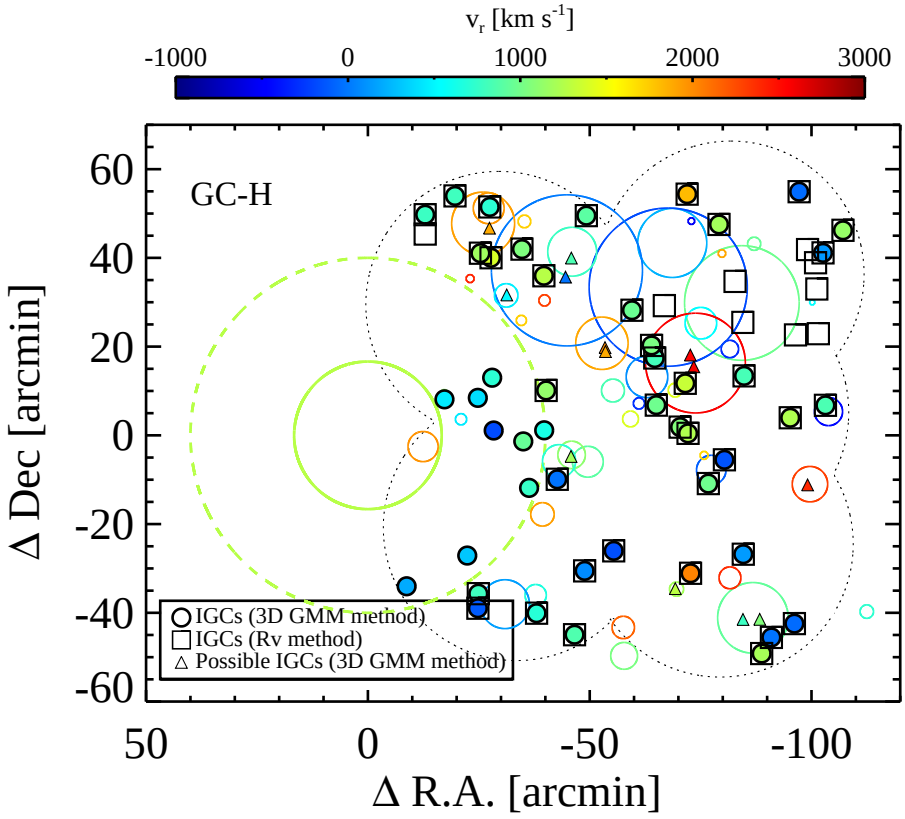

Figure 2.11: Spatial distribution of the IGCs and possible IGCs color-coded by their radial velocities. The filled circles and triangles represent the IGCs and possible IGCs based on the MCLUST results, respectively. The open squares represent the IGCs selected by different criteria, including R $> 2D_{25}$ and $\Delta v_r < 600$ km s^{-1} (Rv method). The dashed line and the dotted outline are the same as in Figure 2.10. The solid-line open circles indicate bright Virgo galaxies in the survey region color-coded by their radial velocities (Kim et al. 2014). The radius of each solid-line open circle represents $2D_{25}$ of each galaxy from the RC3 catalog (de Vaucouleurs et al. 1991).

criteria of the Rv method for 60 IGC candidates based on the 3D GMM method and find that 14 of the 60 GCs are associated with Virgo galaxies. We classify them as possible IGCs. As a result, 46 and 14 are classified as IGCs and possible IGCs, respectively, among 60 IGC candidates based on the 3D GMM method. We use these 46 IGCs for the following analysis.

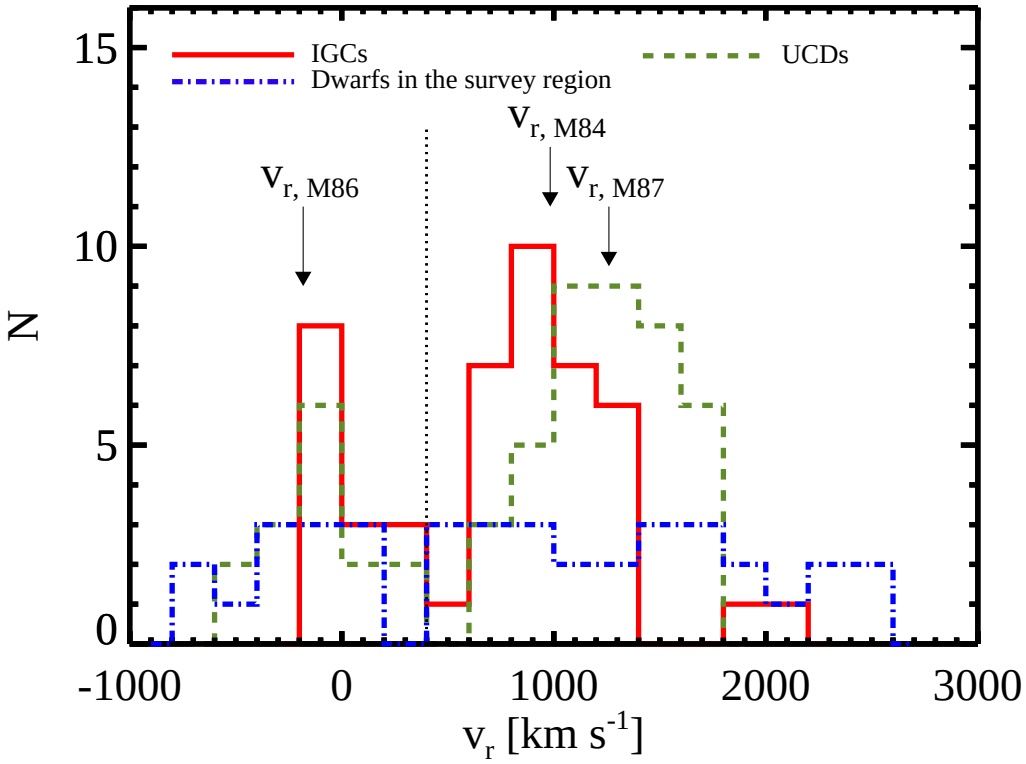

Figure 2.12: Radial velocity distribution of IGCs confirmed in this study (solid histogram), UCDs confirmed in this study (dashed histogram), and dwarfs in the survey region (dotted-dashed histogram; Kim et al. 2014).

2.3.2 Radial Velocity and Velocity Dispersion Profiles of GCs and UCDs

We compare the radial velocity distribution of IGCs, UCDs, and dwarf galaxies in the survey region (see Figure 2.12). The radial velocity distribution of the IGCs shows two prominent peaks at $v_{\rm r} = -100$ and 900 km s^{-1}. The UCDs are also divided into two groups, of which the radial velocities are $v_{\rm r} = -100$ and 1100 km s^{-1}. The peak position of the radial velocity distribution of the UCDs with $v_{\rm r} > 400$ km s^{-1} is higher than that of the IGCs with $v_{\rm r} > 400$ km s^{-1} because there are UCDs in the M87 region (UCD-A and B groups). The radial velocities of the dwarfs in the survey region are almost uniformly distributed, different from those of the IGCs and UCDs. However, there is a dip at $v_{\rm r} \sim 400$ km s^{-1} in the radial velocity distribution of the dwarfs, which is also shown in those of the IGCs and UCDs. We assume that the objects with $v_{\rm r} > 400$ km s^{-1} belong to the main body of the Virgo cluster, while the others are infalling or outgoing populations in the Virgo. Therefore, we divide the IGCs, UCDs, and dwarfs into two groups in each population according to their radial velocities in order to discuss their kinematics separately.

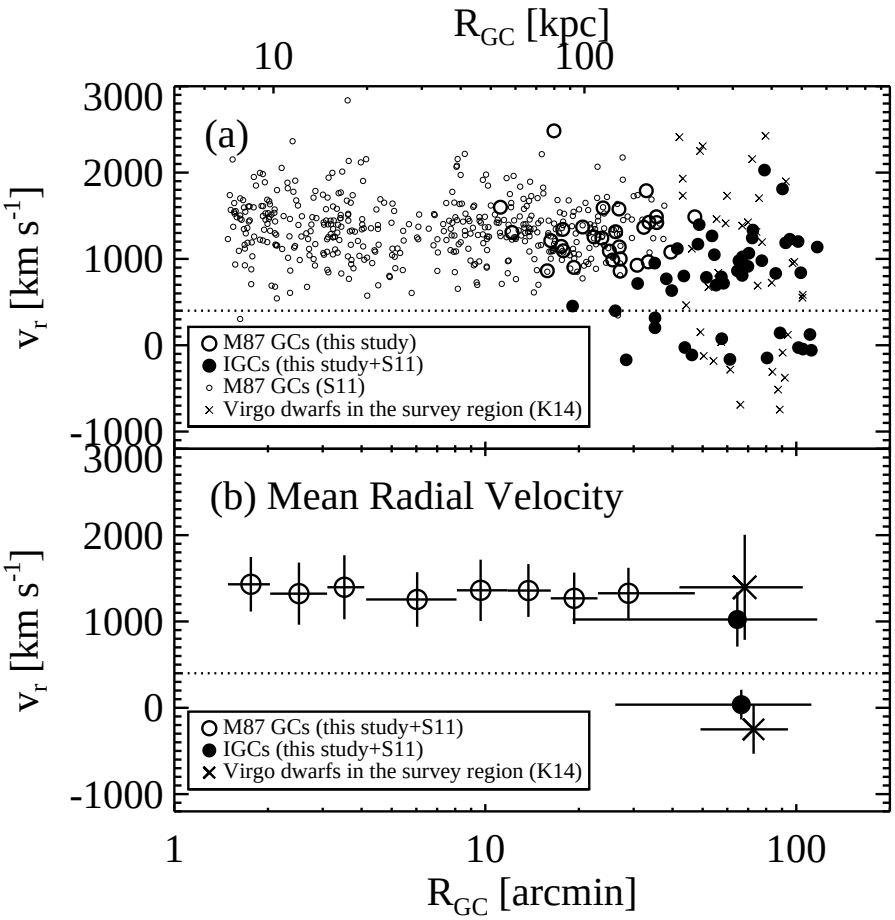

Figure 2.13: (a) Radial velocities of GCs and dwarfs as a function of galactocentric distance from M87. The filled circles, open circles, and crosses represent the IGCs, M87 GCs, and dwarfs in the survey region (Kim et al. 2014), respectively. The small and large open circles represent the M87 GCs in Strader et al. (2011) and in this study, respectively. The dashed horizontal line indicates $v_{\rm r} = 400$ km s^{-1}, where a dip in the radial velocity distribution can be seen (see Figure 2.12). (b) Mean radial velocity of GCs and dwarfs in each radial bin as a function of galactocentric distance from M87. The symbols are the same as in (a). We divided the IGCs and dwarfs into two groups according to their radial velocities: $v_{\rm r} > 400$ km s^{-1} and with $v_{\rm r} < 400$ km s^{-1}. The vertical error bars indicate the root mean square velocities of the objects in each bin.

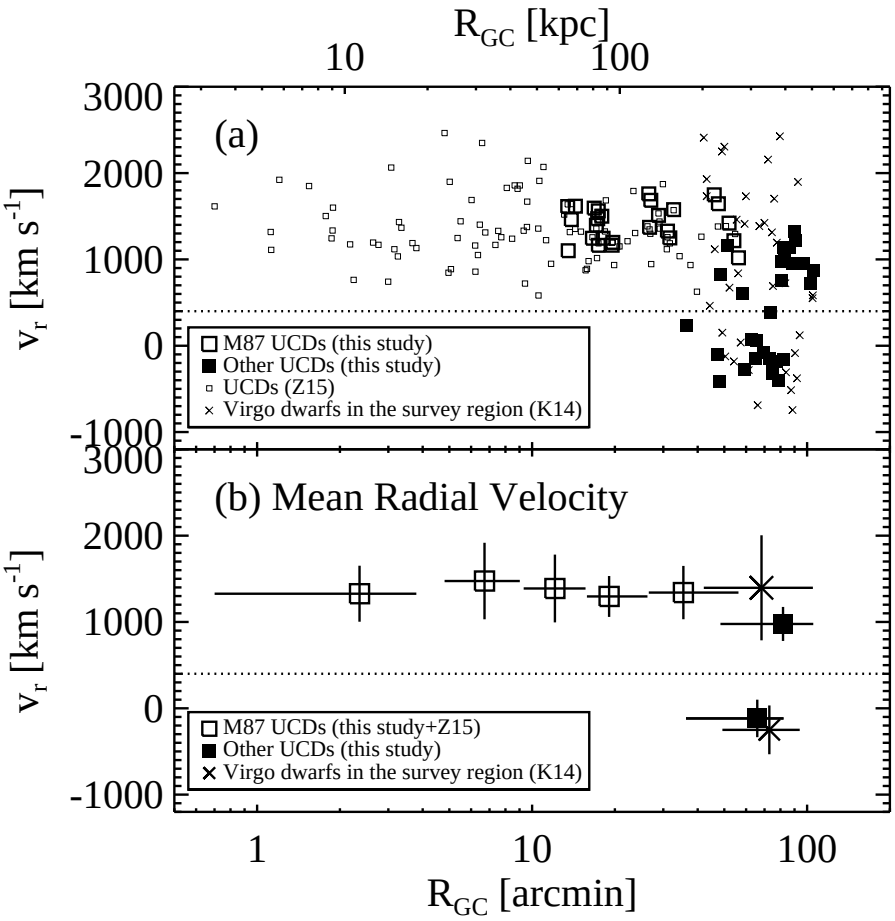

Figure 2.14: (a) Radial velocities of UCDs and dwarf galaxies as a function of galactocentric distance from M87. The open squares, filled squares, and crosses represent the UCDs in the M87 region, the UCDs not in the M87 region, and the dwarfs in the survey region, respectively. The small and large open squares represent the UCDs in Zhang et al. (2015) and in this study, respectively. (b) Mean radial velocity of UCDs and dwarfs in each radial bin as a function of galactocentric distance from M87. The symbols are the same as in (a). We divided the dwarfs into two groups according to their radial velocities: $v_{\rm r} > 400$ km s^{-1} and with $v_{\rm r} < 400$ km s^{-1}. The vertical error bars indicate the root mean square velocities of the objects in each bin.

Figure 2.13(a) shows the radial velocities of the combined GC sample and dwarfs in the survey region as a function of galactocentric distance from M87. The dwarfs in the survey region have the radial velocities with a wide range between –745 and 2426 km s^{-1}. We also divide the dwarfs into two categories, those with $v_r > 400$ km s^{-1} and those with $v_r < 400$ km s^{-1}. Figure 2.13(b) shows the mean radial velocity of the M87 GCs, IGCs, and dwarfs in each radial bin as a function of galactocentric distance from M87. The mean radial velocities of the M87 GCs with $v_r > 400$ km s^{-1} are almost constant ($\overline{v_r} = 1340$ km s^{-1}) within their uncertainties. For the IGCs and dwarfs, we calculate the mean radial velocities of two groups with high and low radial velocities. The mean radial velocity of the IGCs with $v_r > 400$ km s^{-1} ($\overline{v_r} = 1023$ km s^{-1}) is lower than those of the dwarfs with $v_r > 400$ km s^{-1} ($\overline{v_r} = 1396$ km s^{-1}) and the M87 GCs. The mean radial velocities of the IGCs and dwarfs with $v_r < 400$ km s^{-1} are 36 and –250 km s^{-1}, respectively. Figure 2.14 is similar to Figure 2.13, but for the combined UCD sample. The mean radial velocity of the M87 UCDs is almost constant ($\overline{v_r} = 1365$ km s^{-1}). The other UCDs (UCD-C group) include two groups with $v_r > 400$ km s^{-1} and $v_r < 400$ km s^{-1}. The mean radial velocity of the other UCDs with $v_r > 400$ km s^{-1} ($\overline{v_r} = 977$ km s^{-1}) is lower than those of the dwarfs with $v_r > 400$ km s^{-1} and the M87 UCDs. The mean radial velocity of the other UCDs with $v_r < 400$ km s^{-1} is –117 km s^{-1}.

Figure 2.15 shows the radial velocity dispersion profiles of the GCs and UCDs. The radial velocity dispersion and its error of the GCs, UCDs, and dwarfs in each radial bin as well as its error is calculated following the formula in Pryor & Meylan (1993). We use the IGCs, UCDs, and dwarfs with $v_r > 400$ km s^{-1} that are not probably affected by infalling populations to derive the velocity dispersion for each tracer. The radial velocity dispersion of the combined M87 GCs is almost constant at 333 km s^{-1}. The radial velocity dispersion of the IGCs is similar to that of the GCs in M87 ($\sigma = 314$ km s^{-1}). Both are much lower than the radial velocity dispersion of

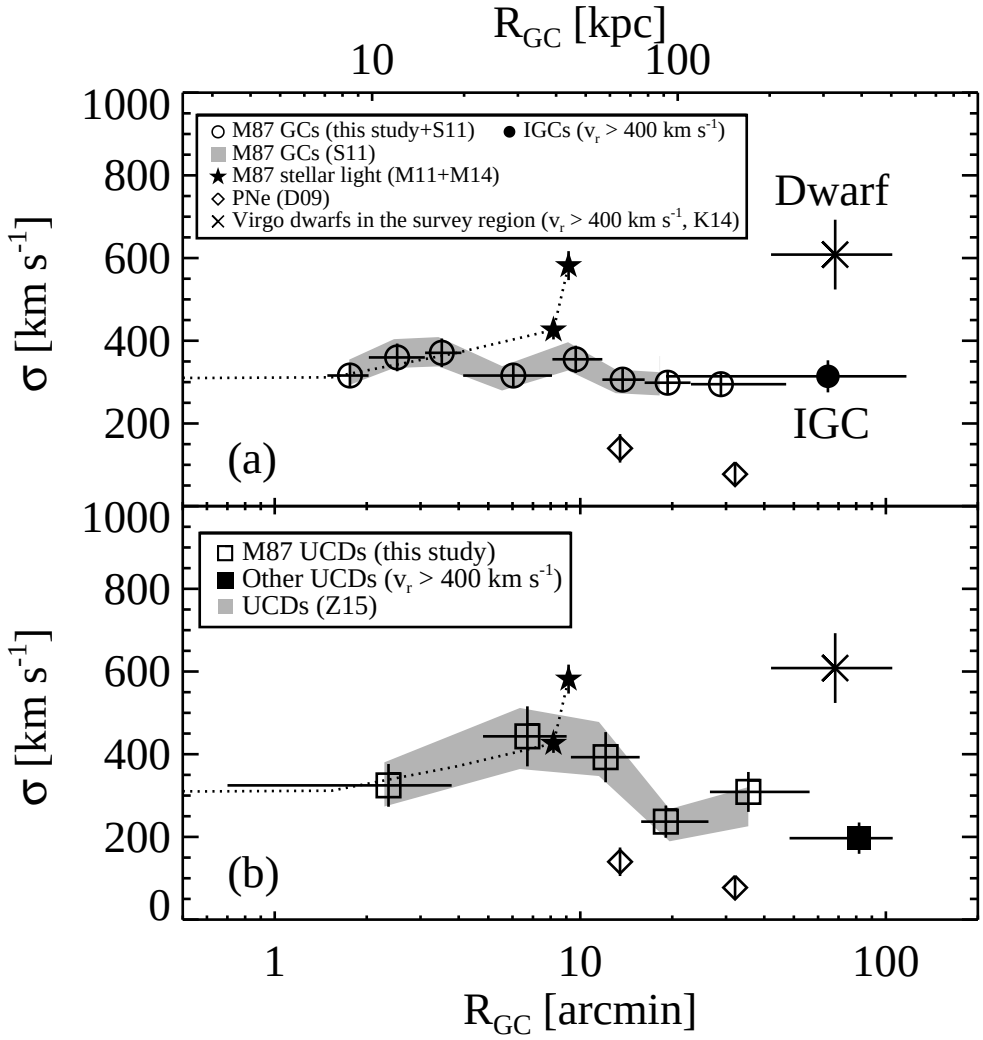

Figure 2.15: Radial velocity dispersion profile of different kinds of objects in the Virgo as a function of galactocentric distance from M87. The diamonds and filled star symbols with the dotted line represent the PNe (Doherty et al. 2009) and the stellar light of M87 (Murphy et al. 2011, 2014), respectively. The open circles, filled circle, open squares, filled square, and crosses represent M87 GCs, IGCs with $v_{\rm r} > 400$ km s^{-1}, M87 UCDs, the other UCDs with $v_{\rm r} > 400$ km s^{-1}, and dwarfs with $v_{\rm r} > 400$ km s^{-1} in the survey region, respectively. The vertical error bars represent the measurement uncertainties of the radial velocity dispersion calculated in each radial bin.

dwarfs in the same survey region ($\sigma = 608$ km s^{-1}) and that of ICPNe superposed on the M87 region ($\sigma = 881$ km s^{-1}; Longobardi et al. 2015). Strader et al. (2011) suggested that the stellar halo of M87 is not truncated at $R_{\rm GC} \sim 30'$, which is different from the result from the planetary nebulae (PNe) of M87 (Doherty et al. 2009). Our results are consistent with Strader et al. (2011); the dispersion profile of the GCs does not show any significant changes with the galactocentric radius. The radial velocity dispersion profile of the combined UCDs is similar to that of the UCDs in Zhang et al. (2015). Similar to the case of the GCs, the dispersion profile of the UCDs does not change much at $R_{\rm GC} > 40'$. The kinematic information of the GCs and UCDs is summarized in Tables 2.6 and 2.7, respectively.

As shown in Figure 2.15, the velocity dispersion profiles of the GCs, UCDs, integrated stellar light, and PNe are remarkably different from one another. The dispersion profile differs significantly at $R_{\rm GC} = 7' - 40'$. This is where the cD halo of M87 may exist (Mihos et al. 2005; Kormendy et al. 2009). The GC velocity dispersion is almost constant at $\sigma \sim 300$ – 350 km s^{-1} in this range, while the stellar velocity dispersion increases steeply and the PN velocity dispersion is much lower than the others. Note that most of the GCs in this range come from Strader et al. (2011), because our observation field is concentrated on the intracluster region (i.e. $R_{\rm GC} = 40' - 120'$). This disagreement between velocity dispersions has already been reported in previous studies (e.g. Romanowsky & Kochanek 2001; Murphy et al. 2014). Murphy et al. (2014) concluded that the kinematic properties of different objects in the Virgo cluster are not necessarily the same because the cluster has not dynamically relaxed yet and because there are several substructures in the cluster. These diverse kinematic properties of various tracers in galaxy clusters are also found in other galaxy clusters (e.g. Richtler et al. 2011; Coccato et al. 2013). A detailed dynamical analysis of different tracers considering their number density profiles, their velocity anisotropies, and the galaxy cluster mass profile is necessary to understand

Table 2.6. GC Kinematics

Radius Range (arcmin)	$\overline{R}$ (arcmin)	N	$\overline{v_r}$ (km s^{-1})	σ (km s^{-1})
M87 GCs (this study + S11)				
1.49 – 2.03	1.76	58	1431 ± 41	316 ± 30
2.03 – 3.10	2.52	58	1322 ± 47	360 ± 34
3.10 – 4.08	3.52	58	1396 ± 49	371 ± 35
4.14 – 8.08	6.04	58	1255 ± 41	316 ± 30
8.11 – 11.81	9.66	58	1361 ± 47	355 ± 33
11.81 – 16.24	13.76	58	1358 ± 40	306 ± 29
16.24 – 22.95	19.31	58	1268 ± 39	299 ± 28
23.03 – 47.18	28.86	54	1327 ± 40	295 ± 29
All M87 GCs (this study + S11)				
1.49 – 47.18	10.52	460	1340 ± 16	333 ± 11
IGCs with $v_r > 400$ km s^{-1} (this study + S11)				
19.08 – 116.79	64.62	33	1023 ± 55	314 ± 39
IGCs with $v_r < 400$ km s^{-1} (this study)				
26.19 – 111.81	66.56	14	36 ± 46	172 ± 33
IGCs regardless of v_r (this study)				
19.08 – 116.79	65.20	47	729 ± 77	530 ± 55

Table 2.7. UCD Kinematics

Radius Range (arcmin)	$\overline{R}$ (arcmin)	N	$\overline{v_r}$ (km s^{-1})	σ (km s^{-1})
UCDs in the M87 region (this study + Z15)				
0.70 – 3.79	2.36	21	1327 ± 70	324 ± 51
4.80 – 9.02	6.71	21	1474 ± 96	443 ± 72
9.32 – 15.64	12.10	21	1387 ± 85	392 ± 60
15.83 – 26.27	19.05	21	1295 ± 51	236 ± 38
26.56 – 56.29	35.49	21	1340 ± 67	308 ± 48
All UCDs in the M87 region (this study + Z15)				
0.70 – 56.29	15.14	105	1365 ± 34	354 ± 25
UCDs not in the M87 region with $v_r > 400$ km s^{-1} (this study)				
48.40 – 105.30	81.75	14	977 ± 52	196 ± 37
UCDs not in the M87 region with $v_r < 400$ km s^{-1} (this study)				
36.28 – 82.06	65.89	15	-117 ± 56	217 ± 41

the kinematic difference.

2.4 Discussion

2.4.1 The Number of Virgo IGCs

The number density of IGCs in the Virgo has been predicted from several photometric studies that assumed a Gaussian form of the GC luminosity funciton. Tamura et al. (2006) suggested a number density of IGCs of ~ 0.2 arcmin^{-2}, ranging from 0.1 to 0.5 arcmin^{-2}. This value is comparable with the result of Durrell et al. (2014). Harris (2009), Strader et al. (2011), and Oldham & Auger (2016) presented a background number density of 0.6, 0.51, and 0.58 arcmin^{-2}, slightly higher than the above results. These background objects may include foreground stars, background galaxies, and IGCs, which could not be distinguished with the photometric data only. Therefore, these numbers are probably overestimated values.

Figure 2.16 shows the radial number density profiles of M87 GCs and Virgo GCs derived from various surveys (Tamura et al. 2006; Lee et al. 2010a; Strader et al. 2011; Durrell et al. 2014; Oldham & Auger 2016). The number density profiles of Strader et al. (2011), Durrell et al. (2014), and Oldham & Auger (2016) are similar in the inner region at $R_{\rm GC} < 20'$ but show some differences in the outer regions. However, the number density profiles of Tamura et al. (2006) and Lee et al. (2010a) at $R_{\rm GC} > 10'$ are steeper than the others. This difference seems to mainly come from the different spatial coverage in the two studies. Tamura et al. (2006) only covered the eastern part of M87, where there are no massive galaxies except M89, while Lee et al. (2010a) masked out the circular region ($R < 2.5D_{25}$) for Virgo galaxies to exclude GCs that belong to those galaxies.

In order to estimate the total number of IGCs, we assume that the luminosity function of the IGCs follows a Gaussian distribution with a peak of $g_0 = 23.8 \pm 0.2$

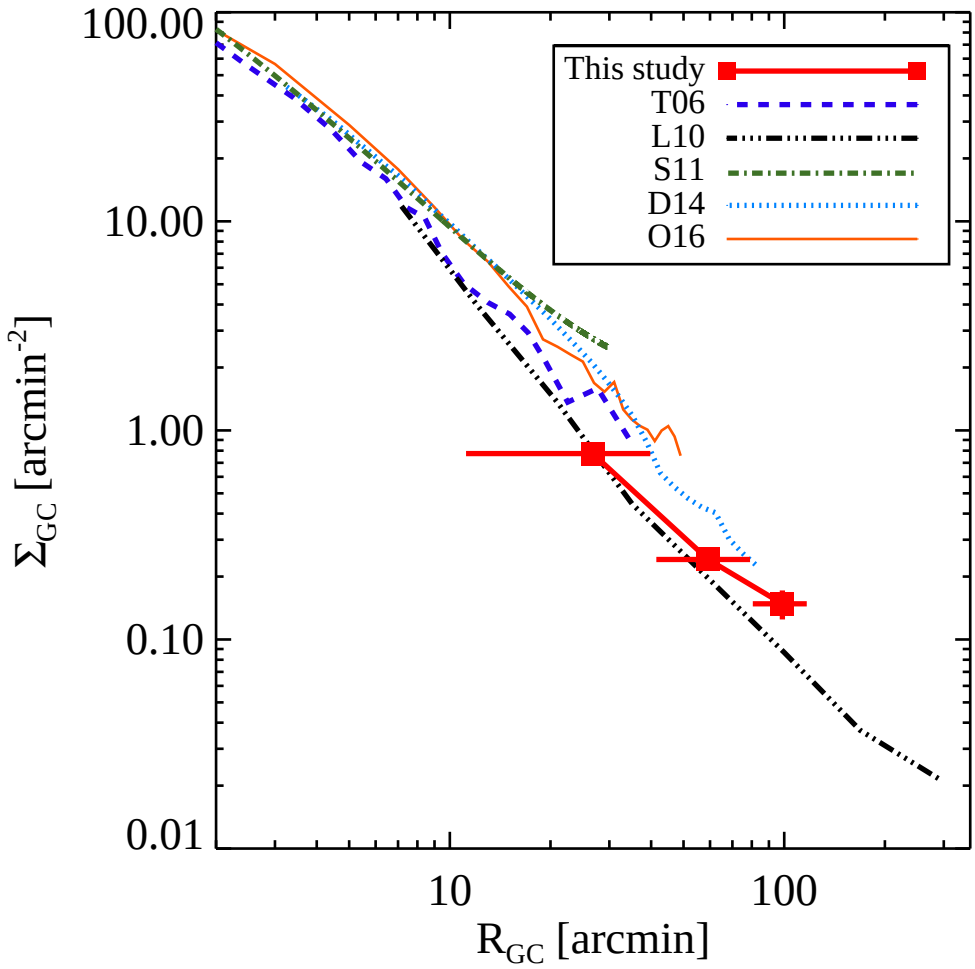

Figure 2.16: Number density of M87 GCs and IGCs estimated within three radial bins (red filled squares) with the radial number density profile of GCs in the Virgo derived by several studies: Tamura et al. (2006; blue dashed line), Lee et al. (2010a; black dotted-dotted-dashed line), Strader et al. (2011; green dotted-dashed line), Durrell et al. (2014; skyblue dotted line), and Oldham & Auger (2016; orange solid line). Note that the GCs within R $< 2.5D_{25}$ for Virgo galaxies are excluded in the profile derived in Lee et al. (2010a).

mag and a width of 1.4 (Durrell et al. 2014). In addition, the spectroscopic targets we selected are one third of the entire point sources with the same range of color and magnitude as the GCs. Considering these factors, we estimate the total number and number density of IGCs in our survey region to be about 2114 and 0.19 ± 0.02 arcmin^{-2}, respectively. This is comparable with the estimates from photometric studies of $\Sigma_{\rm GC} \sim 0.2 - 0.6$ arcmin^{-2} (see Figure 2.16).

Moreover, Strader et al. (2011) predicted that 16-67% of IGCs have extreme radial velocities of $v_{\rm r} < 307$ km s^{-1} or $v_{\rm r} > 2307$ km s^{-1}. In our sample, there are 12 IGCs with $v_{\rm r} < 307$ km s^{-1} and no IGCs with $v_{\rm r} > 2307$ km s^{-1}. Among the 37 dwarf galaxies in the survey region, there are 12 and 2 dwarfs with low and high extreme velocities, respectively. Therefore, the fractions of IGCs and dwarfs with extreme velocities are, respectively, 26% and 38%, consistent with the expectation of Strader et al. (2011).

2.4.2 Color Distribution of IGCs

The GCs in massive early-type galaxies are generally divided into two subpopulations, blue GCs and red GCs (Brodie & Strader 2006 and references therein). The colors of old GCs depend mainly on the GC's metallicity: blue and red GCs are considered as metal-poor and metal-rich populations, respectively. Several photometric surveys of M87 GCs reported that M87 also has these two different GC populations (Peng et al. 2006; Tamura et al. 2006; Harris 2009; Oldham & Auger 2016).

Figure 2.17 shows the color distributions of the spectroscopically confirmed GCs in this study and in Strader et al. (2011). The *gi* magnitudes of Strader et al. (2011) based on the SDSS system are converted to the CFHT AB magnitude system. We divide the GC sample of Strader et al. (2011) into two groups according to the GC magnitudes, bright GCs with $i_0 < 20.9$ and faint GCs with $i_0 > 20.9$, because their sample contains fainter GCs than our sample. All of the M87 GCs within each radial

Table 2.8. Summary of GMM Test Results[a] for the GC Color Distribution

Region	$(g-i)_{0,\mathrm{blue}}$	σ_{blue}	f_{blue}	$(g-i)_{0,\mathrm{red}}$	σ_{red}	f_{red}	N_{GC}	p	D
Faint M87 GCs ($i_0 \geq 20.9$)									
R $< 10'$	0.74 ± 0.01	0.07 ± <0.01	0.61 ± 0.04	0.98 ± 0.01	0.07 ± <0.01	0.39 ± 0.04	216	2.33e-11	3.37 ± 0.25
Bright M87 GCs ($i_0 < 20.9$)									
R $< 10'$	0.72 ± 0.02	0.06 ±0.01	0.65 ± 0.10	0.92 ± 0.03	0.06 ± 0.01	0.35 ± 0.10	51	9.78e-03	3.01 ± 0.66
$10' <$ R $< 20'$	0.75 ± 0.01	0.07 ± 0.01	0.79 ± 0.08	0.95 ± 0.03	0.07 ± 0.01	0.21 ± 0.08	61	1.14e-03	3.00 ± 0.59
R $> 20'$	0.71 ± 0.01	0.04 ± 0.01	0.70 ± 0.07	0.86 ± 0.01	0.04 ± 0.01	0.30 ± 0.07	39	3.56e-04	4.08 ± 0.70
Bright IGCs ($i_0 < 20.9$)									
···	0.74 ± 0.02	0.06 ± 0.01	0.75 ± 0.13	0.90 ± 0.05	0.06 ± 0.01	0.25 ± 0.13	45	6.03e-02	2.59 ± 0.74

[a]Based on the homoscedastic (same variances) option. p represents the probability for unimodality, and D is the difference in color between the two peaks. f indicates the number ratio of each component.

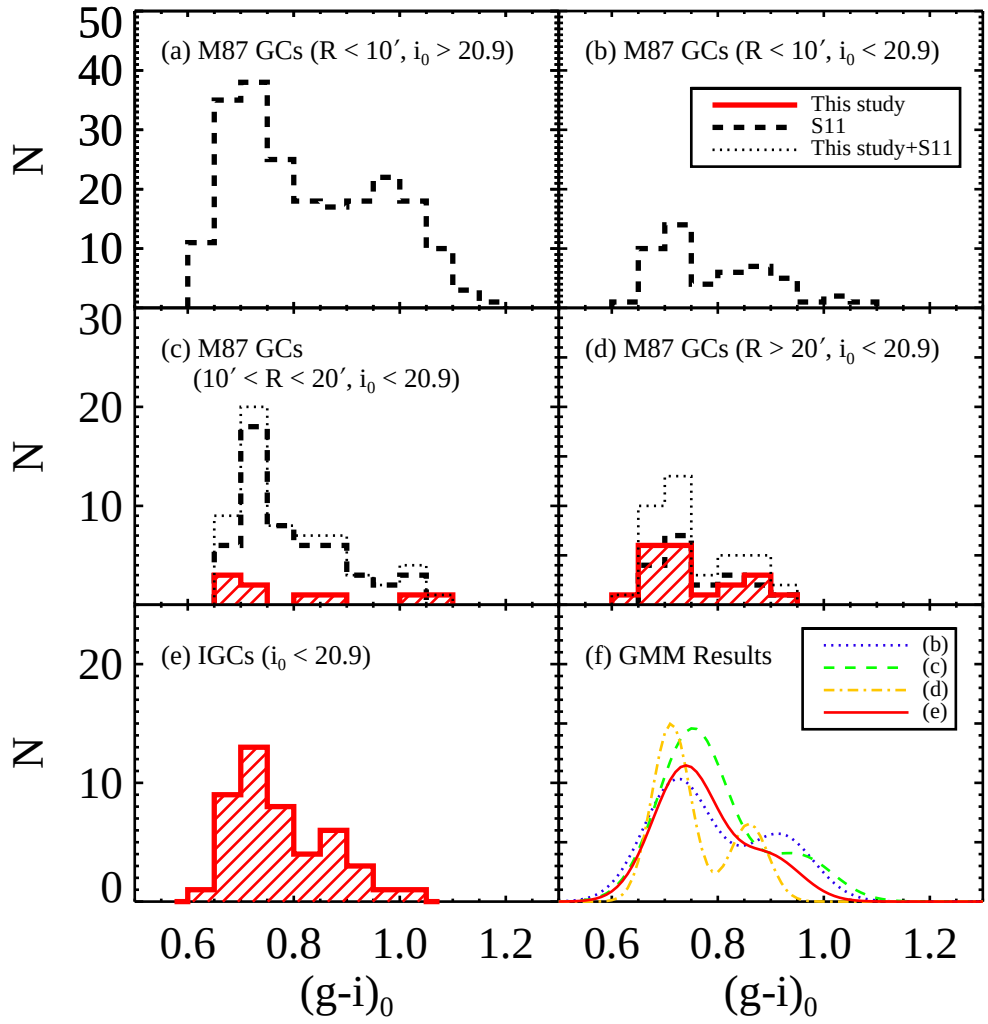

Figure 2.17: Color distributions for M87 GCs and IGCs within several radial bins. (a) M87 GCs with $R_{\rm GC} < 10'$ and $i_0 > 20.9$, (b) M87 GCs with $R_{\rm GC} < 10'$ and $i_0 < 20.9$, (c) M87 GCs with $10' < R_{\rm GC} < 20'$ and $i_0 < 20.9$, (d) M87 GCs with $R_{\rm GC} > 20'$ and $i_0 < 20.9$, (e) IGCs with $i_0 < 20.9$, and (f) the GMM results for the color distribution of GCs in each radial bin in a homoscedastic case (same variances). The solid, dashed, and dotted lines in the (a)-(e) panels represent the GCs confirmed in this study, the GCs presented in Strader et al. (2011), and the combined GC sample, respectively.

bin show a bimodal color distribution, as expected from photometric surveys (see Figure 2.17(a)-(d)). It is noted that the color distribution of the IGCs confirmed in this study is not unimodal (see Figure 2.17(e)). We use the GMM (Muratov & Gnedin 2010) with a homoscedastic case (same variances) to decompose these color distributions of the GCs within each radial bin into two components, blue and red ones. The GMM results are listed in Table 2.8 and are plotted in Figure 2.17(f). We use the probability for the unimodal distribution (p) and the peak separation relative to the widths (D) as indicators for bimodality (e.g. $D > 2$ for the clear separation of two peaks). The GMM results show that the color distributions of M87 GCs at $R_{\rm GC} < 10'$, $10' < R_{\rm GC} < 20'$, and $20' < R_{\rm GC} < 40'$ are probably not unimodal but bimodal ($p < 0.01$ and $D > 2$). The IGC sample shows $p \sim 6\%$ and $D = 2.59 \pm 0.74$. This means that the IGCs have an $\sim 6\%$ probability of unimodal color distribution, and the color distribution of the IGCs marginally shows a peak separation because of a large error for the D value. The blue and red peaks for the IGCs separated from the GMM are similar to those for M87 GCs (see Table 2.8). From this we conclude that there exist red IGC populations even though the color distribution of the IGCs does not show a clear bimodality.

In Figure 2.17(f), the faint GCs ($i_0 > 20.9$) within $R_{\rm GC} < 10'$ have blue and red peaks at redder colors than the bright GCs ($i_0 < 20.9$) in the same region. The color difference of the red peaks is more significant than that of the blue peaks. This trend has already been reported by Harris (2009). On the other hand, the blue and red peaks for bright M87 GCs and IGCs are similar to each other within the uncertainties except for the GCs with $R_{\rm GC} > 20'$.

Many studies have suggested that IGCs are stripped off low-mass dwarf galaxies in galaxy clusters (Williams et al. 2007; Bekki et al. 2008; Georgiev et al. 2009; Lee et al. 2010b). According to this scenario, most IGCs are expected to be metal-poor compared with the GCs hosted by massive early-type galaxies. However, we

detect red IGCs of which the number ratio is about 24% (see Table 2.8). A red IGC population is also detected in the Coma cluster (Peng et al. 2011). The number of red IGCs in the Coma is about 20% the number of the entire IGC population, while the number ratio of the red GCs of NGC 4874, a central massive galaxy of the Coma, is about 50%. Peng et al. (2011) suggested that red IGCs are stripped from more massive galaxies rather than from dwarf galaxies. We also suspect that the red IGCs confirmed spectroscopically in this study originate from massive galaxies capable of hosting red GCs.

2.4.3 Dynamical State of the Virgo Cluster

The Virgo cluster consists of several different subclusters (Binggeli et al. 1985, 1987, 1993): the main cluster A centered on M87; the cluster B centered on M49; three small clouds named M, W, and W′ clouds (de Vaucouleurs 1961); the NGC 4636 group; and so on. In cluster A, there are two distinct substructures associated with M87 and M86, respectively. Several studies have suggested that M86 has its own group apart from the main cluster group centered on M87 (Binggeli et al. 1993; Böhringer et al. 1994; Schindler et al. 1999). The M86 group consists of M86 with $v_{\rm r}$ = –181 km s^{-1}, NGC 4438 with $v_{\rm r}$ = 10 km s^{-1}, and NGC 4402 with $v_{\rm r}$ = 231 km s^{-1}. The map of X-ray gas surrounding these galaxies suggests that these galaxies experience ongoing interaction (Ehlert et al. 2013). The radial velocity of the M86 group ($v_{\rm r} \sim$ –181 km s^{-1}) is $\sim$ 1400 km s^{-1} lower than that of M87 ($v_{\rm r}$ = 1260 km s^{-1}), suggesting that the M86 group may be infalling into the main cluster of the Virgo from behind. Jerjen et al. (2004) found a bimodality in the distance distribution of the galaxies in cluster A and suggested that the M86 group is falling into the main cluster from 1 Mpc behind, and Mei et al. (2007) confirmed this using the surface brightness fluctuation distances of the galaxies.

Figure 2.18(a) and (c) show the spatial distribution of the IGCs and UCDs with

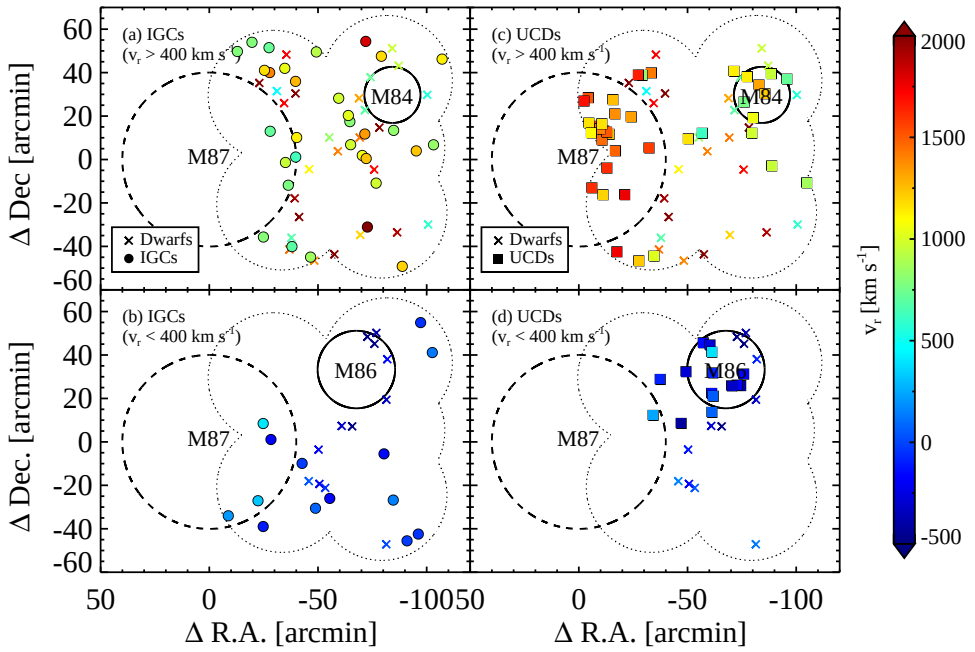

Figure 2.18: (a) Spatial distribution of the IGCs with $v_r > 400$ km s^{-1} (circles) and the dwarfs with $v_r > 400$ km s^{-1} (crosses). (b) The same as (a), but for objects with $v_r < 400$ km s^{-1}. (c) Spatial distribution of the UCDs with $v_r > 400$ km s^{-1} (squares) and the dwarfs with $v_r > 400$ km s^{-1} (crosses). (d) The same as (c), but for objects with $v_r < 400$ km s^{-1}. The dashed-line open circle centered on M87 and the dotted outline are the same as in Figure 2.10. The solid-line open circles show the galaxy regions of M84 and M86, of which the radii are $2D_{25}$.

$v_r > 400$ km s^{-1} , respectively, that probably belong to cluster A of the Virgo. Most of the IGCs spread out the northwestern region of M87, while most of the UCDs are located around M87 and M84. Few IGCs and UCDs with $v_r > 400$ km s^{-1} have radial velocities greater than 2000 km s^{-1}, compared with the dwarfs. Consequently, the radial velocity dispersions of the IGCs and UCDs with $v_r > 400$ km s^{-1} ($\sigma = 314 \pm 39$ km s^{-1} and 361 ± 24 km s^{-1}) are much lower than that of

the dwarfs with $v_{\rm r} > 400$ km s^{-1} in the survey region ($\sigma = 608 \pm 84$ km s^{-1}) (see Figure 2.15). This indicates that the IGCs and UCDs are more dynamically relaxed than the dwarfs. The strong peculiar motions of dwarfs might increase their velocity dispersion. Therefore, the mass of the Virgo based on dwarf galaxy kinematics may be an overestimate. Detailed dynamical analysis with Virgo cluster mass profiles and the surface number density profiles of each tracer is necessary to understand the difference in velocity dispersion between the dwarf galaxies and IGCs/UCDs.

On the other hand, the velocity dispersion of the IGCs and UCDs with $v_{\rm r} < 400$ km s^{-1} ($\sigma = 172 \pm 33$ km s^{-1} and 217 ± 41 km s^{-1}) is similar to that of the dwarfs with $v_{\rm r} < 400$ km s^{-1} ($\sigma = 282 \pm 57$ km s^{-1}) within the uncertainties. The UCDs with $v_{\rm r} < 400$ km s^{-1} are concentrated on the M86 region as well as most of the dwarfs with $v_{\rm r} < 400$ km s^{-1}, while the IGCs with $v_{\rm r} < 400$ km s^{-1} are not (see Figure 2.18(b) and (d)). From this we consider that the UCDs and dwarfs with $v_{\rm r} < 400$ km s^{-1} are related to the infalling group centered on M86.

2.4.4 The Origin of Virgo UCDs

UCDs are very interesting objects whose formation scenario is still widely debated. There are two representative scenarios for the origin of UCDs: "star cluster" and "dwarf galaxy" origins. Some studies have suggested that UCDs are simply the bright end of GCs (Hilker et al. 1999; Mieske et al. 2002, 2012) or massive star clusters that were formed during star cluster mergers (Kroupa 1998; Fellhauer & Kroupa 2002; Maraston et al. 2004; Kissler-Patig et al. 2006). Other studies have proposed that UCDs are the remnant nuclei of dwarf galaxies threshed by tidal interaction in the dense environment (Bassino et al. 1994; Bekki et al. 2001, 2003; Drinkwater et al. 2003; Goerdt et al. 2008; Paudel et al. 2010; Pfeffer & Baumgardt 2013; Seth et al. 2014; Janz et al. 2015).

There have been several observational studies on Virgo UCDs to understand their

formation mechanisms, and most of these studies support the "dwarf galaxy" origin. Haşegan et al. (2005) and Jones et al. (2006) found three and nine UCDs in the Virgo, respectively. Haşegan et al. (2005) suggest that the Virgo UCDs are the stripped nuclei of dwarf galaxies because of their mass-to-light ratios, luminosities, and colors, which are similar to those of nucleated dwarfs, while Jones et al. (2006) did not make a concrete conclusion about the origin of UCDs. Brodie et al. (2011) compiled a larger sample of Virgo UCDs and found that the 34 Virgo UCDs have a color-magnitude trend similar to that of the nuclei of dwarf galaxies and kinematics distinct from those of normal GCs. Recently, Liu et al. (2015) selected UCDs in the NGVS images and divided them into two groups: those with a visible envelope and those without. They found that the UCDs without an envelope are more centrally concentrated on M87 than those with an envelope, which are more centrally concentrated than the nucleated dwarfs. They suggested that this result may reflect a sequential evolution from dwarfs to UCDs. Zhang et al. (2015) found that UCDs near the M87 region show a stronger rotation and more radially biased orbits at large radii than M87 GCs, suggesting that UCDs have a dwarf galaxy origin.

We investigate the cumulative radial distribution of the UCDs, compared with those of M87 GCs, IGCs, and Virgo nucleated dwarfs (see Figure 2.19). We select nucleated dwarfs in the EVCC, and the dwarf galaxy population in the region covered by this study is dominated by nucleated dwarfs. All these objects, which have radial velocities of $v_{\rm r} > 400$ km s^{-1}, belong to the main Virgo cluster. We divide the UCDs into two groups: UCDs in the M87 region (M87 UCDs) and the rest of the UCDs (other UCDs). We estimate p-values from a two-sided Kolmogorov-Smirnov test to compare their cumulative radial distributions. The p-values indicate the probability that the two data come from the same parent population. The p-value for the M87 UCDs and M87 GCs is 0.42. This indicates that the M87 GCs and M87 UCDs show marginally different cumulative distributions. We could not make a concrete con-

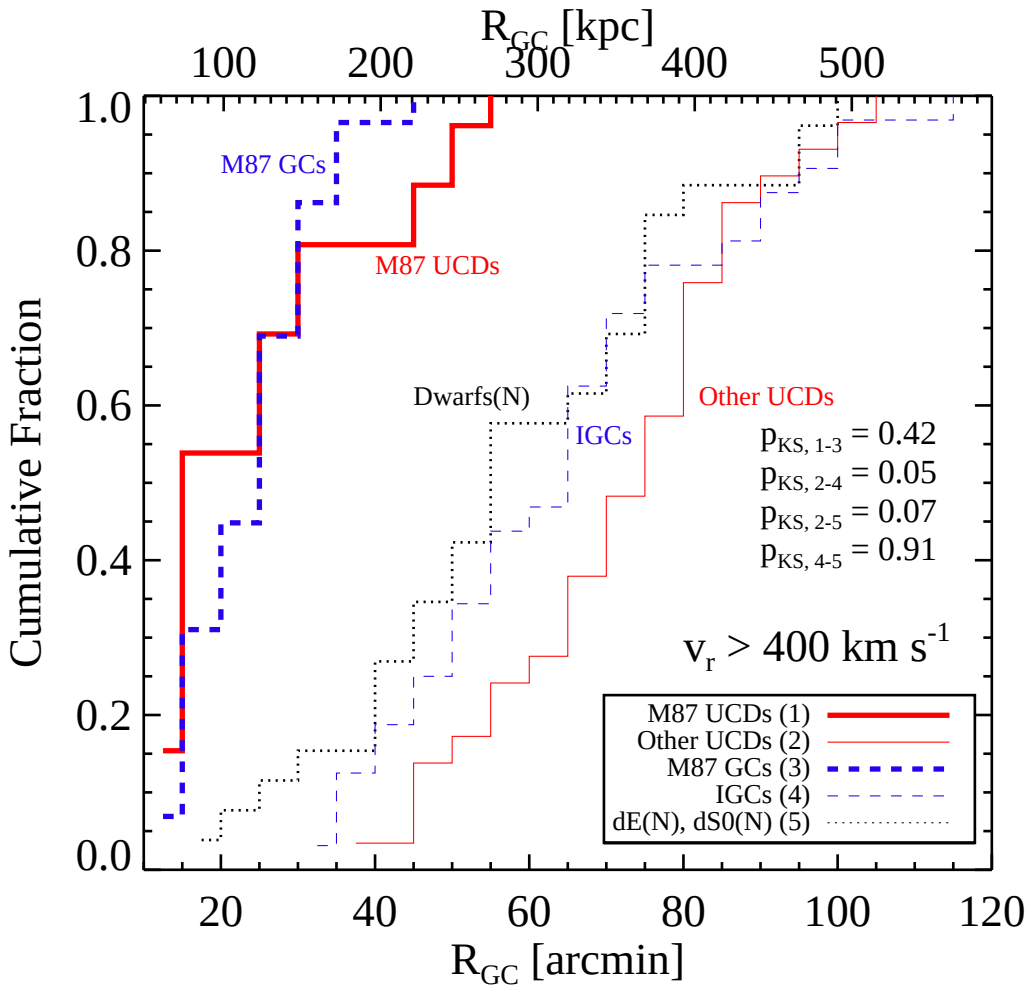

Figure 2.19: Cumulative radial distribution of UCDs in the M87 region (thick solid line), UCDs not in the M87 region (solid line), M87 GCs (thick dashed line), IGCs with $v_{\rm r} > 400$ km s^{-1} (dashed line), and nucleated dwarf galaxies with $v_{\rm r} > 400$ km s^{-1} in the survey region (dotted line; Kim et al. 2014).

clusion because our survey region does not cover the innermost region of M87. The p-values are derived to be 0.05 for the other UCDs and IGCs and 0.07 for the other

UCDs and nucleated dwarfs. This means that the UCDs not in the M87 region have a clearly different radial distribution from that of the IGCs and nucleated dwarfs. Note that the radial distribution of the IGCs is similar to that of the nucleated dwarfs, with a confidence level of 91%.

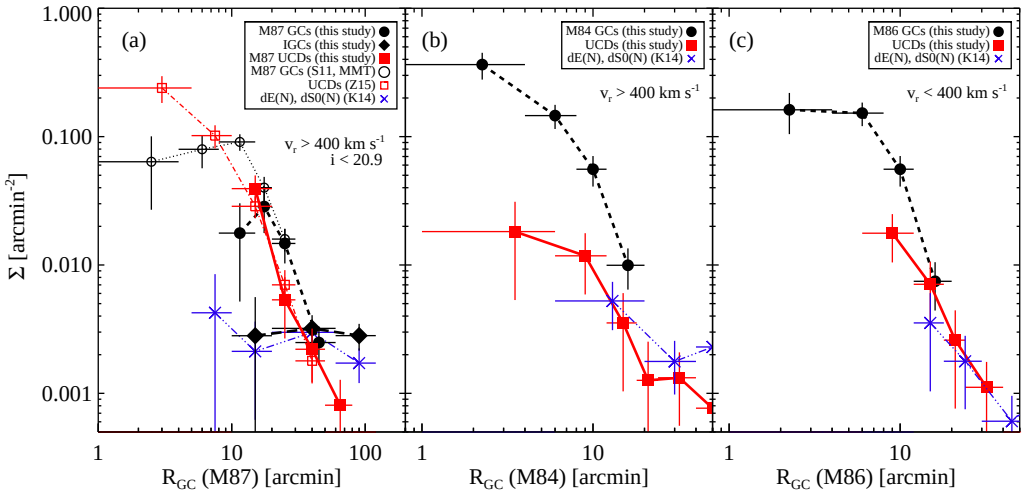

Figure 2.20: (a) Radial number density profiles of M87 GCs/IGCs with $i < 20.9$ (circles), UCDs with $i < 20.9$ (squares), and nucleated dwarfs (crosses). All objects have radial velocities of $v_{\rm r} > 400$ km s^{-1}. The open and filled circles represent the M87 GCs observed with MMT/Hectospec in Strader et al. (2011) and the M87 GCs/IGCs in this study, respectively. The open and filled squares represent the UCDs in Zhang et al. (2015) and the UCDs in the M87 region confirmed in this study, respectively. (b) Radial number density profile of M84 GCs (filled circles), UCDs with $v_{\rm r} > 400$ km s^{-1} (filled squares), and nucleated dwarfs with $v_{\rm r} > 400$ km s^{-1} (crosses) as a function of galactocentric distance from M84. (c) Radial number density profile of M86 GCs (filled circles), UCDs with $v_{\rm r} < 400$ km s^{-1} (filled squares), and nucleated dwarfs with $v_{\rm r} < 400$ km s^{-1} (crosses) as a function of galactocentric distance from M86.

Figure 2.20(a) shows the radial number density profiles of the M87 GCs, IGCs, UCDs in the M87 region, and nucleated dwarfs. We also include the samples of

GCs and UCDs spectroscopically confirmed in previous studies (Strader et al. 2011; Zhang et al. 2015). For fair comparison, we select the GC and UCD samples with $i < 20.9$ and $v_{\rm r} > 400$ km s^{-1} in previous studies. Strader et al. (2011) compiled a GC sample with four different observations, but we select the GCs observed with MMT/Hectospec because of their wide spatial coverage. The MMT/Hectospec observations did not cover the innermost region of M87. The radial number density profiles of the M87 GCs and UCDs confirmed in this study are well consistent in the range of $10' < R_{\rm GC} < 40'$ with those of the M87 GCs in Strader et al. (2011) and Zhang et al. (2015), respectively. The GCs and UCDs show a clear central concentration on M87, while the IGCs and nucleated dwarfs do not. The difference in the radial number density profile between the M87 GCs and UCDs is not significant. Figure 2.20(b) shows the radial number density profiles of the GCs, UCDs, and dwarfs with $v_{\rm r} > 400$ km s^{-1} as a function of galactocentric distance from M84. The GCs in M84 and UCDs show a strong central concentration on M84, but the nucleated dwarfs do not. We notice that the excess on the cumulative radial number distribution of the UCDs at $80' < R_{\rm GC} < 100'$ is caused by the UCDs in the M84 region. The radial velocity dispersion of the UCDs with $v_{\rm r} > 400$ km s^{-1} is 361 ± 24 km s^{-1}, which is much smaller than that of the dwarf galaxies with $v_{\rm r} > 400$ km s^{-1} ($\sigma = 608 \pm 84$ km s^{-1}). The UCDs and IGCs with $v_{\rm r} > 400$ km s^{-1} are more relaxed than the dwarfs as mentioned in Section 2.4.3.

All UCDs with $v_{\rm r} < 400$ km s^{-1} are located in the northwestern region of M87 that is occupied by the M86 group (see Figure 2.18(d)). Figure 2.20(c) shows the radial number density profiles of the M86 GCs, UCDs, and nucleated dwarfs with $v_{\rm r} < 400$ km s^{-1} as a function of galactocentric distance from M86. All these objects show a strong central concentration on M86, which indicates that the infalling structure is centered on M86. The radial velocity dispersion of the UCDs with $v_{\rm r} < 400$ km s^{-1} is 217 ± 41 km s^{-1}, which is similar to that of the dwarf galaxies with $v_{\rm r} <$

400 km s^{-1} ($\sigma = 282 \pm 57$ km s^{-1}) and the IGCs with $v_{\rm r} < 400$ km s^{-1} ($\sigma = 172 \pm 33$ km s^{-1}).

In summary, we found two characteristics of UCDs in the Virgo: (1) the UCDs show a stronger central concentration on massive galaxies (M87, M86, and M84) than the nucleated dwarfs, and (2) the radial velocity dispersion of the UCDs is similar to that of the GCs but much lower than that of the dwarf galaxies. These two aspects of the UCDs are similar to those of the GC system, which implies that UCDs in the Virgo may be simply bright-end GCs. However, recent studies on the GCs and UCDs in Virgo (Liu et al. 2015; Zhang et al. 2015) provide strong evidence supporting the dwarf galaxy origin of the UCDs: a difference in cumulative radial distribution between UCDs with a diffuse envelope and those without and a difference in kinematics between UCDs and GCs around M87. Therefore, more studies are needed to clarify the origin of the UCDs. Our UCD sample does not cover the entire azimuthal range of M87, and the numbers of UCDs in M84 and M86 in this study are small. A larger number of UCDs are needed to understand the origin of UCDs.

2.5 Summary

We present the results of an extensive spectroscopic survey of GCs in the central region of the Virgo, including the outermost region of M87. The GCs, UCDs, foreground stars, and background galaxies are classified using several criteria, including their radial velocities, sizes, and spectral morphology. Finally, we identified 201 GCs and 55 UCDs from 910 spectroscopic targets. The primary results of this chapter are summarized as follows.

- We detect 46 IGCs that do not belong to any individual bright galaxies in the Virgo but wander in the intracluster region. The total number of IGCs is

expected to be about 2114 in the survey region. The number density of the IGCs confirmed in this study is about 0.19 ± 0.02 arcmin^{-2}. This is comparable with the number density expected from photometric surveys in the previous studies.

- The color distribution of the IGCs shows two populations, blue (metal-poor) GCs and red (metal-rich) GCs, as in the case of M87 GCs. The blue IGCs mainly originate from dwarf galaxies (some originate from massive galaxies). On the other hand, the red IGCs are only from intermediate-mass to high-mass galaxies.

- The radial velocity distribution of the IGCs does not follow a single Gaussian distribution. There are two groups with mean radial velocities $v_{\rm r} = 1023$ km s^{-1} and 36 km s^{-1}. The IGCs with high radial velocities are located in the main body of the Virgo, while the IGCs with low radial velocities may be infalling or outgoing populations.

- The radial velocity dispersion of the IGCs and UCDs with $v_{\rm r} > 400$ km s^{-1} ($\sigma = 314 \pm 39$ km s^{-1} and 361 ± 24 km s^{-1}) is much lower than that of the dwarfs with $v_{\rm r} > 400$ km s^{-1} ($\sigma = 608 \pm 84$ km s^{-1}). This indicates that the Virgo, based on the kinematics of the IGCs and UCDs, may be a dynamically more relaxed system than indicated by the dwarfs.

- Most of the UCDs confirmed in this study are located around the main galaxies in the central region of the Virgo–M84, M86, and M87–while the IGCs are not.

These results suggest that both the IGCs and UCDs in the main body of the Virgo are dynamically cooler systems than the dwarfs. IGCs with extremely high radial velocities ($v_{\rm r} > 2300$ km s^{-1}) are not confirmed in this study, unlike the

dwarfs with similar velocities. On the other hand, the IGCs and UCDs with low radial velocities are infalling toward or outgoing from the main body of the Virgo, but their spatial distributions are totally different. The UCDs are thought to be involved in the infalling group centered on M86, but the origin of the IGCs that lie scattered in the survey region is unclear. The size measurement of the compact IGCs will be very helpful to reduce the contamination due to foreground stars in the future.

Chapter 3

A Wide-field Photometry of GCs in the Merger Remnant Galaxy M85

3.1 Introduction

GCs are the oldest population in the Universe, so that have the fossil record of the formation and evolution history of their host galaxies as well as themselves. They are bright enough to detect in galaxies and are well distributed toward the outer edge of galaxies. It makes them an excellent tool in studying the formation process of their host galaxies. There have been extensive studies about the GC population in galaxies so far (Brodie & Strader 2006 and reference therein).

In the stellar halo of early-type galaxies, there are two distinct GC populations, blue and red GCs (BGCs and RGCs). This is called color bimodality of GCs. For the old GCs, these color differences are considered as a proxy for metallicities. The BGCs and RGCs are considered as metal-poor and metal-rich population, respectively. Lee

et al. (2010b) suggested a mixture model that combines the scenarios presented in previous studies (Zepf & Ashman 1993; Forbes et al. 1997; Côté et al. 1998). The metal-poor GCs were formed in low-mass dwarf galaxies, while the metal-rich GCs were formed in massive seed galaxies during early dissipative merging events. The metal-poor GCs in massive galaxies were considered to be accreted from low-mass dwarf galaxies when the massive galaxies grew up.

Most early-type galaxies show clear bimodal color distributions of the GCs, but some exceptions are found. Peng et al. (2006) investigated the $(g - z)$ color distribution of the GCs for 100 early-type galaxies observed in ACS Virgo Cluster Survey (Côté et al. 2004). They reported that most of their target galaxies appear to have bimodal GC color distribution. However, one galaxy has a trimodal GC color distribution, which is M85.

M85 is an S0pec galaxy with various merger-induced fine structures in the northernmost region of the Virgo cluster. It has a second highest find structure index, $\Sigma = 6.85$, in the list of elliptical and S0 galaxies in Schweizer & Seitzer (1992). It shows the distorted isophotes due to its neighbor galaxies (Burstein 1979), a dozen of irregular ripples (Schweizer & Seitzer 1988), and the boxy isophotes within $1''$ (Ferrarese et al. 2006). Kormendy et al. (2009) found that the surface brightness profile of M85 is highly distorted and different from that of typical S0 galaxies. The nucleus of M85 has a blue color (Fisher et al. 1996), is kinematically decoupled (McDermid et al. 2004), and shows two brightness peaks (Lauer et al. 2005). All these features indicate that M85 had experienced merging events.

Lee et al. (2010a) presented the number density map of the GCs in the Virgo cluster using the SDSS data. It is confirmed from their number density map that bright GCs are strongly concentrated on M85 and extended out to $\sim 0.5^{\circ}$ from M85 center. Peng et al. (2006) showed the trimodal color distribution of M85 GCs, but the ACS coverage is too small ($202'' \times 202''$) to investigate the outer halo GCs. The

trimodal color distribution of the GCs located in the central region of M85 can be caused by the contamination of the intermediate-age population. Recently, Trancho et al. (2014) investigated the GC population in the north-western region of M85 with the ACSVCS optical photometry and Gemini-N/NIRI K_s photometry. They found that about 85% of the observed GCs turn out to be the stellar population formed about 1.8 Gyr ago.

In this chapter, we present first wide-field photometric survey of the GCs in M85 covering 1 deg^2 field using CFHT/MegaCam. This chapter is organized as follows. We briefly describe our observations and data reduction in Section 3.2. In Section 3.3, we identify the GCs in the survey region, and investigate the color distribution of the GCs. The radial and spatial distribution of the sub-populations of the GCs are also investigated. We discuss and summarize the results in Sections 3.4 and 3.5, respectively. We adopted a distance to M85 of 17.9 Mpc (Mei et al. 2007). One arcmin corresponds to 5.21 kpc at the distance to M85.

3.2 Observation and Data Reduction

3.2.1 Observation

We carried out a wide-field photometric survey of GC candidates in M85 using MegaCam (Boulade et al. 2003) mounted on the 3.6m Canada-France-Hawaii Telescope (program ID: 14AK06, PI: Myung Gyoon Lee) during 2014 May and July. The CFHT/MegaCam covers 1 deg^2 field and consists of 9 $\times$ 4 CCDs with a pixel scale of $0\farcs187$. We used *ugi* filters because two color combinations are useful to select the GC candidates. The exposures for u, g, and i filters were taken in five times of 720 s, five times of 463 s, and seven times of 575 s, respectively. We used a small dithering pattern for individual exposures of each filter. The small gaps between the individual CCDs are filled by this dithering pattern, while the horizontal large gaps

between the first and second rows and between the third and last rows of the CCDs are not.

3.2.2 Photometry and Standard Calibration

We did astrometry for *ugi* band images using SCAMP (Bertin 2006) using the point source catalog from SDSS-DR7 (Abazajian et al. 2009). The images for each filter were stacked with SWARP (Bertin et al. 2002) after the galaxy light of M85 and NGC 4394 are extracted with IRAF/ELLIPSE. We removed the sky background from each image, and set the sky level as zero.

We used the SExtractor (Bertin & Arnouts 1996) on the *ugi* band stacked images for source detection and photometry. We detected sources in the i image with a threshold of 3σ, and performed aperture photometry with aperture diameters of 8 pixel on the *ugi* images by adopting dual-image mode. The standard calibration of the instrumental magnitudes is done with SDSS DR12 *ugi* PSF photometry (Alam et al. 2015), after the SDSS magnitudes are transformed to CFHT/MegaCam magnitude system. We divided the survey region into several sub-regions, and applied the calibration differently depending on the location of each source. Hereafter, all photometry results of this study are based on the AB magnitude in CFHT/MegaCam filter system.

3.3 Results

3.3.1 GC Selection

We select GCs among the point sources detected in the survey region. Most GCs are expected to be point sources in ground-based images at the distance of the Virgo Cluster. We select point sources based on the concentration index defined as the i band magnitude differences between 4 pix and 8 pix aperture photometry, following

the methods described in Durrell et al. (2014). Figure 3.1 shows the concentration

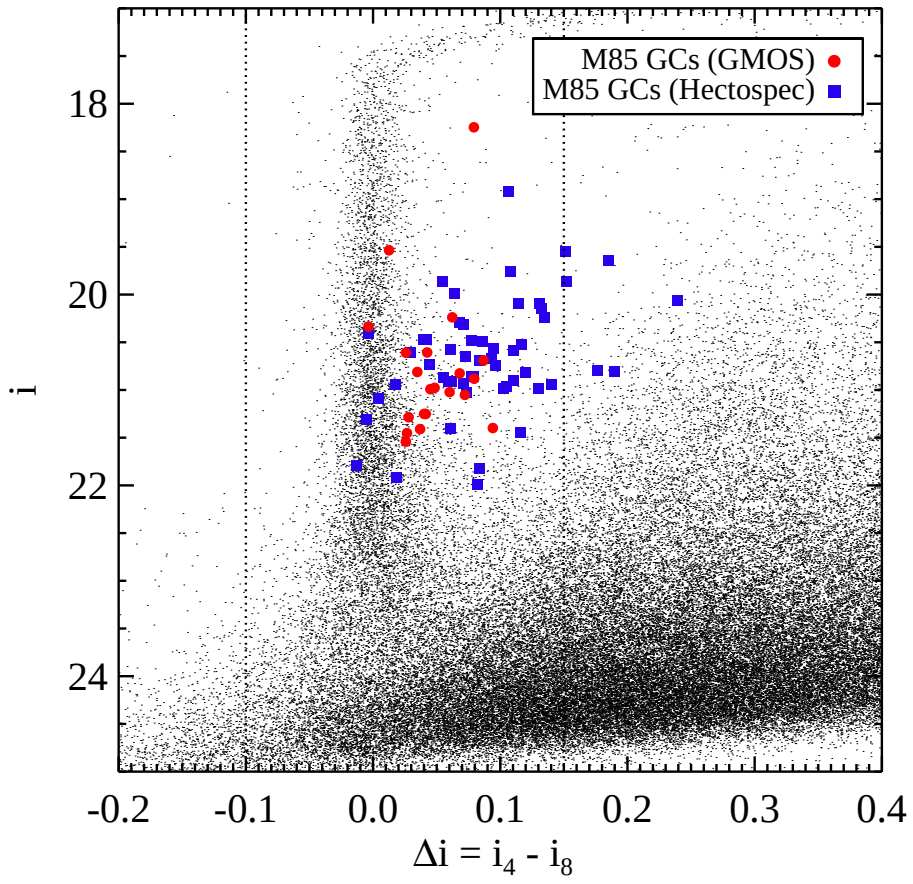

Figure 3.1: i band magnitudes vs. i band concentration index ($\Delta i = i_4 - i_8$) for the sources in the survey region. The stellar sequence is clearly seen at $\Delta i \sim 0$. The filled circles and squares represent the GCs in M85 confirmed by the spectroscopic observations from Gemini/GMOS and MMT/Hectospec, respectively. The filled triangles represents the UCDs near M85 confirmed by MMT/Hectospec observation. Note that the confirmed GCs are slightly more extended than the stars in the i band image taken in this study. The dotted lines represent the Δi criteria for selecting point sources, which are the same as those from Durrell et al. (2014).

index-magnitude diagram. The point source sequence is clearly shown at $\Delta i \sim 0$, while the extended sources have large concentration indices. We use the concentration index criterion as $-0.10 < \Delta i < 0.15$ for selecting point sources. Durrell et al. (2014) suggested this criterion based on the GCs in several Virgo galaxies showing the systemically larger Δi values than point sources. The spectroscopic GC sample of M85 (see Chapters 4 and 5) are marginally resolved as well as the Virgo GCs. This large range of the concentration index can contain the resolved GC candidates as well as point-like GC candidates.

Figure 3.2 shows the $(g-i)_0 - (u-g)_0$ color-color diagram (CCD) for the point sources. We used the foreground galactic extinction values for M85 derived by Schlafly & Finkbeiner (2011), $A_u = 0.128$, $A_g = 0.100$, and $A_i = 0.051$. Lim et al. (2017) presented the guide line for the GC selection using the spectrocopically confirmed GCs in M87. We adopt their color criteria, $0.5 < (g-i)_0 < 1.2$, $0.8 < (u-g)_0 < 1.9$, $(g-i)_0 < 0.571 \times ((u-g)_0 - 0.8) + 0.8$, and $(g-i)_0 > 0.625 \times ((u-g)_0 - 1.1) + 0.5$. We confirm that the spectroscopic GC sample of M85 also satisfy this criterion (see Figure 3.2). In addition to the color criteria, we set the magnitude criterion as $20.0 < g_0 < 23.5$. The point sources with $g_0 < 20.0$ are mainly contaminated by foreground stars. We set the faint limit where the $(g-i)_0$ uncertainty is around 0.1. As a result, we detect 1318 GC candidates in the entire survey field, satisfying all criteria mentioned above. A catalog of the GC candidates is presented in Table 3.1.

3.3.2 Surface density of GC candidates

Figure 3.3 shows the surface density profile of the GC candidates in the survey region. We find that the GCs are strongly concentrated on M85. We fit the radial surface density profile of the GCs with a Sérsic function to measure the size of the GC system and the background level. The Sérsic profile including the background

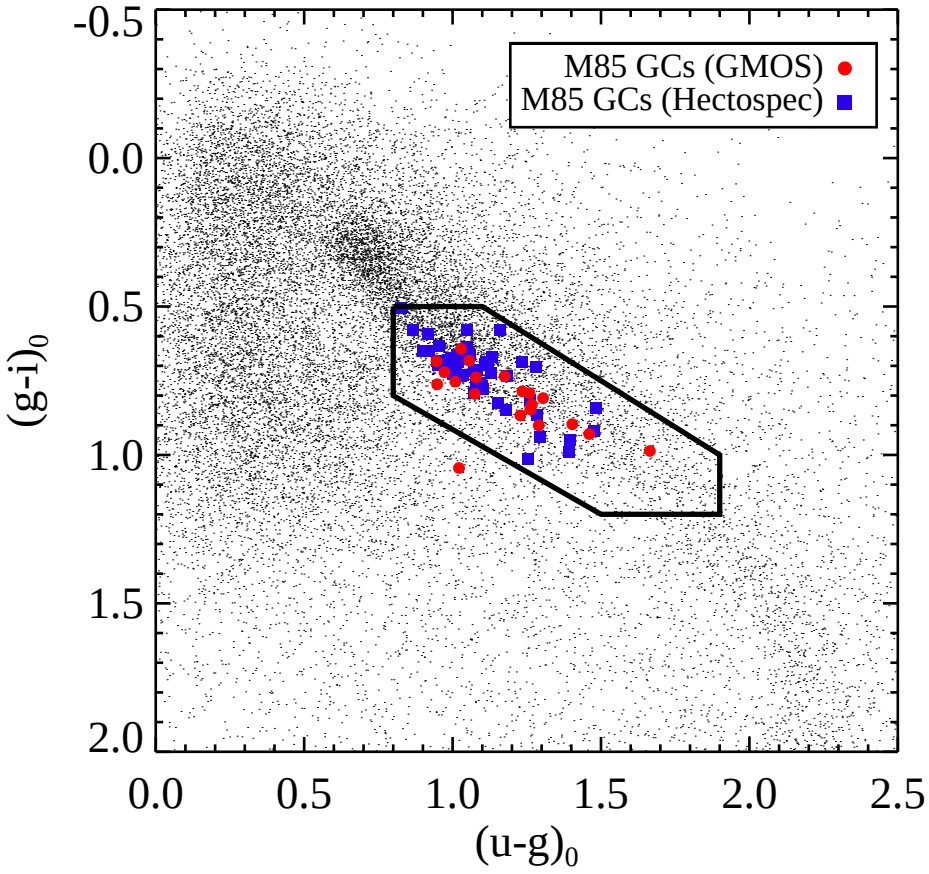

Figure 3.2: $(g-i)_0 - (u-g)_0$ CCD for the point sources in the survey region. The filled circles and squares are the same as Figure 3.1. The large polygon indicates the color criteria for the GC selection (Lim et al. 2017).

level is defined as follows (Graham & Driver 2005):

$$N(R) = N_{\rm e}\ \exp\left(-b_{\rm n}\left[\left(\frac{R}{R_{\rm e}}\right)^{\frac{1}{n}} - 1\right]\right) - bg, \tag{3.1}$$

Table 3.1. A Catalog of the GCs in M85

ID	α (J2000) (deg)	δ (J2000) (deg)	g (mag)	$u-g$ (mag)	$g-i$ (mag)
GC0001	185.831070	18.427156	23.392 ± 0.032	1.03 ± 0.09	0.89 ± 0.05
GC0002	185.832062	18.395197	22.541 ± 0.017	1.11 ± 0.05	0.61 ± 0.03
GC0003	185.834488	18.306896	22.624 ± 0.014	0.96 ± 0.03	0.73 ± 0.02
GC0004	185.835114	18.226645	21.112 ± 0.004	0.96 ± 0.01	0.69 ± 0.01
GC0005	185.835190	18.544601	22.120 ± 0.009	0.97 ± 0.02	0.83 ± 0.01

Note. — The complete version of this table is in Table A.1.

where $N_{\rm e}$ is the number density of the GCs at the effective radius $R_{\rm e}$, n is the Sérsic index, $b_{\rm n}$ is the term related with n ($1.9992n - 0.3271$), and bg is the background level. We derive the Sérsic index as $n = 2.61 \pm 0.72$, the effective radius of the GC system as $R_{\rm e,GCS} = 5\farcm54 \pm 1\farcm27$, and the background level as $bg = 0.19$ arcmin^{-2}. The Sérsic fit parameters are summarized in Table 3.2. The effective radius of the GC system is larger than that of the galaxy light, $R_{\rm e,gal} = 2\farcm15$ (Kormendy et al. 2009). We define the M85 region as $R = 20'$, corresponding to $5R_{\rm e,GCS}$, showing the edge of the M85 GC system. The number of the GCs with $R < 20'$ is 810, and the background contamination is estimated to be about 364 in the galaxy region. We consider the 810 GCs with $R < 20'$ as the GCs that belong to M85 in the further analysis.

We also investigate the two dimensional surface density of the GC candidates in M85 (see Figure 3.4). The GC candidates are well concentrated on the center of M85 as well as shown in the radial number density profile. Figure 3.4(b) shows the smoothed surface number density map of the GC candidates. The spatial distribution

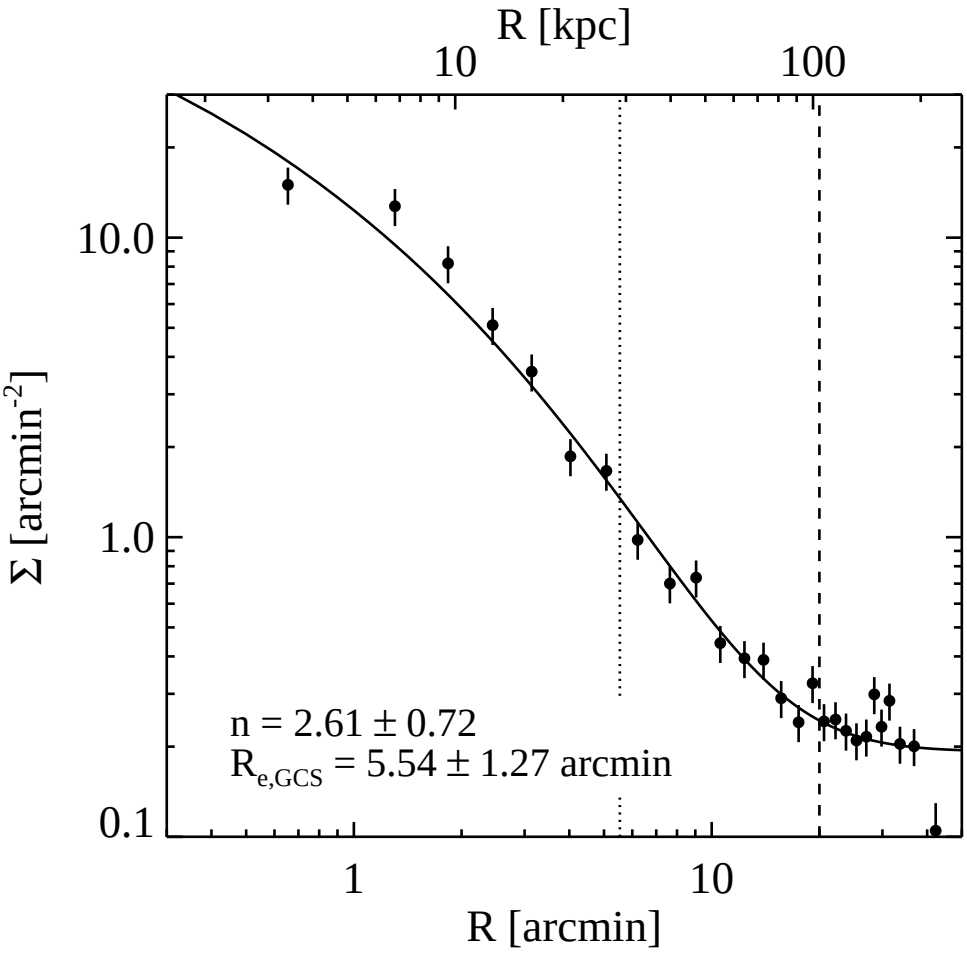

Figure 3.3: Radial number density profile of the GC candidates. The solid line represents the best fit with a Sérsic function including the background level. The dotted and dashed lines represent the effective radius of the GC system and the boundary of M85 GC system ($R = 20'$), respectively.

of the GC candidates is elongated along the east-west direction. We fit the smoothed surface density map of the GC candidates using IRAF/ELLIPSE task, and derive

Table 3.2. Sérsic Fit Parameters for the Surface Density of the GC systems

Sample	N_e (arcmin^{-2})	n	R_e (arcmin)	bg (arcmin^{-2})
All GCs	1.16 ± 0.51	2.61 ± 0.72	5.54 ± 1.27	0.19 ± 0.02
BGCs	0.56 ± 0.28	2.57 ± 0.72	7.41 ± 2.07	0.12 ± 0.02
RGCs	1.49 ± 0.62	1.95 ± 0.88	2.31 ± 0.45	0.08 ± 0.01

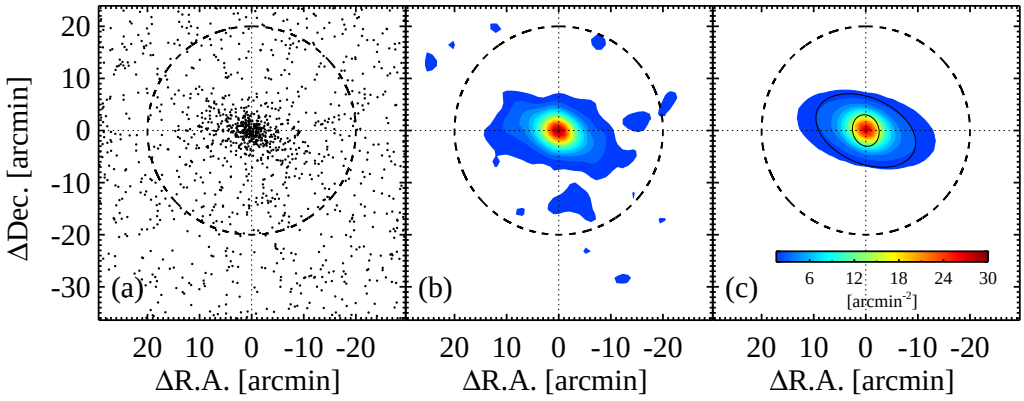

Figure 3.4: (a) Spatial distribution of the GC candidates. (b) Smoothed surface density map of the GC candidates, color-coded by the number density. (c) Surface density map of the GC candidates modelled by IRAF/ELLIPSE. The solid line ellipses indicate two guidelines for the stellar extent of M85 (Kormendy et al. 2009): One is with a major axis of 3 arcmin, a position angle of 16°, and an ellipticity of 0.18, and the other is with a major axis of 10 arcmin, a position angle of 66°, and an ellipticity of 0.38. Note that the position angles of the isophotes of the M85 stellar light rotate counterclockwise between $r_{\rm maj} = 3$ and 10 arcmin. The dashed line circles represent the boundary of M85 GC system ($R = 20'$).

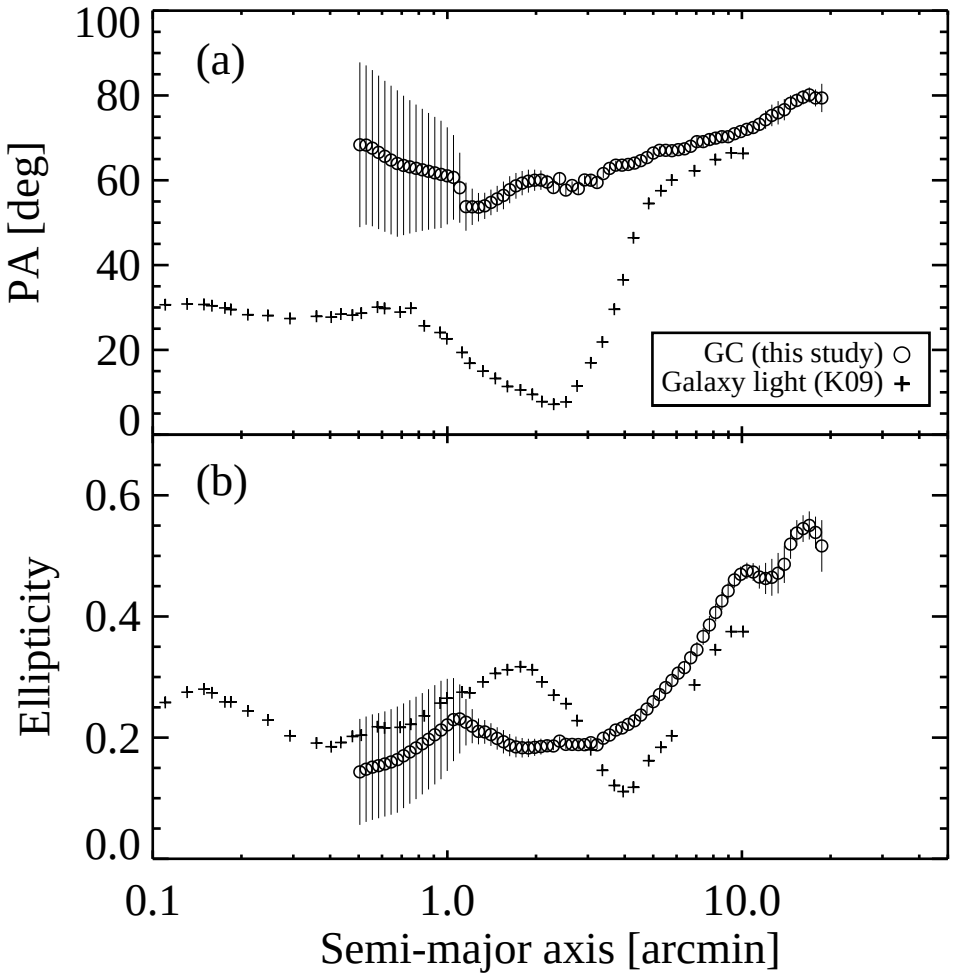

Figure 3.5: Comparison of (a) position angle and (b) ellipticity variations as a function of semi-major axis between the GC system and galaxy light (Kormendy et al. 2009).

the parameters charterizing the fitted ellipses such as ellipticities and position angles with the fixed center position. The fitted model is shown in Figure 3.4(c). The spatial distribution of the GC system in the outer region is comparable with the galaxy light

of M85 (Kormendy et al. 2009). Figure 3.5 shows the comparison of the position angles and ellipticities as a function of semi-major axis between the GC system and galaxy light. The position angles of the GC system and the galaxy light show an overall trend of counterclockwise rotation. Both the GC system and galaxy light become more elongated in the outer region ($R > 4'$) than in the inner region.

3.3.3 Color Distribution of GCs

Figure 3.6(a) shows the color-magnitude diagrams (CMD) for the point sources and GC candidates in the galaxy region, $R < 20'$. The M85 GC candidates have a distinct sequence on the CMD, compared with the GC candidates in the background region, $R > 20'$ (see Figure 3.6(b)). In particular, a strong vertical sequence appears at $(g-i)_0 \sim 0.65$. The GC candidates in the background region are mostly foreground stars. The BGC region of the CMD used to be contaminated by Sgr main-sequence, subgiant, and RGB stars, and the RGC region of the CMD by Milky Way disk stars Durrell et al. (2014). Figure 3.7 shows the CMDs for the point sources and GC candidates in various radial bins. The innermost GC candidates are well concentrated in the GC region of the CMD compared with the GCs in the outer region. The RGCs are rare even beyond $R > 5'$, while the BGCs are dominant at large radii.

Figure 3.8(a) shows the $(g-i)_0$ color distribution of the GC candidates with $R < 20'$ and $R > 20'$. The GC candidates in the background region show flatter color distribution with a bluer peak than those in the galaxy region. We subtracted the background contamination from the color distribution of GC candidates with $R < 20'$, considering the area ratio. The background-subtracted color histogram of the GC candidates with $R < 20'$ ranges from $(g-i)_0 = 0.5$ to 1.1, showing two peaks at $(g-i)_0 = 0.675$ and 0.925. We use the GMM (Muratov & Gnedin 2010) with a heteroscedastic case (different variances) to decompose this background-subtracted color distribution of the GC candidates. The number of the GC candidates with

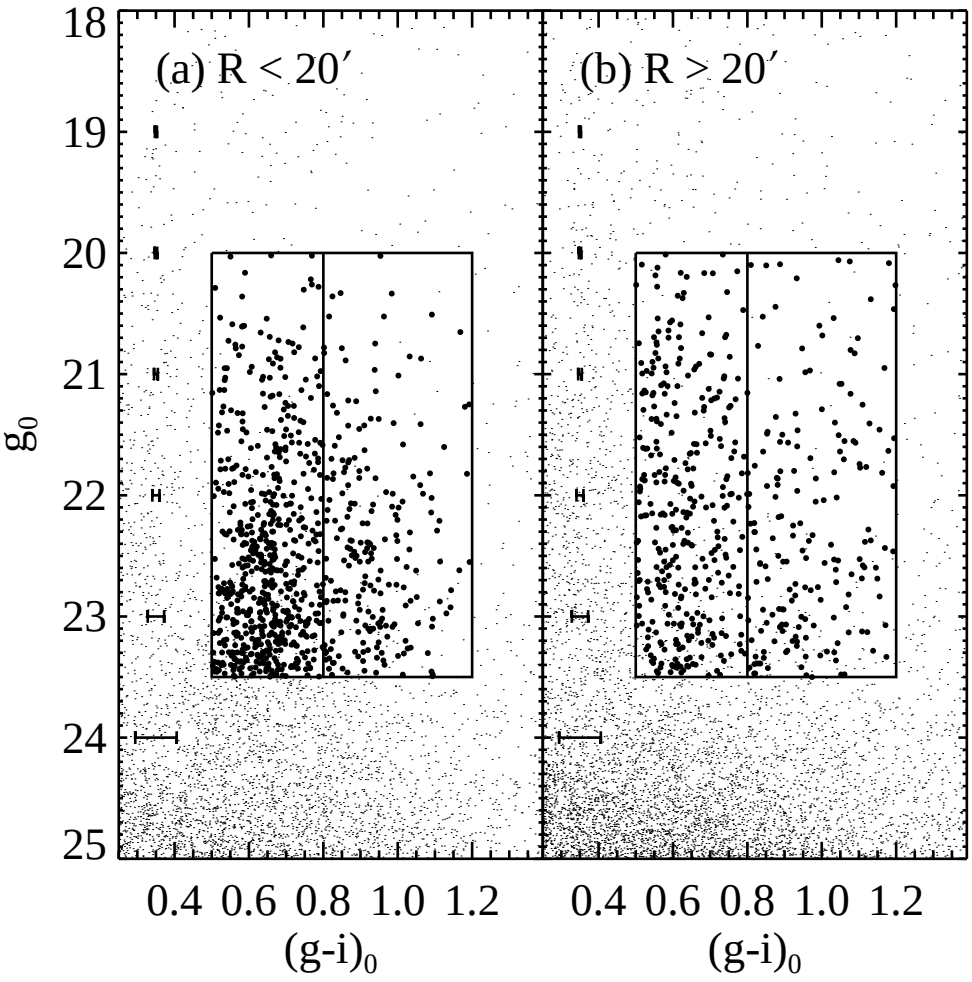

Figure 3.6: $g_0 - (g-i)_0$ CMDs for the point sources in (a) the M85 region ($R < 20'$) and background ($R > 20'$). The large boxes are the color and magnitude criteria for the GC selection, and the vertical line at $(g-i)_0 = 0.8$ indicates the criterion for selecting BGCs and RGCs. The filled circles represent the GC candidates. The error bars on the left side represent the color errors of the point sources in each magnitude bin.

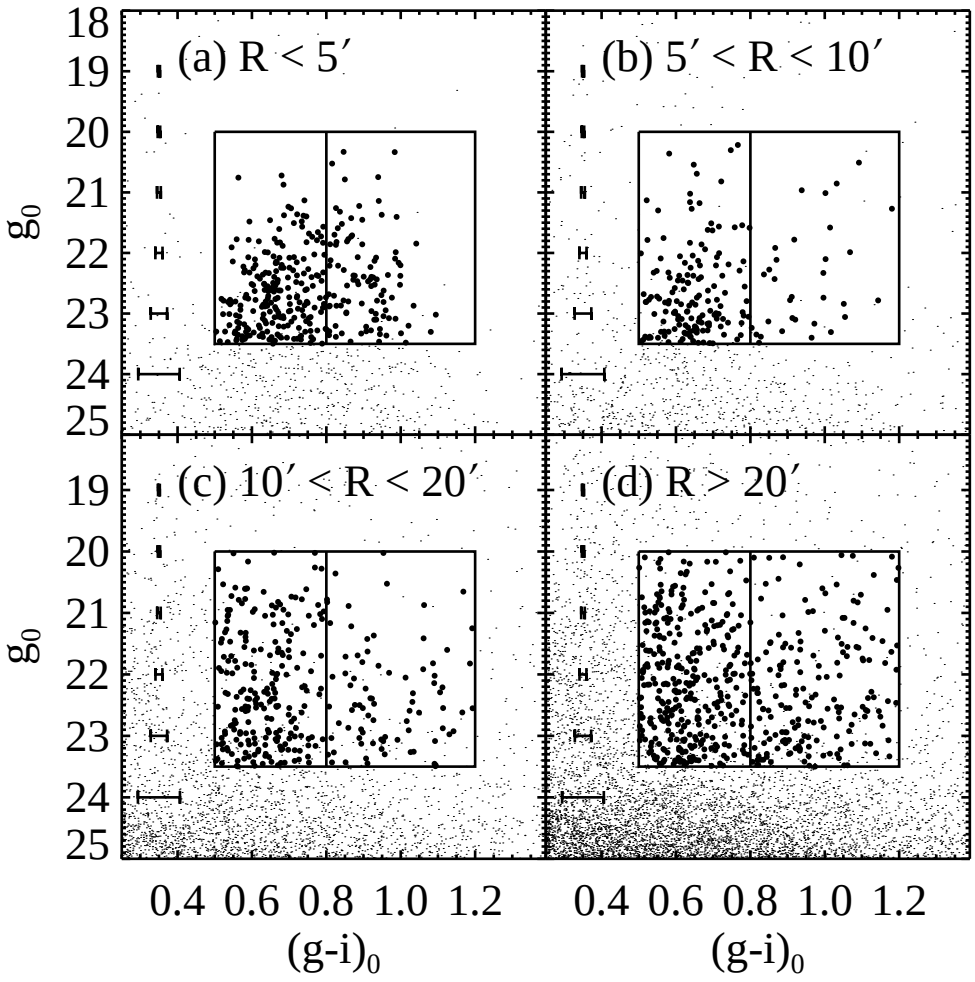

Figure 3.7: $g_0 - (g-i)_0$ CMDs for the point sources in the different radial bins: (a) $R < 5'$, (b) $5' < R < 10'$, (c) $10' < R < 20'$, and (d) $R > 20'$. The symbols and lines are the same as Figure 3.6.

$R > 20'$ is 508, and about 282 contaminants are expected in the galaxy region. We randomly pick 283 GC candidates in the background region, and remove the same number of GC candidates with similar color from the GC candidates in the galaxy

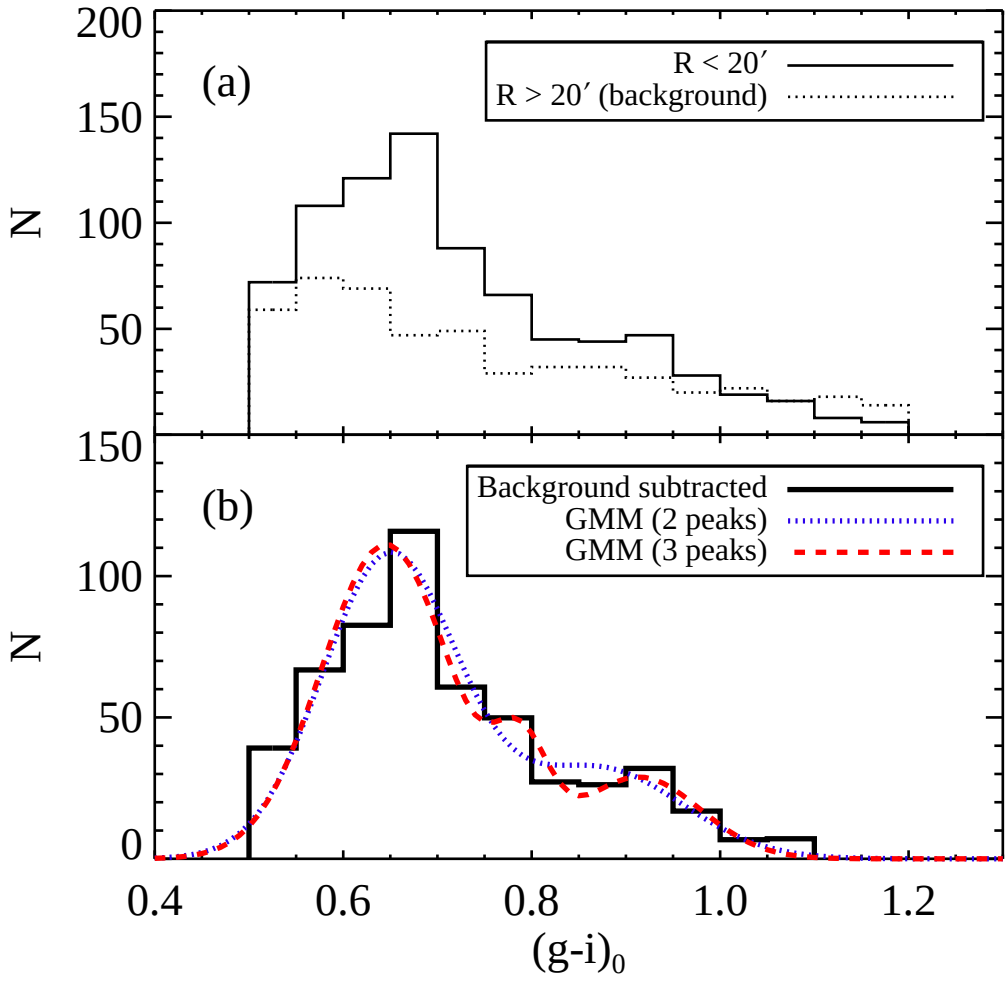

Figure 3.8: (a) $(g-i)_0$ color distribution of the GC candidates with $R < 20'$ (solid line) and $R > 20'$ (dotted line). (b) Background-subtracted $(g-i)_0$ color distribution of the GC candidates with $R < 20'$ (solid line). The dotted and dashed lines show the Gaussian fits from GMM with 2 peaks and 3 peaks, respectively.

region. We run GMM tests 100 times, and measure the Gaussian peaks and widths of the color distribution by adopting the mean values of the 100 GMM results. The

uncertainties of the peaks and widths are the standard deviation of the 100 GMM results. In addition, we try to decompose the color distribution of the GC candidates into three components to confirm the presence of the intermediate-color GCs in M85. The GMM results are summarized in Table 3.3. The p value indicates the probability for the unimodal distribution, and the D value is the peak separation relative to the Gaussian widths. If the D value is greater than 2, it means the multimodal color distribution of the GC candidates.

According to the derived p and D values, we conclude that the color distribution of the M85 GC candidates is not unimodal, but bimodal or trimodal. The color peaks for the bimodal distribution are $(g-i)_0 = 0.65$ and 0.87, and for trimodal case, they are derived as $(g-i)_0 = 0.65$, 0.79, and 0.91. The peaks, widths, and number fractions of the blue components in the bimodal and trimodal cases agree with each other, $\mu = 0.65, \sigma = 0.07$, and $f = 0.73$. The red component in the bimodal case is divided into two components in the trimodal, and the number fraction of the intermediate-color population is very small ($f = 0.09$). Oldham & Auger (2016) found that the mean $(g-i)_0$ colors of BGCs and RGCs in M87 are 0.67 and 0.91, respectively, which are consistent with those derived for the GCs in M85 with trimodal case.

3.3.4 Radial trend of GC colors

Figure 3.9 shows the color distributions of the GC candidates in different radial bins, $R < 2'$, $2' < R < 5'$, $5' < R < 10'$, and $10' < R < 20'$. We remove the background contamination in each color histogram. The color distribution of the GC candidates with $R < 2'$ does not have clear two peaks, while that of the GC candidates with $2' < R < 5'$ is bimodal. The GC candidates with $R > 5'$ are mostly blue, $(g-i)_0 < 0.8$ so that do not show a bimodal color distribution. We perform the GMM tests for the GC candidates with $R < 2'$ and $2' < R < 5'$ with the same process as described in Section 3.3.3. The GMM results for the color distribution of

Table 3.3. GMM Results for $(g-i)_0$ color distribution of the GC candidates in M85

Sample	Unimodal			Bimodal					Trimodal				
	μ	σ	N^a	μ	σ	f	D	p	μ	σ	f	D	p
$R < 20'$	0.71	0.12	528	0.65	0.07	0.73	2.80	3.87e-15	0.65	0.07	0.73	2.70	5.15e-14
				0.87	0.09	0.27			0.79	0.03	0.09		
									0.91	0.07	0.18		
$R < 2'$	0.76	0.13	144	0.68	0.08	0.59	2.27	9.74e-02	0.67	0.08	0.57	2.28	3.28e-01
				0.87	0.09	0.41			0.85	0.08	0.38		
									1.01	0.03	0.04		
$2' < R < 5'$	0.72	0.13	166	0.68	0.09	0.86	3.84	8.50e-08	0.63	0.06	0.59	2.62	1.28e-07
				0.94	0.03	0.15			0.78	0.06	0.25		
									0.94	0.03	0.15		

Note. — [a] The background-subtracted number of GC candidates.

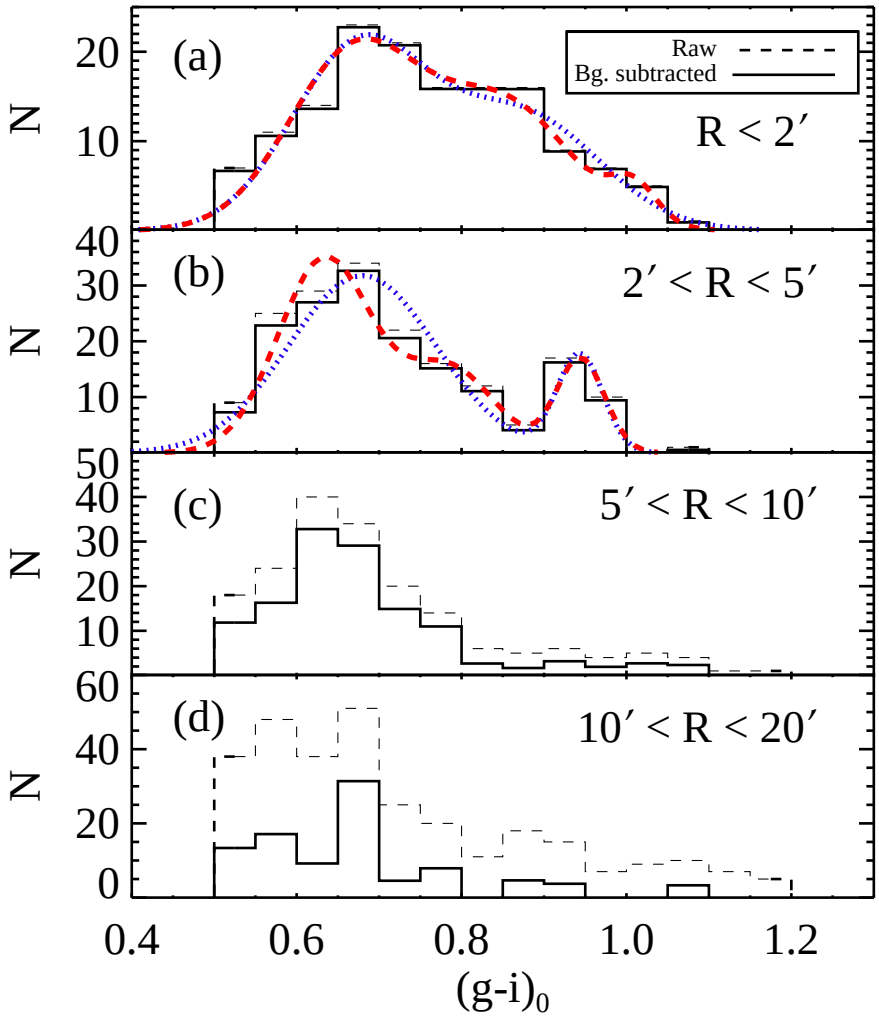

Figure 3.9: $(g-i)_0$ color distribution of the GC candidates in the different radial bins: (a) $R < 2'$, (b) $2' < R < 5'$, (c) $5' < R < 10'$, and (d) $R > 10' < R < 20'$. The dashed and solid lines represent the raw and background-subtracted color distribution, respectively. The thick dotted and dashed lines overplotted on the color histograms in (a) and (b) show the Gaussian fits from GMM with 2 peaks and 3 peaks, respectively.

the GC candidates in these two radial bins are also summarized in Table 3.3.

The $(g-i)_0$ color peaks for the bimodal case of the innermost GC candidates are 0.68 and 0.87, while for the trimodal case, 0.67, 0.85, and 1.01. However, we do not rule out the possibility of the unimodal color distribution for the innermost GC candidates, because the p values for bimodal and trimodal cases are about 0.1 and 0.3. Nevertheless, the peak separations for two cases are meaningful ($D > 2$). On the other hand, the GC candidates with $2' < R < 5'$ show a clear multimodal color distribution, $p < 0.001$ and $D > 2$. In the bimodal test, the peaks appear at $(g-i)_0 = 0.68$ and 0.94, and 85% and 15% of the GC candidates belong to each component, respectively. The trimodal test divide the blue component in the bimodal case into two components, $(g-i)_0 = 0.63$ and 0.78. We detect the intermediate-color GC candidates within $R < 5'$, especially within $R < 2'$.

3.3.5 Surface density of BGCs and RGCs

We divide the GC candidates into two groups, BGCs and RGCs, with a color criterion $(g-i)_0 = 0.8$. Note that although the intermediate-color GC population exists in the central region of M85, it cannot be classified exclusively. Figure 3.10 shows the radial number density profile of the BGCs and RGCs in M85. We fit the Sérsic profile for these two GC systems as well as the entire GC system with the same process described in Section 3.3.2. The Sérsic indices for the BGC and RGC systems are derived as $n = 2.57 \pm 0.72$ and 1.95 ± 0.88, respectively. The slope of the number density profile of the RGCs is steeper than that of the BGCs. The effective radii for the BGC and RGC systems are measured as $R_{e,GCS} = 7'.41 \pm 2'.07$ and $2'.31 \pm 0'.45$, respectively. It indicates that the RGCs are more concentrated in the central region than the BGCs, which is a common feature in the GC system of early-type galaxies. The Sérsic fit parameters for each GC system are summarized in Table 3.2.

Figure 3.11 shows the surface number density map of the BGC and RGC system

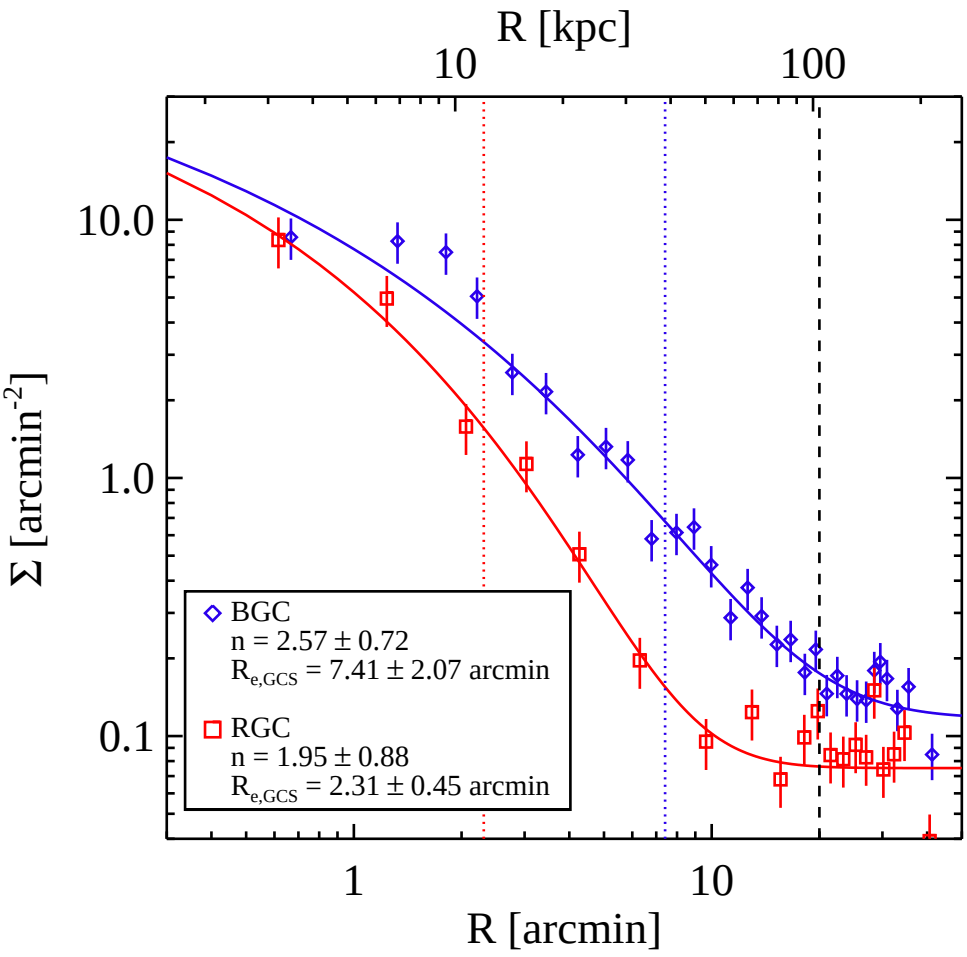

Figure 3.10: Same as Figure 3.3 but for BGC and RGC systems.

of M85. The BGCs and RGCs are well concentrated in the center of M85. The BGCs are more extended toward $R \sim 20'$, while the most RGCs are located within $R < 10'$. We derive the parameters characterizing the two dimensional surface density map for the BGC and RGC system with the same method for the entire GC system described in Section 3.3.2. Figure 3.12 shows the radial changes of the position

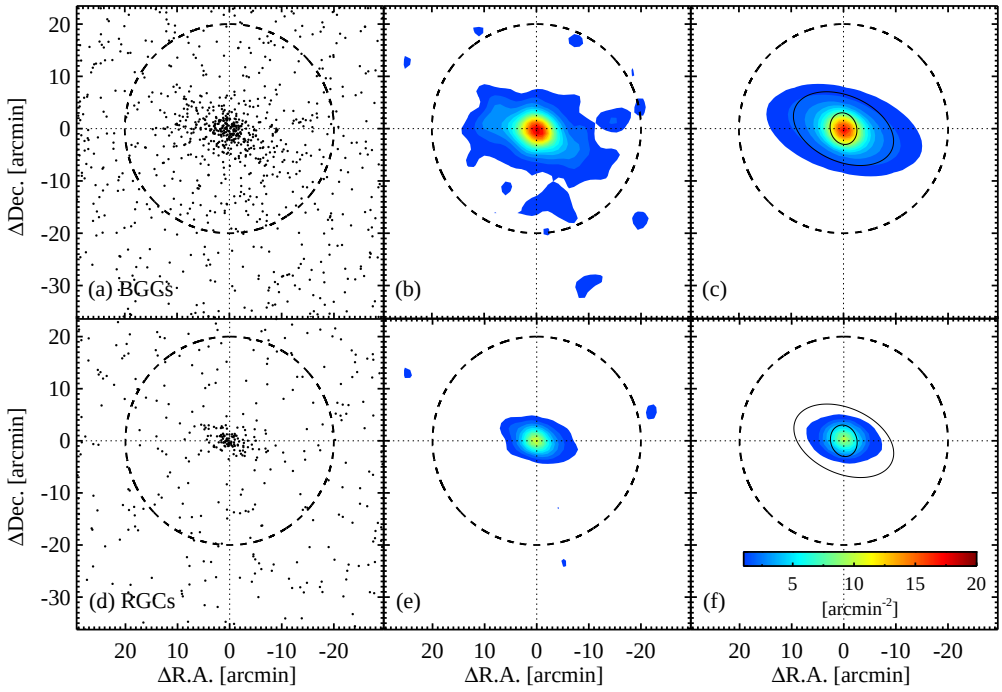

Figure 3.11: Same as Figure 3.4 but for (a)-(c) BGC and (d)-(f) RGC systems.

angles and ellipticities of the iso-density contours of the BGC and RGC systems. The BGCs and RGCs show a similar trend for these parameters. The position angles and ellipticities increases as the distance from M85 center increases. It indicates that there are no significant differences between the shape of two GC sub-systems except their radial extent.

3.4 Discussion

3.4.1 Substructures of M85 GC system

We detect two substructures at the southern and western regions from M85. Figure 3.4(b) shows two substructures showing at (ΔR. A.,ΔDec.) = (–3′, –14′) and (–15′, 1′.5), corresponding to (α, δ) = (186°.297882, 17°.958153) and (186°.087265,

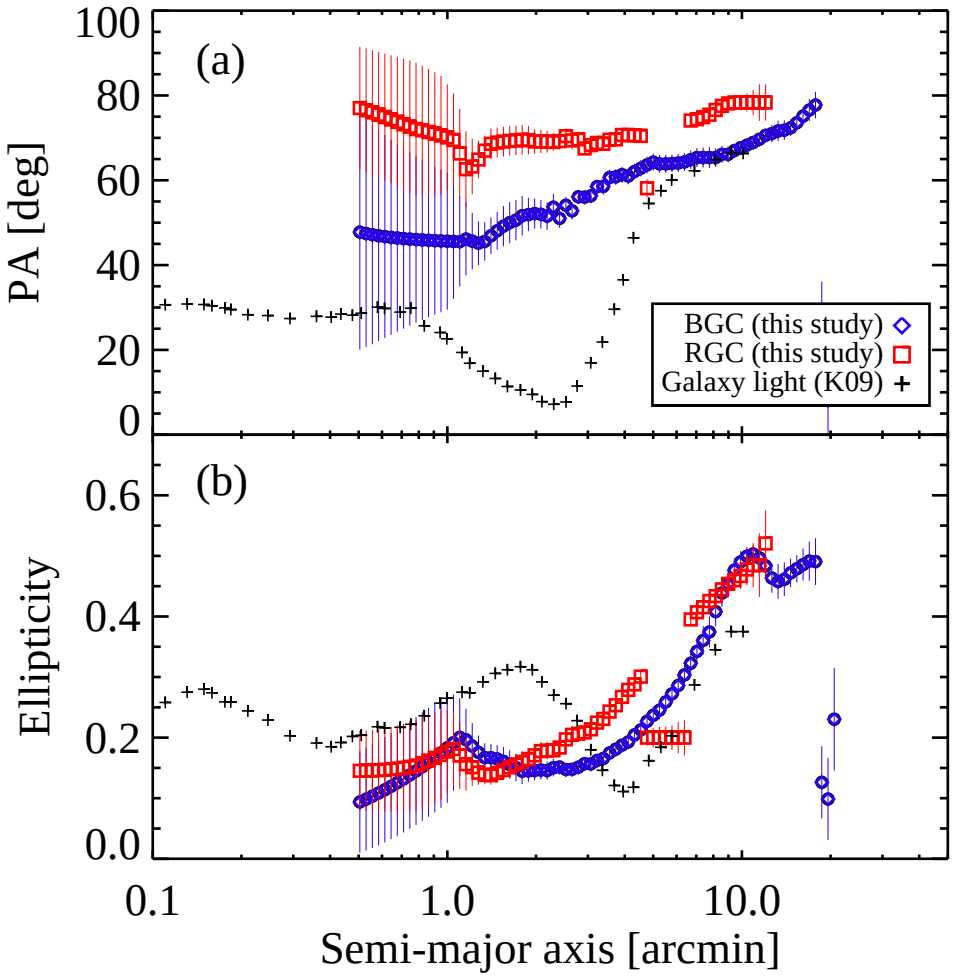

Figure 3.12: Same as Figure 3.5 but for BGC and RGC systems.

18◦216486), respectively. The BGCs mainly belong to these two substructures as clearly shown in Figure 3.11(b). Figure 3.13 shows the radial number density profile of the GC candidates from the center positions of two substructures we defined. The GC candidates are well concentrated on the center positions, so that they are expected to be gravitationally bound systems. We define the southern and western

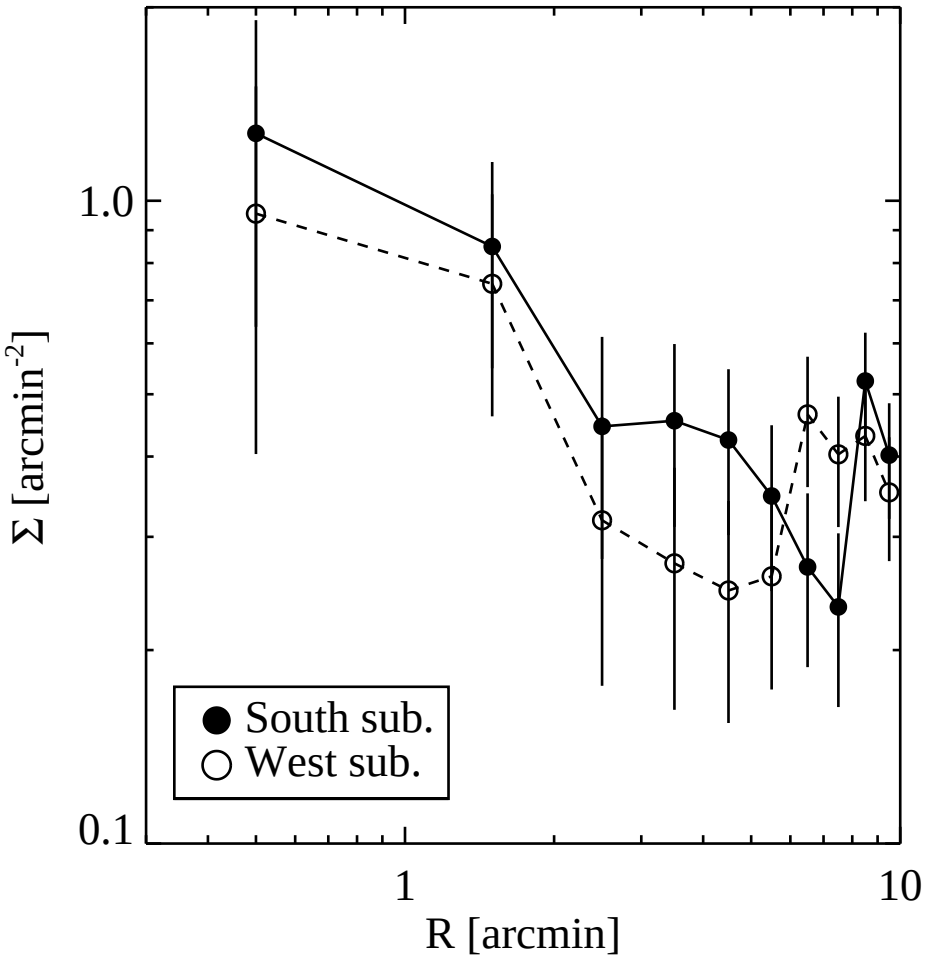

Figure 3.13: Radial number density profile of the GC candidates in substructures. The filled circles and open circles represent the GC candidates in southern and western substructures, respectively.

substructure regions with radial extent of $\sim 8'$ and $\sim 5'$. The radial number density excess at the outer part of each substructure is caused by the GC candidates that belong to M85. In the southern and western substructures, there exist 75 and 28 GC

candidates, respectively.

We investigate the stellar populations in these two substructures. Figure 3.14 shows the $g_0-(g-i)_0$ CMDs of the point sources located in two substructures. They consist of BGCs and RGCs, but most of the GC candidates in both substructures are blue as shown in the background-subtracted color distributions (see Figures 3.14(a) and (b)). These two aggregates of BGCs originate from metal-poor dwarf galaxies, which might interact with M85.

3.4.2 Merging Signatures on M85 GC system

Previous studies on M85 GCs to date covered the center region of M85 ($R < 3'$). They showed that the color distribution of the M85 GCs is not simply bimodal but trimodal (Peng et al. 2006) and predicted that there would be an intermediate-age population with ages of ~ 1.6 Gyr among the M85 GCs (Trancho et al. 2014). In this study, we identify GC candidates in the outermost region of M85 and investigate their color distribution. We confirm the presence of the "green" GCs as well as blue and red GCs within $R < 2'$, but in the outer region, there are few intermediate-color GCs. Instead, we find that the red peak derived by GMM test for bimodal case is slightly greener than that of the GCs in other typical early-type galaxies. But the difference seems to be negligible. If this green population corresponds to an intermediate-age population, it can be assumed that star formation occurred intensely only in the central region of M85 a few Gyrs ago.

The spatial distribution of GCs in M85 also differs significantly from that of the GCs in other typical early-type galaxies. The BGC system generally shows less correlation with the stellar light than the RGC system, whereas the BGCs in M85 show a significant correlation with the stellar light comparable to the RGCs. The spatial distribution of the stellar light and the GC system is elongated in the outermost region of M85. This feature is caused by dry merging rather then the effect of wet

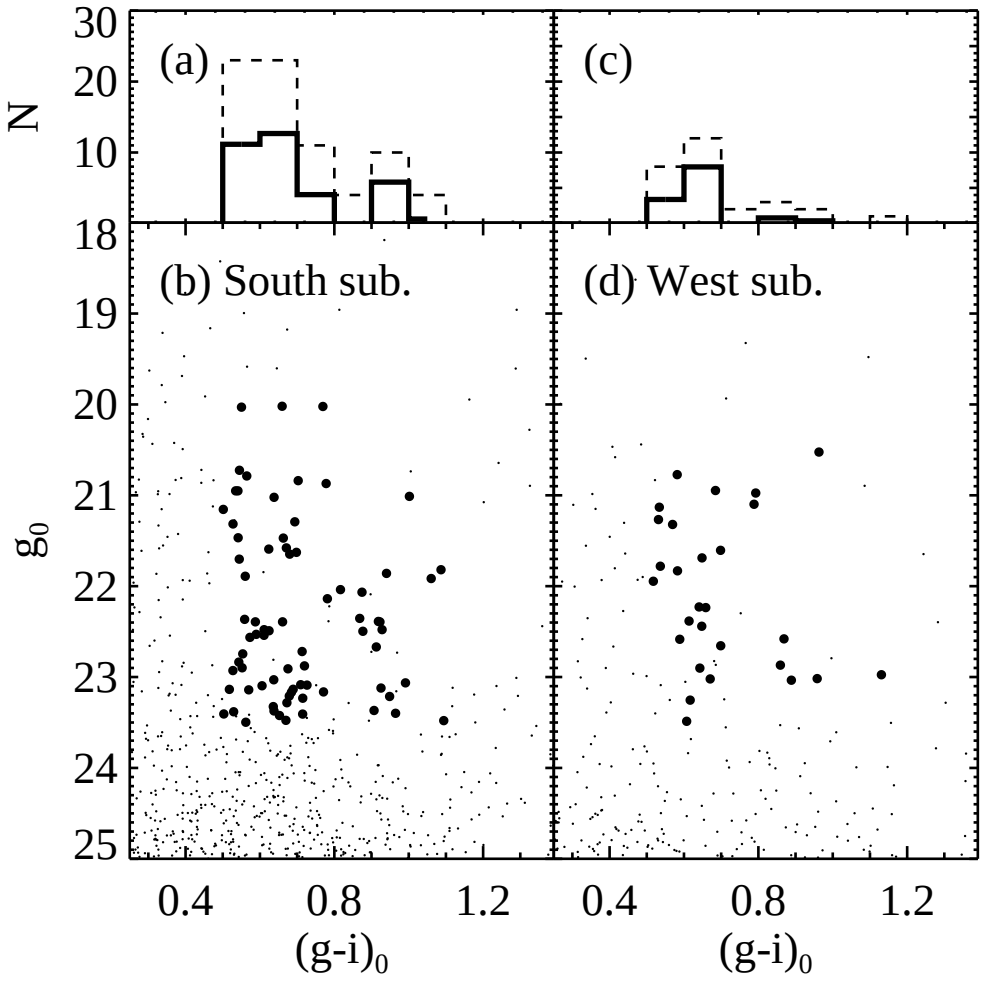

Figure 3.14: (a) $(g-i)_0$ color distribution of the GC candidates in the southern substructure (dashed line). The solid histogram represents the background-subtracted $(g-i)_0$ color distribution of the GC candidates in the southern substructure. (b) $g_0-(g-i)_0$ CMD of the point sources in the southern substructures. The filled circles represent the GC candidates. Panels (c) and (d) are the same as (a) and (b), respectively, but for the western substructure.

merging, because the post-starburst event occurred only in the central region where green GCs are detected. It implies that the M85 has grown as stars and GCs enter from outside with a specific direction.

3.5 Summary

We present the results from a wide-field photometric survey of GCs around 1 $\deg^2$ field around M85 using CFHT/MegaCam. We identify 1318 GC candidates among point sources in the survey region using color and magnitude criteria. The main photometric properties of the GC candidates are summarized as follows.

- The GC candidates show a strong concentration on M85 center. The effective radius of the GC system is $5'.54$, corresponding to 29 kpc, while that of the stellar light of M85 is as small as about $2'.15$.
- The $(g-i)_0$ color distribution of the GC candidates is not unimodal but multimodal. The peaks of the color distribution are $(g-i)_0 = 0.65$ and 0.87 for bimodal case and $(g-i)_0 = 0.65$, 0.79, and 0.91 for trimodal case. The intermediate-color population in trimodal case accounts for only 9% of the total and is mostly located within $R < 2'$.
- The BGC system is much more extended than the RGC system. The effective radii of the BGC and RGC systems are $7'.41 \pm 2'.07$ and $2'.31 \pm 0'.45$, respectively.
- Both BGC and RGC systems show significantly elongated along the stellar light as well as the entire GC system. The ellipticity profiles of both GC systems and the stellar light agree well.

We expect that the presence of the green GCs and the elongated spatial distribution of the BGC and RGC systems are merger-induced features.

Chapter 4

Ages and Metallicities of GCs in the Merger Remnant Galaxy M85

4.1 Introduction

M85 is an intriguing galaxy in the northernmost region of the Virgo Cluster, classified as S0pec. It shows various merging features reported by various studies (Burstein 1979; Schweizer & Seitzer 1988; Ferrarese et al. 2006; Kormendy et al. 2009). Several studies determined when the wet merging occurred by measuring the ages of its stellar light, especially in the core region. Schweizer & Seitzer (1992) developed a simple two-burst model for mergers based on UBV color of galaxies, assuming the merger progenitors and the gas-to-star conversion efficiency. They derived a heuristic merger age of M85, ranging from 3.9 to 7.5 Gyr. Fisher et al. (1996) detected a strong Hβ absorption of the spectrum of M85 nucleus, which indicates that it is as young as about 3 Gyr. Terlevich & Forbes (2002) also estimated the age and [Fe/H] ratio

of M85 as 1.6 Gyr and 0.44 dex, respectively, from Hβ line index and a combination index [MgFe] of the spectrum of M85 nucleus. These suggest that there was a wet merging event for M85 a few Gyr ago.

Consequently, M85 is expected to host numerous GCs younger than 8 Gyr formed via the wet merging process, called intermediate-age GCs. There are two previous studies of the GCs in M85. Peng et al. (2006) presented the color distribution of the GCs observed in the ACS Virgo Cluster Survey (Côté et al. 2004). The GCs in massive early-type galaxies often show a bimodality in their color distribution. This indicates that the massive early-type galaxies host two different GC populations, old metal-poor and old metal-rich GCs. The color distribution of the GCs in M85, however, is not simply bimodal but trimodal, which suggests the presence of intermediate-age GCs as well as old GCs. Recently, Trancho et al. (2014) presented ACSVCS optical photometry and Gemini-N/NIRI K_s photometry of the GCs in central region of M85. They found that about 85% of the observed GCs are formed about 1.8 Gyr ago.

Here, we present a spectroscopic survey of the GCs in M85 with Gemini-N/GMOS. Spectroscopy is efficient for reducing the foreground and background contamination in the photometric GC candidates by deriving their radial velocities. In addition, the spectral analysis allows us to estimate ages and metallicities of the GCs independently, while the photometric studies suffer from the age-metallicity degeneracy. To date, there has been no spectroscopic study of M85 GCs.

This chapter is organized as follows. We briefly describe the spectroscopic target selection, observation, and data reduction in Section 4.2. In Section 4.3, we derive the radial velocities of targets and identify genuine M85 GCs. We describe the methods to measure the ages and metallicities of the M85 GCs in Section 4.4. In Section 4.5, we investigate the age and metallicity distribution of the M85 GCs and present the kinematic properties of the M85 GC system. We discuss and summarize the results

in Sections 4.6 and 4.7, respectively. We adopted a distance to M85 of 17.9 Mpc (Mei et al. 2007). One arcminute corresponds to 5.21 kpc at the distance to M85.

4.2 Observation and Data Reduction

4.2.1 Target Selection for Spectroscopy

We selected GC candidates from the *ugi* band images obtained from CFHT/MegaCam observation (program 14AK06, PI: Myung Gyoon Lee; see Chapter 3). Figure 4.1(a) and (b) show the $(g-i)_0$ color distribution of the GC candidates and $i_0-(g-i)_0$ color-magnitude diagrams (CMDs) for the point sources in the $5\farcm5\times5\farcm5$ field centered on M85, respectively. The magnitudes are based on CFHT/MegaCam AB system. We used the foreground extinction values for M85 derived by Schlafly & Finkbeiner (2011). The GC candidates have a color range of $0.5 < (g-i)_0 < 1.15$ (Lim et al. 2017). We also set the magnitude limit ($19.0 < i_0 < 21.5$) to remove possible contamination by bright foreground stars and to avoid too faint targets. The observation targets have more bluer color than the GC candidates with the same color and magnitude criteria. After assigning the slits, in total, we selected 21 candidates for the spectroscopic observations. In addition, we added a hyper-compact cluster (M85-HCC1) reported by Sandoval et al. (2015) for spectroscopic targets. In total, we have 21 GC candidates, M85-HCC1, and M85 nucleus for spectroscopic targets. The basic information of the spectroscopic targets is listed in Table 4.1.

4.2.2 Spectroscopic Observation and Data Reduction

We carried out spectroscopic observation using the Gemini Multi-Object Spectrograph on the Gemini-North 8.1 m telescope on 2015 March 22 (program ID: GN-2015A-Q-207, PI: Myung Gyoon Lee). We designed a mask with a field of view of $5\farcm5\times5\farcm5$. Figure 4.2 shows the positions of the spectroscopic targets overlaid on the *i*

Table 4.1. Spectroscopic and Photometric Properties of Observation Targets

ID	α (J2000) (deg)	δ (J2000) (deg)	g^a (mag)	$(g-i)^a$ (mag)	g^b (mag)	$(g-z)^b$ (mag)	$v_{\rm r}$ (km s^{-1})
M85-GC01	186.305710	18.160259	22.084 ± 0.007	1.05 ± 0.01	···	···	995 ± 9
M85-GC02	186.307587	18.206360	22.193 ± 0.008	0.79 ± 0.01	···	···	962 ± 29
M85-GC03	186.320374	18.160419	22.133 ± 0.008	0.85 ± 0.01	···	···	715 ± 34
M85-GC04	186.326767	18.193560	21.990 ± 0.007	0.74 ± 0.01	···	···	1127 ± 30
M85-GC05	186.329453	18.159719	21.660 ± 0.005	0.84 ± 0.01	···	···	745 ± 26
M85-GC06	186.333328	18.195629	21.525 ± 0.005	0.91 ± 0.01	21.475 ± 0.021	1.16 ± 0.02	1030 ± 17
M85-GC07	186.336823	18.184280	21.850 ± 0.006	0.84 ± 0.01	21.830 ± 0.021	0.97 ± 0.02	607 ± 19
M85-GC08	186.340759	18.196980	21.507 ± 0.005	1.15 ± 0.01	21.076 ± 0.027	1.19 ± 0.04	646 ± 17
M85-GC09	186.348480	18.175610	21.821 ± 0.006	0.84 ± 0.01	21.857 ± 0.016	1.05 ± 0.02	885 ± 30
M85-GC10	186.352448	18.198999	20.438 ± 0.002	0.90 ± <0.01	20.330 ± 0.025	1.19 ± 0.03	639 ± 19
M85-GC11	186.354111	18.182461	21.550 ± 0.005	0.95 ± 0.01	21.583 ± 0.020	1.23 ± 0.02	674 ± 22
M85-GC12	186.356293	18.172230	21.453 ± 0.005	0.79 ± 0.01	21.509 ± 0.007	0.87 ± 0.01	648 ± 31
M85-GC13	186.360748	18.206301	21.782 ± 0.006	0.81 ± 0.01	21.836 ± 0.018	1.003 ± 0.020	396 ± 36
M85-GC14	186.365677	18.186300	21.688 ± 0.005	0.89 ± 0.01	21.695 ± 0.015	1.13 ± 0.02	686 ± 15
M85-GC15	186.368820	18.185720	20.966 ± 0.003	0.74 ± <0.01	20.951 ± 0.018	0.85 ± 0.02	914 ± 43
M85-GC16	186.373337	18.193729	21.661 ± 0.005	0.79 ± 0.01	21.827 ± 0.009	1.06 ± 0.03	642 ± 10
M85-GC17	186.380371	18.205959	22.235 ± 0.008	0.98 ± 0.01	22.285 ± 0.023	1.31 ± 0.03	468 ± 21
M85-GC18	186.387253	18.186489	22.318 ± 0.009	0.86 ± 0.01	···	···	501 ± 16
M85-GC19	186.389374	18.206619	22.084 ± 0.007	0.70 ± 0.01	22.270 ± 0.028	0.90 ± 0.03	422 ± 30
M85-GC20	186.394760	18.170530	22.480 ± 0.010	0.95 ± 0.01	···	···	620 ± 10
Star01	186.323792	18.172689	21.877 ± 0.006	0.62 ± 0.01	···	···	–17 ± 45
M85-HCC1	186.345184	18.181549	19.127 ± 0.001	0.89 ± < 0.01	19.134 ± 0.026	1.18 ± 0.04	647[c]
M85-Nucleus	186.350327	18.191050	···	···	···	···	743 ± 8

[a] CFHT/MegaCam AB magnitudes.

[b] HST/ACS AB magnitudes (Jordán et al. 2009).

[b] Heliocentric radial velocity of M85-HCC1 presented by SDSS.

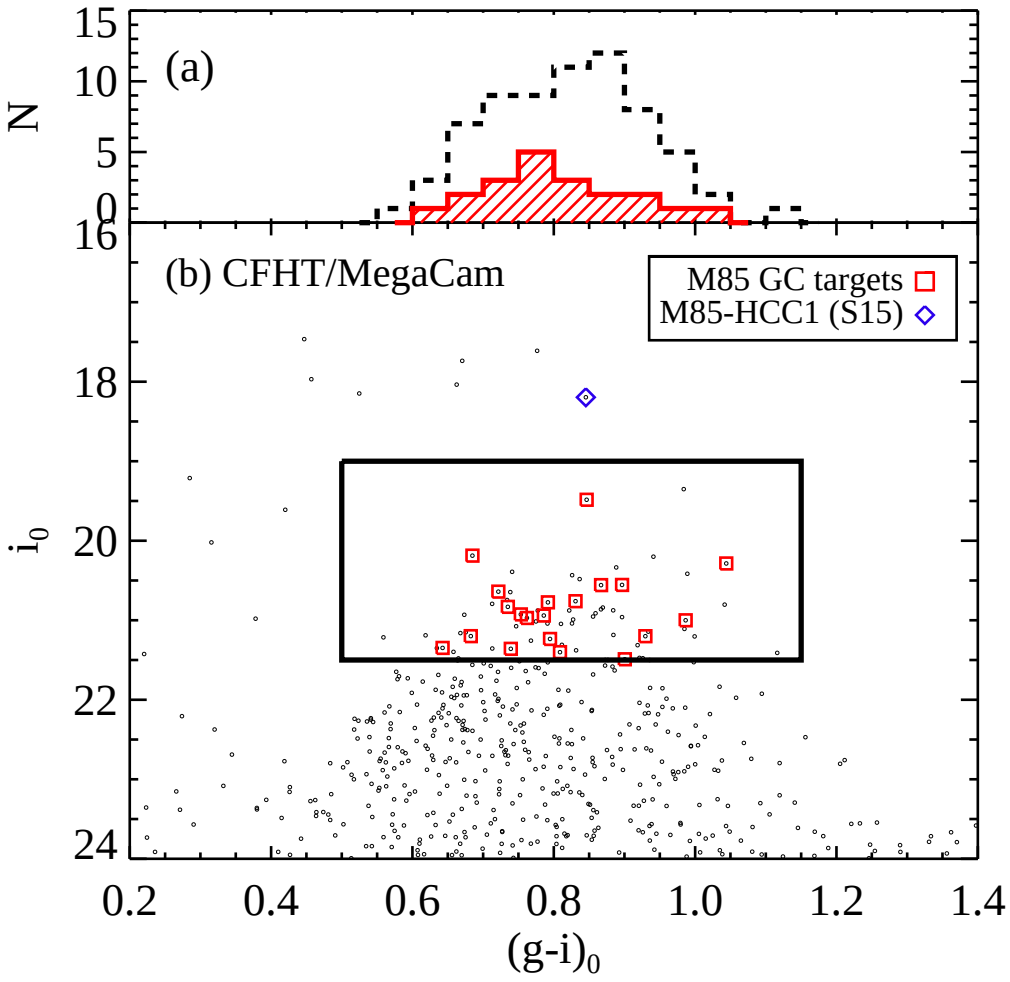

Figure 4.1: (a) $(g-i)_0$ color distribution of the observation targets (solid line) and the point sources with the color and magnitude range same as the observation targets in 5′.5 × 5′.5 field around M85 (dashed line). (b) $i_0 - (g-i)_0$ CMD of the point sources in 5′.5 × 5′.5 field around M85. The open squares and an open diamond represent the spectroscopic targets of M85 GC candidates and M85-HCC1 (Sandoval et al. 2015), respectively. The large box shows the color and magnitude criteria used for the target selection.

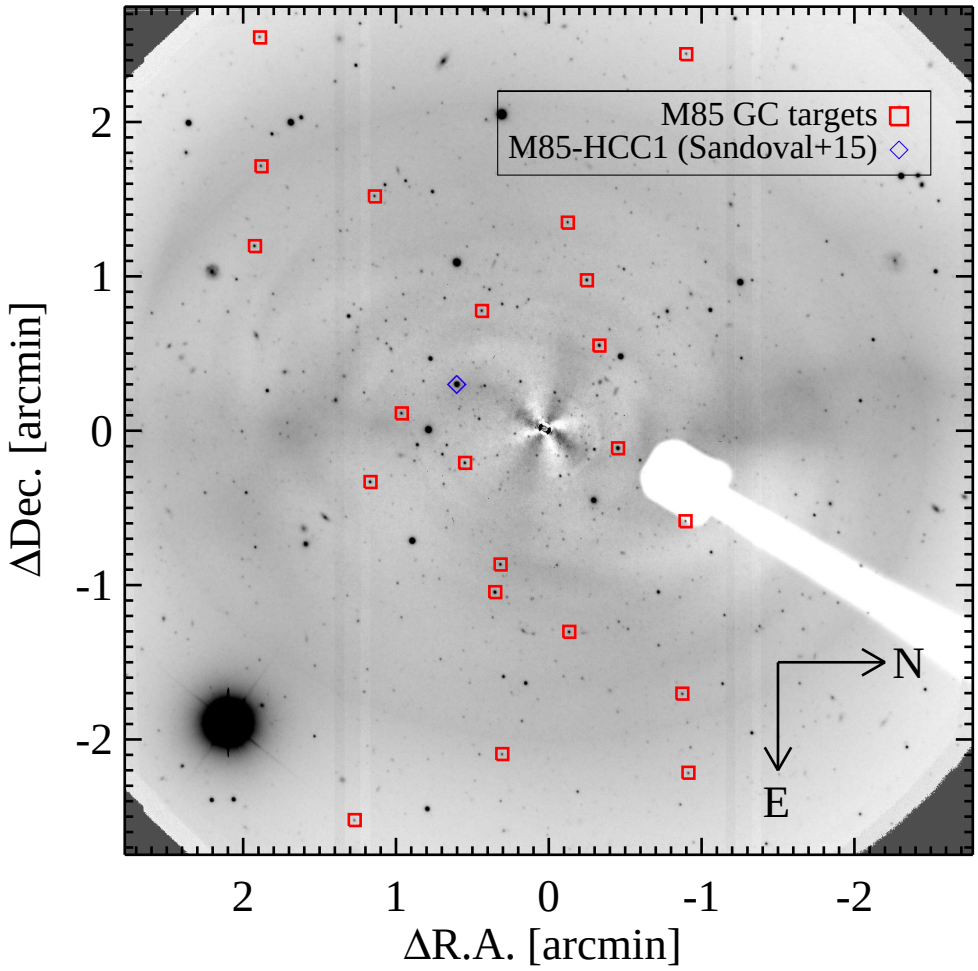

Figure 4.2: Spatial distribution of the spectroscopic targets of GC candidates overlaid on the GMOS i band image of M85. The galaxy light of M85 was subtracted from the original image using IRAF/ELLIPSE fitting. The symbols represent the same as **Figure 4.1**.

band image of M85. The galaxy light of M85 was subtracted from the original image using IRAF/ELLIPSE fitting. Note that most of the GMOS spectroscopic targets

are located along the E-W direction to avoid the collision of slits. We selected a B600_G5307 grating with a dispersion of 0.92 Å pixel^{-1}, covering the wavelength range of about 3800 Å to 6000 Å for most of targets. We did a 2 pixel binning in spectral direction and 4 pixel binning in spatial direction for each target in order to improve the signal-to-noise ratio of the observed spectra. Each target was placed at the central 1.″0 wide slit. The exposures were taken in eight times of 1800 s, so the total integrated exposure time is 4 hours.

We used the Gemini package in IRAF for data reduction[a]. We used GSFLAT task for making a master flat and GSREDUCE task for bias and overscan correction, trimming, and flat-fielding. The wavelength calibration was done with GSWAVELENGTH task using the CuAr arc spectra. The wavelength solution was applied to science data by using GSTRANSFORM task. We used GEMCOMBINE task to combine eight exposures for each target, and GSSKYSUB task to subtract the background level. The spectra were traced and extracted by using GSEXTRACT task. We observed a spectrophotometric standard star Hiltner 600, and derived a sensitivity function using GSSTANDARD. Science spectra were flux-calibrated with GSCALIBRATE using the derived sensitivity function. The mean signal-to-noise ratios of the final spectra of GC candidates at 4000 – 5700 Å range from 12 to 56.

4.3 Radial Velocity Measurements and Membership

We used the Fourier cross-correlation task, FXCOR in IRAF RV package (Tonry & Davis 1979), to estimate heliocentric radial velocities of GC candidates. We observed an SDSS sample, SDSS J122519.52+181053.7, classified as a star in SDSS-DR12 (Alam et al. 2015). This star and M85-HCC1 are used to be spectral templates for the

[a]IRAF is distributed by the National Optical Astronomy Observatory, which is operated by the Association of Universities for Research in Astronomy (AURA) under a cooperative agreement with the National Science Foundation.

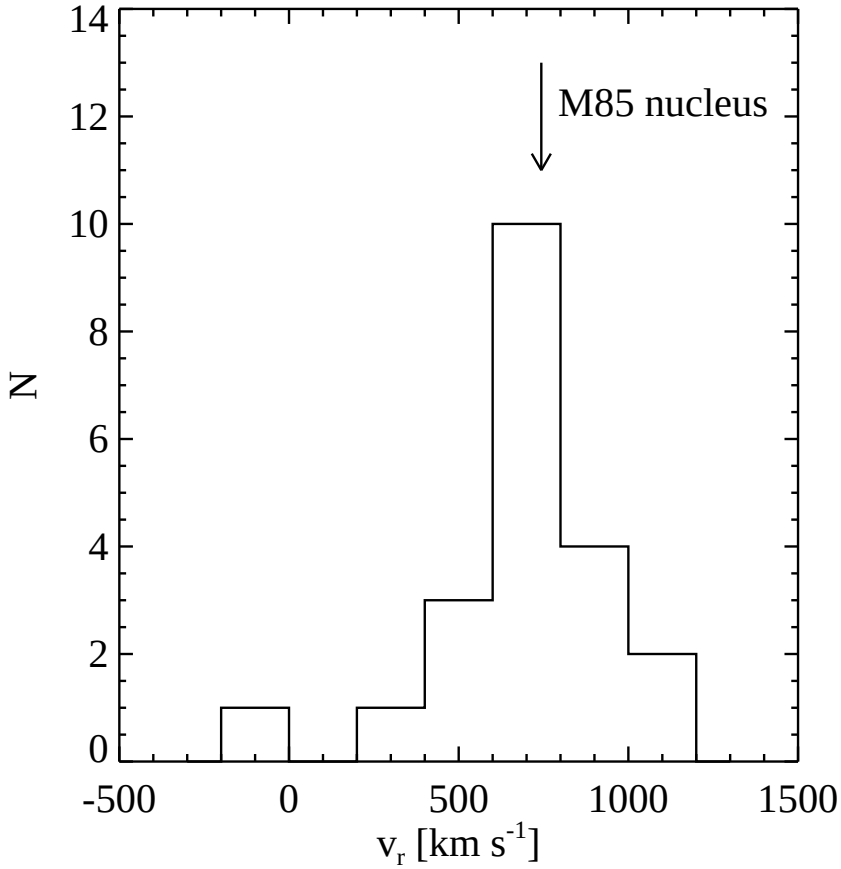

Figure 4.3: Radial velocity distribution of the spectroscopic targets. Note that the target with $v_{\rm r} < 0$ km s^{-1} is considered as a foreground star. The arrow represents the radial velocity of M85 nucleus ($v_{\rm r} = 743$ km s^{-1}).

radial velocity measurements. The radial velocities of the SDSS star and M85-HCC1 are 35 ± 4 km s^{-1} and 659 ± 4 km s^{-1}, respectively, according to the SDSS DR-12. To apply the cross-correlation method, we used prominent absorption features of spectroscopic targets and templates over the wavelength range of 4840 – 5500 Å. For each target, we adopted the error-weighted mean value of the radial velocities

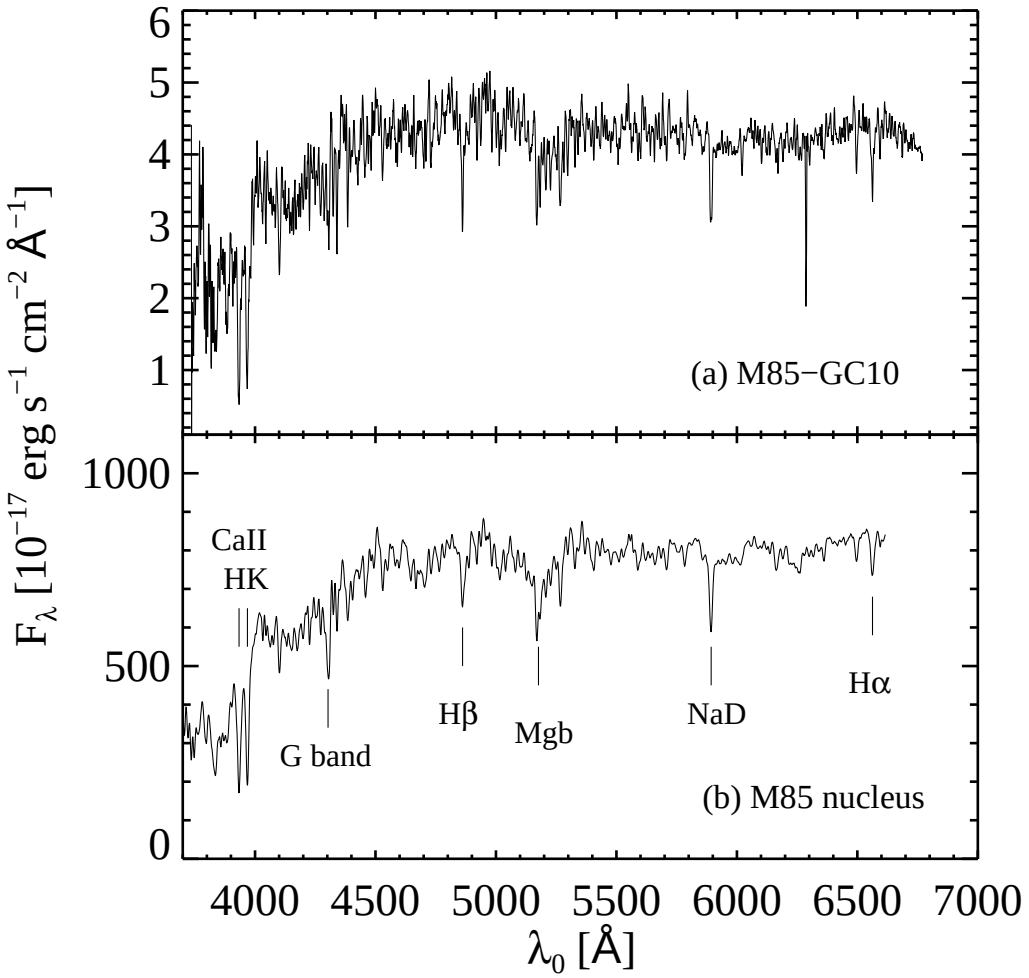

Figure 4.4: Sample spectra of (a) a GC in M85 (ID: M85-GC10) with $i = 19.535$ and $v_r = 639$ km s^{-1}; (b) M85 nucleus. All flux-calibrated spectra are plotted in the rest frame and smoothed using a boxcar filter with a size of 4.5 Å.

determined based on two spectral templates. We measured the radial velocity of M85 nucleus to be 743 ± 8 km s^{-1} , which is similar to the previous measurements, $v_r = 729 \pm 2$ km s^{-1} from Smith et al. (2000) and $v_r = 760$ km s^{-1} from Gavazzi et

al. (2004). The radial velocity uncertainties range from 8 to 46 km s^{-1} with a mean uncertainty is 24 ± 11 km s^{-1}.

Figure 4.3 shows the heliocentric radial velocity distribution of 21 GC candidates. The radial velocity distribution of the GC candidates shows a peak at 700 km s^{-1}, which is similar to that of M85 nucleus. We considered 20 GC candidates with v_r = 396 – 1127 km s^{-1} as the GCs bound to M85. The other one with v_r = –17 km s^{-1} is considered to be a foreground star. Figure 4.4 shows the spectra of the GC confirmed in this study and M85 nucleus. The absorption lines are clearly shown in the sample spectra, which are used to measure their ages and metallicities.

4.4 Age, [Z/H], and [α/Fe] Measurements

4.4.1 Lick Indices

Burstein et al. (1984) measured the strength of 11 prominent absorption lines for the spectra of 17 Galactic GCs with a resolution of about 9Å, which was introduced as the Lick index system. Afterward Worthey et al. (1994) and Worthey & Ottaviani (1997) added 10 and 4 absorption lines to the Lick index system, respectively. Trager et al. (1998) refined the definition of the set of these 25 absorption lines. The Lick line indices are widely used to determine the ages and metallicities of stellar systems, compared with those expected by theoretical models.

We measured the Lick indices in the spectra of 20 GCs, M85-HCC1, and M85 nucleus using the EZ_Ages package (Graves & Schiavon 2008) based on the stellar population model of Schiavon (2007). The Lick indices derived in this study could not be calibrated on to the Lick standard system used in the models. Pierce et al. (2006a,b) also used the non-calibraed Lick indices to determine the ages and metallicities of GCs in NGC 3379 and M60, respectively, but we will note this point in the further analysis. The Lick line indices of all observation targets are listed in

Tables A.2 and A.3, and the Lick line index errors are listed in Tables A.4 and A.5. We used two independent methods based on these line indices to derive ages and metallicities of M85 GCs, M85-HCC1, and M85 nucleus, a Lick index grid method and a χ^2 minimization method. We used the simple stellar population (SSP) models of Thomas et al. (2011). Ages of the SSP models of Thomas et al. (2011) range from 0.1 to 15 Gyr, metallicities [Z/H] from –2.25 to +0.67, and α-element abundances [α/Fe] from –0.3 to +0.5.

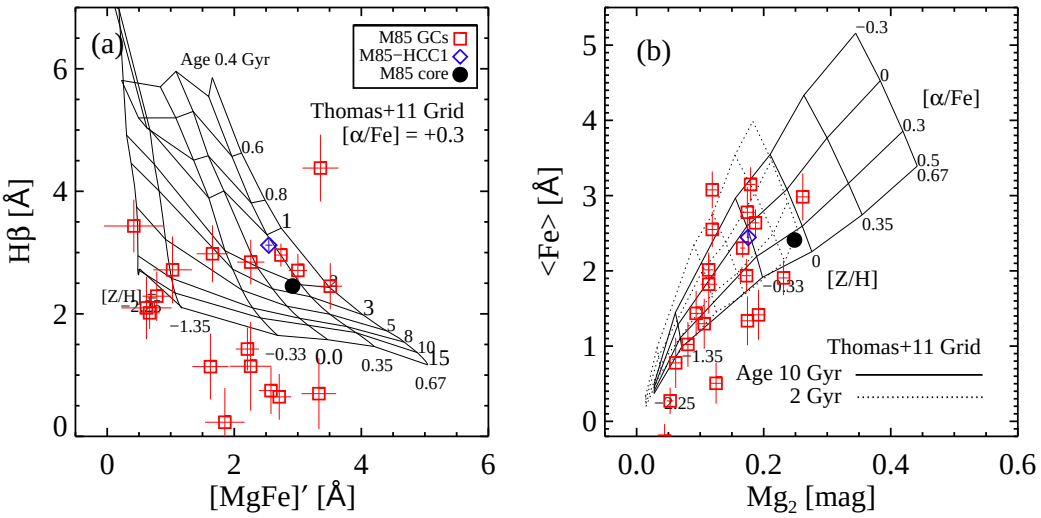

Figure 4.5: (a) Lick line indices for Hβ line vs. [MgFe]′ for M85 GCs (squares), M85-HCC1 (diamond), and M85 nucleus (filled circle) measured in this study. Error bars represent 1σ uncertainties of Lick line indices estimated with EZ_Ages (Graves & Schiavon 2008). The grids present the SSP models for a given [α/Fe] of +0.3 and for various values of [Z/H] (–2.25, –1.35, –0.33, 0, +0.33, and +0.67) and ages (0.4, 0.6, 0.8, 1, 2, 3, 5, 8, 10, and 15 Gyr) of Thomas et al. (2011). (b) <Fe> vs. Mg_2. The symbols are the same as (a). The solid and dotted-line grids are for a given age of 10 Gyr and 2 Gyr, respectively.

Lick Index Grid Method

The Lick index grid method is described by Puzia et al. (2005) using age- and metallicity-sensitive absorption lines such as Balmer lines (Hβ, Hγ, and Hδ), Fe5270, Fe5335, and Mgb lines. Figure 4.5 shows the diagnostic grids with the calibrated Lick indices of M85 GCs, M85-HCC1, and M85 nucleus: (a) Hβ vs. [MgFe]$'$ and (b) <Fe> vs. Mg_2. We selected Hβ index for the age indicator rather than Hγ and Hδ indices because its high signal-to-noise ratio. The [MgFe]$'$ index is defined as [MgFe]$' = \sqrt{\text{Mgb} \times (0.72 \times \text{Fe5270} + 0.28 \times \text{Fe5335})}$, which is a metallicity-sensitive composite index and little affected by [α/Fe]. The <Fe> index is a metallicity indicator defined as <Fe>=(Fe5270+Fe5335)/2, while the Mg_2 index is sensitive to [α/Fe].

In Figure 4.5(a), we found two different groups of M85 GCs with ages of $\sim$ 1-2 Gyr and $>$ 15 Gyr. Most of the GCs with ages of $>$ 15 Gyr might have the metallicities lower than the solar metallicity ([Z/H] = 0). The M85-HCC1 and M85 nucleus might have the intermediate-age ages (1-2 Gyr) and super-solar metallicities. Some of M85 GCs shows the similar ages and metallicities to the M85 nucleus. Figure 4.5(b) shows that the [α/Fe] ratios of most of M85 GCs range from 0 to +0.3. Most of the GCs in M85 are on the grids. We determined the ages, metallicities, and [α/Fe] ratios of all GCs, M85-HCC1, and M85 nucleus through iterations between these two grids. The iteration technique is well described in Puzia et al. (2005); Park et al. (2012b), and we followed their steps. The [Z/H] ratio can be measured from each grid, so we present different [Z/H] ratios from two grids. Note that there are some GCs older than 15 Gyr that fall outside the diagnostic grid. In this case, we adopted the parameters of the nearest point of the model grids in the direction of their error vector.

χ^2 Minimization Method

Proctor et al. (2004) suggested a χ^2 minimization technique based on the residuals

between the observed Lick indices and SSP model predictions. This method does not depend on some specific lines by using as many Lick indices as possible. Among 25 Lick indices, we excluded several lines in each spectrum for the fitting. First, we excluded CN_1, CN_2, Ca4227, and NaD indices as Proctor et al. (2004) did. The nitrogen abundance anomaly is a well-known problem for the Galactic GCs. The CN indices and Ca4227 index are sensitive to the nitrogen abundances, so that they are not fitted well with the typical SSP models. The NaD index is rejected because it is severely affected by interstellar absorption. Second, we only used the absorption lines with the signal-to-noise ratio higher than 10. Third, we excluded some indices after $\sim 2\sigma$ clipping of their χ iterately. After all exclusion, we used 8–20 Lick indices of each GC for the fitting.

4.4.2 Full Spectrum Fitting

We used the spectrum fitting code *ULySS*[b] (Koleva et al. 2009) to derive ages and [Fe/H] ratios of M85 GCs. Koleva et al. (2008) presented the full spectrum fitting results with various combinations of simple stellar population models and stellar librarlies. They showed that the ages and metallicities of GCs derived from the full spectrum fitting are consistent with those from the isochrone fitting method based on photometry of the resolved stars in the GCs. Recently, several studies used the *ULySS* code to obtain stellar population parameters of GCs in nearby galaxies (Sharina et al. 2010; Cezario et al. 2013).

We fitted the GMOS spectra of 20 GCs in M85, adopting the SSP models of Vazdekis et al. (2010) computed with MILES stellar library (Sánchez-Blázquez et al. 2006) and Salpeter IMF. The SSP models cover the optical spectral range of 3540.5–7409.6 Å at a resolution of FWHM $\sim$ 2.3 Å. Ages of the SSP models range from 63 Myr to 18 Gyr, and metallicities [M/H] from –2.32 to +0.22 dex. We used

[b] http://ulyss.univ-lyon1.fr

the wavelength range of 4000–5400 Å for the fitting as adopted in Alves-Brito et al. (2009), Cezario et al. (2013), and Chen et al. (2016). Cezario et al. (2013) suggested that the ages and metallicities of Galactic GCs are reproduced well with the fitting range of 4000–5400 Å. We ran 500 Monte Carlo simulations for each spectrum, and determined the ages and [Fe/H] ratios of the GCs by adopting the mean values of the 500 simulation results. The uncertainties of the parameters are the standard deviation of the simulation results. The ages and metallicities of M85 GCs, M85-HCC1, and M85 nucleus derived by three methods are listed in Table 4.2.

4.5 Results

4.5.1 Comparison of Parameters Derived From Different Methods

We compared the ages, metallicities, and [α/Fe] ratios derived from three different methods. There are some caveats for each method described in Section 4.4. For the Lick index grid method, the ages of the GCs are derived only with Hβ-[MgFe]$'$ grid. We could not measure the ages of GC05 and GC12, because their [MgFe]$'$ indices are not real numbers. The dependence on Hβ in determining ages of the GCs may be problematic because it is strongly affected by the horizontal branch morphology. The blue horizontal branch stars in GCs strengthen the Hβ line, and consequently the ages of the GCs that have blue horizontal branch morphology are measured young. In addition, the α-element abundance is hardly distinguished at low metallicity as shown in Figure 4.5(b). As mentioned before, there is a disadvantage in the Lick index grid method that grid boundary values are only be adopted for GCs that do not fall on the grid.

The χ^2 minimization method uses more indices than the Lick index grid method, but there may be cases where the fitting result depends heavily on some indices. We checked the stability of the fitting results by the further exclusion the Lick indices

Table 4.2. Age, Metallicity, and [α/Fe] of M85 GCs, M85-HCC1, and M85 Nucleus

ID	$\mathrm{Age_{grid}}$ (Gyr)	$\mathrm{[Fe/H]^{[MgFe]'}_{grid}}$ (dex)	$\mathrm{[Fe/H]^{Mg_2}_{grid}}$ (dex)	$\mathrm{[\alpha/Fe]_{grid}}$ (dex)	$\mathrm{Age_{\chi^2}}$ (Gyr)	$\mathrm{[Fe/H]_{\chi^2}}$ (dex)	$\mathrm{[\alpha/Fe]_{\chi^2}}$ (dex)	$\mathrm{Age_{ULySS}}$ (Gyr)	$\mathrm{[Fe/H]_{ULySS}}$ (dex)
M85-GC01	14.9 ± <0.1	0.10 ± 0.09	0.00 ± 0.06	0.00 ± 0.06	$15.0^{+<0.1}_{-2.4}$	$-0.06^{+0.14}_{-0.15}$	0.19 ± 0.13	5.5 ± 1.7	0.04 ± 0.08
M85-GC02	14.0 ± 1.1	–0.96 ± 0.15	–1.30 ± 0.13	0.19 ± 0.13	$15.0^{+<0.1}_{-5.6}$	$-1.83^{+0.10}_{-0.62}$	$0.47^{+0.03}_{-0.60}$	12.9 ± 3.9	–0.82 ± 0.09
M85-GC03	8.4 ± 2.3	–2.03 ± 0.21	–1.09 ± 0.14	0.49 ± 0.01	$5.2^{+3.4}_{-2.2}$	$-0.60^{+0.08}_{-0.10}$	$0.50^{+<0.01}_{-0.07}$	9.6 ± 5.2	–0.93 ± 0.15
M85-GC04	3.5 ± 1.0	–0.73 ± 0.17	–0.85 ± 0.11	0.02 ± 0.11	$6.0^{+3.4}_{-2.2}$	$-1.36^{+0.41}_{-0.43}$	$0.09^{+0.41}_{-0.39}$	10.6 ± 4.4	–1.63 ± 0.16
M85-GC05	···	···	0.10 ± 0.08	–0.30 ± < 0.01	$12.2^{+2.6}_{-2.1}$	$-0.12^{+0.15}_{-0.13}$	$-0.22^{+0.15}_{-0.08}$	2.6 ± 0.6	0.00 ± 0.15
M85-GC06	14.0 ± 0.5	–0.72 ± 0.08	–0.76 ± 0.06	0.22 ± 0.05	$15.0^{+<0.1}_{-2.1}$	$-1.00^{+0.09}_{-0.19}$	$0.46^{+0.04}_{-0.18}$	15.9 ± 1.1	–0.61 ± 0.06
M85-GC07	14.0 ± 0.1	–2.36 ± 0.19	–2.71 ± 0.41	0.49 ± < 0.01	$15.0^{+<0.1}_{-4.6}$	$-1.30^{+0.23}_{-0.29}$	$0.28^{+0.22}_{-0.29}$	2.9 ± 1.5	–0.98 ± 0.10
M85-GC08	1.4 ± 0.1	0.63 ± 0.10	0.27 ± 0.03	–0.01 ± 0.03	1.3 ± 0.1	$0.43^{+0.07}_{-0.13}$	0.26 ± 0.07	1.6 ± 0.1	0.22 ± 0.01
M85-GC09	5.7 ± 0.6	–2.50 ± 0.12	–1.43 ± 0.13	0.27 ± 0.12	$3.3^{+2.2}_{-1.6}$	$-1.49^{+0.14}_{-0.40}$	$0.50^{+<0.01}_{-0.40}$	5.3 ± 2.3	–0.47 ± 0.09
M85-GC10	1.3 ± 0.1	0.30 ± 0.12	0.13 ± 0.03	0.03 ± 0.03	1.8 ± <0.1	–0.01 ± 0.06	0.18 ± 0.06	2.0 ± 0.3	0.20 ± 0.07
M85-GC11	14.9 ± < 0.1	–0.62 ± 0.05	–0.72 ± 0.05	0.49 ± 0.04	$15.0^{+<0.1}_{--1.9}$	$-0.75^{+0.05}_{-0.09}$	$0.50^{+<0.01}_{-0.08}$	15.4 ± 2.9	–0.50 ± 0.05
M85-GC12	···	···	–2.71 ± < 0.01	0.49 ± < 0.01	$13.0^{+2.0}_{-1.8}$	$-2.20^{+0.13}_{-0.25}$	$0.50^{+<0.01}_{-0.23}$	10.0 ± 2.4	–2.19 ± 0.11
M85-GC13	14.9 ± <0.1	0.17 ± 0.05	–0.61 ± 0.06	–0.30 ± 0.04	$14.0^{+1.0}_{-2.0}$	$-0.95^{+0.23}_{-0.25}$	$0.03^{+0.23}_{-0.25}$	9.6 ± 3.8	–0.45 ± 0.17
M85-GC14	1.8 ± 0.3	0.30 ± 0.16	0.24 ± 0.06	–0.30 ± 0.01	$1.3\ ^{+0.2}_{-0.1}$	$-0.02^{+0.16}_{-0.18}$	$0.05^{+0.15}_{-0.14}$	7.3 ± 2.3	–0.68 ± 0.06
M85-GC15	14.0 ± 0.5	–2.30 ± 0.17	–2.71 ± < 0.01	0.49 ± < 0.01	$14.0^{+1.0}_{-2.5}$	$-1.80^{+0.28}_{-0.43}$	$0.23^{+0.27}_{-0.44}$	12.6 ± 1.1	–1.42 ± 0.06
M85-GC16	2.1 ± 0.2	0.94 ± 0.03	0.46 ± 0.04	–0.30 ± 0.03	$1.6^{+0.2}_{-0.1}$	$0.28^{+0.13}_{-0.09}$	0.07 ± 0.09	1.8 ± 0.3	0.20 ± 0.03
M85-GC17	14.9 ± 0.5	–0.79 ± 0.08	–1.30 ± 0.17	0.49 ± 0.05	$8.9^{+2.3}_{-2.6}$	$-0.13^{+0.20}_{-0.18}$	$-0.14^{+0.19}_{-0.16}$	5.4 ± 1.9	–0.28 ± 0.09
M85-GC18	1.1 ± 0.1	0.72 ± 0.08	0.42 ± 0.09	–0.11 ± 0.05	1.5 ± 0.3	–0.03 ± 0.18	0.20 ± 0.17	16.2 ± 2.1	–0.40 ± 0.06
M85-GC19	14.9 ± 0.7	–2.46 ± 0.25	–2.14 ± 0.23	0.34 ± 0.19	$15.0^{+<0.1}_{-7.3}$	$-2.40^{+0.27}_{-0.80}$	$0.50^{+<0.01}_{-0.80}$	10.5 ± 2.9	–1.13 ± 0.10
M85-GC20	14.7 ± 0.9	–0.20 ± 0.12	–0.76 ± 0.11	–0.22 ± 0.10	$14.0^{+1.0}_{-5.0}$	$-0.72^{+0.39}_{-0.28}$	$-0.07^{+0.37}_{-0.23}$	5.1 ± 2.4	–0.23 ± 0.13
M85-HCC1	1.3 ± 0.1	0.20 ± 0.04	0.19 ± 0.02	0.02 ± 0.02	1.6 ± < 0.1	$0.10^{+0.02}_{-0.03}$	$0.17^{+0.02}_{-0.03}$	1.8 ± 0.5	0.18 ± 0.12
M85-Nucleus	2.1 ± 0.1	–0.09 ± 0.01	0.01 ± 0.01	0.31 ± 0.01	3.3 ± < 0.1	–0.08 ± < 0.01	0.27 ± < 0.01	2.6 ± 0.3	0.22 ± 0.02

used for the fitting one by one. The fitting results for GC01 and GC05 are unstable if Mg and Fe lines are rejected. For example, the age and [Fe/H] ratio of GC01 derived from χ^2 minimization method are 15 Gyr and –0.06 dex, respectively. However, they are derived as $\sim$ 2 Gyr and 0.70 dex if Fe5015 index is excluded in the fitting process, respectively. This big difference caused by the exclusion of one line indicates that the fitting result is unstable and not converging. In addition, the ages of five GCs (GC02, GC03, GC17, GC18, and GC20) strongly depend on the Hβ index. For these five GCs, other Balmer lines, Hγ and Hδ, are excluded in the fitting process because of their low signal-to-ratios. The absence of Balmer lines for the fitting process of the χ^2 minimization method little affect the derived ages with the large number of Lick indices, even though the Balmer lines are strong age-sensitive lines (Proctor et al. 2004). But for these GCs, the number of the indices used in the fitting process is too small to exclude the Hβ line. We deal with the derived parameters of these seven GCs carefully in the further comparison.

These two methods based on the Lick indices may give inaccurate parameters because the Lick indices are not calibrated. The full spectrum fitting is not affected by this calibration issue, but we cannot derive the α-element abundances using Vazdekis models.

The ages based on the Lick indices are consistent within uncertainties as shown in Figure 4.6(a). Figure 4.6(b) and (c) show the comparison of the ages obtained from the Lick indices and the full spectrum fitting. They show a reasonable agreement within uncertainties except five GCs (GC01, GC05, GC07, GC14, and GC18). Among them, the χ^2 fitting results for GC01, GC05, and GC18 are not stable as mentioned before. We cannot find any possible clue for explaining the other outliers, GC07 and GC14, but the results do not need to be the same because of the Lick index calibration problem. As result, 85% of the observed GCs show the consistency between the ages from different methods.

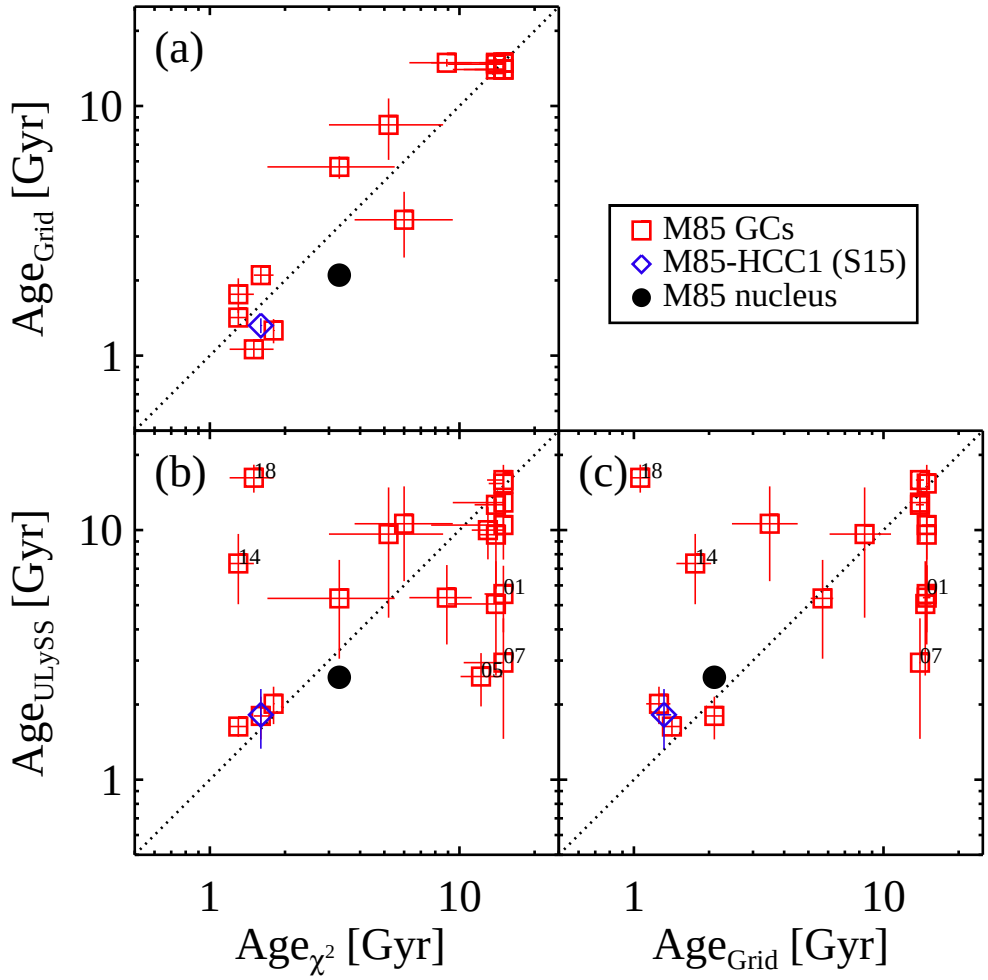

Figure 4.6: Comparison of ages for M85 GCs measured with different methods: (a) Lick index grid method vs. χ^2 minimization method, (b) full spectrum fitting vs. χ^2 minimization method, and (c) full spectrum fitting vs. Lick index grid method. The symbols are the same as in Figure 4.5. The dotted lines represent the one-to-one relation. The IDs of the outliers from one-to-one relation are marked in the panels.

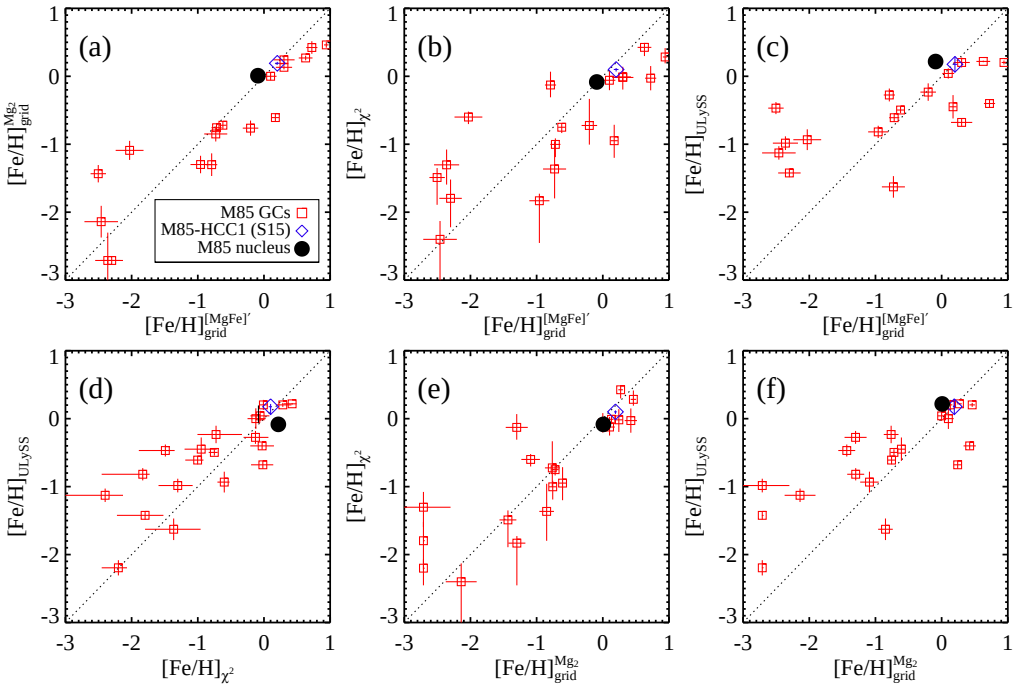

Figure 4.7: Comparison of [Fe/H] ratios for M85 GCs measured with different methods: (a) Mg_2 grid vs. [MgFe]′ grid, (b) χ^2 minimization method vs. [MgFe]′ grid, (c) full spectrum fitting vs. [MgFe]′ grid, (d) full spectrum fitting vs. χ^2 minimization method, (e) χ^2 minimization method vs. Mg_2 grid, and (f) full spectrum fitting vs. Mg_2 grid. The symbols are the same as in Figure 4.5. The dotted lines represent the one-to-one relation.

Figure 4.7 shows the comparison of the metallicities obtained from different methods. We calculate the iron abundance of the GCs based on the Lick indices using the relation presented by Thomas et al. (2003): [Fe/H] = [Z/H] - 0.94[α/Fe]. Figure 4.7(a) shows that the [Fe/H] ratios derived from the Lick index grid method agree well. Figure 4.7(b) and (e) show the correlation of [Fe/H] ratios derived from χ^2 minimization method and grid method, and the [Fe/H] ratios derived from Mg_2 grid show more tight correlation than those from [MgFe]′ grid. Figure 4.7(c) and

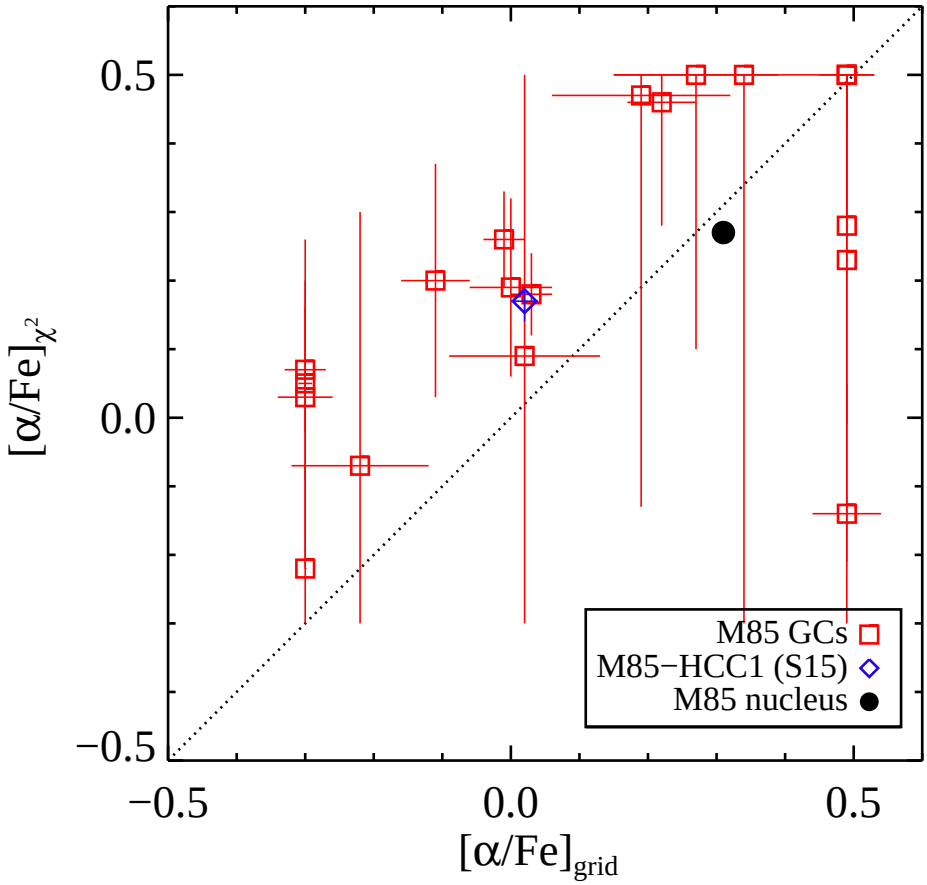

Figure 4.8: Comparison of [α/Fe] ratios derived with χ^2 minimization method and Lick index grid method. The symbols are the same as in Figure 4.5. The dotted lines represent the one-to-one relation.

(f) show the comparison between the [Fe/H] ratios derived from the full spectrum fitting and grid method. They agree well at [Fe/H] > –2, but the full spectrum fitting results in high metallicities at [Fe/H] < –2. This difference is weakened between the

[Fe/H] ratios from the full spectrum fitting and χ^2 minimization method (see Figure 4.7).

Figure 4.8 shows the comparison of the α-element abundances derived from the Lick index grid method and the χ^2 minimization method. We find a loose correlation within uncertainties although the [α/Fe] ratios obtained from χ^2 minimization method are larger than those obtained from Lick index grid method.

The parameters of the GCs obtained from various methods seem to be mostly similar. However, since the parameters obtained using the Lick indices may be inaccurate due to the calibration problem, we adopt the results obtained from the full spectrum fitting in the further analysis and discussion.

We compare the ages and metallicities of M85 nucleus and M85-HCC1 with those derived in previous spectroscopic studies. Fisher et al. (1996) suggested that the age of M85 nucleus is about 3 Gyr and Terlevich & Forbes (2002) derived the age and [Fe/H] ratio of M85 as 1.6 Gyr and 0.44 dex. We measure the age and [Fe/H] ratio of the M85 nucleus as 2.6 $\pm$ 0.3 Gyr and 0.22 $\pm$ 0.02 dex. Sandoval et al. (2015) discovered the M85-HCC1, and presented its age, [Fe/H] ratio, and [Mg/Fe] ratio derived from the SDSS spectrum. The values of parameters are 3.0 $\pm$ 0.4 Gyr, –0.06 $\pm$ 0.07 dex, and 0.05$\pm$ 0.13 dex, respectively. We derive the age and [Fe/H] ratio of M85-HCC1 as 1.8 $\pm$ 0.5 Gyr and 0.18 $\pm$ 0.12 dex. Despite slight differences, we conclude that M85 core and M85-HCC1 have the intermediate age and solar metallicity as well as the results of previous studies.

4.5.2 Age and Metallicity Distribution of M85 GCs

Figure 4.9 shows the age, [Fe/H], and $(g-i)_0$ color distributions of the M85 GCs confirmed in this study. We find two different groups in the M85 GCs according to their ages, intermediate-age GCs with ages of $<$ 9 Gyr and old GCs with ages of $>$ 9 Gyr. The numbers of the intermediate-age GCs and old GCs are 10 and 10,

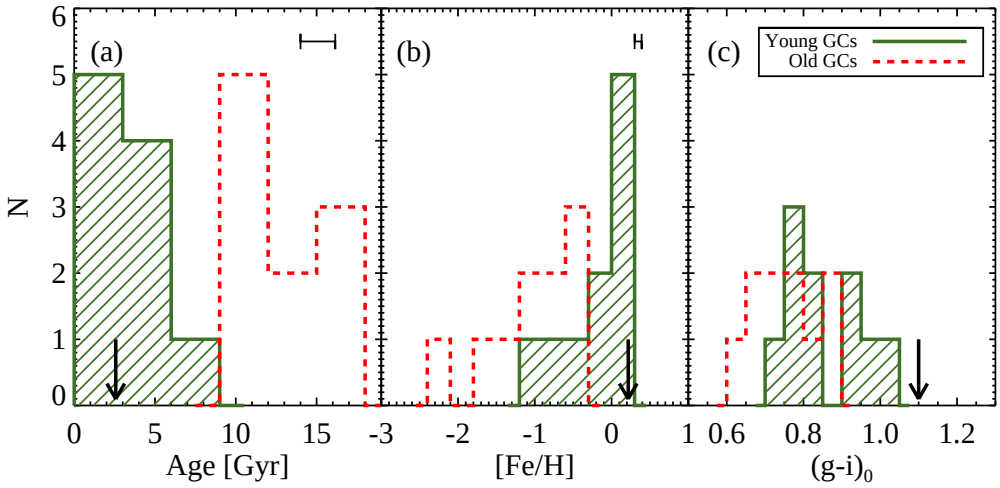

Figure 4.9: (a) Age, (b) [Fe/H], and (c) $(g-i)_0$ color distribution of GCs confirmed in this study. The hatched solid and dashed histogram represent the intermediate-age and old GCs, respectively. The arrows indicate the age, [Fe/H], and $(g-i)_0$ color of M85 nucleus derived in this study. The error bars in the upper right in (a) and (b) indicate the mean error of ages and [Fe/H] ratios, respectively.

respectively. The mean age of the intermediate-age GCs is about 4.0 ± 2.0 Gyr, which is similar to the stellar age of the M85 nucleus (∼ 2.6 ± 0.3 Gyr) within 1σ uncertainty, while the old GCs have the mean age of 12.3 ± 2.7 Gyr. The fraction of the intermediate-age GCs among all observed GCs is 50%, which is much smaller than that estimated by Trancho et al. (2014) (∼ 85%). Trancho et al. (2014) detected 1.8 Gyr-old GC population based on optical and near-infrared photometry. The difference may be caused by the difference of the observation coverage between two studies. We cover 7 times larger area than Trancho et al. (2014), but analyze a third number of GCs detected in Trancho et al. (2014).

We investigate the [Fe/H] and $(g-i)_0$ color distributions of two GC sub-populations separately. The intermediate-age GCs have the solar metallicity with a large disper-

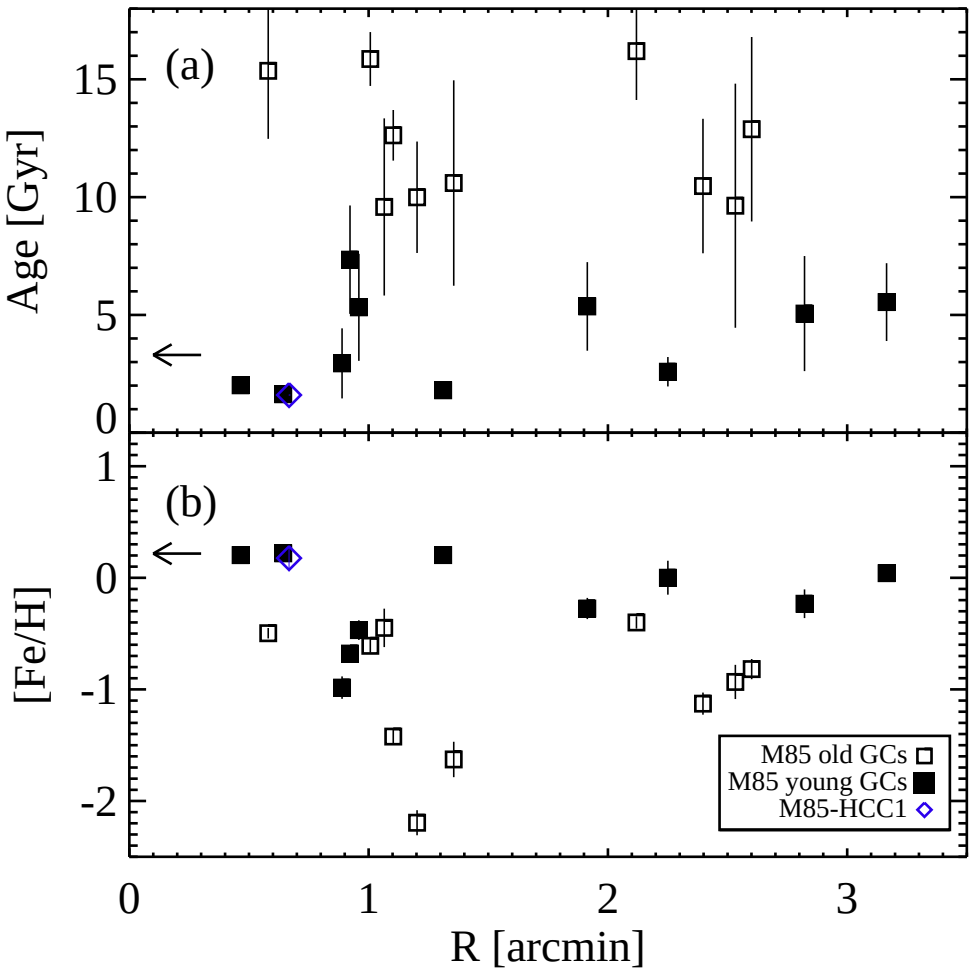

Figure 4.10: (a) Ages and (b) [Fe/H] ratios of M85 GCs as a function of galactocentric distance from M85. The filled squares, open squares, and a diamond represent the intermediate-age GCs, old GCs, and M85-HCC1, respectively. The arrows indicate the parameters of M85 nucleus.

sion, [Fe/H] = –0.19 ± 0.41. The mean metallicity of the old GCs is [Fe/H] = –1.01 ± 0.59, which is more metal-poor than that of the intermediate-age GCs. The color

Table 4.3. Mean Ages, Metallicities, and α-element Abundances of the M85 GC System

Subsample	N	Mean age (Gyr)	Mean [Fe/H] (dex)
All GCs	20	8.14 ± 4.86	–0.60 ± 0.65
$R < 1'.5$	12	7.9 ± 5.2	–0.69 ± 0.76
$R > 1'.5$	8	8.5 ± 4.6	–0.47 ± 0.44
Age < 9 Gyr	10	4.0 ± 2.0	–0.19 ± 0.41
Age > 9 Gyr	10	12.3 ± 2.7	–1.01 ± 0.59

distribution of the intermediate-age GCs has a peak at $(g-i)_0 = 0.75$ and the red tail, while that of the old GCs is uniform in the range of $0.6 < (g-i)_0 < 0.9$ (see Figure 4.9(c)). We expect the intermediate-age GCs could blur the color bimodality of the old GCs, while the old GCs in massive early-type galaxies generally show a color bimodality with a criterion of $(g-i)_0 \sim 0.8$. However, there is no clear color bimodality for the old GCs in M85, and the mean $(g-i)_0$ color of the intermediate-age GCs is redder than that of the old GCs. There could be small number statistics, so it needs to be confirmed with the large number of samples.

Figure 4.10 shows the age and metallicity distribution of the M85 GCs as a function of galactocentric distance from M85. The old and intermediate-age GCs show little difference in the radial distribution. Two GC groups are evenly distributed in all radial range. The mean ages of the GCs with $R < 1'.5$ and $R > 1'.5$ are 7.9 ± 5.2 and 8.5 ± 4.6, respectively. We also do not find any clear trend of the metallicity gradient of the M85 GCs with the galactocentric radii because of the large scatter. The mean metallicities of the GCs with $R < 1'.5$ and $R > 1'.5$ are [Z/H] = –0.69 ± 0.76 and –0.47 ± 0.44, respectively. The mean ages and metallicities of the subgroups of M85 GCs are listed in Table 4.3.

4.5.3 Kinematics of the GC System in M85

The mean radial velocity of M85 GCs is 716 ± 46 km s^{-1}, which is similar to that of M85 nucleus ($v_{\rm r}$ = 743 ± 8 km s^{-1}). We estimate the radial velocity dispersion and its error of M85 GCs following the formulae in Pryor & Meylan (1993) as 200 ± 32 km s^{-1}. It is slightly higher than the velocity dispersion of M85 nucleus (σ = 172 km s^{-1}).

Figure 4.11 shows the spatial distribution of the GCs confirmed in this study with their radial velocities. The GCs with the radial velocities higher than that of the M85 nucleus are mostly located in the western region, while the others are in the eastern region. This spatial segregation of the GCs indicates the rotation of the GC system of M85. It is notable that the rotation signature is clear even though the M85 is almost a face-on galaxy. The GCs rotating along a given axis in the plane of the sky have the radial velocities depending on the position angle sinusoidally. We measure the rotation amplitude and position angle of the rotation axis for M85 GC system by fitting the data to the following function.

$$v_{\rm r}(\Theta) \;=\; v_{\rm sys} + (\Omega R)\,\sin(\Theta - \Theta_0),$$

where the $v_{\rm sys}$ is the systemic velocity of the GC system, ΩR is the rotation amplitude, and Θ_0 is the orientation of the rotation axis. The systemic velocity of M85 GC system is assumed as the radial velocity of M85 nucleus, $v_{\rm r}$ = 743 km s^{-1}. Figure 4.12 shows the radial velocities of the GCs as a function of position angle with the best-fit rotation curves. The rotation amplitude and orientation of the rotation axis of the entire GC system are 179 ± 37 km s^{-1} and 154 ± 16°, respectively. We correct this projected rotation amplitude by considering the inclination of M85. The *sin i* factor is about 0.63, assuming that M85 has equal major and minor axes. Therefore the rotation amplitude is about 1.6 times larger than the projected one, $\Omega R = 284 \pm 59$ km s^{-1}. The position angle of the photometric major axis is about

12° Krajnović et al. (2011), which is orthogonal to that of the orientation of the rotation axis. We discuss the difference of these position angles in Section 4.6.1.

We derive the rotation-corrected radial velocities of the M85 GCs by applying the rotation curve of the entire GC system. The rotation-corrected radial velocity dispersion of the M85 GC system is 154 ± 26 km s^{-1}, which is comparable to the rotation amplitude of the M85 GC system. Figure 4.13 shows the rotation-corrected radial velocities of the M85 GCs relative to the radial velocity of the M85 nucleus as a function of galactocentric distance from M85. The rotation-corrected radial velocity dispersions of the GCs in the inner and outer regions are 173 ± 36 km s^{-1} and 112 ± 48 km s^{-1}, respectively. The radial velocity dispersion of the GC system decreases slightly as the galactocentric distance increases, but more samples are needed to reduce its uncertainties.

4.6 Discussion

4.6.1 Kinematically Decoupled System Between GCs and Stellar Light

We compare the kinematics of the GC system with that of the stellar light invesigated by ATLAS^{3D} (Cappellari et al. 2011; Krajnović et al. 2011; Emsellem et al. 2011). Krajnović et al. (2011) presented the kinematic maps of 260 early-type galaxies and measured the kinematic misalignment angles. According to their analysis, the central stellar light of M85 is dominated by ordered rotation and shows a smooth variation of the kinematic orientation. The photometric and kinematic position angles of the M85 stellar light derived by Krajnović et al. (2011) are $PA_{phot} = 12.^{\circ}3 \pm 11.^{\circ}0$ and $PA_{kin} = 19.^{\circ}5 \pm 4.^{\circ}8$, respectively. The kinematic position angle is defined as the angle from the north to the maximum receding part of the velocity map. The kinematic misalignment is not significant in the central stellar light.

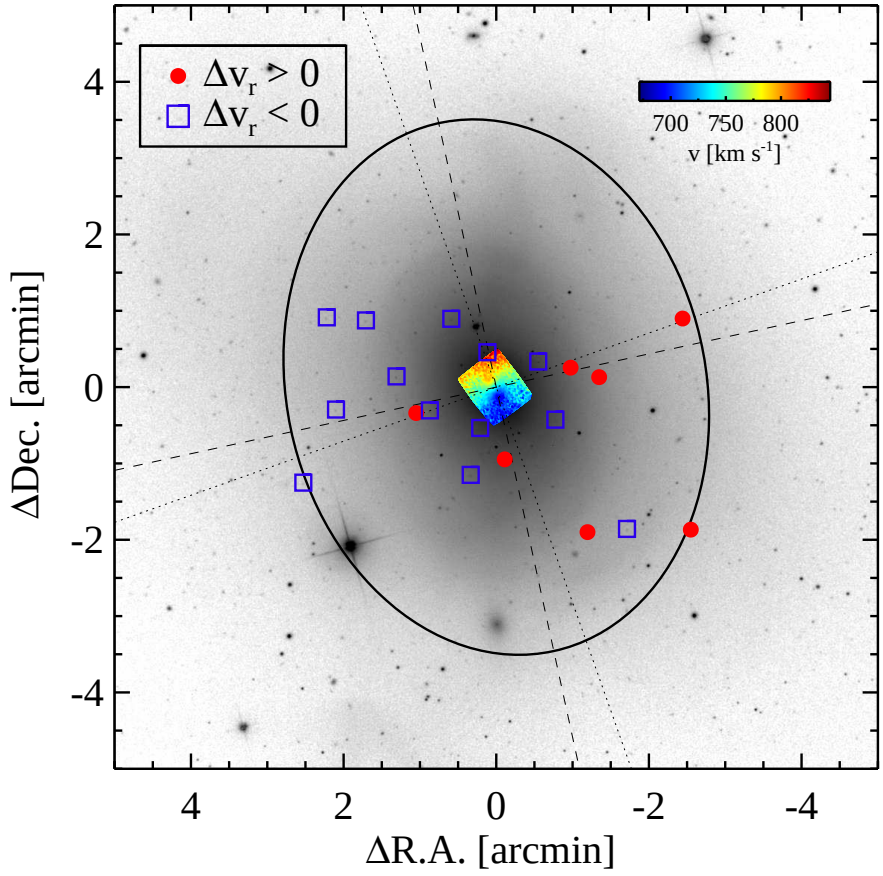

Figure 4.11: Spatial distribution of 20 M85 GCs confirmed in this study. The filled circles and open squares represent the GCs with the radial velocities higher and lower than that of the M85 nucleus, respectively. The solid line ellipse shows the stellar extent of M85 with a major axis of 7 arcmin, corresponding to D_{25} of M85, and an ellipticity of 0.22 (de Vaucouleurs et al. 1991). The stellar velocity field derived from the SAURON project (Emsellem et al. 2007) is overlaid on the SDSS image, of which velocity scales are displayed on the right corner. The photometric and kinematic position angles of the stellar light of M85 is taken from Krajnović et al. (2011) ($PA_{phot} = 12.^{\circ}3 \pm 11.^{\circ}0$ and $PA_{kin} = 19.^{\circ}5 \pm 4.^{\circ}8$). The dashed lines and dotted lines represent the photometric major/minor axes and kinematics major/minor axes, respectively.

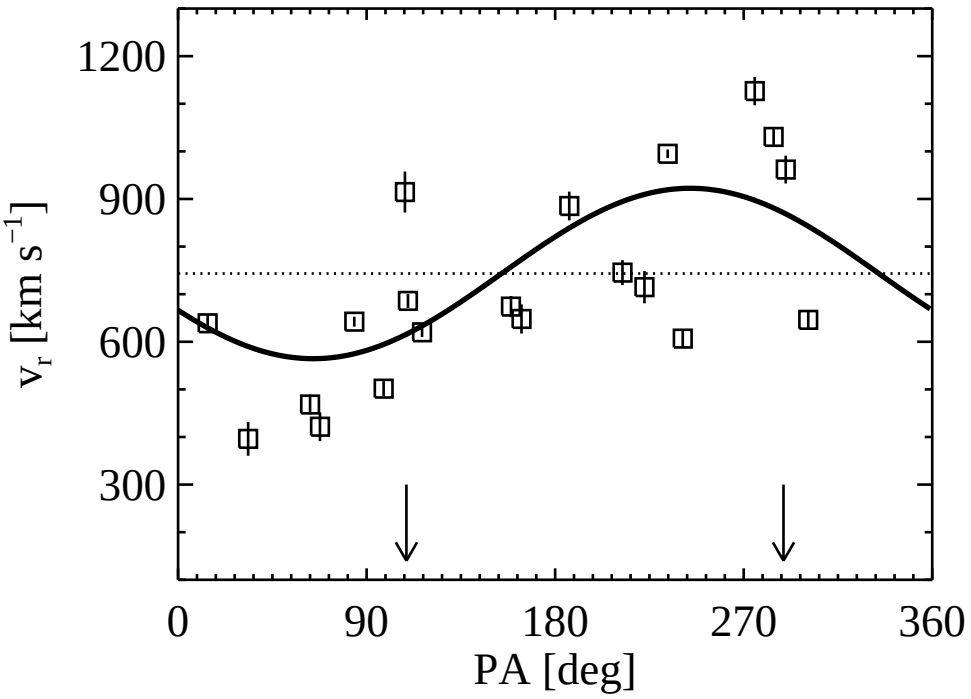

Figure 4.12: Radial velocities of 20 GCs confirmed in this study as a function of position angle. The solid line curve and dotted line represent the best fit rotation curve and the radial velocity of M85 nucleus derived in this study, respectively. The vertical arrows show the photometric minor axis of M85 (Krajnović et al. 2011).

The kinematic position angle of the M85 GCs is derived as $PA_{GCkin} = 244°$ (see Section 4.5.3 and Figure 4.12). The GC system shows a rotation about the photometric major axis, while the stars rotate about the photometric minor axis (see Figure 4.11). Li et al. (2015) previously investigated the kinematics of the central stellar light and the GC system in the outer region of four early-type Virgo Cluster galaxies. They found that two of them, VCC 2000 and VCC 685, show a clear misalignment of the kinematic position angles of the stars and GC system.

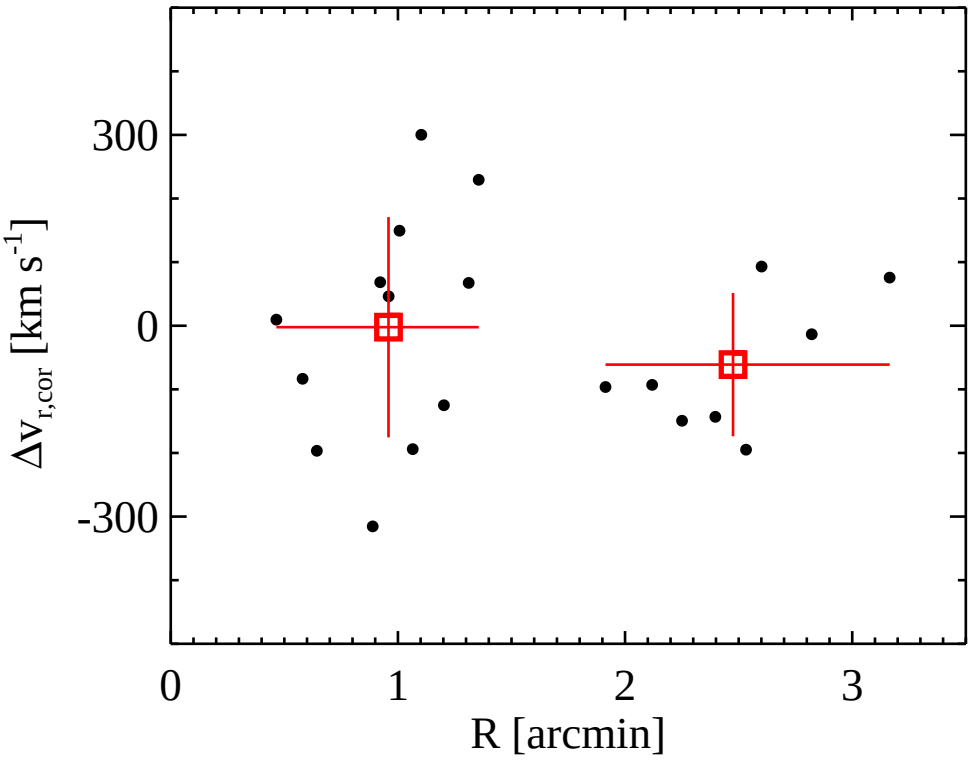

Figure 4.13: Rotation-corrected radial velocity of 20 M85 GCs relative to the radial velocity of M85 nucleus vs. galactocentric distance from M85. The open squares represent the mean radial velocities of the GCs in each radial bin. The vertical error bars indicate the radial velocity dispersions of the GCs in each bin.

These differences imply that the formation process of stars in the galaxy center is distinct from that of the GC system in the outer region. The outer region of galaxies preserves merging or accretion signatures related to its formation history. The decoupled rotation features of the stars and GC system of M85 support that M85 has undergone the merging events.

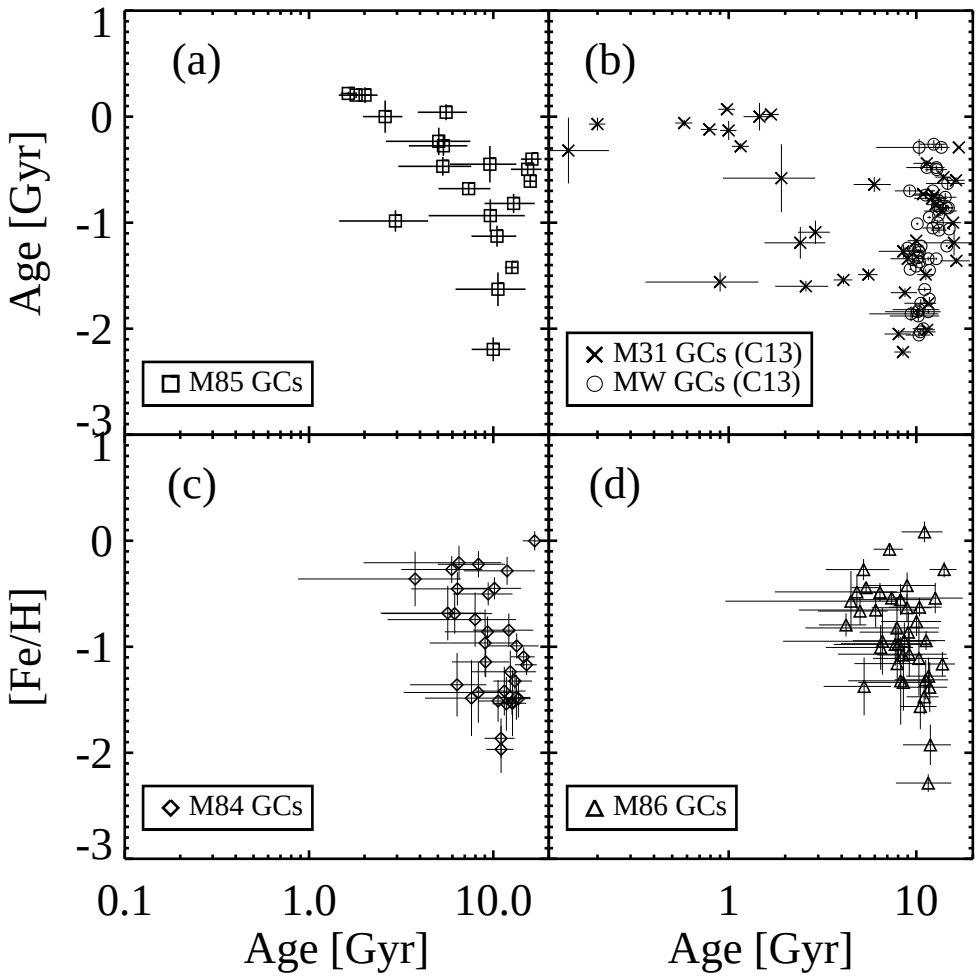

Figure 4.14: Age-metallicity relation of (a) GCs in M85, (b) GCs in the Milky Way (open circles) and M31 (crosses), (c) GCs in M84, and (d) GCs in M86 from full spectrum fitting. The ages and metallicities of GCs in the Milky Way and M31 are adopted from Cezario et al. (2013) The GCs in M84 and M86 are confirmed in Chapter 2.

4.6.2 Merging History of M85

Figure 4.14 shows the ages and metallicities of M85 GCs, Galactic GCs, M31 GCs, M84 GCs, and M86 GCs. Cezario et al. (2013) presented the ages and metallicities of Galactic GCs and M31 GCs derived from the full spectrum fitting with *ULySS*. We derive the ages and metallicities of M84 and M86 GCs confirmed in Chapter 2 using the full spectrum fitting with *ULySS* as well. The MMT/Hectospec spectra of these M84 and M86 GCs have the signal-to-noise ratios higher than 10.

The Galactic, M84, and M86 GCs are predominantly old ($>$ 10 Gyr), while M31 and M85 GCs consist of not only old GCs but also intermediate-age GCs with age $<$ 8 Gyr. The intermediate-age GCs in M31 and M85 are more metal-rich on average than the old GCs. Several studies reported that there is an overall trend of the anti-correlation between ages and metallicities of GCs in massive early-type galaxies (Puzia et al. 2005; Pierce et al. 2006a; Park et al. 2012b).

Recently, Forbes et al. (2015) inferred the formation epoch of metal-poor and metal-rich old GCs with $\sim$ 1000 GCs in a dozen of massive early-type galaxies. They concluded that the metal-poor GCs formed about 1 Gyr earlier than the metal-rich GCs. This observational result is consistent with the expectation of cosmological models of the GC formation presented by Muratov & Gnedin (2010) and Li & Gnedin (2014). They suggested that metal-poor GCs formed by early mergers between small host galaxies, while metal-rich GCs formed by late mergers between massive halos. However, the old GCs in M85 confirmed in this study were formed at similar epoch ($>$ 10 Gyr ago), and it is hard to find a clear anti-correlation between ages and metallicities of M85 old GCs because of the large scatter.

We detect the intermediate-age ($<$ 9 Gyr) GC population in M85. The intermediate-age GCs have the age of 4.0 Gyr and metallicity of [Z/H] $\sim$ –0.19 on average, while the old GCs have lower mean metallicity. It means that they were formed 4.0 Gyr ago when the metallicity enrichment of M85 had proceeded. This star formation

may result in removing gas in the central region of M85. Hibbard & Sansom (2003) reported that M85 has no HI gas. The intermediate-age GCs comprise 50% of the observed GCs. Note that our GC sample only contains bright GCs ($i < 21.5$) in the inner region of M85. Despite the small number of GC sample, we conclude that M85 experienced a wet merging event about 4.0 Gyr ago.

4.7 Summary

We present a spectroscopic study of GCs in a merger remnant galaxy M85 using Gemini-N/GMOS. The spectroscopic targets include 20 GCs, 1 foreground stars, M85-HCC1 (Sandoval et al. 2015), and M85 nucleus. Our main results are summarized as follows.

- The GCs in M85 has two distinct sub-populations, old GCs (> 9 Gyr) and intermediate-age GCs (< 9 Gyr). The mean ages of the old and intermediate-age GCs are 12.3 ± 2.7 Gyr and 4.0 ± 2.0 Gyr, respectively. The mean metallicity of the intermediate-age GCs ([Fe/H] = –0.19) is higher than that of the old GCs ([Fe/H] = –1.01).

- The mean radial velocity of the GCs in M85 is $v_{\rm r} = 716 \pm 45$ km s^{-1}. The GC system shows a considerable rotation feature of which amplitude is $\Omega R = 179 \pm 37$ km s^{-1}, although M85 is almost face-on galaxy. The rotation features of the GC system of M85 are orthogonal to those of the central stellar light, indicative of one of merging evidence.

- The rotation-corrected radial velocity dispersion of the GC system of M85 is $\sigma_r = 154 \pm 27$ km s^{-1}.

Our results suggest that the merger remnant galaxy M85 experienced a wet

merger 4 Gyr ago. Our GC sample contains only bright GCs in the inner region of M85. The further spectroscopic survey of the large number of GCs in M85 is helpful to investigate the merging history of M85.

Chapter 5

A Wide-field Spectroscopy of the GC System of the Merger Remnant Galaxy M85

5.1 Introduction

M85, one of the merger remnant galaxies, experienced wet merging events several Gyrs ago. The distorted isophotes, shells, and ripples discovered by various studies were produced by merging events (Burstein 1979; Schweizer & Seitzer 1988; Ferrarese et al. 2006; Kormendy et al. 2009). The stellar age of M85 core is derived by both photometric and spectroscopic studies (Schweizer & Seitzer 1992; Fisher et al. 1996; Terlevich & Forbes 2002). It ranges from 1.6 Gyr to 7.5 Gyr, which indicates that M85 underwent a wet merging several Gyrs ago.

The GCs in M85 show the merging signature. Peng et al. (2006) showed a tri-modal color distribution of the GCs in M85 and suspected the presence of intermediate-age GCs as well as old GCs. The old GCs in early-type galaxies show bimodal

color distribution, corresponding to the bimodal metallicity distribution. If there are intermediate-age GCs, they could blur the bimodality of the color distribution. Trancho et al. (2014) estimated the ages of the GCs in M85 using optical and near-infrared photometry and expected that there are 1.6 Gyr-old GC populations formed during merging process. We confirmed the presence of the intermediate-color GCs in the central region of M85 ($R < 2'$), and the spatial distributions of the both blue and red GCs are strongly elongated to the outer region (see Chapter 3). We also detected 4 Gyr-old GC populations in M85 (see Chapter 4).

Kinematic analysis of the GC system provides a clue to trace their own formation mechanism as well as the formation history of their host galaxy. The rotation, velocity dispersion, and orbits of the GC system vary according to its formation mechanism. If the GCs form with stars in galaxies during merging process, the kinematic parameters of the GCs are expected to be the same as those of the stellar light of host galaxies. On the other hand, if the GCs are accreted from other galaxies, their kinematics does not have to follow the stellar light of host galaxies. We investigated the kinematics of the GCs with small sample within $R < 3'$ and found that the GCs show distinct rotation features from the stellar light of M85 (see Chapter 4). However, it needs to be confirmed more sample GCs because the survey coverage and the number of the GCs are small.

Here, we present a wide-field spectroscopic survey of the GCs in M85 with MMT/Hectospec. We identify the GCs within $R < 30'$ and investigate their kinematic properties. This GC survey covers the widest area around M85 so far. This chapter is organized as follows. We briefly describe the spectroscopic target selection, observation, and data reduction in Section 5.2. In Section 5.3, we identify genuine M85 GCs as well as IGCs and analyze the kinematics of the GC systems of M85. We compare the kinematics of the GC system with that of the stellar light of M85 in Section 5.4. We also investigate the kinematics of the IGCs and derive the dynamical

mass of M85 in Section 5.4. In Section 5.5, we investigate the age and metallicity distribution of the We summarize the results in Section 5.5. We adopted a distance to M85 of 17.9 Mpc (Mei et al. 2007). One arcminute corresponds to 5.21 kpc at the distance to M85.

5.2 Observation and Data Reduction

5.2.1 Target Selection for Spectroscopy

We selected GC candidates from the *gi* band images obtained from CFHT/MegaCam observation (program 14AK06, PI: Myung Gyoon Lee; see Chapter 3). Figure 5.1(a) shows $(g-i)_0$ color distribution of the observation targets and the point sources of which color and magnitude ranges are the same as the observation targets. These two color distributions are similar to each other, so that there are no color bias for the selection of the observation targets. The color and magnitude ranges for selecting the GC candidates are shown in Figure 5.1(b). The magnitudes for constructing the $i_0 - (g-i)_0$ color magnitude diagram (CMD) are based on CFHT/MegaCam AB system. We used the foreground extinction values for M85 derived by Schlafly & Finkbeiner (2011). The GC candidates have a color range of $0.5 < (g-i)_0 < 1.15$ (Lim et al. 2017). To minimize the contamination of the foreground stars, we set the magnitude range for the target selection as $18.0 < i_0 < 22.0$. After assigning the fibers, in total, we selected 589 GC candidates for the spectroscopic observations. In addition, we added the nucleus of four galaxies that consist of a small galaxy group, M85, NGC 4394, IC 3292, and VCC 797.

5.2.2 Spectroscopic Observation and Data Reduction

We carried out spectroscopic observation using Hectospec (Fabricant et al. 2005) mounted on the 6.5m Multiple-Mirror Telescope (program ID: 2016A-UAO-G4, PI:

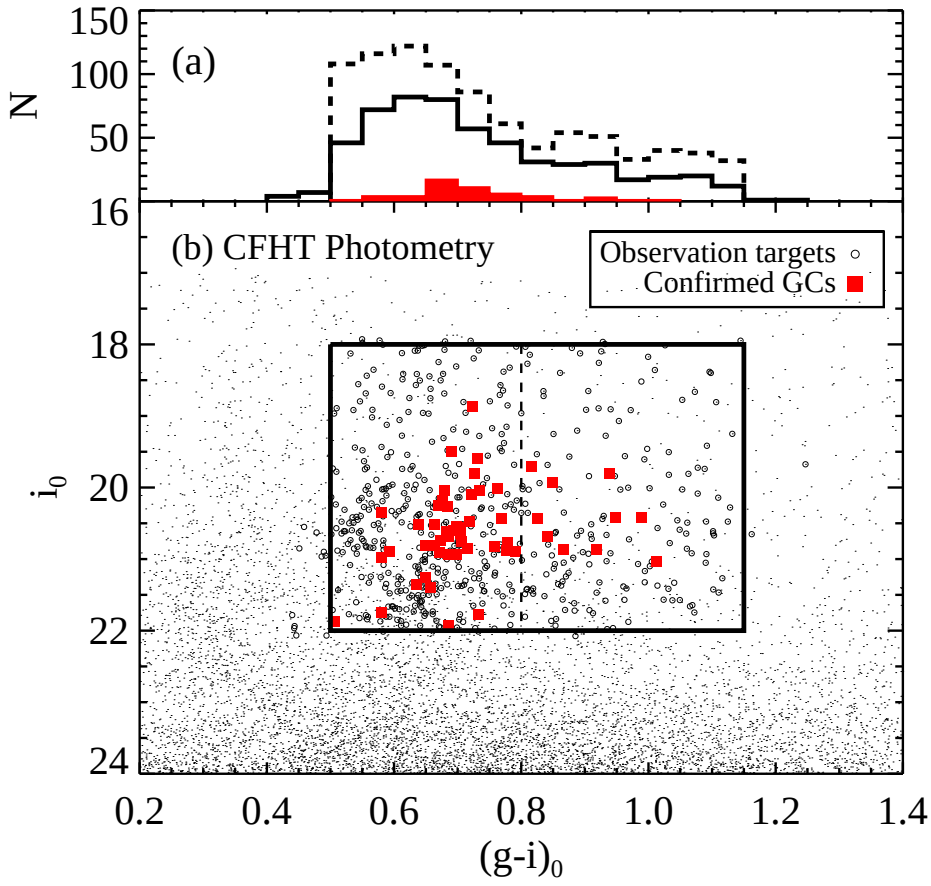

Figure 5.1: (a) $(g-i)_0$ color distribution of the observation targets (solid line) and the point sources with the color and magnitude range same as the observation targets in the survey region (dashed line). (b) $i_0-(g-i)_0$ CMD of the point sources in the survey region. The open circles and filled sqaures represent the spectroscopic targets of M85 GC candidates and the GCs confirmed in this study, respectively. The large box shows the color and magnitude criteria used for the target selection. The vertical dashed line is $(g-i)_0=0.8$, which indicates the color criterion to divided GCs into blue and red ones.

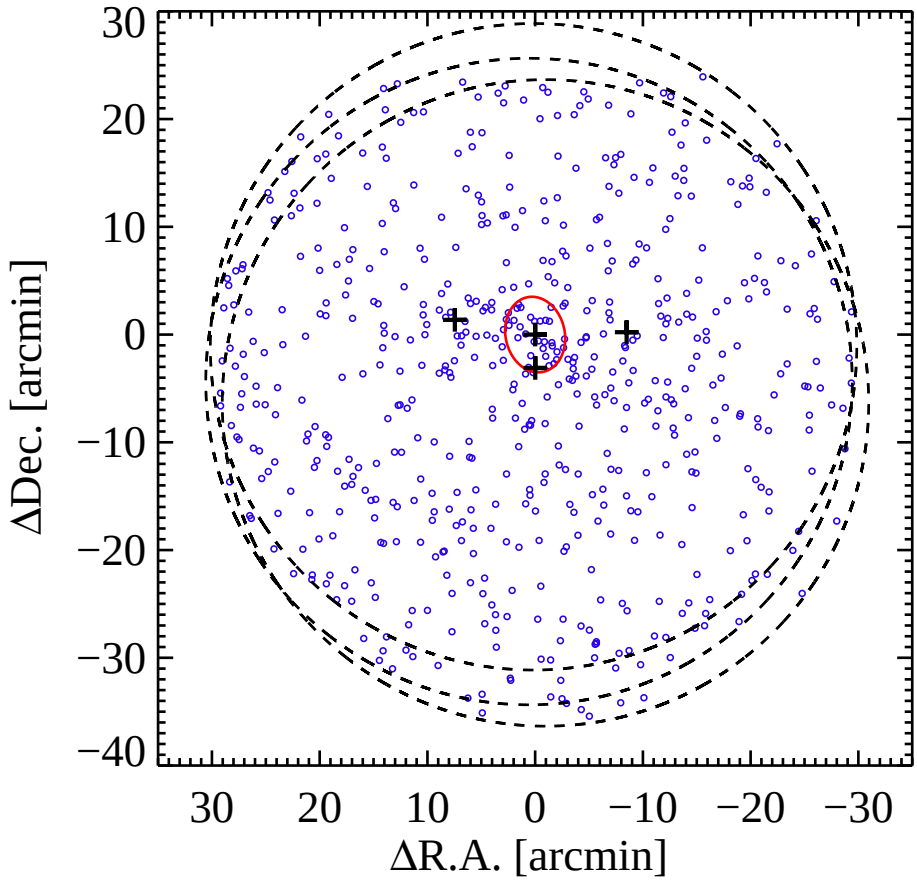

Figure 5.2: Spatial distribution of the spectroscopic targets of GC candidates. A dashed-line circle represents a field of view of MMT/Hectospec with a 1° diameter. The crosses indicates the positions of main galaxies in the survey region, M85 (0,0), NGC 4394 (east), IC 3292 (west), and VCC 797 (south). The solid-line ellipse shows the stellar extent of M85 with a major axis of 7 arcmin, corresponding to D_{25} of M85, and an ellipticity of 0.22 (de Vaucouleurs et al. 1991).

Table 5.1. Observation Log for the MMT/Hectospec Run

Mask Name	α (J2000)	δ (J2000)	N[a]	Exp. time	Date(UT)
M85-B1	12:25:24.74	+18:10:21.3	256	5 × 1440 s	Mar 7, 2016
M85-B2	12:25:20.08	+18:05:08.9	260	5 × 1440 s	Mar 16, 2016
M85-F1	12:25:26.52	+18:07:07.6	250	5 × 1800 s	Mar 17, 2016

Note. — [a] Number of object fibers among 300 fibers in each field. The remaining fibers are assigned to sky regions.

Youkyung Ko) during 2016 March. We selected a 270 mm^{-1} grating with a dispersion of 1.2 Å $pixel^{-1}$, covering the wavelength range of 3650 – 9200 Å. Three different configurations covering $R < 30'$ region around M85 were made, shown in Figure 5.2. The exposures were taken in five times of 1440 s for two configurations, and five times of 1800 s for one configuration. The field coordinates and exposure times are given in Table 5.1.

We used version 2.0 of the HSRED reduction pipeline[a] for data reduction. It includes bias and dark correction, flat-fielding, aperture extraction of spectra, and wavelength calibration. Flux calibration was done following the methods described by Fabricant et al. (2008). Most of the observation targets with $i > 21.0$ have low signal-to-noise ratios (< 5). The median signal-to-noise ratios of the spectra of GC candidates with $i < 21.0$ at 4000 – 5700 Å range from 1 to 59.

[a]This is an updated reduction pipeline originally developed by Richard Cool; more details can be found at http://www.mmto.org/node/536.

5.2.3 Radial Velocity Measurements

We estimated the heliocentric radial velocities of Hectospec spectroscopic targets using the xcsao task in the IRAF RVSAO package (Kurtz & Mink 1998). The prominent absorption lines at wavelength range of 3800 – 5400 Å were used to apply the cross-correlation method (Tonry & Davis 1979). There are several radial velocity templates in the RVSAO package, including the spectra of an A star, M31 GCs, elliptical and spiral galaxies. We used 10 templates, and matched the targets with $v_{\rm r} > 3000$ km s^{-1} and $v_{\rm r} < 3000$ km s^{-1} with galaxy spectra and GC spectra, respectively. For 115 of the 589 targets, we could not determine the radial velocities because of low signal-to-noise ratios (< 5). We measured the radial velocity of M85 nucleus to be 696 $\pm$ 16 km s^{-1} , which is marginally consistent with that derived by several previous studies, $v_{\rm r} = 729$ –760 km s^{-1} (Smith et al. 2000; Gavazzi et al. 2004; Ko et al. 2017), within its uncertainty. The mean radial velocity uncertainties of GC candidates is 26 km s^{-1}.

5.3 Results

5.3.1 GC Selection and Membership Determination

We classify the observation targets into foreground stars, background galaxies, and GCs. First, 68 targets with $v_{\rm r} > 3000$ km s^{-1} are classified as background galaxies. The radial velocity distribution of the galaxies in the Virgo Cluster field shows a clear separation at $v_{\rm r} = 3000$ km s^{-1}(Kim et al. 2014). We adopted this criterion to dividing the targets into the objects bound to the Virgo Cluster and background galaxies. The radial velocities of background galaxies range from 17303 km s^{-1} to 222214 km s^{-1}, which are much higher than that of the Virgo Cluster.

Figure 5.3 shows the heliocentric radial velocity distribution and $(g-i)_0$ color distribution of 406 observation targets with $v_{\rm r} < 3000$ km s^{-1} of which radial ve-

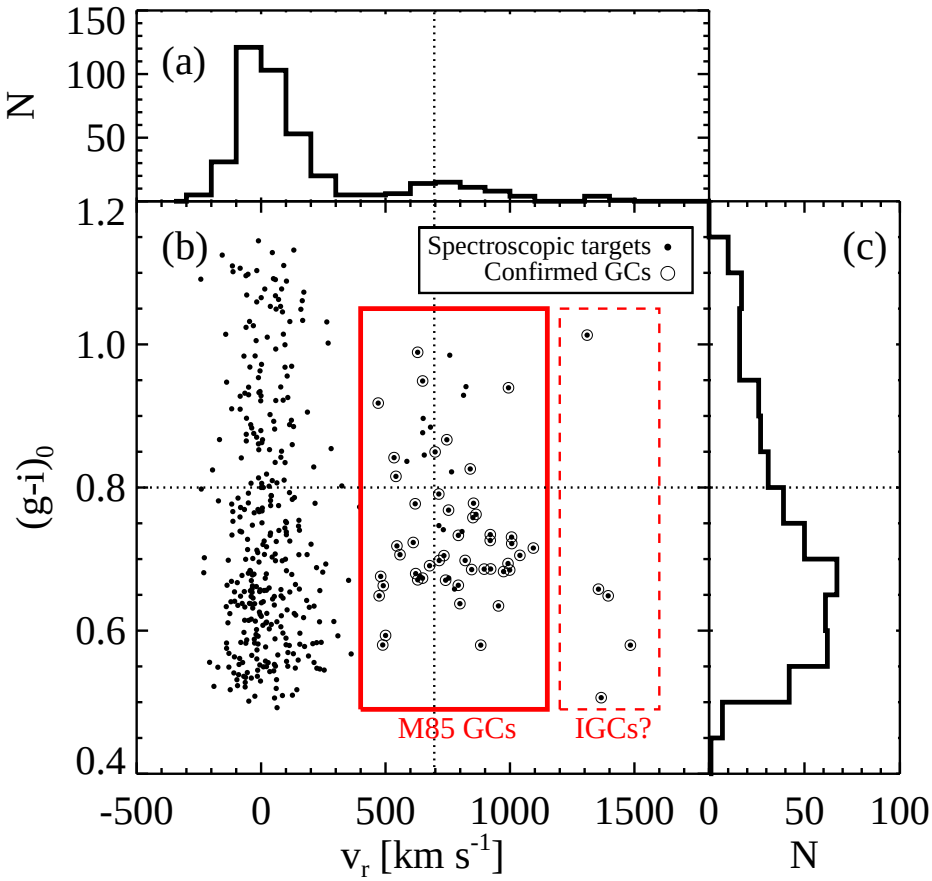

Figure 5.3: (a) Radial velocity distribution of the spectroscopic targets. (b) $(g-i)_0$ colors vs. radial velocities of the spectroscopic targets (filled circles) and the GCs confirmed in this study (open circles). The thick solid line box indicates the criteria of $(g-i)_0$ colors and radial velocities for the selection of the GCs that belong to M85. The GCs with $v_r > 1200$ km s^{-1} are considered as IGCs, of which selection criteria are drawn as dashed line box. (c) $(g-i)_0$ color distribution of the spectroscopic targets. The dotted vertical and horizontal lines indicates the radial velocities of M85 core derived in this study ($v_r = 696$ km s^{-1}) and the color criterion for dividing the GCs into blue and red ones ($(g-i)_0 = 0.8$), respectively.

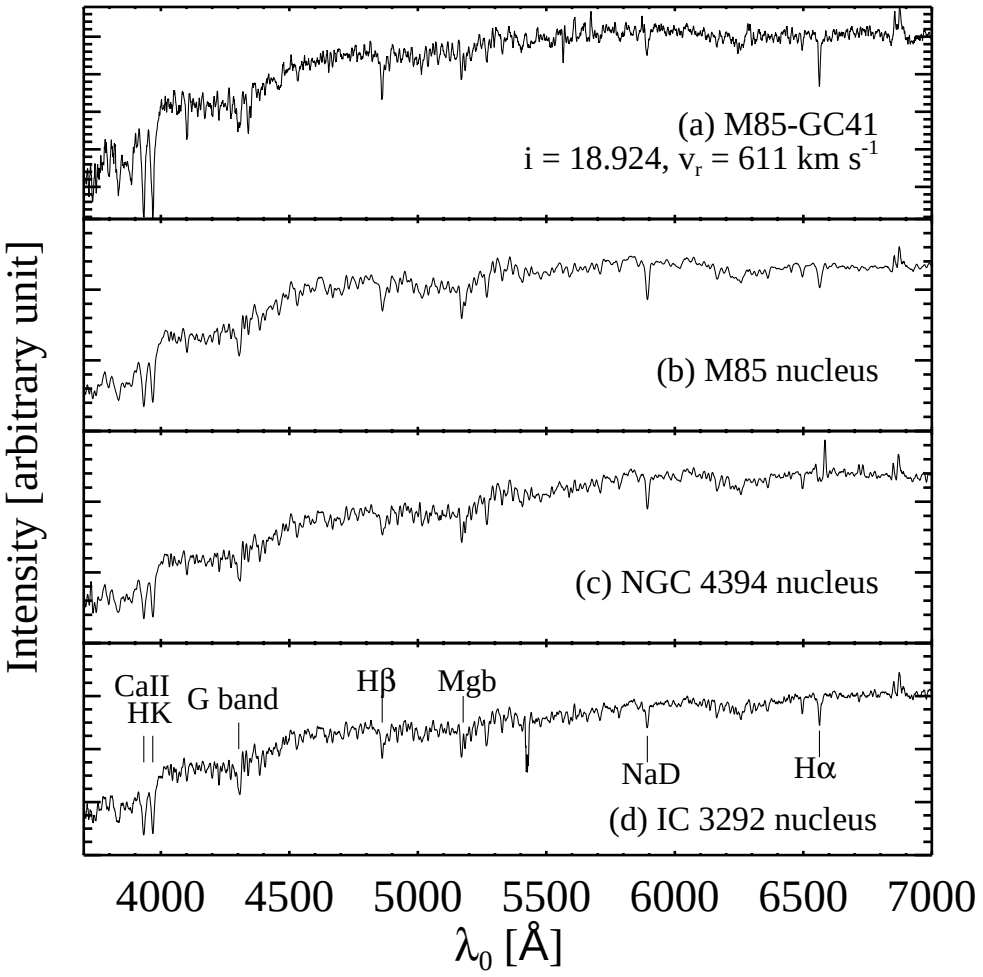

Figure 5.4: Sample spectra of (a) a GC in M85 (ID: M85-GC41); (b) M85 nucleus; (c) NGC 4394 nucleus, and IC 3292 nucleus. All flux-calibrated spectra are plotted in the rest frame and smoothed using a boxcar filter with a size of 4.5 Å.

locities are measured. The radial velocity distribution of the GC candidates shows two peaks at about 0 km s^{-1} and 700 km s^{-1}, which are considered as foreground stars and GCs, respectively. Among the targets with $v_{\rm r} \sim 700$ km s^{-1}, we exclude the targets within $R < 2'.5$ in the final GC catalog because the galaxy light is not well subtracted in their spectra. Most of the GCs observed in this study are blue, $(g-i)_0 < 0.8$. As a result, we identify 53 GCs, 68 background galaxies, and 338 foreground stars. Figure 5.4 shows the spectra of the GC confirmed in this study, M85 nucleus, NGC 4394 nucleus, and IC 3292 nucleus, where the absorption lines are clearly shown. Table 5.2 lists foreground stars and background galaxies observed in this study, and Table 5.3 lists photometric and spectroscopic parameters of the GCs and, respectively.

We classify the GCs into two groups, the GCs that belong to M85 and IGCs. The IGCs are not bound to any galaxy, and wander in the cluster region. We use two criteria to select the IGCs: (1) $v_{\rm r} > 1200$ km s^{-1}, or (2) $R > 20'$. There are five GCs with $v_{\rm r} > 1200$ km s^{-1}, which are not included in the Gaussian distribution of the radial velocities of the GCs (see Figure 5.3). In addition, we set the boundary of M85 as $R = 20'$ from the radial number density profile of the GCs in the photometric study (see Chapter 3). According to these criteria, there are 42 GCs bound to M85 and 11 IGCs among 53 GCs confirmed in this study. The sub-population of the GCs is listed in Table 5.3.

5.3.2 Kinematics of the GC System in M85

The M85 GCs confirmed in this study are located in a radial range of $2'.6$ – $18'.9$, corresponding to 13.5 – 98 kpc. The mean radial velocity and the radial velocity dispersion of the M85 GC system are 765 ± 27 km s^{-1} and 174 ± 20 km s^{-1}, respectively. The radial velocity dispersion and its error of the GC system are calculated following the formulae presented by Pryor & Meylan (1993).

Table 5.2. Spectroscopic and photometric properties of foreground stars and background galaxies

ID	α (J2000) (deg)	δ (J2000) (deg)	i^a (mag)	$(g-i)^a$ (mag)	$v_{\rm r}$ (km s^{-1})
Star001	185.835114	18.226645	20.423 ± 0.004	0.689 ± 0.006	–121 ± 40
Star002	185.835785	18.116449	20.406 ± 0.004	0.849 ± 0.006	0 ± 22
Star003	185.839340	18.155159	20.080 ± 0.002	1.005 ± 0.004	105 ± 20
Star004	185.849579	18.077505	20.706 ± 0.004	0.789 ± 0.006	154 ± 37
Star005	185.860168	17.903006	20.527 ± 0.003	1.140 ± 0.006	58 ± 28
Gal01	185.900116	17.980145	21.834 ± 0.010	0.489 ± 0.013	50373 ± 15
Gal02	185.904617	18.043806	19.892 ± 0.002	0.955 ± 0.004	37263 ± 13
Gal03	185.906403	18.110588	21.971 ± 0.011	0.832 ± 0.017	50311 ± 11
Gal04	185.973541	18.411480	21.354 ± 0.006	0.761 ± 0.010	75329 ± 11
Gal05	185.987747	18.048506	21.319 ± 0.006	0.775 ± 0.010	47322 ± 13

Note. — The complete version of this table is in Table A.6.

[a]CFHT/MegaCam AB magnitudes.

Table 5.3. Spectroscopic and photometric properties of the GCs confirmed in this study.

ID	α (J2000) (deg)	δ (J2000) (deg)	g^a (mag)	$(g-i)^a$ (mag)	$v_{\rm r}$ (km s^{-1})	Class
GC01	185.846497	18.014795	20.407 ± 0.003	0.629 ± 0.005	489 ± 46	IGC
GC02	185.973221	17.820648	20.941 ± 0.005	0.840 ± 0.008	714 ± 105	IGC
GC03	186.040955	18.078588	20.691 ± 0.004	0.754 ± 0.006	735 ± 55	M85/BGC
GC04	186.095642	18.139322	20.314 ± 0.003	0.734 ± 0.005	999 ± 39	M85/BGC
GC05	186.153976	18.049810	20.094 ± 0.002	0.783 ± 0.004	921 ± 20	M85/BGC

Note. — The complete version of this table is in Table A.7.

[a]CFHT/MegaCam AB magnitudes.

Figure 5.5 shows the radial velocities of the GCs as a function of galactocentric distance from M85. We also investigate the radial velocity profile of the BGCs and RGCs. The GCs with $R < 20'$ are concentrated at the radial velocity of M85 nucleus, except two IGCs. Note that the M85 RGCs are all located within $R < 6'$, while the M85 BGCs are distributed to $R = 20'$. Most of the radial velocities of the IGCs are higher than that of M85 nucleus, which indicates the different kinematics from the M85 GCs.

Figure 5.6 shows the spatial distribution of the GCs confirmed in this study with their radial velocities. The spatial distribution of the M85 GCs are elongated along the stellar light of the outer region of M85, while that of the IGCs are uniformly distributed despite the small number. The stellar light of M85 is not simple, but disturbed because of the merging features. The position angles and ellipticities of the M85 stellar light vary with the galactocentric distance from M85 as shown in

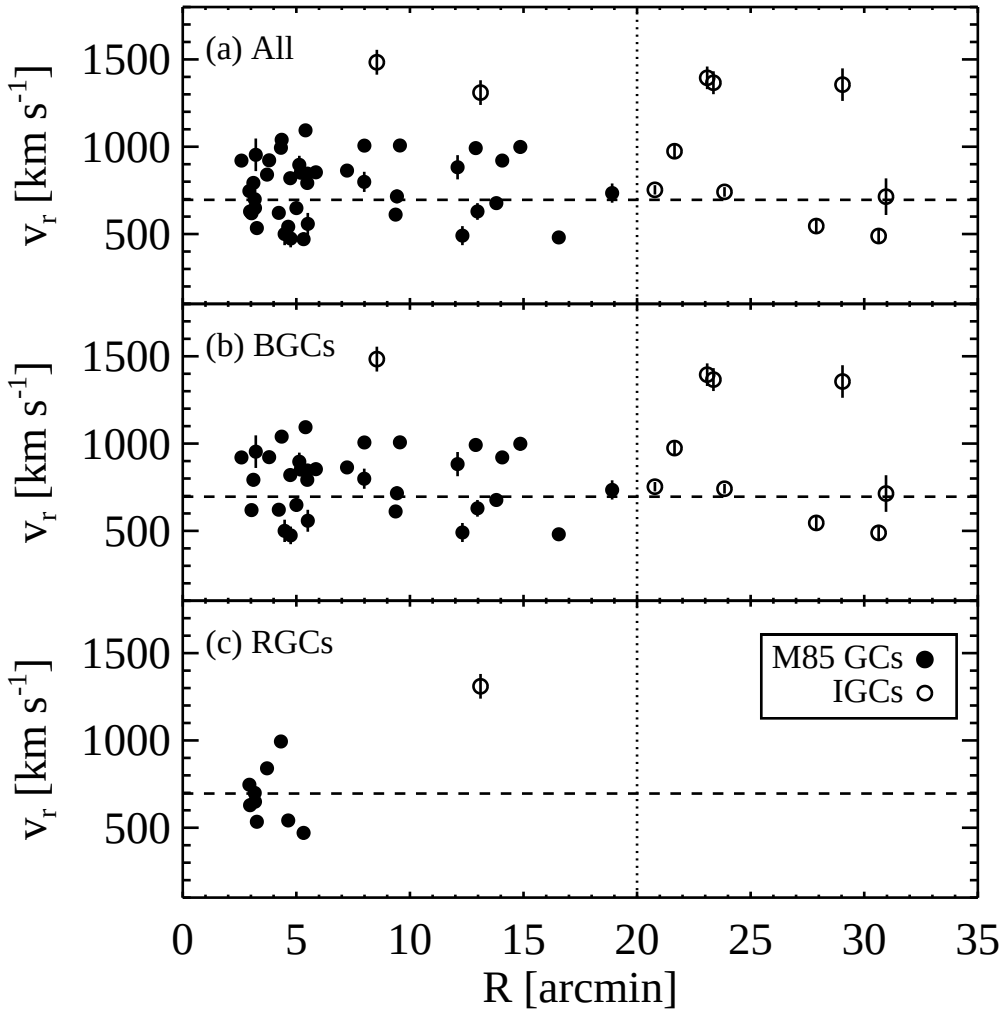

Figure 5.5: (a) Radial velocity vs. galactocentric distance from M85 for the GCs confirmed in this study. (b) Same as (a), but for the BGCs. (c) Same as (a), but for the RGCs. The dashed and dotted lines indicate the radial velocity of M85 nucleus and the boundary of M85 from the radial number density profile of M85 GCs (see Chapter 3), respectively.

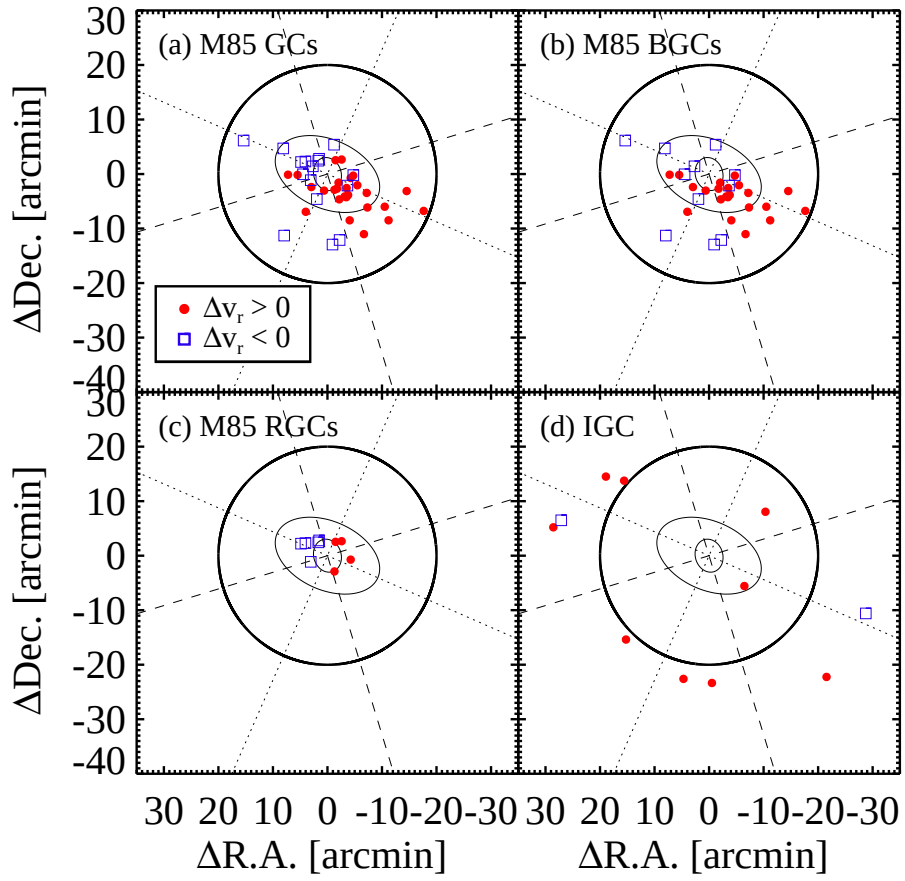

Figure 5.6: Spatial distribution of (a) 42 M85 GCs, (b) 33 M85 BGCs, (c) 9 M85 RGCs, and (d) 11 IGCs confirmed in this study. The filled circles and open squares represent the GCs with the radial velocities higher and lower than that of the M85 nucleus, respectively. The solid line ellipses are two guidelines for the stellar extent of M85 (Kormendy et al. 2009): One is with a major axis of 3 arcmin, a position angle of 16°, and an ellipticity of 0.18, and the other is with a major axis of 10 arcmin, a position angle of 66°, and an ellipticity of 0.38. Note that the position angles of the isophotes of the M85 stellar light rotate counterclockwise between $r_{\rm maj} = 3$ and 10 arcmin. The dashed and dotted lines represent the photometric major and minor axes at $r_{\rm maj} = 3$ arcmin and 10 arcmin, respectively.

Figure 5.6. The position angle changes from 16° to 66°, and the ellipticity from 0.18 to 0.38. The position angle of the elongated spatial distribution of the M85 GC system is similar to that of the stellar light at $R_{\rm maj} = 10'$, rather than that of the stellar light in the inner region ($R_{\rm maj} = 3'$).

The GCs with the radial velocities higher than that of the M85 nucleus are mostly located in the south-western region, while the others are in the north-eastern region. This spatial segregation of the GCs indicates the rotation of the GC system of M85. The rotation feature for the GC system is also detected with the small sample (see Section 4.5.3). All sub-groups of the M85 GCs show the rotation features, while the IGCs do not.

The GCs rotating along a given axis in the plane of the sky have the radial velocities depending on the position angle sinusoidally. We measure the rotation amplitude and position angle of the rotation axis for M85 GC system by fitting the data to the following function.

$$v_{\rm r}(\Theta) \;=\; v_{\rm sys} + (\Omega R)\,\sin(\Theta - \Theta_0),$$

where the $v_{\rm sys}$ is the systemic velocity of the GC system, ΩR is the rotation amplitude, and Θ_0 is the orientation of the rotation axis. The systemic velocity of M85 GC system is assumed as the radial velocity of M85 nucleus, $v_{\rm r} = 696$ km s^{-1}. Figure 5.7 shows the radial velocities of the all GCs, BGCs, and RGCs in M85 as a function of position angle with the best-fit rotation curves. The rotation amplitude and orientation of the rotation axis of the entire GC system are 137 ± 26 km s^{-1} and $164 \pm 17°$, respectively. We correct this projected rotation amplitude by considering the inclination of M85. The *sini* factor is about 0.63, assuming that M85 has equal major and minor axes. Therefore the rotation amplitude is about 1.6 times larger than the projected one, $\Omega R = 219 \pm 42$ km s^{-1}. However, this inclination correction may be larger because the spatial distribution of the GCs is more elongated than the galaxy light. The rotation axis is close to the minor axis of the stellar light at

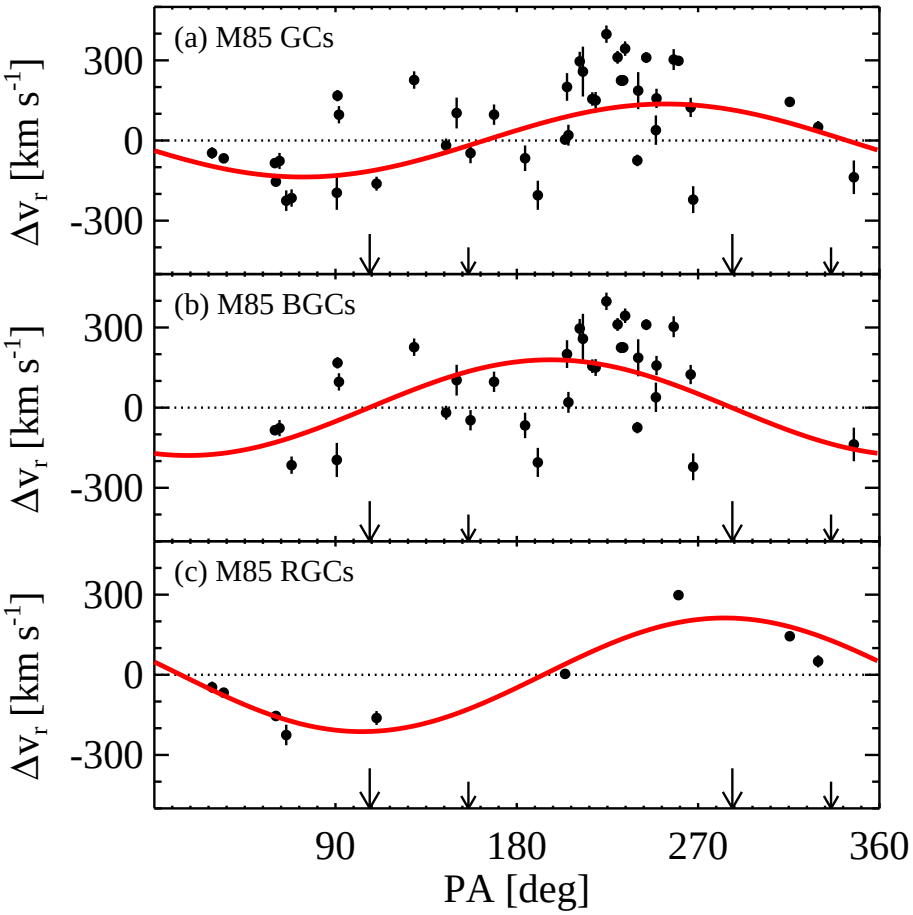

Figure 5.7: Radial velocities relative to that of M85 nucleus as a function of position angle for (a) 42 M85 GCs, (b) 33 M85 BGCs, and (c) 9 M85 RGCs. The solid and dotted line indicate the best fit rotation curve and zero velocity line, respectively. The large and small vertical arrows mark the photometric minor axis of M85 at $r_{\rm maj} = 3$ arcmin and 10 arcmin, respectively (Kormendy et al. 2009).

$R_{\rm maj} = 10'$, $\rm PA_{phot} = 156°$, within 1σ uncertainty.

The BGC and RGC system of M85 also rotate, but the rotation features are different from each other (see Figure 5.7(b) and (c)). The rotation amplitudes of the

BGC and RGC systems are 179 ± 45 km s^{-1} and 213 ± 34 km s^{-1}, respectively, which are consistent within their uncertainties. The orientations of the rotation axes of the BGC and RGC systems are 107 ± 15° and 193 ± 7 km s^{-1}, which are orthogonal. In other words, the BGC and RGC systems rotate around the minor and major axes of the stellar light at $R_{\rm maj} = 3'$ ($\rm PA_{phot} = 106°$ and 16°), respectively.

In addition, we measure the rotation parameters of several GC subgroups, according to the radial bin: the GCs and BGCs in the inner region ($R < 6'$) and the GCs in the outer region ($R > 6'$). Note that the GCs in the outer region are all BGCs. We cannot divide the RGCs into sub-groups because all M85 RGCs are located in the inner region. Figure 5.8(a) shows the rotation curves for 27 GCs in the inner region. The rotation amplitude and the orientations of the rotation axis of the GC system in the inner region are 151 ± 36 km s^{-1} and 174 ± 15°, respectively, which is consistent with those of the entire GC system. The rotation curves for 18 and 15 BGCs in the outer region are also shown in Figure 5.8. The inner BGC system rotates faster than the outer BGC system, while the orientations of the rotation axes are almost same. However, there are few BGCs in the north region, 0° < PA < 90° and 270° < PA < 360°, so that their rotation parameters may be changed with more samples.

We derive the rotation-corrected radial velocities of the M85 GCs by applying the rotation curves of the GC systems. Figure 5.9 shows the rotation-corrected radial velocities of the M85 GCs relative to the radial velocity of the M85 nucleus as a function of galactocentric distance from M85. The rotation-corrected radial velocity dispersions of the entire GC, BGC, and RGC systems are 144 ± 18 km s^{-1}, 149 ± 23 km s^{-1}, and 51 ± 14 km s^{-1}, respectively. There are no significant differences in the rotation-corrected radial velocity dispersions between inner and outer regions. The kinematics of the GC subsamples are summarized in Table 5.4.

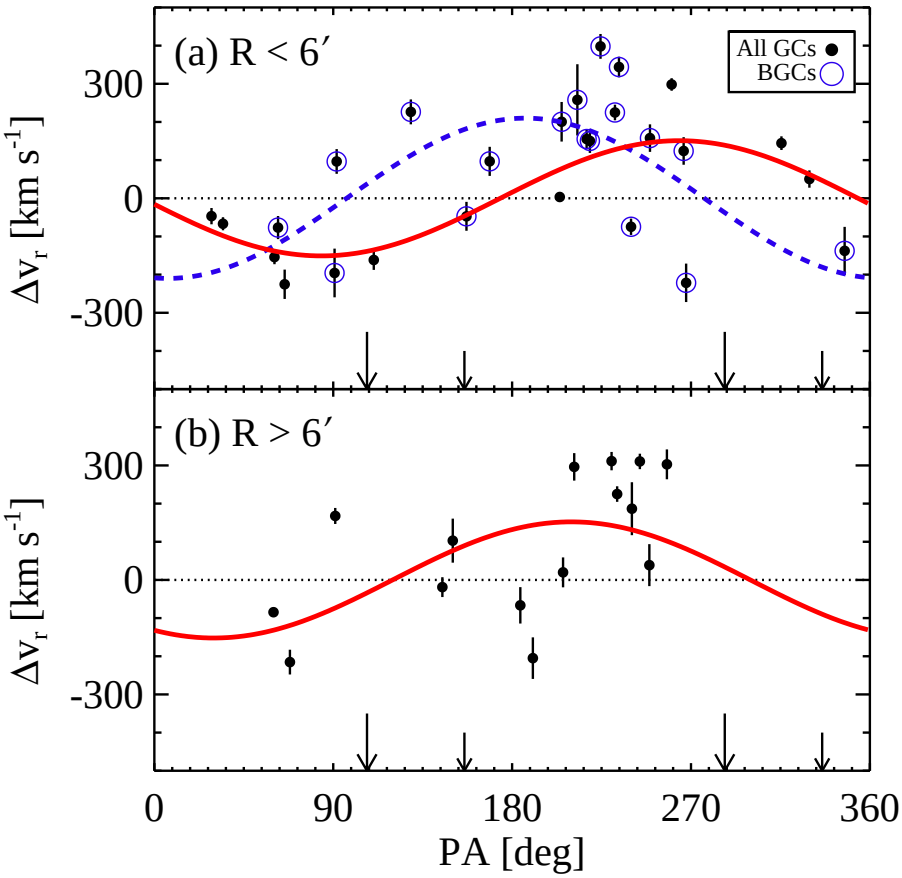

Figure 5.8: Radial velocities relative to that of M85 nucleus as a function of position angle for (a) 27 M85 GCs and 18 BGCs with $R < 6'$, (b) 15 M85 GCs with $R > 6'$. Note that all GCs with $R > 6'$ in (b) are blue. The lines and arrows are the same as Figure 5.7.

5.4 Discussion

5.4.1 Rotation of the GC System of M85

We compare the kinematics of the GC system with the stellar light of the central region of M85. The rotation feature of the stellar light derived by ATLAS^{3D} (Cap-

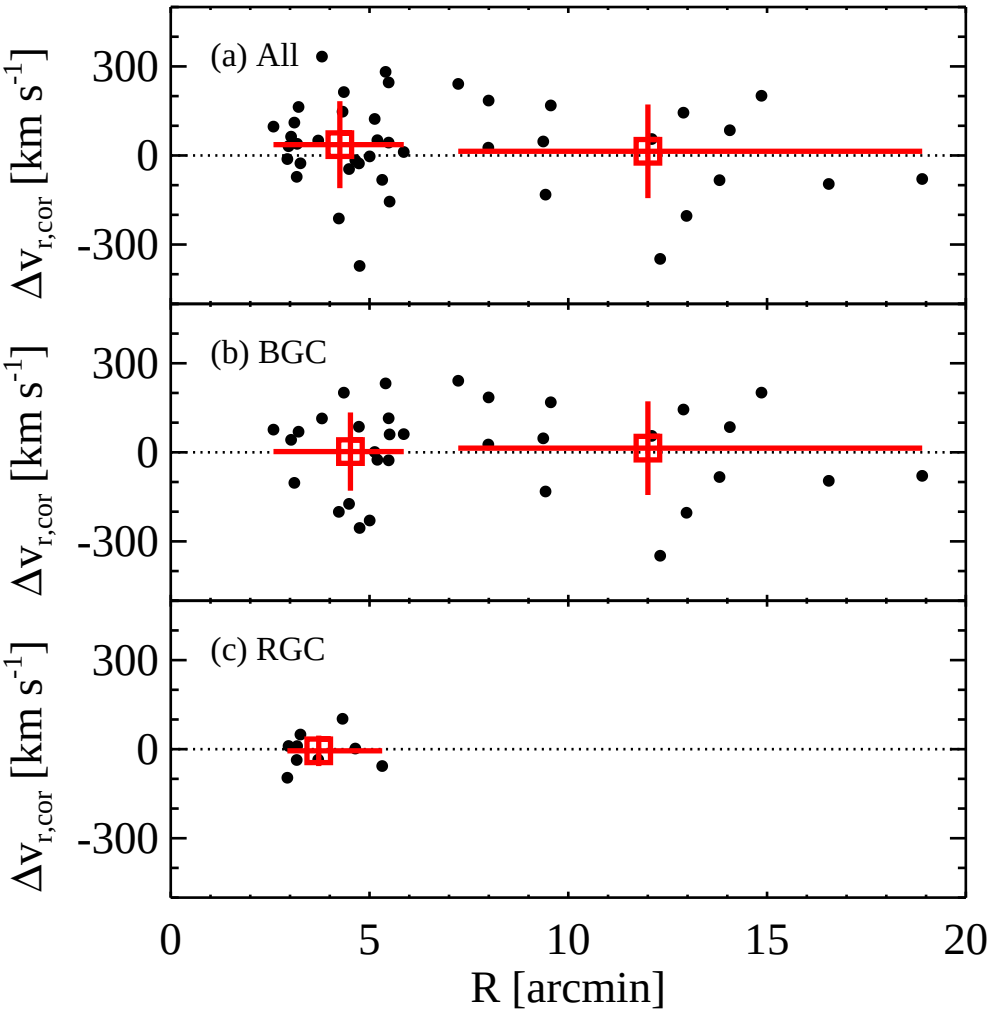

Figure 5.9: Rotation-corrected radial velocity vs, galactocentric distance from M85 for (a) 42 M85 GCs, (b) 33 M85 BGCs, and (c) 9 M85 RGCs. The open squares represent the mean radial velocities of the GCs in each radial bin. The vertical error bars indicate the radial velocity dispersions of the GCs in each bin.

pellari et al. 2011; Krajnović et al. 2011; Emsellem et al. 2011) is shown in Figure 4.11. The photometric and kinematic position angles of the M85 stellar light derived

Table 5.4. Kinematics of the M85 GC System

R (arcmin)	$\overline{R}$ (arcmin)	N	$\overline{v_r}$ (km s^{-1})	σ_r (km s^{-1})	ΩR (km s^{-1})	Θ_0 (deg)	$\sigma_{r,cor}$ (km s^{-1})	$\Omega R/\sigma_{r,cor}$
All GCs in M85								
2.6–18.9	7.0	42	765 ± 27	174 ± 20	137 ± 26	164 ± 17	144 ± 18	0.95
2.6– 5.9	4.3	27	752 ± 34	173 ± 25	151 ± 36	174 ± 15	147 ± 23	1.03
BGCs with $(g-i)_0 < 0.8$ in M85								
2.6–18.9	7.9	33	788 ± 31	171 ± 22	179 ± 45	107 ± 15	149 ± 20	1.20
2.6– 5.9	4.5	18	789 ± 41	170 ± 31	210 ± 63	97 ± 16	132 ± 23	1.59
7.2–18.9	12.0	15	787 ± 46	173 ± 33	152 ± 60	120 ± 33	158 ± 31	0.96
RGCs with $(g-i)_0 > 0.8$ in M85								
2.9– 5.3	3.7	9	678 ± 52	154 ± 37	213 ± 34	193 ± 7	51 ± 14	4.14

by Krajnović et al. (2011) are $\mathrm{PA_{phot}} = 12\overset{\circ}{.}3 \pm 11\overset{\circ}{.}0$ and $\mathrm{PA_{kin}} = 19\overset{\circ}{.}5 \pm 4\overset{\circ}{.}8$, respectively. The kinematic position angle is defined as the angle from the north to the maximum receding part of the velocity map. In Section 5.3.2, we find that the rotation axis of the M85 GC system is significantly different from that of the stellar light. This feature is also confirmed with more sample in the outer halo of M85 (see Figure 5.6). We derive the kinematic position angle of the entire GC system is 254°± 17°, which is consistent with the small sample taken from Gemini-N/GMOS observation (244°± 16°). The rotation features of both BGC and RGC systems also do not agree with the stellar rotation although the BGCs and RGCs rotates orthogonally. The kinematic position angles of BGC and RGC systems are 197° and 283°, respectively. The difference in the rotation axes between the GC system and the stellar light might be merger-induced feature as discussed in Section 4.6.1.

The BGC and RGC systems show the kinematically decoupled features as well.

This indicates that the formation processes of the BGCs and RGCs are different from each other. However, we cannot make a firm conclusion since the rotation axes are likely to change with more sample in the north region from M85 ($-90° < \mathrm{PA} < 90°$).

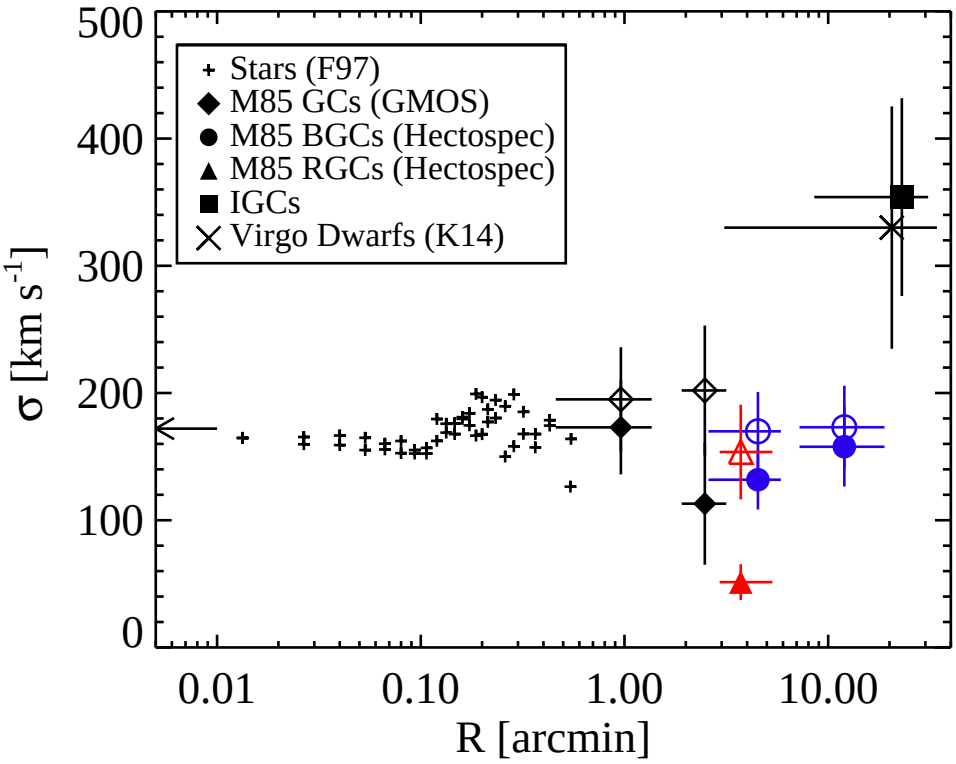

Figure 5.10: Radial velocity dispersion profile for the stars (crosses; Fisher et al. 1997), GCs within $R < 2'$ (diamonds; Ko et al. in prep), BGCs/RGCs of M85 confirmed in this study (circles/triangles), IGCs confirmed in this study (square), and Virgo dwarfs in the survey region of this study (x mark; Kim et al. 2014). The filled symbols for the M85 GCs represent the radial velocity dispersion about the mean GC velocity in each bin, while open symbols for the M85 GCs the radial velocity dispersion about the best fit rotation curve in each bin.

The strong rotation of the GC system in the outskirts is not common for typ-

ical early-type galaxies. Several simulation studies suggested that various kinds of merging events cause this rotation feature of the GC system in the outer region of galaxies: major dry merging of MW-like progenitors (Bekki et al. 2005), uneven-mass galaxy mergers with 1:4.5 mass ratio (Bournaud et al. 2005), and gas-rich major merger with the gas fraction of 30-40% (Hoffman et al. 2010). However, It is hard to confirm which types of mergers are dominant to explain the strong rotation of the GC system in the outskirts with our observation results to date.

5.4.2 Kinematics of IGCs

We investigate the kinematics of 11 IGCs confirmed in this study. The mean radial velocity of the IGCs is 1012 $\pm$ 108 km s^{-1}, which is higher than that of the GCs ($v_{\rm r}$ = 765 $\pm$ 27 km s^{-1}). We derive the radial velocity dispersion and its error of the IGCs following the formula in Pryor & Meylan (1993). The radial velocity dispersion of the IGCs is 354 $\pm$ 78 km s^{-1}, which is higher than those of the BGCs and RGCs (see Figure 5.10).

We also compare the kinematics of the IGCs with that of dwarf galaxies in the survey region of this study although the number of the dwarf galaxies in the survey region is as small as six. We use the radial velocity of dwarf galaxies presented in the extended Virgo cluster catalog (Kim et al. 2014). The mean radial velocity and radial velocity dispersion of the dwarf galaxies in the survey region are $v_{\rm r}$ = 1113 $\pm$ 135 km s^{-1} and σ = 330 $\pm$ 95 km s^{-1}. These are consistent with the kinematics of the IGCs.

The IGCs are the GCs wandering around the galaxy cluster region, not associated with any single galaxy. Several studies suggested a hypothesis that the IGCs originate from low-mass dwarf galaxies and are metal-poor (Williams et al. 2007; Bekki et al. 2008; Georgiev et al. 2009; Lee et al. 2010a). They could be accreted to the gravitational potential well of their host galaxy cluster. The dwarf galaxies are also

governed by the gravitational potential of their host galaxy cluster. Therefore, it is expected that the kinematic properties of the IGCs and dwarf galaxies are similar to each other. Note that all IGCs have blue color, $(g-i)_0 < 0.8$, except one. The IGCs confirmed in this study are metal-poor and show the similar kinematics to that of dwarfs, which supports the origin of IGCs described above.

5.4.3 Dynamical Mass of M85

We estimate the dynamical mass of M85 using the kinematics of M85 GCs confirmed in this study. Since the M85 GC system shows a rotation feature as mentioned in Section 3.2, we consider two different mass components of M85, rotation-supported and pressure-supported mass components. The total dynamical mass of M85 is the sum of these two components.

First, we estimate the rotation-supported mass of M85 simply using the following equation, assuming that the M85 GCs rotate with the simple circular orbit.

$$M_{\rm rot} = \frac{R_{\rm max} V_{\rm max}^2}{G},$$

where $\rm V_{max}$ is the inclination-corrected rotation amplitude of the GC system, $\rm R_{max}$ is the maximum projected distance of the GCs in the sample, and G is the gravitational constant. According to this equation, we estimate the mass of rotation-supported system of M85 as $M_{\rm rot} = 1.83^{+0.45}_{-0.51} \times 10^{12} M_{\odot}$.

Second, the pressure-supported mass of M85 is estimated using two methods: projected mass estimator (PME; Heisler et al. 1985) and tracer mass estimator (TME; Evans et al. 2003). Heisler et al. (1985) presented the PME method to estimate the mass of a galaxy group using the kinematics of its member galaxies, assuming that the number density of the member galaxies is proportional to the dark matter mass density. The mass based on the PME method is given by

$$M_{\rm PME} = \frac{C_{\rm proj}}{GN} \sum_{i}^{N} (v_i - v_{\rm sys})^2 R_i,$$

where N is the number of objects, v_i is the rotation-corrected radial velocity of a given object, $v_{\rm sys}$ is the systemic velocity of the objects, and R_i is the projected galactocentric distance. The constant $C_{\rm proj}$ is $32/\pi$ and $64/\pi$ for the objects with an isotropic orbit and a radial orbit, respectively. We obtain the mass of M85, $M_{\rm PME} = 4.72 \times 10^{13} M_{\odot}$ with an assumption of the isotropic orbit, using 42 GCs out to $R \sim 18\farcm9$ corresponding to $\sim$ 98.5 kpc.

Evans et al. (2003) presented the generalized version of the PME method, called as the TME method, with an assumption that the number density of mass tracers is different from the dark matter mass density. Assuming the isotropic velocity distribution of the tracers, $C_{\rm proj}$ in the TME method is not a simple constant but defined as follows:

$$C_{\rm proj} = \frac{4(\alpha+\gamma)(4-\alpha-\gamma)(1-(r_{\rm in}/r_{\rm out})^{(3-\gamma)})}{\pi(3-\gamma)(1-(r_{\rm in}/r_{\rm out})^{(4-\alpha-\gamma)})},$$

where α is the power-law slope of the underlying gravitational force field profile, γ is the power-law slope of the volume number density profile of tracers, and $r_{\rm in}$ and $r_{\rm out}$ are the innermost and outermost galactocentric distance of the tracers, respectively. The α parameter is zero for the isothermal dark matter halo where the flat rotation curve occurs, and about 0.55 for the NFW dark matter profile (Navarro et al. 1996; Watkins et al. 2010). We estimate the power-law slope of the GC volume number density profile using the GCs detected in CFHT/MegaCam images (see Chapter 3), and find $\gamma \sim 3.65$. The $r_{\rm in}$ and $r_{\rm out}$ are $2\farcm6$ and $18\farcm9$, corresponding to 13.5 kpc and 98.5 kpc, respectively. The enclosed mass based on the TME method is $M_{\rm TME} = 1.78 \times 10^{13} M_{\odot}$ for the isothermal halo and $6.12 \times 10^{13} M_{\odot}$ for the NFW dark matter profile.

In conclusion, the dynamical mass of M85 mainly consists of the pressure-supported mass component, $\sim 10^{13} M_{\odot}$, while the rotation-supported mass component is about one tenth of the pressure-supported one.

5.5 Summary

We present a wide-field spectroscopic study of GCs in a merger remnant galaxy M85 using MMT/Hectospec. We confirm 53 GCs among the spectroscopic targets including 42 GCs that belong to M85 and 11 IGCs. Our main results are summarized as follows.

- The mean radial velocity of the GCs in M85 is $v_{\rm r} = 765 \pm 27$ km s^{-1}. The GC system shows a considerable rotation feature of which amplitude is $\Omega R = 137 \pm 26$ km s^{-1}. The rotation-corrected radial velocity dispersion of the GC system of M85 is $\sigma_r = 144 \pm 18$ km s^{-1}. The GC system shows the counter-rotation feature, compared with the central stellar light.

- The RGC system show more clear rotation than the BGC system. The rotation parameter of the RGC system ($\Omega/\sigma_{r,cor} = 4.14$) is much higher than that of the BGC system ($\Omega/\sigma_{r,cor} = 1.2$).

- The mean radial velocity and the radial velocity dispersion of the IGCs confirmed in this study are 1012 ± 108 km s^{-1} and 354 ± 78 km s^{-1}, respectively. These are clearly different from the kinematic properties of the GCs in M85, but consistent with those of dwarf galaxies in the survey region. It indicates that the IGCs are governed by the gravitational potential of the Virgo cluster. Most of the IGCs have blue color, which supports the scenario that IGCs are stripped from low-mass dwarf galaxies.

- We derive the dynamical mass of M85 constituted by two components, rotation-supported and pressure-supported mass components. The dynamical mass of M85 is derived as about 2–6 $\times$ $10^{13} M_{\odot}$.

Chapter 6

Summary and Conclusion

The GCs are an efficient tool to investigate the formation and evolution history of their host environments. They are ubiquitous in various types of galaxies and bright enough to detect in galaxies. The outskirts of galaxies where the stellar light is faint could be traced by the GCs. In this thesis, we carry out comprehensive surveys of IGCs in the Virgo cluster and GCs in the merger remnant galaxy M85. We identify a few tens of GCs for each environment and analyze the photometric and spectroscopic properties of the GC system.

We perform an extensive spectroscopic survey of GCs in the 2 $\deg^2$ field around the Virgo center using MMT/Hectospec. They cover three main galaxies in the central region of the Virgo cluster: M84, M86, and part of M87. We obtain spectra of 910 spectroscopic targets and classify them into GCs, UCDs, and foreground stars. We identify 201 GCs and 55 UCDs. The primary results are summarized as follows.

Among 201 GCs, we detect 46 IGCs that do not belong to any individual bright galaxies in the Virgo with spatial and kinematic information. The total number of IGCs is expected to be about 2114 in the survey region. The number density of the IGCs confirmed in this study is about 0.19 ± 0.02 arcmin^{-2}. This is comparable with the number density expected from photometric surveys in the previous studies. The

color distribution of the spectroscopically confirmed IGCs shows two populations, blue (metal-poor) GCs and red (metal-rich) GCs, as in the case of M87 GCs. The blue IGCs mainly originate from dwarf galaxies (some originate from massive galaxies). On the other hand, the red IGCs are only from intermediate-mass to high-mass galaxies.

The IGCs consist of two groups with mean radial velocities $v_{\rm r} = 1023$ km s^{-1} and 36 km s^{-1}. The IGCs with high radial velocities are associated with the main body of the Virgo, while the IGCs with low radial velocities may be infalling or outgoing populations. The dwarf galaxies in the Virgo cluster show the similar radial velocity distribution with the IGCs. The radial velocity dispersion of the IGCs and UCDs with $v_{\rm r} > 400$ km s^{-1} ($\sigma = 314 \pm 39$ km s^{-1} and 361 ± 24 km s^{-1}) is much lower than that of the dwarfs with $v_{\rm r} > 400$ km s^{-1} ($\sigma = 608 \pm 84$ km s^{-1}). This indicates that the Virgo, based on the kinematics of the IGCs and UCDs, may be a dynamically more relaxed system than indicated by the dwarfs. Most of the UCDs confirmed in this study are located around the main galaxies in the central region of the Virgo–M84, M86, and M87–while the IGCs are not.

These results suggest that both the IGCs and UCDs in the main body of the Virgo are dynamically cooler systems than the dwarfs. IGCs with extremely high radial velocities ($v_{\rm r} > 2300$ km s^{-1}) are not confirmed in this study, unlike the dwarfs with similar velocities. On the other hand, the IGCs and UCDs with low radial velocities are infalling toward or outgoing from the main body of the Virgo, but their spatial distributions are totally different. The UCDs are thought to be involved in the infalling group centered on M86, but the origin of the IGCs that lie scattered in the survey region is unclear. The size measurement of the compact IGCs will be very helpful to reduce the contamination due to foreground stars in the future.

We carry out a wide-field photometric survey and spectroscopic survey of GCs

in M85 using CFHT/MegaCam, Gemini-N/GMOS, and MMT/Hectospec. First, we identify the GCs in M85 with *ugi*-band images taken from CFHT/MegaCam covering 1 deg^2 field around M85. Second, we measure the ages and metallicities of 20 GCs based on the full spectrum fitting method with spectra obtained from Gemini-N/GMOS. Third, we investigate the wide-field kinematics of 53 GCs with radial velocity data from MMT/Hectospec spectra. The main results are summarized as follows.

We identify 1318 GC candidates in *ugi*-band images among point sources in the survey region using color and magnitude criteria. These GC candidates show a strong concentration on M85 center, but are more extended than the stellar light. The effective radius of the GC system is 5′.54, corresponding to 29 kpc, while that of the stellar light of M85 is as small as about 2′.15.

The $(g-i)_0$ color distribution of the GC candidates is not unimodal but multimodal. The peaks of the color distribution are $(g-i)_0 = 0.65$ and 0.87 for bimodal case and $(g-i)_0 = 0.65$, 0.79, and 0.91 for trimodal case. We divided the GC sample into two categories, BGCs and RGCs, because the intermediate-color population in trimodal case accounts for only 9% of the total and is mostly located within $R < 2'$.

The BGC system is much more extended than the RGC system. The effective radii of the BGC and RGC systems are 7′.41 ± 2′.07 and 2′.31 ± 0′.45, respectively. Both BGC and RGC systems show significantly elongated along the stellar light as well as the entire GC system. The ellipticity profiles of both GC systems and the stellar light agree well.

We expect that the presence of the green GCs and the elongated spatial distribution of the BGC and RGC systems are merger-induced features. The green GCs in the central region of M85 indicates that the post-starburst induced by wet mering occurred at the center intensively. The elongated spatial distribution of the stellar light and GC system implies that the stars are accreted with specific direction. This

accretion seems to be due to dry merging, which is not related to star formation.

We obtain spectra of 21 GC candidates in the central region ($R < 2\farcm$) identified from photometric study described above as well as M85 nucleus. We identify 20 GCs with radial velocity criterion. The mean radial velocity of the GCs in M85 is $v_{\rm r} = 716 \pm 45$ km s^{-1}, which is consistent of that of M85 nucleus. The GCs in M85 has two distinct sub-populations, old GCs (> 9 Gyr) and intermediate-age GCs (< 9 Gyr). The mean ages of the old and intermediate-age GCs are 12.3 ± 2.7 Gyr and 4.0 ± 2.0 Gyr, respectively. The mean metallicity of the intermediate-age GCs ([Fe/H] = –0.19) is higher than that of the old GCs ([Fe/H] = –1.01).

The GC system shows a considerable rotation feature of which amplitude is $\Omega R = 179 \pm 37$ km s^{-1}, although M85 is almost face-on galaxy. The rotation features of the GC system of M85 are orthogonal to those of the central stellar light, indicative of one of merging evidence. The rotation-corrected radial velocity dispersion of the GC system of M85 is $\sigma_r = 154 \pm 27$ km s^{-1}. We design a wide-field spectroscopic study of the GCs in M85, since the further spectroscopic survey is needed to confirm this kinematic properties.

We obtain spectra of 53 GCs with $2\farcm5 < R < 31'$ using MMT/Hectospec. They include 42 GCs that belong to M85 and 11 IGCs. The mean radial velocity of the GCs in M85 is $v_{\rm r} = 765 \pm 27$ km s^{-1}. The GC system shows a considerable rotation feature of which amplitude is $\Omega R = 137 \pm 26$ km s^{-1}. The rotation-corrected radial velocity dispersion of the GC system of M85 is $\sigma_r = 144 \pm 18$ km s^{-1}. We derive the dynamical mass of M85 constituted by two components, rotation-supported and pressure-supported mass components from the radial velocities of the GCs. The dynamical mass of M85 is derived as about 2–6 $\times 10^{13} M_{\odot}$.

The GC system shows the rotation feature different from that of the central stellar light. This agrees with the rotation feature previously confirmed from the small sample within $R < 2\farcm5$. The RGC system show clearer rotation than the BGC

system. The rotation parameter of the RGC system ($\Omega/\sigma_{r,cor} = 4.14$) is much higher than that of the BGC system ($\Omega/\sigma_{r,cor} = 1.2$).

Based on photometric and spectroscopic analysis of M85 GCs, we suggest the formation and evolution history of M85 as follows. The old metal-poor and metal-rich GCs in M85 formed at early epoch (> 10 Gyr), similar to the GCs in typical early-type galaxies. About 4 Gyr ago, a wet merging with the intense star formation in the central region of M85 occurred. Consequently, new GCs with green or red color, $(g - i)_0 > 0.8$, formed. The strong rotation features of the GC system in the outer region of M85 is rarely shown in typical early-type galaxies. These are expected to result from the merging process of M85. Several simulation studies can explain these features from various combination between major/minor and dry/wet mergers, but further studies are needed to reveal the origin. The spatial distribution of the BGCs in M85 are strongly elongated along the stellar light, which is different from the BGCs in typical early-type galaxies as well. It might imply that M85 has been grown by dissipationless merging along a certain direction.

In addition to the IGCs discovered in the central region of the Virgo, we find the IGCs near M85. The mean radial velocity and the radial velocity dispersion of the IGCs near M85 are 1012 ± 108 km s^{-1} and 354 ± 78 km s^{-1}, respectively. These are clearly different from the kinematic properties of the GCs in M85, but consistent with those of dwarf galaxies in the survey region. It indicates that the IGCs near M85 are governed by the gravitational potential of the Virgo cluster. Most of the IGCs have blue color, which supports the scenario that IGCs are stripped from low-mass dwarf galaxies. These kinematic properties of the IGCs near M85 are totally different from those of the IGCs in the central region of the Virgo. The IGCs in the central region of the Virgo have the radial velocity dispersion much lower than that of dwarf galaxies. It indicates that the central region of the Virgo is not dynamically relaxed, while a small group near M85 located in the northernmost region is a well

relaxed system.

Bibliography

Abazajian, K. N., Adelman-McCarthy, J. K., Agüeros, M. A., et al. 2009, ApJS, 182, 543-558

Adami, C., Slezak, E., Durret, F., et al. 2005, A&A, 429, 39

Alam, S., Albareti, F. D., Allende Prieto, C., et al. 2015, ApJS, 219, 12

Alamo-Martínez, K. A., Blakeslee, J. P., Jee, M. J., et al. 2013, ApJ, 775, 20

Alves-Brito, A., Forbes, D. A., Mendel, J. T., Hau, G. K. T., & Murphy, M. T. 2009, MNRAS, 395, L34

Ashman, K. M., & Zepf, S. E. 1992, ApJ, 384, 50

Barmby, P., Huchra, J. P. 2001, AJ, 122, 2458

Bassino, L. P., Muzzio, J. C., & Rabolli, M. 1994, ApJ, 431, 634

Bassino, L. P., Cellone, S. A., Forte, J. C., & Dirsch, B. 2003, A&A, 399, 489

Bassino, L. P., & Caso, J. P. 2017, MNRAS, 466, 4259

Beasley, M. A., & Trujillo, I. 2016, ApJ, 830, 23

Bedin, L. R., Piotto, G., Anderson, J., et al. 2004, ApJ, 605, L125

Bekki, K., Couch, W. J., & Drinkwater, M. J. 2001, ApJ, 552, L105

Bekki, K., Couch, W. J., Drinkwater, M. J., & Shioya, Y. 2003, MNRAS, 344, 399

Bekki, K., Beasley, M. A., Brodie, J. P., & Forbes, D. A. 2005, MNRAS, 363, 1211

Bekki, K., & Yahagi, H. 2006, MNRAS, 372, 1019

Bekki, K., Yahagi, H., Nagashima, M., & Forbes, D. A. 2008, MNRAS, 387, 1131

Bergond, G., Athanassoula, E., Leon, S., et al. 2007, A&A, 464, L21

Bertin, E., & Arnouts, S. 1996, A&AS, 117, 393

Bertin, E., Mellier, Y., Radovich, M., et al. 2002, Astronomical Data Analysis Software and Systems XI, 281, 228

Bertin, E. 2006, Astronomical Data Analysis Software and Systems XV, 351, 112

Binggeli, B., Sandage, A., & Tammann, G. A. 1985, AJ, 90, 1681

Binggeli, B., Tammann, G. A., & Sandage, A. 1987, AJ, 94, 251

Binggeli, B., Popescu, C. C., & Tammann, G. A. 1993, A&AS, 98, 275

Blakeslee, J. P., Jordán, A., Mei, S., et al. 2009, ApJ, 694, 556

Böhringer, H., Briel, U. G., Schwarz, R. A., et al. 1994, Nature, 368, 828

Boulade, O., Charlot, X., Abbon, P., et al. 2003, Proc. SPIE, 4841, 72

Brodie, J. P., & Strader, J. 2006, ARA&A, 44, 193

Brodie, J. P., Romanowsky, A. J., Strader, J., & Forbes, D. A. 2011, AJ, 142, 199

Bournaud, F., Jog, C. J., & Combes, F. 2005, A&A, 437, 69

Burke, C., Collins, C. A., Stott, J. P., & Hilton, M. 2012, MNRAS, 425, 2058

Burstein, D. 1979, ApJS, 41, 435

Burstein, D., Faber, S. M., Gaskell, C. M., & Krumm, N. 1984, ApJ, 287, 586

Caldwell, N., Strader, J., Romanowsky, A. J., et al. 2014, ApJ, 787, L11

Cappellari, M., Emsellem, E., Krajnović, D., et al. 2011, MNRAS, 413, 813

Cezario, E., Coelho, P. R. T., Alves-Brito, A., Forbes, D. A., & Brodie, J. P. 2013, A&A, 549, A60

Chen, B., Liu, X., Xiang, M., et al. 2016, AJ, 152, 45

Coccato, L., Arnaboldi, M., & Gerhard, O. 2013, MNRAS, 436, 1322

Cohen, J. G. 1981, ApJ, 247, 869

Côté, P., Marzke, R. O., & West, M. J. 1998, ApJ, 501, 554

Côté, P., McLaughlin, D. E., Hanes, D. A., et al. 2001, ApJ, 559, 828

Côté, P., Blakeslee, J. P., Ferrarese, L., et al. 2004, ApJS, 153, 223

D'Abrusco, R., Cantiello, M., Paolillo, M., et al. 2016, ApJ, 819, L31

Da Costa, G. S., Held, E. V., & Saviane, I. 2014, MNRAS, 438, 3507

de Vaucouleurs, G. 1961, ApJS, 6, 213

de Vaucouleurs, G., de Vaucouleurs, A., Corwin, H. G., Jr., et al. 1991, Third Reference Catalogue of Bright Galaxies. Volume I: Explanations and references. Volume II: Data for galaxies between 0^h and 12^h. Volume III: Data for galaxies between 12^h and 24^h. (New York, USA: Springer)

Doherty, M., Arnaboldi, M., Das, P., et al. 2009, A&A, 502, 771

Dotter, A., Sarajedini, A., & Anderson, J. 2011, ApJ, 738, 74

Drinkwater, M. J., Gregg, M. D., Hilker, M., et al. 2003, Nature, 423, 519

Durrell, P. R., Côté, P., Peng, E. W., et al. 2014, ApJ, 794, 103

Ehlert, S., Werner, N., Simionescu, A., et al. 2013, MNRAS, 430, 2401

Emsellem, E., Cappellari, M., Krajnović, D., et al. 2007, MNRAS, 379, 401

Emsellem, E., Cappellari, M., Krajnović, D., et al. 2011, MNRAS, 414, 888

Evans, N. W., Wilkinson, M. I., Perrett, K. M., & Bridges, T. J. 2003, ApJ, 583, 752

Fabricant, D., Fata, R., Roll, J., et al. 2005, PASP, 117, 1411

Fabricant, D. G., Kurtz, M. J., Geller, M. J., et al. 2008, PASP, 120, 1222

Fellhauer, M., & Kroupa, P. 2002, MNRAS, 330, 642

Ferrarese, L., Côté, P., Jordán, A., et al. 2006, ApJS, 164, 334

Ferrarese, L., Côté, P., Cuillandre, J.-C., et al. 2012, ApJS, 200, 4

Firth, P., Drinkwater, M. J., & Karick, A. M. 2008, MNRAS, 389, 1539

Fisher, D., Franx, M., & Illingworth, G. 1996, ApJ, 459, 110

Forbes, D. A., Brodie, J. P., & Grillmair, C. J. 1997, AJ, 113, 1652

Forbes, D. A., Ponman, T., & O'Sullivan, E. 2012, MNRAS, 425, 66

Forbes, D. A., Pastorello, N., Romanowsky, A. J., et al. 2015, MNRAS, 452, 1045

Fraley, C., & Raftery, A. E. 2002, Model-based Clustering, Discriminant Analysis and Density Estimation, Journal of the American Statistical Association 97:611-631

Fraley, C., Raftery, A. E., Murphy, T. B., and Scrucca, L. 2012, mclust Version 4 for R: Normal Mixture Modeling for Model-Based Clustering, Classification, and Density Estimation Technical Report No. 597, Department of Statistics, University of Washington

Freeman, K. C., & Rodgers, A. W. 1975, ApJ, 201, L71

Gavazzi, G., Zaccardo, A., Sanvito, G., Boselli, A., & Bonfanti, C. 2004, A&A, 417, 499

Georgiev, I. Y., Hilker, M., Puzia, T. H., Goudfrooij, P., & Baumgardt, H. 2009, MNRAS, 396, 1075

Goerdt, T., Moore, B., Kazantzidis, S., et al. 2008, MNRAS, 385, 2136

Gonzalez, A. H., Zabludoff, A. I., & Zaritsky, D. 2005, ApJ, 618, 195

Goudfrooij, P., Mack, J., Kissler-Patig, M., Meylan, G., & Minniti, D. 2001, MNRAS, 322, 643

Goudfrooij, P., Alonso, M. V., Maraston, C., & Minniti, D. 2001, MNRAS, 328, 237

Goudfrooij, P., Gilmore, D., Whitmore, B. C., & Schweizer, F. 2004, ApJ, 613, L121

Graham, A. W., & Driver, S. P. 2005, PASA, 22, 118

Gratton, R. G., Carretta, E., & Bragaglia, A. 2012, A&A Rev., 20, 50

Graves, G. J., & Schiavon, R. P. 2008, ApJS, 177, 446-464

Harris, W. E. 1996, AJ, 112, 1487

Harris, W. E. 2009, ApJ, 703, 939

Haşegan, M., Jordán, A., Côté, P., et al. 2005, ApJ, 627, 203

Heisler, J., Tremaine, S., & Bahcall, J. N. 1985, ApJ, 298, 8

Herschel, J., 1847, in Results of Astronomical Observations made at the Cape of Good Hope, (London: Smith, Elder, & Co.)

Hibbard, J. E., & Sansom, A. E. 2003, AJ, 125, 667

Hilker, M., Infante, L., & Richtler, T. 1999, A&AS, 138, 55

Hoffman, L., Cox, T. J., Dutta, S., & Hernquist, L. 2010, ApJ, 723, 818

Hubble, E. 1932, ApJ, 76, 44

Huxor, A. P., Mackey, A. D., Ferguson, A. M. N., et al. 2014, MNRAS, 442, 2165

Hwang, N., Park, H. S., Lee, M. G., et al. 2014, ApJ, 783, 49

Janz, J., Forbes, D. A., Norris, M. A., et al. 2015, MNRAS, 449, 1716

Jerjen, H., Binggeli, B., & Barazza, F. D. 2004, AJ, 127, 771

Jones, J. B., Drinkwater, M. J., Jurek, R., et al. 2006, AJ, 131, 312

Jordán, A., West, M. J., Côté, P., & Marzke, R. O. 2003, AJ, 125, 1642

Jordán, A., Peng, E. W., Blakeslee, J. P., et al. 2009, ApJS, 180, 54

Kim, S., Rey, S.-C., Jerjen, H., et al. 2014, ApJS, 215, 22

Kissler-Patig, M., Richtler, T., Storm, J., & della Valle, M. 1997, A&A, 327, 503

Kissler-Patig, M., Jordán, A., & Bastian, N. 2006, A&A, 448, 1031

Ko, Y., Hwang, H. S., Lee, M. G., et al. 2017, ApJ, 835, 212

Koleva, M., Prugniel, P., Ocvirk, P., Le Borgne, D., & Soubiran, C. 2008, MNRAS, 385, 1998

Koleva, M., Prugniel, P., Bouchard, A., & Wu, Y. 2009, A&A, 501, 1269

Kormendy, J., Fisher, D. B., Cornell, M. E., & Bender, R. 2009, ApJS, 182, 216

Krajnović, D., Emsellem, E., Cappellari, M., et al. 2011, MNRAS, 414, 2923

Krick, J. E., Bernstein, R. A., & Pimbblet, K. A. 2006, AJ, 131, 168

Krick, J. E., & Bernstein, R. A. 2007, AJ, 134, 466

Kroupa, P. 1998, MNRAS, 300, 200

Kurtz, M. J., & Mink, D. J. 1998, PASP, 110, 934

Larsen, S. S. 1999, A&AS, 139, 393

Lauer, T. R., Faber, S. M., Gebhardt, K., et al. 2005, AJ, 129, 2138

Leaman, R., VandenBerg, D. A., & Mendel, J. T. 2013, MNRAS, 436, 122

Lee, M. G., Kim, E., & Geisler, D. 1998, AJ, 115, 947

Lee, Y.-W., Joo, J.-M., Sohn, Y.-J., et al. 1999, Nature, 402, 55

Lee, J.-W., Lee, J., Kang, Y.-W., et al. 2009, ApJ, 695, L78

Lee, M. G., Park, H. S., & Hwang, H. S. 2010, Science, 328, 334

Lee, M. G., Park, H. S., Hwang, H. S., et al. 2010, ApJ, 709, 1083

Lee, M. G., Lim, S., Park, H. S., Hwang, H. S., & Hwang, N. 2011, EAS Publications Series, 48, 243

Lee, M. G., & Jang, I. S. 2016, ApJ, 831, 108

Li, H., & Gnedin, O. Y. 2014, ApJ, 796, 10

Li, B., Peng, E. W., Zhang, H.-x., et al. 2015, ApJ, 806, 133

Lim, S., Peng, E. W., Duc, P.-A., et al. 2017, ApJ, 835, 123

Liu Y., Zhou X., Ma J., Wu H., Yang Y., Li J., & Chen J. 2005, AJ, 129, 2628

Liu, C., Peng, E. W., Côté, P., et al. 2015, ApJ, 812, 34

Longobardi, A., Arnaboldi, M., Gerhard, O., & Hanuschik, R. 2015, A&A, 579, A135

Mackey, A. D., & Broby Nielsen, P. 2007, MNRAS, 379, 151

Maraston, C., Bastian, N., Saglia, R. P., et al. 2004, A&A, 416, 467

Marín-Franch, A., Aparicio, A., Piotto, G., et al. 2009, ApJ, 694, 1498

McDermid, R., Emsellem, E., Cappellari, M., et al. 2004, Astronomische Nachrichten, 325, 100

Mei, S., Blakeslee, J. P., Côté, P., et al. 2007, ApJ, 655, 144

Meylan, G. 2003, New Horizons in Globular Cluster Astronomy, 296, 17

Mieske, S., Hilker, M., & Infante, L. 2002, A&A, 383, 823

Mieske, S., Hilker, M., & Misgeld, I. 2012, A&A, 537, A3

Mihos, J. C., Harding, P., Feldmeier, J., & Morrison, H. 2005, ApJ, 631, L41

Mihos, J. C. 2015, arXiv:1510.01929

Misgeld, I., Mieske, S., Hilker, M., et al. 2011, A&A, 531, A4

Muñoz, R. P., Puzia, T. H., Lançon, A., et al. 2014, ApJS, 210, 4

Muratov, A. L., & Gnedin, O. Y. 2010, ApJ, 718, 1266

Murphy, J. D., Gebhardt, K., & Adams, J. J. 2011, ApJ, 729, 129

Murphy, J. D., Gebhardt, K., & Cradit, M. 2014, ApJ, 785, 143

Muzzio, J. C. 1987, PASP, 99, 245

Navarro, J. F., Frenk, C. S., & White, S. D. M. 1996, ApJ, 462, 563

Norris, J. E. 2004, ApJ, 612, L25

Oldham, L. J., & Auger, M. W. 2016, MNRAS, 455, 820

Ostrov, P., Geisler, D., & Forte, J. C. 1993, AJ, 105, 1762

Park, H. S., Lee, M. G., & Hwang, H. S. 2012, ApJ, 757, 184

Park, H. S., Lee, M. G., Hwang, H. S., et al. 2012, ApJ, 759, 116

Park, H. S., & Lee, M. G. 2013, ApJ, 773, 27

Paudel, S., Lisker, T., & Janz, J. 2010, ApJ, 724, L64

Peacock, M. B., Maccarone, T. J., Knigge, C., et al. 2010, MNRAS, 402, 803

Peng, E. W., Jordán, A., Côté, P., et al. 2006, ApJ, 639, 95

Peng, E. W., Ferguson, H. C., Goudfrooij, P., et al. 2011, ApJ, 730, 23

Peng, E. W., & Lim, S. 2016, ApJ, 822, L31

Pfeffer, J., & Baumgardt, H. 2013, MNRAS, 433, 1997

Pierce, M., Beasley, M. A., Forbes, D. A., et al. 2006a, MNRAS, 366, 1253

Pierce, M., Bridges, T., Forbes, D. A., et al. 2006b, MNRAS, 368, 325

Piotto, G., Villanova, S., Bedin, L. R., et al. 2005, ApJ, 621, 777

Pota, V., Forbes, D. A., Romanowsky, A. J., et al. 2013, MNRAS, 428, 389

Proctor, R. N., Forbes, D. A., & Beasley, M. A. 2004, MNRAS, 355, 1327

Pryor, C., & Meylan, G. 1993, Structure and Dynamics of Globular Clusters, Astronomical Society of the Pacific Conference Series, 50, 357

Puzia, T. H., Kissler-Patig, M., Thomas, D., et al. 2005, A&A, 439, 997

Rhode, K. L., & Zepf, S. E. 2001, AJ, 121, 210

Richtler, T., Salinas, R., Misgeld, I., et al. 2011, A&A, 531, A119

Richtler, T., Bassino, L. P., Dirsch, B., & Kumar, B. 2012, A&A, 543, A131

Romanowsky, A. J., Strader, J., Brodie, J. P., et al. 2012, ApJ, 748, 29

Sánchez-Blázquez, P., Peletier, R. F., Jiménez-Vicente, J., et al. 2006, MNRAS, 371, 703

Sandoval, M. A., Vo, R. P., Romanowsky, A. J., et al. 2015, ApJ, 808, L32

Santos, J. F. C., Jr., Alloin, D., Bica, E., & Bonatto, C. 2001, VizieR Online Data Catalog, 3219, 0

Schiavon, R. P. 2007, ApJS, 171, 146

Schindler, S., Binggeli, B., & Böhringer, H. 1999, A&A, 343, 420

Schlafly, E. F., & Finkbeiner, D. P. 2011, ApJ, 737, 103

Schuberth, Y., Richtler, T., Bassino, L., & Hilker, M. 2008, A&A, 477, L9

Schuberth, Y., Richtler, T., Hilker, M., et al. 2010, A&A, 513, A52

Schwarz, G. 1978, Ann. Stat., 6, 461

Schweizer, F., & Seitzer, P. 1988, ApJ, 328, 88

Schweizer, F., Seitzer, P., Faber, S. M., et al. 1990, ApJ, 364, L33

Schweizer, F., & Seitzer, P. 1992, AJ, 104, 1039

Seth, A. C., van den Bosch, R., Mieske, S., et al. 2014, Nature, 513, 398

Sharina, M. E., Chandar, R., Puzia, T. H., Goudfrooij, P., & Davoust, E. 2010, MNRAS, 405, 839

Smith, R. J., Lucey, J. R., Hudson, M. J., Schlegel, D. J., & Davies, R. L. 2000, MNRAS, 313, 469

Strader, J., Brodie, J. P., Schweizer, F., Larsen, S. S., & Seitzer, P. 2003, AJ, 125, 626

Strader, J., Brodie, J. P., & Forbes, D. A. 2004, AJ, 127, 295

Strader, J., Romanowsky, A. J., Brodie, J. P., et al. 2011, ApJS, 197, 33

Tamura, N., Sharples, R. M., Arimoto, N., et al. 2006, MNRAS, 373, 601

Terlevich, A. I., & Forbes, D. A. 2002, MNRAS, 330, 547

Thomas, D., Maraston, C., & Bender, R. 2003, MNRAS, 339, 897

Thomas, D., Maraston, C., & Johansson, J. 2011, MNRAS, 412, 2183

Tonry, J., & Davis, M. 1979, AJ, 84, 1511

Toomre, A. 1977, In Evolution of Galaxies and Stellar Populations, ed. BM Tinsley, RB Larson, p. 40. Proc. Conf. Yale Univ. New Haven: Yale Univ. Obs.

Toomre, A., & Toomre, J. 1972, ApJ, 178, 623

Trager, S. C., Worthey, G., Faber, S. M., Burstein, D., & González, J. J. 1998, ApJS, 116, 1

Trancho, G., Miller, B. W., Schweizer, F., Burdett, D. P., & Palamara, D. 2014, ApJ, 790, 122

van Dokkum, P., Abraham, R., Brodie, J., et al. 2016, ApJ, 828, L6

Vazdekis, A., Sánchez-Blázquez, P., Falcón-Barroso, J., et al. 2010, MNRAS, 404, 1639

Watkins, L. L., Evans, N. W., & An, J. H. 2010, MNRAS, 406, 264

Wang, Q., Peng, E. W., Blakeslee, J. P., et al. 2013, ApJ, 769, 145

West, M. J., Côté, P., Jones, C., Forman, W., & Marzke, R. O. 1995, ApJ, 453, L77

West, M. J., Côté, P., Marzke, R. O., & Jordán, A. 2004, Nature, 427, 31

West, M. J., Jordán, A., Blakeslee, J. P., et al. 2011, A&A, 528, A115

White, R. E., III 1987, MNRAS, 227, 185

Williams, B. F., Ciardullo, R., Durrell, P. R., et al. 2007, ApJ, 654, 835

Woodley, K. A., Harris, W. E., Puzia, T. H., et al. 2010, ApJ, 708, 1335

Worthey, G., Faber, S. M., Gonzalez, J. J., & Burstein, D. 1994, ApJS, 94, 687

Worthey, G., & Ottaviani, D. L. 1997, ApJS, 111, 377

Zepf, S. E., & Ashman, K. M. 1993, MNRAS, 264, 611

Zhang, H.-X., Peng, E. W., Côté, P., et al. 2015, ApJ, 802, 30

Zibetti, S., White, S. D. M., Schneider, D. P., & Brinkmann, J. 2005, MNRAS, 358, 949

Zhu, L., Long, R. J., Mao, S., et al. 2014, ApJ, 792, 59

Appendix A

Database for M85 GCs

In this chapter, we list the photometric and spectroscopic properties of GCs around M85. Table A.1 show the list of the GC candidates in 1 deg^2 field around M85 (see Chapter 3). Tables A.2, A.3, A.4, and A.5 show the Lick line indices and index errors of Gemini-N/GMOS observation targets (see Chapter 4). Tables A.6 and A.7 show the spectroscopic and photometric properties of contaminants and GCs confirmed by MMT/Hectospec observation (see Chapter 5), respectively.

Table A.1: A Catalog of the GCs in M85

ID	α (J2000) (deg)	δ (J2000) (deg)	g (mag)	$u-g$ (mag)	$g-i$ (mag)
GC0001	185.831070	18.427156	23.392 ± 0.032	1.03 ± 0.09	0.89 ± 0.05
GC0002	185.832062	18.395197	22.541 ± 0.017	1.11 ± 0.05	0.61 ± 0.03
GC0003	185.834488	18.306896	22.624 ± 0.014	0.96 ± 0.03	0.73 ± 0.02
GC0004	185.835114	18.226645	21.112 ± 0.004	0.96 ± 0.01	0.69 ± 0.01
GC0005	185.835190	18.544601	22.120 ± 0.009	0.97 ± 0.02	0.83 ± 0.01
GC0006	185.835785	18.116451	21.255 ± 0.005	1.22 ± 0.01	0.85 ± 0.01
GC0007	185.837219	18.007915	22.969 ± 0.017	1.59 ± 0.06	0.97 ± 0.02
GC0008	185.838165	17.852100	23.308 ± 0.024	1.50 ± 0.09	0.98 ± 0.03
GC0009	185.839340	18.155157	21.085 ± 0.004	1.55 ± 0.01	1.00 ± 0.00
GC0010	185.840866	17.914825	23.422 ± 0.022	1.49 ± 0.08	1.04 ± 0.03
GC0011	185.841064	17.871552	20.199 ± 0.002	1.29 ± 0.01	0.86 ± 0.00
GC0012	185.845245	18.407497	23.152 ± 0.017	1.31 ± 0.05	0.90 ± 0.02
GC0013	185.846497	18.014795	21.036 ± 0.004	0.89 ± 0.01	0.63 ± 0.00
GC0014	185.849609	18.077490	21.496 ± 0.005	1.16 ± 0.01	0.79 ± 0.01
GC0015	185.850937	18.004560	22.515 ± 0.010	1.12 ± 0.03	0.70 ± 0.01
GC0016	185.851425	17.591354	22.409 ± 0.011	1.34 ± 0.03	0.69 ± 0.02

Table A.1: (cont'd)

ID	α (J2000) (deg)	δ (J2000) (deg)	g (mag)	$u-g$ (mag)	$g-i$ (mag)
GC0017	185.852173	17.928823	22.508 ± 0.010	1.48 ± 0.04	1.07 ± 0.01
GC0018	185.852432	18.471004	20.837 ± 0.003	0.95 ± 0.01	0.60 ± 0.00
GC0019	185.853912	17.780943	21.986 ± 0.007	1.13 ± 0.02	0.63 ± 0.01
GC0020	185.859528	18.377144	21.008 ± 0.004	0.98 ± 0.01	0.56 ± 0.00
GC0021	185.860168	17.903008	21.666 ± 0.005	1.59 ± 0.02	1.14 ± 0.01
GC0022	185.861267	17.905943	23.370 ± 0.020	0.93 ± 0.05	0.67 ± 0.03
GC0023	185.861832	17.879999	23.390 ± 0.021	1.92 ± 0.11	1.06 ± 0.03
GC0024	185.862350	17.803667	23.023 ± 0.016	1.66 ± 0.06	1.11 ± 0.02
GC0025	185.863434	18.273386	20.640 ± 0.003	0.95 ± 0.01	0.61 ± 0.00
GC0026	185.863647	17.641190	22.615 ± 0.011	1.24 ± 0.03	0.79 ± 0.01
GC0027	185.865143	17.703972	23.571 ± 0.025	1.49 ± 0.09	0.87 ± 0.03
GC0028	185.865952	18.450796	22.659 ± 0.011	1.42 ± 0.04	1.06 ± 0.01
GC0029	185.866516	18.272341	23.383 ± 0.020	1.89 ± 0.10	1.19 ± 0.02
GC0030	185.867615	18.468483	23.463 ± 0.022	1.57 ± 0.09	1.09 ± 0.03
GC0031	185.867889	17.869299	20.184 ± 0.002	1.58 ± 0.01	1.23 ± 0.00
GC0032	185.868011	18.082602	21.652 ± 0.006	1.51 ± 0.02	1.11 ± 0.01
GC0033	185.869827	18.393970	20.170 ± 0.002	1.76 ± 0.01	1.12 ± 0.00
GC0034	185.870712	17.625296	20.196 ± 0.002	1.01 ± 0.01	0.57 ± 0.00
GC0035	185.871292	17.848301	21.301 ± 0.005	1.11 ± 0.01	0.76 ± 0.01
GC0036	185.872253	18.123211	22.635 ± 0.011	1.09 ± 0.03	0.76 ± 0.02
GC0037	185.873184	17.876640	22.111 ± 0.007	1.15 ± 0.02	0.73 ± 0.01
GC0038	185.873688	17.973415	21.395 ± 0.005	0.88 ± 0.01	0.57 ± 0.01
GC0039	185.877335	17.792635	21.977 ± 0.007	0.98 ± 0.02	0.57 ± 0.01
GC0040	185.877640	17.932137	23.184 ± 0.018	1.09 ± 0.05	0.67 ± 0.03
GC0041	185.879471	17.707243	23.224 ± 0.018	1.88 ± 0.09	1.16 ± 0.02
GC0042	185.879608	17.796457	21.434 ± 0.005	0.92 ± 0.01	0.63 ± 0.01
GC0043	185.880234	17.781399	23.552 ± 0.024	0.93 ± 0.06	0.61 ± 0.04
GC0044	185.880783	18.092958	22.273 ± 0.008	1.34 ± 0.03	0.94 ± 0.01
GC0045	185.883835	18.374079	22.800 ± 0.013	0.84 ± 0.03	0.63 ± 0.02
GC0046	185.884247	18.575441	20.423 ± 0.003	1.27 ± 0.01	0.79 ± 0.00
GC0047	185.884354	17.794626	22.686 ± 0.012	1.24 ± 0.04	0.90 ± 0.02
GC0048	185.884872	17.869125	22.961 ± 0.015	0.96 ± 0.04	0.59 ± 0.02
GC0049	185.886307	18.454311	21.390 ± 0.005	1.44 ± 0.01	1.05 ± 0.01
GC0050	185.886322	18.108820	21.663 ± 0.005	1.34 ± 0.02	0.82 ± 0.01
GC0051	185.887802	17.982182	23.188 ± 0.018	1.49 ± 0.07	0.94 ± 0.02
GC0052	185.890579	18.215181	21.176 ± 0.004	0.98 ± 0.01	0.62 ± 0.01
GC0053	185.892273	18.367609	20.264 ± 0.002	1.02 ± 0.01	0.67 ± 0.00
GC0054	185.892609	18.149979	20.251 ± 0.002	1.23 ± 0.01	0.82 ± 0.00
GC0055	185.893143	18.128994	22.369 ± 0.009	1.17 ± 0.02	0.67 ± 0.01
GC0056	185.893967	18.516197	23.261 ± 0.019	1.34 ± 0.06	0.79 ± 0.03
GC0057	185.894882	18.516455	20.998 ± 0.004	0.92 ± 0.01	0.59 ± 0.00
GC0058	185.895828	17.925560	23.412 ± 0.021	1.08 ± 0.06	0.81 ± 0.03
GC0059	185.895905	18.231794	22.476 ± 0.010	1.65 ± 0.04	1.01 ± 0.01
GC0060	185.899597	17.721710	23.588 ± 0.025	1.19 ± 0.07	0.74 ± 0.03
GC0061	185.900223	18.316137	22.678 ± 0.012	1.71 ± 0.05	1.16 ± 0.01
GC0062	185.904175	18.066795	21.952 ± 0.007	0.99 ± 0.02	0.66 ± 0.01
GC0063	185.907196	18.306534	22.838 ± 0.013	1.11 ± 0.03	0.61 ± 0.02
GC0064	185.908752	18.502176	22.068 ± 0.007	0.84 ± 0.02	0.56 ± 0.01

Table A.1: (cont'd)

ID	α (J2000) (deg)	δ (J2000) (deg)	g (mag)	$u-g$ (mag)	$g-i$ (mag)
GC0065	185.910172	17.752142	22.366 ± 0.009	1.01 ± 0.02	0.65 ± 0.01
GC0066	185.910690	17.744719	21.622 ± 0.005	0.87 ± 0.01	0.56 ± 0.01
GC0067	185.911560	18.039831	22.963 ± 0.015	1.48 ± 0.05	1.05 ± 0.02
GC0068	185.911682	18.111794	20.957 ± 0.004	1.38 ± 0.01	0.80 ± 0.00
GC0069	185.912003	17.990101	23.166 ± 0.017	1.64 ± 0.07	0.95 ± 0.02
GC0070	185.912094	18.390686	22.369 ± 0.009	0.93 ± 0.02	0.60 ± 0.01
GC0071	185.916626	17.791075	20.867 ± 0.003	1.20 ± 0.01	0.88 ± 0.00
GC0072	185.920578	18.411375	23.220 ± 0.018	1.24 ± 0.05	0.94 ± 0.02
GC0073	185.923218	18.147017	23.029 ± 0.015	1.14 ± 0.04	0.66 ± 0.02
GC0074	185.925339	18.466970	22.752 ± 0.012	1.57 ± 0.05	1.13 ± 0.01
GC0075	185.926453	18.298054	20.113 ± 0.002	0.91 ± 0.01	0.63 ± 0.00
GC0076	185.927734	18.442884	22.859 ± 0.014	1.83 ± 0.06	1.00 ± 0.02
GC0077	185.929352	17.711063	22.589 ± 0.011	1.19 ± 0.03	0.79 ± 0.01
GC0078	185.930038	17.598215	21.564 ± 0.005	1.80 ± 0.02	0.98 ± 0.01
GC0079	185.937027	18.395432	22.014 ± 0.007	1.14 ± 0.02	0.93 ± 0.01
GC0080	185.937286	17.637087	23.523 ± 0.023	1.61 ± 0.10	0.85 ± 0.03
GC0081	185.937393	17.929399	23.276 ± 0.019	1.72 ± 0.09	1.01 ± 0.02
GC0082	185.938782	18.480637	23.431 ± 0.021	1.30 ± 0.07	0.87 ± 0.03
GC0083	185.939590	17.998053	23.157 ± 0.017	1.13 ± 0.05	0.67 ± 0.02
GC0084	185.940125	18.146076	21.609 ± 0.005	1.26 ± 0.01	0.75 ± 0.01
GC0085	185.942902	17.883011	23.454 ± 0.023	1.17 ± 0.07	0.66 ± 0.03
GC0086	185.950027	18.305702	22.792 ± 0.015	1.11 ± 0.04	0.90 ± 0.02
GC0087	185.950760	17.795385	23.396 ± 0.025	1.35 ± 0.09	1.08 ± 0.03
GC0088	185.952606	18.052462	23.549 ± 0.024	1.01 ± 0.06	0.77 ± 0.04
GC0089	185.954056	17.712774	20.858 ± 0.003	0.87 ± 0.01	0.61 ± 0.00
GC0090	185.955399	17.775682	22.118 ± 0.008	1.66 ± 0.03	1.09 ± 0.01
GC0091	185.957489	18.277870	23.488 ± 0.022	1.54 ± 0.09	0.88 ± 0.03
GC0092	185.958054	17.609131	23.232 ± 0.019	1.00 ± 0.05	0.60 ± 0.03
GC0093	185.958801	17.747894	23.231 ± 0.018	1.81 ± 0.10	1.12 ± 0.02
GC0094	185.959503	18.121189	23.103 ± 0.016	1.74 ± 0.08	0.99 ± 0.02
GC0095	185.960693	18.480829	23.514 ± 0.023	1.02 ± 0.06	0.69 ± 0.03
GC0096	185.961594	18.098154	21.967 ± 0.007	1.11 ± 0.02	0.79 ± 0.01
GC0097	185.962646	17.744928	22.092 ± 0.007	1.35 ± 0.02	0.80 ± 0.01
GC0098	185.963974	17.669844	23.466 ± 0.022	1.32 ± 0.08	0.79 ± 0.03
GC0099	185.967575	18.168270	23.118 ± 0.016	1.15 ± 0.05	0.70 ± 0.02
GC0100	185.968491	17.693716	22.858 ± 0.014	1.63 ± 0.06	1.04 ± 0.02
GC0101	185.969269	18.294512	23.098 ± 0.016	1.40 ± 0.06	0.73 ± 0.02
GC0102	185.969452	18.307156	23.382 ± 0.020	1.43 ± 0.08	0.96 ± 0.03
GC0103	185.969986	17.948120	21.426 ± 0.005	1.40 ± 0.02	0.98 ± 0.01
GC0104	185.970062	18.324877	21.981 ± 0.007	1.03 ± 0.02	0.65 ± 0.01
GC0105	185.970352	17.918602	20.285 ± 0.002	0.97 ± 0.01	0.60 ± 0.00
GC0106	185.970840	18.042912	20.203 ± 0.002	1.35 ± 0.01	0.90 ± 0.00
GC0107	185.973221	17.820646	21.781 ± 0.006	1.10 ± 0.02	0.84 ± 0.01
GC0108	185.973541	18.257473	21.872 ± 0.006	1.74 ± 0.03	1.15 ± 0.01
GC0109	185.974884	18.516031	22.280 ± 0.009	1.47 ± 0.03	0.93 ± 0.01
GC0110	185.975433	18.373178	22.648 ± 0.012	1.49 ± 0.04	0.95 ± 0.01
GC0111	185.976547	18.059031	23.567 ± 0.024	0.89 ± 0.06	0.61 ± 0.04
GC0112	185.976898	18.271927	20.626 ± 0.003	1.34 ± 0.01	0.89 ± 0.00

Table A.1: (cont'd)

ID	α (J2000) (deg)	δ (J2000) (deg)	g (mag)	$u-g$ (mag)	$g-i$ (mag)
GC0113	185.978271	18.494030	23.115 ± 0.016	1.39 ± 0.06	0.78 ± 0.02
GC0114	185.978500	18.578121	22.200 ± 0.008	1.17 ± 0.02	0.74 ± 0.01
GC0115	185.982697	18.021963	21.634 ± 0.005	0.96 ± 0.01	0.77 ± 0.01
GC0116	185.982941	17.955271	22.350 ± 0.009	1.57 ± 0.03	0.97 ± 0.01
GC0117	185.984665	18.196972	22.727 ± 0.012	1.13 ± 0.03	0.62 ± 0.02
GC0118	185.986710	18.126427	20.221 ± 0.002	0.86 ± 0.01	0.61 ± 0.00
GC0119	185.987503	18.313053	21.352 ± 0.004	1.71 ± 0.02	1.16 ± 0.01
GC0120	185.988266	17.818172	23.319 ± 0.020	1.41 ± 0.07	0.73 ± 0.03
GC0121	185.988693	18.554302	23.159 ± 0.017	0.92 ± 0.04	0.57 ± 0.03
GC0122	185.990311	18.463865	20.885 ± 0.003	0.99 ± 0.01	0.67 ± 0.00
GC0123	185.991302	18.246317	23.272 ± 0.018	1.09 ± 0.05	0.58 ± 0.03
GC0124	185.993088	18.278391	21.576 ± 0.005	1.44 ± 0.02	0.90 ± 0.01
GC0125	185.994247	18.551008	21.180 ± 0.004	1.61 ± 0.01	1.10 ± 0.00
GC0126	185.995331	18.194185	22.563 ± 0.010	1.83 ± 0.05	1.24 ± 0.01
GC0127	185.998154	17.811069	21.697 ± 0.006	1.48 ± 0.02	0.98 ± 0.01
GC0128	186.000320	18.420012	22.087 ± 0.007	1.42 ± 0.03	0.81 ± 0.01
GC0129	186.000931	18.425795	22.935 ± 0.014	0.97 ± 0.04	0.67 ± 0.02
GC0130	186.001282	17.639526	21.199 ± 0.004	1.03 ± 0.01	0.63 ± 0.01
GC0131	186.002411	18.246710	20.571 ± 0.003	1.21 ± 0.01	0.84 ± 0.00
GC0132	186.002823	18.563046	22.262 ± 0.009	1.06 ± 0.02	0.63 ± 0.01
GC0133	186.003647	18.525599	23.229 ± 0.018	1.92 ± 0.10	1.17 ± 0.02
GC0134	186.003983	18.221037	22.969 ± 0.014	1.61 ± 0.06	0.91 ± 0.02
GC0135	186.004410	17.984024	21.886 ± 0.006	0.93 ± 0.02	0.69 ± 0.01
GC0136	186.006088	17.872534	21.375 ± 0.004	1.19 ± 0.01	0.80 ± 0.01
GC0137	186.006241	17.900064	21.877 ± 0.006	0.89 ± 0.02	0.63 ± 0.01
GC0138	186.009033	18.206093	22.684 ± 0.011	1.03 ± 0.03	0.64 ± 0.02
GC0139	186.009399	18.271673	21.584 ± 0.005	0.97 ± 0.01	0.65 ± 0.01
GC0140	186.009750	17.921347	23.244 ± 0.018	1.32 ± 0.06	0.76 ± 0.03
GC0141	186.010605	18.351515	22.158 ± 0.008	1.11 ± 0.02	0.56 ± 0.01
GC0142	186.011261	18.317654	22.253 ± 0.008	1.02 ± 0.02	0.65 ± 0.01
GC0143	186.012085	17.912752	22.252 ± 0.008	1.09 ± 0.02	0.69 ± 0.01
GC0144	186.012360	18.421366	21.738 ± 0.006	1.38 ± 0.02	0.81 ± 0.01
GC0145	186.013489	17.908564	23.560 ± 0.024	1.01 ± 0.06	0.64 ± 0.04
GC0146	186.013763	18.278435	22.615 ± 0.011	1.17 ± 0.03	0.71 ± 0.01
GC0147	186.015060	17.789726	20.378 ± 0.002	0.83 ± 0.01	0.61 ± 0.00
GC0148	186.015305	17.601789	21.447 ± 0.005	1.10 ± 0.01	0.66 ± 0.01
GC0149	186.015854	17.821278	23.159 ± 0.017	0.84 ± 0.04	0.65 ± 0.03
GC0150	186.016449	18.229490	23.121 ± 0.016	1.37 ± 0.06	0.72 ± 0.02
GC0151	186.017563	18.065157	21.180 ± 0.004	1.72 ± 0.02	1.10 ± 0.00
GC0152	186.017761	17.851498	22.667 ± 0.012	1.59 ± 0.05	0.88 ± 0.02
GC0153	186.020142	17.900862	22.265 ± 0.008	0.84 ± 0.02	0.58 ± 0.01
GC0154	186.021545	18.173914	21.706 ± 0.006	1.22 ± 0.02	0.75 ± 0.01
GC0155	186.023117	18.036995	21.808 ± 0.006	1.16 ± 0.02	0.65 ± 0.01
GC0156	186.026459	18.352169	23.484 ± 0.023	0.83 ± 0.05	0.60 ± 0.04
GC0157	186.031326	17.630072	23.449 ± 0.022	0.92 ± 0.06	0.60 ± 0.03
GC0158	186.031403	18.427853	20.193 ± 0.002	1.36 ± 0.01	0.94 ± 0.00
GC0159	186.032669	17.701750	23.440 ± 0.022	1.35 ± 0.08	0.69 ± 0.03
GC0160	186.033127	18.307018	22.104 ± 0.007	1.31 ± 0.02	0.74 ± 0.01

Table A.1: (cont'd)

ID	α (J2000) (deg)	δ (J2000) (deg)	g (mag)	$u-g$ (mag)	$g-i$ (mag)
GC0161	186.033173	17.857195	20.795 ± 0.003	1.25 ± 0.01	0.79 ± 0.00
GC0162	186.033218	18.514971	23.238 ± 0.018	1.38 ± 0.06	0.78 ± 0.02
GC0163	186.033936	18.030806	22.607 ± 0.011	1.03 ± 0.03	0.66 ± 0.02
GC0164	186.034866	18.100954	23.474 ± 0.022	0.90 ± 0.06	0.56 ± 0.03
GC0165	186.035034	17.732637	22.822 ± 0.013	1.11 ± 0.04	0.71 ± 0.02
GC0166	186.037079	18.382946	22.691 ± 0.012	1.45 ± 0.04	0.81 ± 0.02
GC0167	186.037277	18.243841	20.624 ± 0.003	1.64 ± 0.01	1.01 ± 0.00
GC0168	186.037827	18.530136	23.165 ± 0.017	1.26 ± 0.05	0.70 ± 0.02
GC0169	186.038834	17.707664	23.526 ± 0.023	1.68 ± 0.11	0.90 ± 0.03
GC0170	186.040359	18.410135	22.249 ± 0.008	0.93 ± 0.02	0.62 ± 0.01
GC0171	186.040955	18.078585	21.444 ± 0.005	1.03 ± 0.01	0.75 ± 0.01
GC0172	186.041458	17.740894	23.132 ± 0.017	1.50 ± 0.07	0.85 ± 0.02
GC0173	186.043533	17.766817	23.499 ± 0.023	1.02 ± 0.06	0.71 ± 0.03
GC0174	186.043716	18.500673	22.798 ± 0.013	1.39 ± 0.04	0.75 ± 0.02
GC0175	186.044540	18.547138	22.472 ± 0.010	1.76 ± 0.05	1.18 ± 0.01
GC0176	186.045654	18.161198	22.680 ± 0.011	1.25 ± 0.04	0.92 ± 0.01
GC0177	186.046692	17.651157	22.489 ± 0.010	1.17 ± 0.03	0.60 ± 0.01
GC0178	186.047256	17.723751	23.044 ± 0.015	1.22 ± 0.05	0.89 ± 0.02
GC0179	186.047760	18.124247	21.013 ± 0.004	0.99 ± 0.01	0.71 ± 0.00
GC0180	186.047775	18.382896	22.388 ± 0.009	1.16 ± 0.03	0.66 ± 0.01
GC0181	186.051819	18.176947	23.117 ± 0.016	1.41 ± 0.06	1.01 ± 0.02
GC0182	186.053436	17.933474	22.447 ± 0.009	1.23 ± 0.03	0.77 ± 0.01
GC0183	186.055573	17.599510	20.297 ± 0.002	0.90 ± 0.01	0.69 ± 0.00
GC0184	186.055710	18.226814	22.329 ± 0.009	0.87 ± 0.02	0.69 ± 0.01
GC0185	186.055908	18.271410	23.354 ± 0.020	1.04 ± 0.06	0.67 ± 0.03
GC0186	186.056702	18.358818	23.146 ± 0.017	1.22 ± 0.05	0.80 ± 0.02
GC0187	186.057144	18.239655	23.587 ± 0.025	1.12 ± 0.07	0.66 ± 0.04
GC0188	186.063889	17.951944	23.174 ± 0.021	1.06 ± 0.05	0.55 ± 0.03
GC0189	186.067841	17.609518	22.553 ± 0.012	1.01 ± 0.03	0.83 ± 0.02
GC0190	186.068970	18.313255	23.045 ± 0.015	1.56 ± 0.06	0.95 ± 0.02
GC0191	186.069702	17.660740	23.293 ± 0.020	1.09 ± 0.05	0.66 ± 0.03
GC0192	186.069901	17.937668	23.579 ± 0.024	1.71 ± 0.11	1.10 ± 0.03
GC0193	186.070709	18.492115	22.317 ± 0.009	1.40 ± 0.03	0.81 ± 0.01
GC0194	186.071060	18.021452	23.539 ± 0.023	1.27 ± 0.07	0.73 ± 0.03
GC0195	186.071503	18.182728	22.756 ± 0.012	1.04 ± 0.03	0.75 ± 0.02
GC0196	186.071915	18.196117	21.199 ± 0.004	1.15 ± 0.01	0.84 ± 0.00
GC0197	186.072189	18.234346	21.931 ± 0.007	1.10 ± 0.02	0.63 ± 0.01
GC0198	186.074783	18.582335	22.502 ± 0.010	1.17 ± 0.03	0.68 ± 0.02
GC0199	186.075302	17.741085	21.676 ± 0.005	1.13 ± 0.02	0.71 ± 0.01
GC0200	186.076691	18.590168	20.888 ± 0.005	1.21 ± 0.01	1.00 ± 0.01
GC0201	186.076797	18.105156	22.824 ± 0.013	1.08 ± 0.03	0.70 ± 0.02
GC0202	186.077881	18.217253	21.881 ± 0.006	0.92 ± 0.02	0.59 ± 0.01
GC0203	186.080414	17.601734	20.740 ± 0.003	0.99 ± 0.01	0.64 ± 0.00
GC0204	186.081299	17.709890	21.073 ± 0.004	0.88 ± 0.01	0.58 ± 0.00
GC0205	186.081848	17.851328	22.331 ± 0.009	1.82 ± 0.04	0.99 ± 0.01
GC0206	186.083878	18.275702	21.075 ± 0.004	1.33 ± 0.01	0.84 ± 0.00
GC0207	186.088226	18.536264	21.140 ± 0.004	1.40 ± 0.01	0.94 ± 0.00
GC0208	186.088928	17.977184	22.084 ± 0.007	1.26 ± 0.02	0.90 ± 0.01

Table A.1: (cont'd)

ID	α (J2000) (deg)	δ (J2000) (deg)	g (mag)	$u-g$ (mag)	$g-i$ (mag)
GC0209	186.090012	18.004398	23.139 ± 0.017	1.03 ± 0.04	0.66 ± 0.02
GC0210	186.090469	18.228901	23.135 ± 0.016	1.45 ± 0.06	0.94 ± 0.02
GC0211	186.090836	17.737196	20.700 ± 0.003	1.68 ± 0.01	1.04 ± 0.00
GC0212	186.091690	18.113478	22.721 ± 0.012	1.13 ± 0.03	0.78 ± 0.02
GC0213	186.094086	18.218550	21.421 ± 0.005	0.88 ± 0.01	0.62 ± 0.01
GC0214	186.095261	17.923819	21.013 ± 0.004	0.94 ± 0.01	0.66 ± 0.00
GC0215	186.095535	17.979103	20.124 ± 0.002	1.62 ± 0.01	1.00 ± 0.00
GC0216	186.095642	18.139320	21.047 ± 0.004	0.97 ± 0.01	0.73 ± 0.00
GC0217	186.096436	18.131054	21.513 ± 0.005	1.85 ± 0.02	1.11 ± 0.01
GC0218	186.099274	18.158401	23.075 ± 0.015	1.90 ± 0.08	1.18 ± 0.02
GC0219	186.100891	17.776356	21.758 ± 0.006	1.08 ± 0.02	0.69 ± 0.01
GC0220	186.101395	17.706512	23.394 ± 0.021	1.44 ± 0.08	0.95 ± 0.03
GC0221	186.101868	18.199028	22.046 ± 0.007	0.98 ± 0.02	0.57 ± 0.01
GC0222	186.103561	18.223017	21.367 ± 0.004	0.84 ± 0.01	0.58 ± 0.01
GC0223	186.103989	18.006329	22.629 ± 0.011	1.14 ± 0.03	0.72 ± 0.02
GC0224	186.104416	17.970583	21.811 ± 0.006	1.53 ± 0.02	0.90 ± 0.01
GC0225	186.104813	18.396175	23.024 ± 0.015	1.86 ± 0.07	1.19 ± 0.02
GC0226	186.105545	18.518890	20.430 ± 0.003	1.04 ± 0.01	0.68 ± 0.00
GC0227	186.106216	18.107685	22.331 ± 0.009	1.17 ± 0.02	0.83 ± 0.01
GC0228	186.107758	17.821865	23.436 ± 0.022	0.84 ± 0.05	0.73 ± 0.03
GC0229	186.108093	18.429928	21.129 ± 0.004	0.88 ± 0.01	0.59 ± 0.01
GC0230	186.108414	17.623615	23.038 ± 0.015	1.32 ± 0.05	0.93 ± 0.02
GC0231	186.108643	17.968847	23.320 ± 0.019	1.09 ± 0.05	0.57 ± 0.03
GC0232	186.111404	17.760189	20.657 ± 0.003	0.93 ± 0.01	0.65 ± 0.00
GC0233	186.111877	18.212389	22.336 ± 0.009	1.14 ± 0.02	0.71 ± 0.01
GC0234	186.112534	18.020769	21.791 ± 0.006	1.58 ± 0.02	0.93 ± 0.01
GC0235	186.112534	18.484570	21.367 ± 0.004	0.99 ± 0.01	0.60 ± 0.01
GC0236	186.113388	17.722887	21.558 ± 0.005	1.47 ± 0.02	1.20 ± 0.01
GC0237	186.113388	18.093340	23.237 ± 0.018	1.01 ± 0.05	0.55 ± 0.03
GC0238	186.114639	18.056395	22.524 ± 0.010	0.94 ± 0.03	0.66 ± 0.01
GC0239	186.115463	17.680225	22.443 ± 0.010	1.32 ± 0.03	0.84 ± 0.01
GC0240	186.116608	18.210728	20.873 ± 0.003	0.89 ± 0.01	0.63 ± 0.00
GC0241	186.117279	17.859287	23.421 ± 0.022	1.17 ± 0.06	0.59 ± 0.03
GC0242	186.117584	18.406212	22.358 ± 0.009	0.97 ± 0.02	0.65 ± 0.01
GC0243	186.118408	17.747602	23.453 ± 0.023	1.20 ± 0.07	0.69 ± 0.03
GC0244	186.122787	18.396017	23.009 ± 0.015	1.75 ± 0.07	1.07 ± 0.02
GC0245	186.123245	18.116182	23.154 ± 0.016	1.04 ± 0.04	0.71 ± 0.02
GC0246	186.124207	17.802868	22.814 ± 0.013	1.15 ± 0.04	0.87 ± 0.02
GC0247	186.125015	18.084370	21.119 ± 0.004	1.20 ± 0.01	0.83 ± 0.01
GC0248	186.125870	18.046839	21.124 ± 0.004	1.16 ± 0.01	0.75 ± 0.00
GC0249	186.125931	18.220694	22.484 ± 0.010	1.02 ± 0.03	0.66 ± 0.01
GC0250	186.127182	17.946404	23.240 ± 0.018	0.96 ± 0.05	0.64 ± 0.03
GC0251	186.128342	18.504547	21.770 ± 0.006	1.02 ± 0.02	0.59 ± 0.01
GC0252	186.130737	18.370804	22.159 ± 0.008	1.04 ± 0.02	0.65 ± 0.01
GC0253	186.131012	17.691833	21.567 ± 0.005	1.11 ± 0.01	0.75 ± 0.01
GC0254	186.134232	18.558718	23.384 ± 0.021	1.43 ± 0.07	0.83 ± 0.03
GC0255	186.134506	18.216639	21.789 ± 0.006	1.11 ± 0.02	0.70 ± 0.01
GC0256	186.135620	18.247936	22.541 ± 0.010	0.99 ± 0.03	0.70 ± 0.01

Table A.1: (cont'd)

ID	α (J2000) (deg)	δ (J2000) (deg)	g (mag)	$u-g$ (mag)	$g-i$ (mag)
GC0257	186.137177	18.086174	23.554 ± 0.024	1.10 ± 0.08	0.68 ± 0.04
GC0258	186.137512	18.094961	21.701 ± 0.005	1.80 ± 0.02	1.17 ± 0.01
GC0259	186.137512	18.208090	21.231 ± 0.004	0.91 ± 0.01	0.58 ± 0.01
GC0260	186.137650	18.354204	21.265 ± 0.005	1.40 ± 0.01	0.86 ± 0.01
GC0261	186.137665	17.990137	20.944 ± 0.003	0.89 ± 0.01	0.62 ± 0.00
GC0262	186.138184	17.722990	22.022 ± 0.007	1.06 ± 0.02	0.70 ± 0.01
GC0263	186.139847	18.563206	23.431 ± 0.022	1.62 ± 0.09	1.01 ± 0.03
GC0264	186.139999	18.466343	22.404 ± 0.009	1.05 ± 0.02	0.87 ± 0.01
GC0265	186.140671	17.720589	22.024 ± 0.007	1.69 ± 0.03	1.24 ± 0.01
GC0266	186.140884	18.565172	20.925 ± 0.003	0.96 ± 0.01	0.60 ± 0.00
GC0267	186.142609	18.472055	23.343 ± 0.020	1.66 ± 0.08	0.98 ± 0.03
GC0268	186.148163	18.035870	23.438 ± 0.021	1.49 ± 0.08	0.80 ± 0.03
GC0269	186.150421	17.727280	20.776 ± 0.003	1.41 ± 0.01	0.79 ± 0.00
GC0270	186.151199	17.750290	22.927 ± 0.014	1.56 ± 0.06	0.98 ± 0.02
GC0271	186.153976	18.049810	20.877 ± 0.003	1.06 ± 0.01	0.78 ± 0.00
GC0272	186.154953	18.120216	20.847 ± 0.003	1.30 ± 0.01	0.77 ± 0.00
GC0273	186.155930	17.640390	22.763 ± 0.012	1.06 ± 0.03	0.64 ± 0.02
GC0274	186.156662	17.725107	22.283 ± 0.009	0.96 ± 0.02	0.68 ± 0.01
GC0275	186.160629	18.142023	23.536 ± 0.023	1.12 ± 0.06	0.74 ± 0.03
GC0276	186.160706	17.940697	21.991 ± 0.007	1.01 ± 0.02	0.61 ± 0.01
GC0277	186.163834	17.623285	23.043 ± 0.015	1.56 ± 0.06	0.95 ± 0.02
GC0278	186.163986	18.520267	22.618 ± 0.011	1.80 ± 0.05	1.01 ± 0.01
GC0279	186.164017	18.124855	23.405 ± 0.020	1.15 ± 0.06	0.85 ± 0.03
GC0280	186.164688	18.549360	22.874 ± 0.014	1.05 ± 0.04	0.58 ± 0.02
GC0281	186.166245	18.091394	21.655 ± 0.005	1.19 ± 0.02	0.63 ± 0.01
GC0282	186.167053	18.248693	23.002 ± 0.014	0.97 ± 0.04	0.69 ± 0.02
GC0283	186.168518	18.125076	22.621 ± 0.011	0.97 ± 0.03	0.63 ± 0.02
GC0284	186.168869	18.325640	22.152 ± 0.008	1.28 ± 0.02	1.06 ± 0.01
GC0285	186.169861	18.450649	23.067 ± 0.016	0.84 ± 0.04	0.62 ± 0.02
GC0286	186.170303	18.153851	22.993 ± 0.014	1.48 ± 0.05	0.94 ± 0.02
GC0287	186.170456	17.721823	23.492 ± 0.023	0.94 ± 0.06	0.70 ± 0.03
GC0288	186.172226	18.085499	22.407 ± 0.010	1.13 ± 0.03	0.66 ± 0.01
GC0289	186.172913	18.118235	23.408 ± 0.021	1.10 ± 0.06	0.66 ± 0.03
GC0290	186.174347	17.719864	21.933 ± 0.007	1.20 ± 0.02	0.60 ± 0.01
GC0291	186.177719	18.154879	22.654 ± 0.014	1.26 ± 0.05	0.68 ± 0.02
GC0292	186.179977	18.580851	21.236 ± 0.005	0.88 ± 0.01	0.57 ± 0.01
GC0293	186.181076	18.331556	20.361 ± 0.003	0.88 ± 0.01	0.82 ± 0.00
GC0294	186.181442	18.052681	22.308 ± 0.009	1.22 ± 0.03	0.78 ± 0.01
GC0295	186.183411	17.917240	20.123 ± 0.002	1.28 ± 0.01	0.82 ± 0.00
GC0296	186.184555	17.670424	23.300 ± 0.020	1.18 ± 0.06	0.74 ± 0.03
GC0297	186.188278	17.695885	22.762 ± 0.012	1.23 ± 0.04	0.80 ± 0.02
GC0298	186.188919	17.873171	21.085 ± 0.004	1.02 ± 0.01	0.63 ± 0.00
GC0299	186.188965	18.187378	22.500 ± 0.010	1.02 ± 0.03	0.72 ± 0.01
GC0300	186.189880	18.038763	23.241 ± 0.018	0.98 ± 0.05	0.62 ± 0.03
GC0301	186.190948	18.135885	21.959 ± 0.007	0.94 ± 0.02	0.72 ± 0.01
GC0302	186.191223	18.477064	23.548 ± 0.024	1.54 ± 0.09	0.96 ± 0.03
GC0303	186.191452	18.182806	20.642 ± 0.003	1.10 ± 0.01	0.70 ± 0.00
GC0304	186.191498	18.300648	21.491 ± 0.005	1.04 ± 0.01	0.63 ± 0.01

Table A.1: (cont'd)

ID	α (J2000) (deg)	δ (J2000) (deg)	g (mag)	$u-g$ (mag)	$g-i$ (mag)
GC0305	186.193054	18.219391	23.089 ± 0.016	1.02 ± 0.04	0.65 ± 0.02
GC0306	186.193115	18.581020	23.109 ± 0.016	1.61 ± 0.07	1.08 ± 0.02
GC0307	186.193192	18.191574	23.128 ± 0.017	1.15 ± 0.05	0.72 ± 0.02
GC0308	186.193329	18.186749	23.175 ± 0.017	0.95 ± 0.05	0.71 ± 0.02
GC0309	186.194244	18.532860	21.260 ± 0.004	0.87 ± 0.01	0.57 ± 0.01
GC0310	186.194336	18.315338	22.073 ± 0.007	0.89 ± 0.02	0.58 ± 0.01
GC0311	186.195572	18.180128	22.916 ± 0.014	1.04 ± 0.04	0.69 ± 0.02
GC0312	186.195724	18.176336	23.336 ± 0.020	1.16 ± 0.06	0.85 ± 0.03
GC0313	186.197235	17.630808	22.693 ± 0.012	0.93 ± 0.03	0.63 ± 0.02
GC0314	186.197906	17.702610	22.510 ± 0.010	0.99 ± 0.03	0.70 ± 0.01
GC0315	186.198029	18.116800	22.391 ± 0.009	1.09 ± 0.03	0.82 ± 0.01
GC0316	186.198334	18.457767	22.346 ± 0.009	1.17 ± 0.03	0.63 ± 0.01
GC0317	186.201019	18.130308	22.510 ± 0.010	0.97 ± 0.03	0.63 ± 0.01
GC0318	186.201477	17.734390	23.326 ± 0.019	1.10 ± 0.06	0.66 ± 0.03
GC0319	186.201523	18.069286	23.042 ± 0.016	1.13 ± 0.05	0.69 ± 0.02
GC0320	186.202255	18.101448	23.227 ± 0.018	0.97 ± 0.05	0.66 ± 0.03
GC0321	186.202682	17.795822	22.883 ± 0.014	1.50 ± 0.05	1.02 ± 0.02
GC0322	186.204773	18.169119	23.334 ± 0.020	1.08 ± 0.06	0.70 ± 0.03
GC0323	186.204849	18.174356	20.403 ± 0.002	1.13 ± 0.01	0.80 ± 0.00
GC0324	186.205429	18.045401	21.051 ± 0.004	0.97 ± 0.01	0.59 ± 0.00
GC0325	186.205460	17.628372	21.763 ± 0.006	1.02 ± 0.02	0.61 ± 0.01
GC0326	186.207687	18.150602	21.371 ± 0.005	1.24 ± 0.01	0.69 ± 0.01
GC0327	186.207718	18.203129	23.592 ± 0.025	1.02 ± 0.07	0.75 ± 0.04
GC0328	186.208801	17.775620	21.591 ± 0.005	1.28 ± 0.02	0.90 ± 0.01
GC0329	186.209198	18.198370	23.449 ± 0.022	1.13 ± 0.07	0.78 ± 0.03
GC0330	186.210724	18.470192	22.499 ± 0.010	1.05 ± 0.03	0.64 ± 0.01
GC0331	186.210892	18.281275	22.700 ± 0.012	1.10 ± 0.03	0.67 ± 0.02
GC0332	186.212997	18.197521	23.107 ± 0.016	1.05 ± 0.05	0.59 ± 0.02
GC0333	186.213013	18.099842	22.878 ± 0.014	1.66 ± 0.06	0.96 ± 0.02
GC0334	186.213959	18.410166	21.265 ± 0.004	1.18 ± 0.01	0.73 ± 0.01
GC0335	186.214340	18.115713	23.378 ± 0.021	1.18 ± 0.06	0.73 ± 0.03
GC0336	186.215271	18.269194	23.256 ± 0.019	1.30 ± 0.06	0.83 ± 0.02
GC0337	186.217117	17.684755	21.879 ± 0.006	0.93 ± 0.02	0.70 ± 0.01
GC0338	186.217224	17.799515	22.796 ± 0.013	0.96 ± 0.03	0.61 ± 0.02
GC0339	186.219177	18.132841	23.135 ± 0.017	1.16 ± 0.05	0.83 ± 0.02
GC0340	186.219223	18.512978	23.172 ± 0.017	1.88 ± 0.09	1.22 ± 0.02
GC0341	186.219284	18.465088	21.423 ± 0.005	1.14 ± 0.01	0.63 ± 0.01
GC0342	186.219452	17.635511	21.714 ± 0.006	0.91 ± 0.01	0.61 ± 0.01
GC0343	186.219666	17.675686	20.113 ± 0.002	1.24 ± 0.01	0.78 ± 0.00
GC0344	186.221741	18.159443	23.482 ± 0.022	1.17 ± 0.07	0.88 ± 0.03
GC0345	186.221909	18.454258	20.926 ± 0.003	1.23 ± 0.01	0.85 ± 0.00
GC0346	186.221970	18.089117	20.919 ± 0.004	1.04 ± 0.01	0.77 ± 0.00
GC0347	186.222565	18.485859	23.343 ± 0.020	1.36 ± 0.07	0.78 ± 0.03
GC0348	186.223663	18.242970	22.893 ± 0.014	1.03 ± 0.04	0.74 ± 0.02
GC0349	186.223679	18.372290	23.186 ± 0.018	1.44 ± 0.06	1.00 ± 0.02
GC0350	186.224304	18.041693	23.130 ± 0.017	1.34 ± 0.06	0.69 ± 0.02
GC0351	186.224457	18.437485	23.532 ± 0.023	1.15 ± 0.07	0.86 ± 0.03
GC0352	186.224747	17.916216	22.630 ± 0.011	1.11 ± 0.03	0.64 ± 0.02

Table A.1: (cont'd)

ID	α (J2000) (deg)	δ (J2000) (deg)	g (mag)	$u-g$ (mag)	$g-i$ (mag)
GC0353	186.225449	17.897383	23.333 ± 0.020	1.23 ± 0.06	0.76 ± 0.03
GC0354	186.225586	17.621237	23.209 ± 0.018	1.03 ± 0.05	0.58 ± 0.03
GC0355	186.227066	17.983067	20.120 ± 0.002	1.15 ± 0.01	0.71 ± 0.00
GC0356	186.227310	18.108709	22.655 ± 0.011	1.25 ± 0.04	0.83 ± 0.02
GC0357	186.227310	18.155323	22.883 ± 0.014	1.79 ± 0.07	1.19 ± 0.02
GC0358	186.227539	18.076555	23.380 ± 0.021	1.08 ± 0.06	0.70 ± 0.03
GC0359	186.227646	18.224768	23.487 ± 0.023	1.11 ± 0.07	0.69 ± 0.03
GC0360	186.227783	17.882936	20.887 ± 0.003	0.98 ± 0.01	0.61 ± 0.00
GC0361	186.228363	18.214207	20.954 ± 0.003	1.54 ± 0.01	1.08 ± 0.00
GC0362	186.229828	18.166574	23.267 ± 0.019	1.33 ± 0.07	1.02 ± 0.02
GC0363	186.229996	18.420700	22.291 ± 0.009	1.25 ± 0.03	0.79 ± 0.01
GC0364	186.230270	18.225111	22.202 ± 0.008	1.43 ± 0.03	1.05 ± 0.01
GC0365	186.230576	18.546295	22.153 ± 0.008	1.66 ± 0.03	1.03 ± 0.01
GC0366	186.231339	18.290047	22.039 ± 0.007	1.01 ± 0.02	0.73 ± 0.01
GC0367	186.231461	18.326488	22.091 ± 0.008	0.83 ± 0.02	0.72 ± 0.01
GC0368	186.231705	18.073151	23.383 ± 0.021	1.10 ± 0.06	0.72 ± 0.03
GC0369	186.233246	18.007668	21.392 ± 0.005	1.14 ± 0.01	0.74 ± 0.01
GC0370	186.233261	18.055918	22.494 ± 0.010	1.56 ± 0.04	0.97 ± 0.01
GC0371	186.234634	18.041647	23.235 ± 0.018	0.98 ± 0.05	0.74 ± 0.03
GC0372	186.235565	18.464968	20.757 ± 0.003	1.10 ± 0.01	0.68 ± 0.00
GC0373	186.236725	18.132036	23.570 ± 0.024	1.18 ± 0.08	0.66 ± 0.04
GC0374	186.236923	18.098551	22.422 ± 0.009	1.08 ± 0.03	0.63 ± 0.01
GC0375	186.237625	18.151476	23.300 ± 0.019	1.16 ± 0.06	0.74 ± 0.03
GC0376	186.238403	18.025757	23.425 ± 0.021	1.05 ± 0.06	0.68 ± 0.03
GC0377	186.238846	17.927687	22.493 ± 0.010	1.13 ± 0.03	0.71 ± 0.01
GC0378	186.238922	18.129967	23.583 ± 0.024	1.14 ± 0.08	0.71 ± 0.03
GC0379	186.239029	18.384697	23.544 ± 0.024	0.91 ± 0.06	0.57 ± 0.04
GC0380	186.240265	17.952278	22.465 ± 0.010	1.00 ± 0.03	0.61 ± 0.01
GC0381	186.240936	17.920532	23.164 ± 0.017	1.73 ± 0.09	1.04 ± 0.02
GC0382	186.242859	17.813288	23.012 ± 0.015	0.88 ± 0.04	0.56 ± 0.02
GC0383	186.243073	18.541914	23.175 ± 0.017	1.65 ± 0.07	1.03 ± 0.02
GC0384	186.243317	18.147371	23.250 ± 0.019	1.31 ± 0.07	0.72 ± 0.03
GC0385	186.243805	17.919592	23.580 ± 0.024	1.55 ± 0.11	1.14 ± 0.03
GC0386	186.244064	17.781050	21.070 ± 0.004	1.64 ± 0.01	1.02 ± 0.00
GC0387	186.244156	18.019112	22.845 ± 0.013	1.04 ± 0.04	0.60 ± 0.02
GC0388	186.246567	18.094349	23.090 ± 0.016	1.07 ± 0.05	0.64 ± 0.02
GC0389	186.246796	18.212234	22.837 ± 0.013	0.93 ± 0.03	0.71 ± 0.02
GC0390	186.246964	18.129673	23.468 ± 0.022	1.21 ± 0.07	0.62 ± 0.03
GC0391	186.247070	18.086771	23.233 ± 0.020	1.28 ± 0.08	0.71 ± 0.03
GC0392	186.248291	17.902937	21.255 ± 0.004	0.96 ± 0.01	0.55 ± 0.01
GC0393	186.249176	18.477621	21.814 ± 0.006	0.95 ± 0.02	0.57 ± 0.01
GC0394	186.250504	18.082481	21.122 ± 0.004	1.17 ± 0.01	0.69 ± 0.00
GC0395	186.250534	18.369202	21.145 ± 0.004	1.32 ± 0.01	0.80 ± 0.00
GC0396	186.251358	18.211557	23.456 ± 0.022	1.23 ± 0.07	0.82 ± 0.03
GC0397	186.251556	18.164345	22.374 ± 0.009	1.26 ± 0.03	0.90 ± 0.01
GC0398	186.251587	17.799530	21.629 ± 0.005	1.81 ± 0.02	1.24 ± 0.01
GC0399	186.251923	17.722717	22.942 ± 0.014	1.10 ± 0.04	0.55 ± 0.02
GC0400	186.253052	17.712444	21.908 ± 0.007	1.00 ± 0.02	0.61 ± 0.01

Table A.1: (cont'd)

ID	α (J2000) (deg)	δ (J2000) (deg)	g (mag)	$u-g$ (mag)	$g-i$ (mag)
GC0401	186.253555	18.094990	22.289 ± 0.009	1.21 ± 0.03	0.79 ± 0.01
GC0402	186.253967	17.691429	20.309 ± 0.002	1.40 ± 0.01	0.98 ± 0.00
GC0403	186.254181	18.264185	23.054 ± 0.016	1.08 ± 0.05	0.74 ± 0.02
GC0404	186.254257	18.157011	21.643 ± 0.005	1.13 ± 0.02	0.83 ± 0.01
GC0405	186.254578	18.286182	23.534 ± 0.023	1.11 ± 0.07	0.56 ± 0.04
GC0406	186.257645	18.230148	23.587 ± 0.025	0.98 ± 0.07	0.74 ± 0.03
GC0407	186.257950	17.894594	22.819 ± 0.013	1.24 ± 0.04	0.76 ± 0.02
GC0408	186.258118	18.137899	20.608 ± 0.003	1.76 ± 0.01	1.14 ± 0.00
GC0409	186.258865	17.973232	23.577 ± 0.024	1.35 ± 0.09	0.72 ± 0.03
GC0410	186.259644	18.256388	22.430 ± 0.009	1.57 ± 0.04	1.05 ± 0.01
GC0411	186.260651	18.185684	22.935 ± 0.014	0.92 ± 0.04	0.63 ± 0.02
GC0412	186.261017	18.311522	23.157 ± 0.017	1.67 ± 0.08	1.10 ± 0.02
GC0413	186.261108	18.169905	22.306 ± 0.009	1.01 ± 0.02	0.71 ± 0.01
GC0414	186.261658	18.096773	23.067 ± 0.016	1.06 ± 0.05	0.62 ± 0.02
GC0415	186.261703	18.129946	22.940 ± 0.014	1.90 ± 0.08	1.10 ± 0.02
GC0416	186.261887	18.168114	22.758 ± 0.012	1.22 ± 0.04	0.78 ± 0.02
GC0417	186.262543	18.191803	22.838 ± 0.013	1.43 ± 0.05	1.05 ± 0.02
GC0418	186.264511	17.812170	22.547 ± 0.010	1.35 ± 0.03	0.87 ± 0.01
GC0419	186.265076	17.987562	22.596 ± 0.011	1.61 ± 0.05	0.93 ± 0.01
GC0420	186.265503	17.766890	21.899 ± 0.006	1.48 ± 0.02	0.97 ± 0.01
GC0421	186.266205	18.228365	22.213 ± 0.008	1.26 ± 0.03	0.92 ± 0.01
GC0422	186.266556	18.097090	23.174 ± 0.017	1.22 ± 0.06	0.96 ± 0.02
GC0423	186.267166	18.127392	22.476 ± 0.010	0.98 ± 0.03	0.70 ± 0.01
GC0424	186.267181	18.188093	21.559 ± 0.005	0.95 ± 0.01	0.70 ± 0.01
GC0425	186.267487	18.203516	22.647 ± 0.011	1.34 ± 0.04	0.97 ± 0.01
GC0426	186.267578	18.186394	21.337 ± 0.004	0.98 ± 0.01	0.75 ± 0.01
GC0427	186.268814	18.136595	22.873 ± 0.014	0.86 ± 0.03	0.58 ± 0.02
GC0428	186.269165	17.815039	23.582 ± 0.024	1.28 ± 0.08	0.78 ± 0.03
GC0429	186.269745	18.481710	23.135 ± 0.017	1.51 ± 0.06	0.86 ± 0.02
GC0430	186.270096	18.260567	23.260 ± 0.019	1.00 ± 0.05	0.74 ± 0.03
GC0431	186.270294	17.949614	23.506 ± 0.023	0.89 ± 0.06	0.55 ± 0.03
GC0432	186.270508	17.828228	22.455 ± 0.016	1.07 ± 0.04	0.92 ± 0.02
GC0433	186.270737	17.584892	23.500 ± 0.040	1.25 ± 0.13	0.65 ± 0.05
GC0434	186.270859	17.821850	22.556 ± 0.011	1.59 ± 0.04	1.00 ± 0.01
GC0435	186.270859	18.197256	23.518 ± 0.023	1.08 ± 0.07	0.61 ± 0.03
GC0436	186.271057	18.566973	21.919 ± 0.007	1.21 ± 0.02	0.83 ± 0.01
GC0437	186.271133	18.173223	22.947 ± 0.014	1.08 ± 0.04	0.59 ± 0.02
GC0438	186.271362	18.164711	23.470 ± 0.022	1.21 ± 0.07	0.72 ± 0.03
GC0439	186.272034	17.972349	23.221 ± 0.018	1.53 ± 0.08	0.97 ± 0.02
GC0440	186.272766	18.164988	22.463 ± 0.010	1.50 ± 0.04	1.01 ± 0.01
GC0441	186.275620	17.611372	21.418 ± 0.005	1.10 ± 0.01	0.71 ± 0.01
GC0442	186.275726	18.179281	20.848 ± 0.003	1.32 ± 0.01	0.99 ± 0.00
GC0443	186.275894	17.740608	21.665 ± 0.005	1.35 ± 0.02	0.96 ± 0.01
GC0444	186.276505	18.562443	22.311 ± 0.009	1.22 ± 0.03	0.76 ± 0.01
GC0445	186.277588	18.129929	22.801 ± 0.013	1.03 ± 0.04	0.71 ± 0.02
GC0446	186.277649	18.154390	22.982 ± 0.015	1.02 ± 0.04	0.68 ± 0.02
GC0447	186.278412	18.432827	22.497 ± 0.010	1.21 ± 0.03	0.70 ± 0.01
GC0448	186.278961	18.049803	21.728 ± 0.006	1.15 ± 0.02	0.75 ± 0.01

Table A.1: (cont'd)

ID	α (J2000) (deg)	δ (J2000) (deg)	g (mag)	$u-g$ (mag)	$g-i$ (mag)
GC0449	186.280380	18.109083	23.356 ± 0.020	1.17 ± 0.06	0.65 ± 0.03
GC0450	186.280441	17.975746	20.970 ± 0.004	1.39 ± 0.01	0.83 ± 0.00
GC0451	186.280869	17.881035	22.167 ± 0.008	1.43 ± 0.03	0.92 ± 0.01
GC0452	186.281006	18.514906	23.158 ± 0.017	1.84 ± 0.08	1.00 ± 0.02
GC0453	186.281525	18.280136	22.396 ± 0.009	0.93 ± 0.02	0.60 ± 0.01
GC0454	186.281693	18.171696	22.006 ± 0.007	0.89 ± 0.02	0.59 ± 0.01
GC0455	186.281769	18.262348	22.107 ± 0.007	0.85 ± 0.02	0.55 ± 0.01
GC0456	186.283142	17.999973	23.029 ± 0.015	1.02 ± 0.04	0.58 ± 0.02
GC0457	186.283691	18.046427	23.482 ± 0.023	0.96 ± 0.06	0.58 ± 0.03
GC0458	186.283875	18.448830	20.701 ± 0.003	0.97 ± 0.01	0.64 ± 0.00
GC0459	186.284042	18.127207	21.664 ± 0.005	1.11 ± 0.02	0.76 ± 0.01
GC0460	186.284927	18.355280	23.393 ± 0.021	1.16 ± 0.06	0.69 ± 0.03
GC0461	186.284973	18.177767	22.524 ± 0.010	0.88 ± 0.03	0.67 ± 0.01
GC0462	186.285995	17.964558	22.664 ± 0.012	0.90 ± 0.03	0.62 ± 0.02
GC0463	186.286331	18.156071	20.821 ± 0.003	1.01 ± 0.01	0.73 ± 0.00
GC0464	186.286819	18.201422	23.403 ± 0.021	1.06 ± 0.06	0.63 ± 0.03
GC0465	186.287354	17.964912	22.579 ± 0.011	1.17 ± 0.03	0.98 ± 0.01
GC0466	186.287399	17.916517	22.579 ± 0.011	1.01 ± 0.03	0.66 ± 0.01
GC0467	186.288422	18.138565	21.884 ± 0.007	1.12 ± 0.02	0.64 ± 0.01
GC0468	186.288757	18.237013	23.338 ± 0.021	1.15 ± 0.06	0.61 ± 0.03
GC0469	186.288834	18.148577	21.362 ± 0.004	1.31 ± 0.01	0.75 ± 0.01
GC0470	186.288986	18.171019	22.934 ± 0.015	1.74 ± 0.07	0.94 ± 0.02
GC0471	186.289078	18.191790	22.477 ± 0.010	1.69 ± 0.05	1.05 ± 0.01
GC0472	186.289780	18.120611	21.719 ± 0.006	1.26 ± 0.02	0.73 ± 0.01
GC0473	186.292465	18.358299	23.120 ± 0.020	0.84 ± 0.05	0.81 ± 0.03
GC0474	186.294037	17.928774	21.748 ± 0.007	1.06 ± 0.02	0.73 ± 0.01
GC0475	186.294342	18.191433	23.585 ± 0.031	1.15 ± 0.09	0.81 ± 0.04
GC0476	186.294495	18.213915	23.219 ± 0.022	0.89 ± 0.05	0.68 ± 0.03
GC0477	186.294846	17.959843	22.998 ± 0.018	0.85 ± 0.04	0.60 ± 0.03
GC0478	186.294846	18.383482	22.647 ± 0.013	1.77 ± 0.06	1.16 ± 0.02
GC0479	186.294983	18.122747	21.676 ± 0.006	1.12 ± 0.02	0.81 ± 0.01
GC0480	186.295212	18.106997	21.854 ± 0.007	0.99 ± 0.02	0.62 ± 0.01
GC0481	186.295792	18.102346	23.552 ± 0.030	1.03 ± 0.08	0.70 ± 0.04
GC0482	186.295990	18.267624	20.460 ± 0.003	0.97 ± 0.01	0.63 ± 0.00
GC0483	186.296204	18.209558	23.564 ± 0.031	1.10 ± 0.08	0.99 ± 0.04
GC0484	186.296478	18.210873	20.857 ± 0.004	0.85 ± 0.01	0.61 ± 0.00
GC0485	186.296570	17.967035	23.314 ± 0.024	1.52 ± 0.10	1.00 ± 0.03
GC0486	186.296951	18.153208	22.180 ± 0.008	0.85 ± 0.02	0.72 ± 0.01
GC0487	186.296997	18.125923	22.941 ± 0.015	1.20 ± 0.05	0.84 ± 0.02
GC0488	186.297302	18.387188	23.144 ± 0.017	1.12 ± 0.05	0.75 ± 0.03
GC0489	186.298294	18.073446	23.184 ± 0.018	1.00 ± 0.05	0.76 ± 0.03
GC0490	186.298584	18.155226	22.884 ± 0.015	1.19 ± 0.04	0.90 ± 0.02
GC0491	186.298660	18.225899	22.721 ± 0.013	1.35 ± 0.04	1.00 ± 0.02
GC0492	186.299561	17.620918	20.689 ± 0.003	1.02 ± 0.01	0.67 ± 0.00
GC0493	186.299591	18.157404	22.399 ± 0.010	1.00 ± 0.02	0.71 ± 0.01
GC0494	186.299759	17.863098	21.567 ± 0.005	0.83 ± 0.01	0.59 ± 0.01
GC0495	186.299973	18.142979	23.440 ± 0.023	1.33 ± 0.07	0.99 ± 0.03
GC0496	186.300186	18.313124	21.398 ± 0.005	0.90 ± 0.01	0.60 ± 0.01

Table A.1: (cont'd)

ID	α (J2000) (deg)	δ (J2000) (deg)	g (mag)	$u-g$ (mag)	$g-i$ (mag)
GC0497	186.300217	18.158819	23.498 ± 0.024	1.10 ± 0.06	0.73 ± 0.03
GC0498	186.300735	18.148701	23.352 ± 0.021	1.27 ± 0.06	0.85 ± 0.03
GC0499	186.301056	18.279520	22.306 ± 0.009	1.21 ± 0.03	0.76 ± 0.01
GC0500	186.301086	17.982721	22.493 ± 0.010	1.08 ± 0.03	0.64 ± 0.01
GC0501	186.301697	18.240011	22.258 ± 0.009	0.94 ± 0.02	0.72 ± 0.01
GC0502	186.302460	18.149967	23.396 ± 0.022	1.10 ± 0.06	0.60 ± 0.03
GC0503	186.302460	18.158230	22.836 ± 0.014	0.93 ± 0.03	0.63 ± 0.02
GC0504	186.302551	18.184599	20.435 ± 0.002	1.52 ± 0.01	1.03 ± 0.00
GC0505	186.303650	17.856285	20.939 ± 0.003	1.05 ± 0.01	0.75 ± 0.00
GC0506	186.304199	18.171179	21.956 ± 0.007	1.24 ± 0.02	0.86 ± 0.01
GC0507	186.304291	18.360704	21.523 ± 0.005	0.92 ± 0.01	0.57 ± 0.01
GC0508	186.304550	18.175583	22.972 ± 0.015	1.36 ± 0.05	0.86 ± 0.02
GC0509	186.304825	18.235582	21.359 ± 0.004	1.18 ± 0.01	0.87 ± 0.01
GC0510	186.305008	18.277096	23.582 ± 0.026	1.38 ± 0.09	0.87 ± 0.03
GC0511	186.305099	17.751259	22.576 ± 0.011	1.06 ± 0.03	0.75 ± 0.01
GC0512	186.305756	18.160341	22.087 ± 0.008	1.69 ± 0.03	1.04 ± 0.01
GC0513	186.305893	18.194708	23.176 ± 0.018	1.56 ± 0.07	1.02 ± 0.02
GC0514	186.305954	18.216736	22.424 ± 0.010	0.97 ± 0.02	0.64 ± 0.01
GC0515	186.307175	18.035717	23.499 ± 0.023	1.76 ± 0.12	1.01 ± 0.03
GC0516	186.307343	18.145058	23.402 ± 0.022	1.65 ± 0.09	1.13 ± 0.03
GC0517	186.307632	18.206402	22.198 ± 0.008	1.11 ± 0.02	0.79 ± 0.01
GC0518	186.307678	18.187901	22.924 ± 0.015	0.93 ± 0.04	0.59 ± 0.02
GC0519	186.308411	18.526564	23.168 ± 0.017	1.26 ± 0.05	0.72 ± 0.02
GC0520	186.310196	18.199703	23.038 ± 0.016	0.98 ± 0.04	0.62 ± 0.02
GC0521	186.310684	18.008722	23.264 ± 0.019	1.37 ± 0.07	0.82 ± 0.03
GC0522	186.311142	18.141041	23.597 ± 0.026	1.04 ± 0.07	0.71 ± 0.04
GC0523	186.311371	17.989689	21.571 ± 0.005	1.04 ± 0.01	0.71 ± 0.01
GC0524	186.311493	18.034088	22.977 ± 0.015	1.40 ± 0.06	0.77 ± 0.02
GC0525	186.311493	18.174776	22.720 ± 0.013	1.05 ± 0.03	0.73 ± 0.02
GC0526	186.311707	18.200094	23.267 ± 0.020	1.21 ± 0.06	0.80 ± 0.03
GC0527	186.312393	18.149954	22.638 ± 0.012	1.39 ± 0.04	0.90 ± 0.01
GC0528	186.312546	18.113943	22.721 ± 0.013	1.14 ± 0.03	0.73 ± 0.02
GC0529	186.312653	18.019138	22.769 ± 0.013	1.30 ± 0.04	0.96 ± 0.02
GC0530	186.313156	18.467438	21.757 ± 0.006	1.30 ± 0.02	0.79 ± 0.01
GC0531	186.313217	18.180035	23.176 ± 0.018	1.33 ± 0.06	0.73 ± 0.02
GC0532	186.313965	18.530319	20.795 ± 0.003	0.87 ± 0.01	0.60 ± 0.00
GC0533	186.314041	18.085363	23.189 ± 0.018	1.25 ± 0.06	0.78 ± 0.03
GC0534	186.314331	18.178501	23.255 ± 0.019	1.05 ± 0.05	0.70 ± 0.03
GC0535	186.314667	17.976414	21.803 ± 0.006	1.12 ± 0.02	0.59 ± 0.01
GC0536	186.315308	18.198467	23.450 ± 0.023	0.92 ± 0.05	0.61 ± 0.03
GC0537	186.315506	17.959724	23.468 ± 0.022	1.76 ± 0.11	0.96 ± 0.03
GC0538	186.315842	18.166494	22.902 ± 0.014	1.02 ± 0.04	0.69 ± 0.02
GC0539	186.315903	18.159546	23.355 ± 0.021	1.72 ± 0.09	0.99 ± 0.03
GC0540	186.315994	17.753437	23.434 ± 0.021	1.78 ± 0.11	1.22 ± 0.03
GC0541	186.318115	18.220491	22.594 ± 0.011	0.86 ± 0.03	0.71 ± 0.02
GC0542	186.318466	18.168663	23.108 ± 0.017	1.02 ± 0.04	0.59 ± 0.03
GC0543	186.318481	18.097374	22.749 ± 0.013	0.93 ± 0.03	0.64 ± 0.02
GC0544	186.318634	18.271505	22.169 ± 0.008	1.08 ± 0.02	0.76 ± 0.01

Table A.1: (cont'd)

ID	α (J2000) (deg)	δ (J2000) (deg)	g (mag)	$u-g$ (mag)	$g-i$ (mag)
GC0545	186.318680	18.104076	22.895 ± 0.014	1.05 ± 0.04	0.65 ± 0.02
GC0546	186.318878	18.189228	23.458 ± 0.023	1.42 ± 0.08	0.86 ± 0.03
GC0547	186.319565	18.194515	22.964 ± 0.015	0.89 ± 0.04	0.69 ± 0.02
GC0548	186.319885	18.146456	22.085 ± 0.008	0.98 ± 0.02	0.68 ± 0.01
GC0549	186.319916	18.448999	23.439 ± 0.022	1.07 ± 0.06	0.64 ± 0.03
GC0550	186.320190	18.189035	23.424 ± 0.022	0.88 ± 0.05	0.60 ± 0.03
GC0551	186.320251	18.200861	23.400 ± 0.022	1.20 ± 0.06	0.79 ± 0.03
GC0552	186.320389	18.160458	22.130 ± 0.008	1.10 ± 0.02	0.84 ± 0.01
GC0553	186.320740	18.448013	22.675 ± 0.011	1.09 ± 0.03	0.60 ± 0.02
GC0554	186.322052	18.176081	21.607 ± 0.005	1.04 ± 0.01	0.76 ± 0.01
GC0555	186.322067	17.863630	22.591 ± 0.011	1.00 ± 0.03	0.67 ± 0.02
GC0556	186.322495	18.173845	21.484 ± 0.005	1.09 ± 0.01	0.79 ± 0.01
GC0557	186.322723	18.176508	23.317 ± 0.020	1.59 ± 0.08	0.96 ± 0.03
GC0558	186.322906	18.198841	23.144 ± 0.018	1.57 ± 0.07	1.00 ± 0.02
GC0559	186.323151	18.173859	23.429 ± 0.023	1.22 ± 0.07	0.68 ± 0.03
GC0560	186.323273	18.178986	21.241 ± 0.004	1.39 ± 0.01	0.99 ± 0.00
GC0561	186.323608	18.211613	23.159 ± 0.018	1.11 ± 0.05	0.73 ± 0.02
GC0562	186.323776	18.172712	21.874 ± 0.007	0.86 ± 0.02	0.61 ± 0.01
GC0563	186.324371	18.233639	21.829 ± 0.006	1.31 ± 0.02	0.92 ± 0.01
GC0564	186.324570	18.173801	23.529 ± 0.024	1.09 ± 0.07	0.70 ± 0.03
GC0565	186.324646	18.138645	23.397 ± 0.022	1.05 ± 0.06	0.58 ± 0.03
GC0566	186.325577	18.168703	23.336 ± 0.021	0.97 ± 0.05	0.63 ± 0.03
GC0567	186.325653	18.200468	23.020 ± 0.016	1.34 ± 0.05	0.77 ± 0.02
GC0568	186.326447	18.170223	23.529 ± 0.024	0.91 ± 0.06	0.78 ± 0.03
GC0569	186.326752	18.193594	21.982 ± 0.007	1.08 ± 0.02	0.73 ± 0.01
GC0570	186.327103	18.238573	22.667 ± 0.012	1.05 ± 0.03	0.70 ± 0.02
GC0571	186.327148	18.212042	22.438 ± 0.010	1.04 ± 0.03	0.79 ± 0.01
GC0572	186.327271	18.185566	22.943 ± 0.015	0.90 ± 0.04	0.75 ± 0.02
GC0573	186.327332	18.231735	23.489 ± 0.024	1.32 ± 0.08	0.81 ± 0.03
GC0574	186.327454	18.207651	23.082 ± 0.017	1.42 ± 0.06	0.90 ± 0.02
GC0575	186.327682	18.169752	23.086 ± 0.017	1.22 ± 0.05	0.72 ± 0.02
GC0576	186.327881	18.143227	20.886 ± 0.003	1.21 ± 0.01	0.90 ± 0.00
GC0577	186.328461	17.871548	23.507 ± 0.023	1.03 ± 0.07	0.76 ± 0.03
GC0578	186.328949	18.221581	22.168 ± 0.008	1.01 ± 0.02	0.76 ± 0.01
GC0579	186.329468	18.159744	21.667 ± 0.006	1.29 ± 0.02	0.84 ± 0.01
GC0580	186.329514	18.182695	22.989 ± 0.015	1.04 ± 0.04	0.68 ± 0.02
GC0581	186.330353	17.954664	23.009 ± 0.015	1.36 ± 0.05	0.72 ± 0.02
GC0582	186.330460	18.186016	22.612 ± 0.011	1.14 ± 0.03	0.65 ± 0.02
GC0583	186.330582	18.096113	22.596 ± 0.011	1.12 ± 0.03	0.68 ± 0.02
GC0584	186.330872	18.094975	22.263 ± 0.009	0.90 ± 0.02	0.67 ± 0.01
GC0585	186.331268	18.208511	22.332 ± 0.009	1.37 ± 0.03	0.97 ± 0.01
GC0586	186.331787	17.675274	23.098 ± 0.016	0.97 ± 0.04	0.83 ± 0.02
GC0587	186.331802	18.199108	22.887 ± 0.014	1.00 ± 0.04	0.57 ± 0.02
GC0588	186.332077	18.252735	22.297 ± 0.009	0.96 ± 0.02	0.66 ± 0.01
GC0589	186.332092	18.199678	21.908 ± 0.007	1.03 ± 0.02	0.67 ± 0.01
GC0590	186.332474	18.147547	23.519 ± 0.024	1.40 ± 0.08	0.76 ± 0.03
GC0591	186.332672	18.551842	22.821 ± 0.013	1.12 ± 0.04	0.78 ± 0.02
GC0592	186.332748	18.223265	22.268 ± 0.009	0.97 ± 0.02	0.71 ± 0.01

Table A.1: (cont'd)

ID	α (J2000) (deg)	δ (J2000) (deg)	g (mag)	$u-g$ (mag)	$g-i$ (mag)
GC0593	186.332809	18.298668	23.502 ± 0.024	1.03 ± 0.06	0.57 ± 0.04
GC0594	186.333069	18.175032	23.484 ± 0.024	1.04 ± 0.06	0.87 ± 0.03
GC0595	186.333267	18.157808	21.922 ± 0.007	1.11 ± 0.02	0.80 ± 0.01
GC0596	186.333328	18.195673	21.525 ± 0.005	1.26 ± 0.02	0.92 ± 0.01
GC0597	186.333359	18.213547	22.194 ± 0.008	1.64 ± 0.03	1.03 ± 0.01
GC0598	186.333511	18.309078	23.312 ± 0.020	1.22 ± 0.06	0.70 ± 0.03
GC0599	186.333588	18.205744	23.181 ± 0.018	1.06 ± 0.05	0.68 ± 0.03
GC0600	186.333862	18.186453	23.499 ± 0.024	1.08 ± 0.06	0.74 ± 0.03
GC0601	186.334122	17.975805	21.679 ± 0.006	1.08 ± 0.02	0.72 ± 0.01
GC0602	186.334152	18.184526	22.835 ± 0.014	0.96 ± 0.03	0.77 ± 0.02
GC0603	186.334396	18.185143	21.930 ± 0.007	1.08 ± 0.02	0.72 ± 0.01
GC0604	186.334915	18.161758	22.566 ± 0.011	1.42 ± 0.04	0.93 ± 0.01
GC0605	186.334976	18.175808	22.486 ± 0.010	0.89 ± 0.02	0.66 ± 0.01
GC0606	186.335388	18.180281	22.169 ± 0.008	1.27 ± 0.02	0.93 ± 0.01
GC0607	186.335464	18.199610	23.149 ± 0.018	1.22 ± 0.05	0.62 ± 0.03
GC0608	186.335556	18.189352	22.325 ± 0.009	1.17 ± 0.03	0.63 ± 0.01
GC0609	186.335739	17.605860	23.296 ± 0.019	1.07 ± 0.05	0.86 ± 0.03
GC0610	186.335785	18.211061	23.068 ± 0.017	0.96 ± 0.04	0.70 ± 0.02
GC0611	186.336044	18.186487	21.872 ± 0.007	1.33 ± 0.02	0.91 ± 0.01
GC0612	186.336090	17.962748	22.488 ± 0.010	1.44 ± 0.04	0.97 ± 0.01
GC0613	186.336090	18.152025	22.702 ± 0.012	1.16 ± 0.03	0.71 ± 0.02
GC0614	186.336395	18.188139	22.124 ± 0.008	1.13 ± 0.02	0.82 ± 0.01
GC0615	186.336533	18.206522	23.046 ± 0.016	1.20 ± 0.05	1.01 ± 0.02
GC0616	186.336670	18.171236	22.580 ± 0.011	1.05 ± 0.03	0.77 ± 0.01
GC0617	186.336823	18.184296	21.833 ± 0.006	0.98 ± 0.02	0.81 ± 0.01
GC0618	186.336960	18.156870	22.470 ± 0.010	0.95 ± 0.02	0.77 ± 0.01
GC0619	186.337097	18.148678	22.504 ± 0.010	1.47 ± 0.04	0.98 ± 0.01
GC0620	186.337555	18.203434	22.221 ± 0.008	1.24 ± 0.02	0.86 ± 0.01
GC0621	186.337799	18.176037	22.546 ± 0.011	1.03 ± 0.03	0.72 ± 0.01
GC0622	186.337967	18.173931	22.505 ± 0.010	1.01 ± 0.03	0.75 ± 0.01
GC0623	186.337967	18.204639	23.338 ± 0.021	1.28 ± 0.06	0.67 ± 0.03
GC0624	186.338013	18.153765	23.149 ± 0.018	1.17 ± 0.05	0.72 ± 0.02
GC0625	186.338089	18.573561	21.679 ± 0.005	1.09 ± 0.01	0.71 ± 0.01
GC0626	186.338638	18.203276	22.781 ± 0.013	1.30 ± 0.04	0.86 ± 0.02
GC0627	186.338959	18.198118	22.643 ± 0.012	1.39 ± 0.04	0.81 ± 0.02
GC0628	186.339279	18.170761	23.004 ± 0.016	1.50 ± 0.06	0.84 ± 0.02
GC0629	186.340012	18.173067	22.971 ± 0.015	1.55 ± 0.06	1.08 ± 0.02
GC0630	186.340561	18.173994	22.472 ± 0.010	1.27 ± 0.03	0.92 ± 0.01
GC0631	186.340805	17.689392	22.045 ± 0.007	0.90 ± 0.02	0.56 ± 0.01
GC0632	186.340836	18.206772	22.905 ± 0.014	1.42 ± 0.05	0.80 ± 0.02
GC0633	186.341232	17.802233	22.476 ± 0.010	0.86 ± 0.02	0.56 ± 0.01
GC0634	186.341782	18.205120	22.587 ± 0.011	0.98 ± 0.03	0.72 ± 0.02
GC0635	186.341873	18.203438	23.110 ± 0.017	1.03 ± 0.04	0.57 ± 0.03
GC0636	186.342239	18.212379	21.799 ± 0.006	1.20 ± 0.02	0.87 ± 0.01
GC0637	186.342346	18.244028	22.926 ± 0.015	0.96 ± 0.04	0.80 ± 0.02
GC0638	186.343155	18.205261	23.426 ± 0.022	1.75 ± 0.10	1.05 ± 0.03
GC0639	186.343277	18.146862	23.362 ± 0.021	0.87 ± 0.05	0.64 ± 0.03
GC0640	186.343704	18.174572	22.367 ± 0.009	0.97 ± 0.02	0.80 ± 0.01

Table A.1: (cont'd)

ID	α (J2000) (deg)	δ (J2000) (deg)	g (mag)	$u-g$ (mag)	$g-i$ (mag)
GC0641	186.343765	18.165020	22.677 ± 0.012	1.09 ± 0.03	0.75 ± 0.02
GC0642	186.343796	18.154434	23.053 ± 0.016	1.04 ± 0.04	0.75 ± 0.02
GC0643	186.343994	17.872988	21.051 ± 0.004	0.85 ± 0.01	0.58 ± 0.00
GC0644	186.344177	18.287603	22.475 ± 0.010	0.99 ± 0.03	0.66 ± 0.01
GC0645	186.344849	18.177988	22.535 ± 0.011	1.44 ± 0.04	0.98 ± 0.01
GC0646	186.344894	18.188473	21.945 ± 0.007	1.69 ± 0.03	1.09 ± 0.01
GC0647	186.345016	18.127443	23.398 ± 0.022	0.94 ± 0.05	0.55 ± 0.03
GC0648	186.345169	18.196371	22.808 ± 0.013	0.97 ± 0.03	0.69 ± 0.02
GC0649	186.345367	18.184614	21.909 ± 0.007	1.56 ± 0.02	0.90 ± 0.01
GC0650	186.345856	18.110813	22.901 ± 0.014	0.94 ± 0.04	0.60 ± 0.02
GC0651	186.346146	18.171583	22.499 ± 0.010	1.06 ± 0.03	0.81 ± 0.01
GC0652	186.346146	18.192202	21.926 ± 0.007	1.35 ± 0.02	0.72 ± 0.01
GC0653	186.346497	18.196770	22.245 ± 0.009	1.09 ± 0.02	0.71 ± 0.01
GC0654	186.348221	18.221474	22.914 ± 0.015	1.47 ± 0.05	0.78 ± 0.02
GC0655	186.348495	18.175611	21.827 ± 0.006	1.26 ± 0.02	0.83 ± 0.01
GC0656	186.348816	18.183544	23.430 ± 0.023	1.71 ± 0.10	0.94 ± 0.03
GC0657	186.348846	18.072474	23.268 ± 0.019	1.11 ± 0.06	0.73 ± 0.03
GC0658	186.349136	18.184010	21.966 ± 0.007	1.31 ± 0.02	0.87 ± 0.01
GC0659	186.349579	18.223717	23.557 ± 0.025	1.11 ± 0.07	0.56 ± 0.04
GC0660	186.349594	18.163279	22.810 ± 0.013	1.17 ± 0.04	0.77 ± 0.02
GC0661	186.349915	18.182001	23.157 ± 0.018	1.48 ± 0.07	0.81 ± 0.02
GC0662	186.350204	18.245874	23.161 ± 0.018	1.19 ± 0.05	0.71 ± 0.02
GC0663	186.350571	18.158396	22.480 ± 0.010	1.47 ± 0.04	0.83 ± 0.01
GC0664	186.350830	18.162514	23.030 ± 0.016	1.07 ± 0.04	0.71 ± 0.02
GC0665	186.350983	18.166348	23.462 ± 0.023	1.02 ± 0.06	0.64 ± 0.03
GC0666	186.351334	18.211821	23.202 ± 0.019	1.58 ± 0.07	0.98 ± 0.02
GC0667	186.352142	18.180483	21.957 ± 0.007	1.26 ± 0.02	0.95 ± 0.01
GC0668	186.352478	18.199026	20.431 ± 0.002	1.29 ± 0.01	0.90 ± 0.00
GC0669	186.353287	18.185965	22.626 ± 0.012	1.62 ± 0.05	1.05 ± 0.01
GC0670	186.353607	18.184656	23.305 ± 0.020	1.11 ± 0.06	0.87 ± 0.03
GC0671	186.353745	18.183407	22.608 ± 0.011	1.13 ± 0.03	0.68 ± 0.02
GC0672	186.353775	18.132654	22.538 ± 0.011	1.48 ± 0.04	0.97 ± 0.01
GC0673	186.353867	18.201429	21.932 ± 0.007	1.03 ± 0.02	0.84 ± 0.01
GC0674	186.353912	18.177019	22.542 ± 0.011	1.23 ± 0.03	0.92 ± 0.01
GC0675	186.354156	18.128738	23.521 ± 0.024	1.04 ± 0.06	0.70 ± 0.03
GC0676	186.354156	18.182451	21.552 ± 0.005	1.43 ± 0.02	0.95 ± 0.01
GC0677	186.354218	18.239136	22.710 ± 0.012	0.92 ± 0.03	0.68 ± 0.02
GC0678	186.354843	18.114815	23.379 ± 0.022	1.10 ± 0.06	0.82 ± 0.03
GC0679	186.355606	18.174520	23.580 ± 0.026	1.69 ± 0.11	1.06 ± 0.03
GC0680	186.355637	18.192793	21.918 ± 0.007	1.33 ± 0.02	0.88 ± 0.01
GC0681	186.356293	18.157513	23.137 ± 0.018	1.10 ± 0.05	0.79 ± 0.02
GC0682	186.356308	18.172222	21.462 ± 0.005	1.00 ± 0.01	0.77 ± 0.01
GC0683	186.356308	18.222734	23.143 ± 0.018	0.89 ± 0.04	0.72 ± 0.02
GC0684	186.356598	18.201838	22.967 ± 0.015	0.99 ± 0.04	0.62 ± 0.02
GC0685	186.356750	18.238337	23.163 ± 0.018	1.07 ± 0.05	0.73 ± 0.02
GC0686	186.357178	18.186234	22.858 ± 0.014	1.10 ± 0.04	0.57 ± 0.02
GC0687	186.357529	18.154406	22.346 ± 0.009	1.12 ± 0.03	0.73 ± 0.01
GC0688	186.357529	18.158842	21.705 ± 0.006	0.99 ± 0.01	0.72 ± 0.01

Table A.1: (cont'd)

ID	α (J2000) (deg)	δ (J2000) (deg)	g (mag)	$u-g$ (mag)	$g-i$ (mag)
GC0689	186.357773	18.218245	22.155 ± 0.008	0.93 ± 0.02	0.71 ± 0.01
GC0690	186.357773	18.227306	23.261 ± 0.020	0.88 ± 0.05	0.62 ± 0.03
GC0691	186.358353	17.949957	23.523 ± 0.023	1.00 ± 0.06	0.70 ± 0.03
GC0692	186.358704	18.220577	23.309 ± 0.020	1.14 ± 0.06	0.72 ± 0.03
GC0693	186.358765	18.296740	23.572 ± 0.025	1.11 ± 0.07	0.63 ± 0.04
GC0694	186.358810	17.942966	21.959 ± 0.007	1.51 ± 0.03	0.99 ± 0.01
GC0695	186.358932	18.206938	23.467 ± 0.023	1.34 ± 0.08	0.78 ± 0.03
GC0696	186.358978	18.192762	22.424 ± 0.010	1.30 ± 0.03	0.69 ± 0.01
GC0697	186.359116	18.111214	22.171 ± 0.008	0.94 ± 0.02	0.64 ± 0.01
GC0698	186.359421	18.199125	22.806 ± 0.013	1.12 ± 0.04	0.87 ± 0.02
GC0699	186.359467	17.971296	21.919 ± 0.007	1.89 ± 0.03	1.14 ± 0.01
GC0700	186.359482	17.951792	21.692 ± 0.006	1.18 ± 0.02	0.67 ± 0.01
GC0701	186.359619	18.180607	23.095 ± 0.017	1.28 ± 0.05	0.90 ± 0.02
GC0702	186.359756	18.230375	23.427 ± 0.022	1.42 ± 0.08	0.89 ± 0.03
GC0703	186.359879	18.212259	21.324 ± 0.004	1.21 ± 0.01	0.94 ± 0.01
GC0704	186.359909	18.190884	23.104 ± 0.017	1.32 ± 0.05	0.98 ± 0.02
GC0705	186.359909	18.197384	22.831 ± 0.014	0.85 ± 0.03	0.75 ± 0.02
GC0706	186.360107	18.052252	21.112 ± 0.004	1.40 ± 0.01	1.05 ± 0.00
GC0707	186.360275	18.169582	23.226 ± 0.019	1.08 ± 0.05	0.79 ± 0.03
GC0708	186.360367	18.217230	23.480 ± 0.023	0.83 ± 0.05	0.63 ± 0.03
GC0709	186.360413	18.516840	23.589 ± 0.024	0.97 ± 0.06	0.61 ± 0.04
GC0710	186.360611	18.196459	23.186 ± 0.018	1.17 ± 0.05	1.03 ± 0.02
GC0711	186.360764	18.206337	21.780 ± 0.006	1.04 ± 0.02	0.80 ± 0.01
GC0712	186.360886	18.444323	23.555 ± 0.023	1.74 ± 0.11	1.14 ± 0.03
GC0713	186.361084	18.269943	22.262 ± 0.009	1.37 ± 0.03	1.04 ± 0.01
GC0714	186.361130	18.140671	22.601 ± 0.011	1.21 ± 0.03	0.78 ± 0.01
GC0715	186.361221	18.208429	23.596 ± 0.026	1.37 ± 0.09	0.84 ± 0.03
GC0716	186.361526	18.180431	22.891 ± 0.014	0.97 ± 0.04	0.59 ± 0.02
GC0717	186.361786	18.190502	23.337 ± 0.021	1.45 ± 0.07	0.78 ± 0.03
GC0718	186.362091	18.222855	22.343 ± 0.009	0.95 ± 0.02	0.75 ± 0.01
GC0719	186.362350	18.232096	22.873 ± 0.014	1.01 ± 0.04	0.59 ± 0.02
GC0720	186.362564	18.290384	23.250 ± 0.019	1.31 ± 0.06	0.79 ± 0.03
GC0721	186.362854	18.193123	22.851 ± 0.014	1.14 ± 0.04	0.69 ± 0.02
GC0722	186.363373	18.031410	23.473 ± 0.022	0.99 ± 0.06	0.69 ± 0.03
GC0723	186.363510	18.241329	22.838 ± 0.014	1.42 ± 0.05	1.03 ± 0.02
GC0724	186.363647	18.191370	22.968 ± 0.015	1.32 ± 0.05	0.89 ± 0.02
GC0725	186.363754	18.149618	23.297 ± 0.020	1.08 ± 0.05	0.67 ± 0.03
GC0726	186.364014	17.612448	22.429 ± 0.009	1.63 ± 0.04	1.02 ± 0.01
GC0727	186.364334	18.209112	21.579 ± 0.005	0.88 ± 0.01	0.78 ± 0.01
GC0728	186.365265	18.173244	23.463 ± 0.023	1.64 ± 0.10	1.01 ± 0.03
GC0729	186.365707	18.186291	21.691 ± 0.006	1.30 ± 0.02	0.88 ± 0.01
GC0730	186.365799	18.192427	22.421 ± 0.010	1.46 ± 0.03	0.84 ± 0.01
GC0731	186.365845	17.929651	20.130 ± 0.002	1.02 ± 0.01	0.60 ± 0.00
GC0732	186.366058	18.130508	22.179 ± 0.008	1.03 ± 0.02	0.75 ± 0.01
GC0733	186.366074	17.922523	23.309 ± 0.020	1.15 ± 0.06	0.73 ± 0.03
GC0734	186.366135	17.594398	22.433 ± 0.009	1.31 ± 0.03	0.97 ± 0.01
GC0735	186.366425	18.250799	22.731 ± 0.013	1.08 ± 0.03	0.69 ± 0.02
GC0736	186.367020	18.177967	23.059 ± 0.016	0.94 ± 0.04	0.65 ± 0.02

Table A.1: (cont'd)

ID	α (J2000) (deg)	δ (J2000) (deg)	g (mag)	$u-g$ (mag)	$g-i$ (mag)
GC0737	186.367340	18.179701	22.993 ± 0.016	1.00 ± 0.04	0.71 ± 0.02
GC0738	186.367416	18.136906	23.262 ± 0.020	1.04 ± 0.05	0.69 ± 0.03
GC0739	186.367508	18.207092	23.366 ± 0.021	1.50 ± 0.08	0.85 ± 0.03
GC0740	186.367554	18.045042	22.238 ± 0.008	1.36 ± 0.03	0.83 ± 0.01
GC0741	186.367844	18.175184	22.617 ± 0.012	1.49 ± 0.04	0.94 ± 0.01
GC0742	186.368484	18.423977	23.395 ± 0.020	1.07 ± 0.06	0.60 ± 0.03
GC0743	186.368637	18.265491	23.128 ± 0.018	1.09 ± 0.05	0.61 ± 0.03
GC0744	186.368835	18.216465	22.909 ± 0.014	1.04 ± 0.04	0.58 ± 0.02
GC0745	186.368881	18.185701	20.972 ± 0.004	0.97 ± 0.01	0.73 ± 0.00
GC0746	186.369003	18.067013	23.196 ± 0.018	0.95 ± 0.05	0.65 ± 0.03
GC0747	186.369232	18.169748	23.075 ± 0.017	1.20 ± 0.05	0.83 ± 0.02
GC0748	186.369278	18.554213	21.996 ± 0.007	0.97 ± 0.02	0.66 ± 0.01
GC0749	186.369324	18.114891	22.344 ± 0.009	1.10 ± 0.02	0.73 ± 0.01
GC0750	186.369385	18.135767	22.844 ± 0.014	1.25 ± 0.04	0.83 ± 0.02
GC0751	186.369446	18.187000	22.887 ± 0.014	1.44 ± 0.05	0.99 ± 0.02
GC0752	186.369461	18.205717	23.119 ± 0.017	1.47 ± 0.06	1.14 ± 0.02
GC0753	186.369690	18.201820	23.483 ± 0.023	1.45 ± 0.08	0.78 ± 0.03
GC0754	186.370071	18.222790	22.560 ± 0.011	1.15 ± 0.03	0.84 ± 0.01
GC0755	186.370346	18.246073	23.233 ± 0.019	0.91 ± 0.05	0.75 ± 0.03
GC0756	186.371017	18.216812	22.467 ± 0.010	1.17 ± 0.03	0.82 ± 0.01
GC0757	186.371216	18.226027	22.495 ± 0.010	1.27 ± 0.03	0.71 ± 0.01
GC0758	186.371490	18.210533	22.303 ± 0.009	1.47 ± 0.03	1.05 ± 0.01
GC0759	186.371506	18.085026	21.611 ± 0.005	0.97 ± 0.01	0.74 ± 0.01
GC0760	186.371719	18.175594	22.738 ± 0.013	1.17 ± 0.04	0.71 ± 0.02
GC0761	186.371750	18.185471	22.982 ± 0.015	1.46 ± 0.05	0.86 ± 0.02
GC0762	186.372055	18.139395	23.474 ± 0.023	1.16 ± 0.07	0.62 ± 0.03
GC0763	186.372208	18.199083	22.420 ± 0.010	1.03 ± 0.03	0.63 ± 0.01
GC0764	186.372330	18.239212	22.615 ± 0.012	1.02 ± 0.03	0.68 ± 0.02
GC0765	186.372757	18.214319	22.310 ± 0.009	1.23 ± 0.03	0.88 ± 0.01
GC0766	186.372940	18.197918	23.378 ± 0.022	1.33 ± 0.07	0.97 ± 0.03
GC0767	186.373062	18.200102	22.386 ± 0.010	0.92 ± 0.02	0.63 ± 0.01
GC0768	186.373260	18.117455	22.790 ± 0.013	1.07 ± 0.03	0.63 ± 0.02
GC0769	186.373413	18.193731	21.666 ± 0.006	1.20 ± 0.02	0.78 ± 0.01
GC0770	186.373703	18.233467	22.177 ± 0.008	1.44 ± 0.03	0.98 ± 0.01
GC0771	186.374191	18.152559	23.523 ± 0.024	1.29 ± 0.08	0.81 ± 0.03
GC0772	186.374939	18.203411	22.476 ± 0.010	1.40 ± 0.03	0.93 ± 0.01
GC0773	186.375458	18.253899	22.457 ± 0.010	1.00 ± 0.03	0.68 ± 0.01
GC0774	186.375534	18.182299	23.549 ± 0.025	0.89 ± 0.06	0.71 ± 0.03
GC0775	186.375900	18.263441	22.297 ± 0.009	0.94 ± 0.02	0.73 ± 0.01
GC0776	186.376541	18.160290	23.060 ± 0.016	1.35 ± 0.05	0.97 ± 0.02
GC0777	186.376724	17.862450	22.016 ± 0.007	1.54 ± 0.03	1.11 ± 0.01
GC0778	186.376724	18.192282	23.297 ± 0.020	0.89 ± 0.05	0.75 ± 0.03
GC0779	186.377213	18.018139	21.415 ± 0.005	0.96 ± 0.01	0.58 ± 0.01
GC0780	186.377228	18.166256	22.963 ± 0.015	1.22 ± 0.04	0.79 ± 0.02
GC0781	186.377289	18.237934	21.470 ± 0.005	1.42 ± 0.02	1.00 ± 0.01
GC0782	186.377563	17.953196	23.236 ± 0.018	0.85 ± 0.05	0.57 ± 0.03
GC0783	186.377625	18.171926	22.840 ± 0.014	1.12 ± 0.04	0.72 ± 0.02
GC0784	186.378464	18.193140	23.301 ± 0.020	1.58 ± 0.08	1.07 ± 0.02

Table A.1: (cont'd)

ID	α (J2000) (deg)	δ (J2000) (deg)	g (mag)	$u-g$ (mag)	$g-i$ (mag)
GC0785	186.378479	18.186632	21.419 ± 0.005	1.21 ± 0.01	0.89 ± 0.01
GC0786	186.378830	18.503677	22.074 ± 0.007	1.70 ± 0.03	1.02 ± 0.01
GC0787	186.379196	18.182981	23.387 ± 0.022	1.00 ± 0.05	0.81 ± 0.03
GC0788	186.379257	18.218636	22.386 ± 0.010	1.00 ± 0.02	0.76 ± 0.01
GC0789	186.379303	18.210320	21.810 ± 0.006	1.26 ± 0.02	0.92 ± 0.01
GC0790	186.379929	18.232170	21.504 ± 0.005	1.42 ± 0.02	1.04 ± 0.01
GC0791	186.380188	18.171579	22.718 ± 0.012	1.07 ± 0.03	0.72 ± 0.02
GC0792	186.380295	18.187510	23.290 ± 0.020	1.16 ± 0.06	0.59 ± 0.03
GC0793	186.380447	18.205965	22.230 ± 0.009	1.49 ± 0.03	0.98 ± 0.01
GC0794	186.380768	18.163036	23.201 ± 0.019	1.46 ± 0.07	0.98 ± 0.02
GC0795	186.381073	18.190340	23.489 ± 0.024	1.01 ± 0.06	0.70 ± 0.03
GC0796	186.381805	18.214922	23.486 ± 0.024	0.97 ± 0.06	0.68 ± 0.03
GC0797	186.382660	18.290487	22.556 ± 0.011	0.96 ± 0.03	0.67 ± 0.02
GC0798	186.383148	18.357384	20.977 ± 0.004	1.03 ± 0.01	0.70 ± 0.00
GC0799	186.383682	18.206514	23.394 ± 0.022	1.03 ± 0.06	0.86 ± 0.03
GC0800	186.384186	18.219034	23.113 ± 0.017	1.16 ± 0.05	0.68 ± 0.02
GC0801	186.384537	18.149446	23.176 ± 0.018	1.22 ± 0.05	0.80 ± 0.02
GC0802	186.384888	18.213478	21.232 ± 0.004	1.09 ± 0.01	0.79 ± 0.01
GC0803	186.385315	18.216326	23.002 ± 0.016	1.13 ± 0.04	0.82 ± 0.02
GC0804	186.385406	18.264565	22.672 ± 0.012	1.00 ± 0.03	0.69 ± 0.02
GC0805	186.386337	18.171919	23.543 ± 0.025	1.02 ± 0.06	0.61 ± 0.04
GC0806	186.386444	17.609869	23.012 ± 0.015	0.99 ± 0.04	0.63 ± 0.02
GC0807	186.386536	18.206844	22.649 ± 0.012	0.89 ± 0.03	0.69 ± 0.02
GC0808	186.386658	18.106119	22.531 ± 0.011	1.04 ± 0.03	0.71 ± 0.01
GC0809	186.386765	18.132792	22.875 ± 0.014	1.04 ± 0.04	0.66 ± 0.02
GC0810	186.387314	18.184025	22.699 ± 0.012	1.14 ± 0.03	0.80 ± 0.02
GC0811	186.387314	18.186472	22.310 ± 0.009	1.33 ± 0.03	0.86 ± 0.01
GC0812	186.387848	17.795679	20.799 ± 0.003	0.84 ± 0.01	0.64 ± 0.00
GC0813	186.387848	17.994797	22.138 ± 0.008	1.36 ± 0.03	0.87 ± 0.01
GC0814	186.388535	17.853893	20.366 ± 0.002	1.89 ± 0.01	1.25 ± 0.00
GC0815	186.388687	18.145676	23.277 ± 0.020	0.92 ± 0.05	0.63 ± 0.03
GC0816	186.389450	18.206604	22.091 ± 0.008	1.06 ± 0.02	0.69 ± 0.01
GC0817	186.390808	17.659903	20.482 ± 0.003	1.75 ± 0.01	1.18 ± 0.00
GC0818	186.391434	18.546051	23.302 ± 0.019	1.52 ± 0.07	0.97 ± 0.02
GC0819	186.391983	18.419512	22.722 ± 0.012	1.55 ± 0.05	1.10 ± 0.01
GC0820	186.392609	18.186319	22.717 ± 0.012	0.94 ± 0.03	0.70 ± 0.02
GC0821	186.392807	18.468626	21.556 ± 0.005	1.11 ± 0.01	0.75 ± 0.01
GC0822	186.392853	18.142134	22.631 ± 0.012	0.93 ± 0.03	0.65 ± 0.02
GC0823	186.393021	18.205732	22.494 ± 0.010	1.48 ± 0.04	0.97 ± 0.01
GC0824	186.393082	18.136415	22.834 ± 0.014	1.24 ± 0.04	0.85 ± 0.02
GC0825	186.394089	18.225119	21.890 ± 0.007	1.15 ± 0.02	0.82 ± 0.01
GC0826	186.394745	18.170521	22.491 ± 0.010	1.32 ± 0.03	0.95 ± 0.01
GC0827	186.395157	18.228525	22.921 ± 0.015	1.06 ± 0.04	0.70 ± 0.02
GC0828	186.395508	18.231909	22.909 ± 0.014	1.41 ± 0.05	1.00 ± 0.02
GC0829	186.396088	17.755241	21.842 ± 0.006	1.65 ± 0.03	1.15 ± 0.01
GC0830	186.396454	18.191378	23.571 ± 0.025	0.97 ± 0.06	0.58 ± 0.04
GC0831	186.396942	18.566505	23.187 ± 0.017	1.57 ± 0.07	0.99 ± 0.02
GC0832	186.397003	17.975775	22.641 ± 0.011	0.98 ± 0.03	0.66 ± 0.02

Table A.1: (cont'd)

ID	α (J2000) (deg)	δ (J2000) (deg)	g (mag)	$u-g$ (mag)	$g-i$ (mag)
GC0833	186.397308	18.207159	22.955 ± 0.015	0.97 ± 0.04	0.68 ± 0.02
GC0834	186.397446	18.214991	21.756 ± 0.006	1.13 ± 0.02	0.83 ± 0.01
GC0835	186.397476	17.863077	22.651 ± 0.011	1.87 ± 0.06	1.24 ± 0.01
GC0836	186.397705	18.376612	20.987 ± 0.004	1.28 ± 0.01	0.91 ± 0.00
GC0837	186.398087	18.193789	23.537 ± 0.025	0.93 ± 0.06	0.62 ± 0.04
GC0838	186.398270	17.704031	22.917 ± 0.014	1.23 ± 0.04	0.71 ± 0.02
GC0839	186.398560	17.589792	23.522 ± 0.028	0.99 ± 0.07	0.62 ± 0.04
GC0840	186.398666	17.924862	22.936 ± 0.014	1.04 ± 0.04	0.59 ± 0.02
GC0841	186.398880	18.205355	22.861 ± 0.014	1.13 ± 0.04	0.71 ± 0.02
GC0842	186.399323	18.176071	22.728 ± 0.013	0.98 ± 0.03	0.66 ± 0.02
GC0843	186.399963	18.175274	22.854 ± 0.014	0.91 ± 0.03	0.64 ± 0.02
GC0844	186.399994	18.202095	23.518 ± 0.024	1.09 ± 0.07	0.63 ± 0.04
GC0845	186.400085	18.200121	23.473 ± 0.023	1.15 ± 0.07	0.67 ± 0.03
GC0846	186.401413	18.185404	22.973 ± 0.015	0.94 ± 0.04	0.69 ± 0.02
GC0847	186.401901	18.171749	22.381 ± 0.009	1.38 ± 0.03	0.90 ± 0.01
GC0848	186.402054	18.199120	22.713 ± 0.012	1.21 ± 0.04	0.79 ± 0.02
GC0849	186.402267	18.151554	21.478 ± 0.005	1.05 ± 0.01	0.74 ± 0.01
GC0850	186.402466	18.126282	23.143 ± 0.018	0.90 ± 0.04	0.73 ± 0.02
GC0851	186.403305	18.236071	23.562 ± 0.026	1.16 ± 0.07	0.91 ± 0.03
GC0852	186.403336	18.176249	22.900 ± 0.015	1.61 ± 0.06	0.91 ± 0.02
GC0853	186.403488	18.113260	22.103 ± 0.008	1.33 ± 0.02	0.76 ± 0.01
GC0854	186.403931	18.249685	22.240 ± 0.009	0.94 ± 0.02	0.60 ± 0.01
GC0855	186.404083	18.172537	21.620 ± 0.006	1.51 ± 0.02	0.89 ± 0.01
GC0856	186.404099	18.176178	22.432 ± 0.010	1.13 ± 0.03	0.69 ± 0.01
GC0857	186.404190	17.867220	21.583 ± 0.005	1.10 ± 0.02	0.57 ± 0.01
GC0858	186.404236	18.260929	22.155 ± 0.008	1.09 ± 0.02	0.66 ± 0.01
GC0859	186.404572	18.211876	23.413 ± 0.023	0.99 ± 0.06	0.65 ± 0.03
GC0860	186.404846	18.179823	22.206 ± 0.009	1.14 ± 0.02	0.66 ± 0.01
GC0861	186.410751	18.189440	23.170 ± 0.021	1.09 ± 0.06	0.76 ± 0.03
GC0862	186.410873	18.564915	21.192 ± 0.004	0.86 ± 0.01	0.62 ± 0.01
GC0863	186.411789	18.152060	23.042 ± 0.019	1.01 ± 0.05	0.78 ± 0.03
GC0864	186.412811	18.274725	23.428 ± 0.023	0.95 ± 0.06	0.67 ± 0.03
GC0865	186.412903	17.803812	23.442 ± 0.023	1.26 ± 0.08	0.89 ± 0.03
GC0866	186.413483	17.707903	22.239 ± 0.009	1.04 ± 0.02	0.68 ± 0.01
GC0867	186.413834	18.186165	22.633 ± 0.012	1.06 ± 0.03	0.71 ± 0.02
GC0868	186.413940	18.207966	23.393 ± 0.022	1.57 ± 0.09	0.96 ± 0.03
GC0869	186.414719	17.929039	20.825 ± 0.003	0.90 ± 0.01	0.59 ± 0.00
GC0870	186.414856	17.758154	20.268 ± 0.002	1.22 ± 0.01	0.76 ± 0.00
GC0871	186.415146	18.185661	21.866 ± 0.007	1.09 ± 0.02	0.71 ± 0.01
GC0872	186.417755	18.200327	23.444 ± 0.022	1.27 ± 0.07	0.72 ± 0.03
GC0873	186.417999	18.239515	23.316 ± 0.020	1.24 ± 0.06	0.73 ± 0.03
GC0874	186.418228	18.258064	23.397 ± 0.022	0.94 ± 0.05	0.62 ± 0.03
GC0875	186.418854	18.200792	23.235 ± 0.019	1.08 ± 0.05	0.61 ± 0.03
GC0876	186.419632	18.143559	22.254 ± 0.009	1.32 ± 0.03	0.77 ± 0.01
GC0877	186.419632	18.185848	22.971 ± 0.015	1.52 ± 0.06	0.88 ± 0.02
GC0878	186.419876	18.370522	23.184 ± 0.018	1.65 ± 0.07	1.14 ± 0.02
GC0879	186.420181	18.076006	21.261 ± 0.004	1.08 ± 0.01	0.69 ± 0.01
GC0880	186.420197	18.124525	23.527 ± 0.024	1.44 ± 0.09	0.81 ± 0.03

Table A.1: (cont'd)

ID	α (J2000) (deg)	δ (J2000) (deg)	g (mag)	$u-g$ (mag)	$g-i$ (mag)
GC0881	186.420303	18.042883	22.819 ± 0.013	1.15 ± 0.04	0.60 ± 0.02
GC0882	186.420319	18.044241	22.190 ± 0.008	1.03 ± 0.02	0.61 ± 0.01
GC0883	186.420410	17.593491	23.096 ± 0.016	1.01 ± 0.04	0.56 ± 0.02
GC0884	186.420822	17.773270	22.032 ± 0.007	0.99 ± 0.02	0.78 ± 0.01
GC0885	186.421066	18.241089	22.016 ± 0.007	1.42 ± 0.02	0.92 ± 0.01
GC0886	186.421082	18.156641	22.796 ± 0.013	1.62 ± 0.05	1.00 ± 0.02
GC0887	186.421295	18.229660	20.624 ± 0.003	1.29 ± 0.01	0.86 ± 0.00
GC0888	186.421631	18.492929	22.600 ± 0.011	1.63 ± 0.04	0.94 ± 0.01
GC0889	186.422318	17.891716	21.286 ± 0.004	1.02 ± 0.01	0.71 ± 0.01
GC0890	186.422897	18.250065	22.891 ± 0.014	1.06 ± 0.04	0.63 ± 0.02
GC0891	186.423859	18.206835	22.569 ± 0.011	1.57 ± 0.04	0.96 ± 0.01
GC0892	186.424942	18.519096	21.716 ± 0.006	1.12 ± 0.02	0.58 ± 0.01
GC0893	186.425613	17.915064	23.597 ± 0.025	0.85 ± 0.06	0.61 ± 0.04
GC0894	186.426498	18.304455	22.917 ± 0.014	1.04 ± 0.04	0.62 ± 0.02
GC0895	186.426819	17.754980	22.267 ± 0.008	0.85 ± 0.02	0.57 ± 0.01
GC0896	186.426849	18.207462	23.516 ± 0.024	1.44 ± 0.09	0.77 ± 0.03
GC0897	186.427216	18.229856	23.397 ± 0.022	1.04 ± 0.06	0.69 ± 0.03
GC0898	186.427277	18.195351	22.623 ± 0.011	1.52 ± 0.04	0.98 ± 0.01
GC0899	186.427780	18.165043	23.452 ± 0.023	0.99 ± 0.06	0.61 ± 0.03
GC0900	186.428284	18.364117	21.555 ± 0.005	1.02 ± 0.01	0.63 ± 0.01
GC0901	186.429123	18.190605	21.581 ± 0.005	0.95 ± 0.01	0.64 ± 0.01
GC0902	186.429520	18.164227	21.497 ± 0.005	1.22 ± 0.01	0.80 ± 0.01
GC0903	186.431519	18.233503	22.454 ± 0.010	1.37 ± 0.03	0.89 ± 0.01
GC0904	186.431641	18.219053	22.353 ± 0.009	1.05 ± 0.02	0.65 ± 0.01
GC0905	186.432281	17.744194	22.919 ± 0.014	1.47 ± 0.05	1.12 ± 0.02
GC0906	186.432617	17.814722	22.005 ± 0.007	0.93 ± 0.02	0.70 ± 0.01
GC0907	186.432648	18.204823	23.064 ± 0.016	1.25 ± 0.05	0.75 ± 0.02
GC0908	186.432739	18.360220	22.860 ± 0.013	1.91 ± 0.07	1.07 ± 0.02
GC0909	186.433121	18.092716	23.370 ± 0.022	0.91 ± 0.05	0.71 ± 0.03
GC0910	186.433197	18.158579	23.070 ± 0.016	0.97 ± 0.04	0.68 ± 0.02
GC0911	186.433228	18.221083	22.854 ± 0.014	0.96 ± 0.03	0.60 ± 0.02
GC0912	186.434509	17.665598	22.695 ± 0.012	1.63 ± 0.05	1.16 ± 0.01
GC0913	186.435379	17.790684	21.095 ± 0.004	0.93 ± 0.01	0.57 ± 0.00
GC0914	186.435425	18.228130	21.880 ± 0.007	1.50 ± 0.02	0.97 ± 0.01
GC0915	186.435730	18.240477	23.391 ± 0.021	1.52 ± 0.08	0.93 ± 0.03
GC0916	186.436203	17.606211	21.255 ± 0.004	0.92 ± 0.01	0.60 ± 0.01
GC0917	186.436554	17.635128	22.062 ± 0.007	0.87 ± 0.02	0.68 ± 0.01
GC0918	186.436996	18.375525	22.414 ± 0.009	0.96 ± 0.02	0.69 ± 0.01
GC0919	186.437210	18.503738	22.399 ± 0.009	1.03 ± 0.02	0.58 ± 0.01
GC0920	186.437271	18.138191	23.435 ± 0.022	1.09 ± 0.06	0.68 ± 0.03
GC0921	186.437469	17.805870	23.181 ± 0.017	1.33 ± 0.06	0.94 ± 0.02
GC0922	186.437775	18.361656	20.705 ± 0.003	0.88 ± 0.01	0.63 ± 0.00
GC0923	186.437790	18.224007	22.909 ± 0.014	1.01 ± 0.04	0.57 ± 0.02
GC0924	186.437958	18.158665	23.330 ± 0.020	0.94 ± 0.05	0.68 ± 0.03
GC0925	186.438904	18.302069	21.370 ± 0.005	1.92 ± 0.02	1.23 ± 0.01
GC0926	186.440567	18.258642	23.416 ± 0.022	1.23 ± 0.07	0.67 ± 0.03
GC0927	186.440796	18.513153	23.369 ± 0.020	1.48 ± 0.08	0.87 ± 0.03
GC0928	186.441025	18.103270	21.886 ± 0.007	0.92 ± 0.02	0.57 ± 0.01

Table A.1: (cont'd)

ID	α (J2000) (deg)	δ (J2000) (deg)	g (mag)	$u-g$ (mag)	$g-i$ (mag)
GC0929	186.442490	18.393070	22.916 ± 0.014	1.16 ± 0.04	0.60 ± 0.02
GC0930	186.443100	18.407099	22.692 ± 0.012	1.71 ± 0.05	1.07 ± 0.01
GC0931	186.443878	18.294334	22.909 ± 0.014	1.00 ± 0.04	0.57 ± 0.02
GC0932	186.446365	18.242985	22.530 ± 0.011	1.47 ± 0.04	0.91 ± 0.01
GC0933	186.446533	18.193928	23.068 ± 0.016	1.00 ± 0.04	0.65 ± 0.02
GC0934	186.446548	18.188711	21.277 ± 0.004	1.09 ± 0.01	0.71 ± 0.01
GC0935	186.446808	17.947796	21.881 ± 0.006	0.91 ± 0.02	0.60 ± 0.01
GC0936	186.446823	18.159986	22.825 ± 0.013	1.61 ± 0.05	0.96 ± 0.02
GC0937	186.446854	18.079725	23.142 ± 0.017	1.00 ± 0.04	0.66 ± 0.02
GC0938	186.446869	17.951204	21.728 ± 0.006	1.50 ± 0.02	0.96 ± 0.01
GC0939	186.448059	18.296482	23.292 ± 0.020	0.98 ± 0.05	0.67 ± 0.03
GC0940	186.448807	18.008175	23.046 ± 0.016	1.24 ± 0.05	0.69 ± 0.02
GC0941	186.449112	18.274927	23.077 ± 0.016	1.49 ± 0.06	0.83 ± 0.02
GC0942	186.449142	18.156229	22.463 ± 0.010	1.05 ± 0.03	0.68 ± 0.01
GC0943	186.450043	18.221039	22.780 ± 0.013	1.08 ± 0.03	0.56 ± 0.02
GC0944	186.450470	17.899105	23.593 ± 0.025	1.84 ± 0.13	1.14 ± 0.03
GC0945	186.451492	18.453445	23.328 ± 0.020	1.22 ± 0.06	0.73 ± 0.03
GC0946	186.452209	18.010960	23.050 ± 0.016	1.10 ± 0.04	0.71 ± 0.02
GC0947	186.453110	18.482006	20.459 ± 0.003	1.41 ± 0.01	0.87 ± 0.00
GC0948	186.453247	18.000303	20.388 ± 0.002	0.92 ± 0.01	0.56 ± 0.00
GC0949	186.453705	18.213924	22.969 ± 0.015	1.01 ± 0.04	0.68 ± 0.02
GC0950	186.454330	18.147741	23.406 ± 0.022	1.71 ± 0.10	1.07 ± 0.03
GC0951	186.455750	18.239452	20.792 ± 0.003	1.09 ± 0.01	0.70 ± 0.00
GC0952	186.457047	18.001663	21.083 ± 0.004	1.09 ± 0.01	0.65 ± 0.00
GC0953	186.457962	18.026218	22.384 ± 0.009	1.00 ± 0.02	0.68 ± 0.01
GC0954	186.459473	18.247969	21.932 ± 0.007	1.05 ± 0.02	0.69 ± 0.01
GC0955	186.459671	17.629105	21.275 ± 0.004	0.87 ± 0.01	0.59 ± 0.01
GC0956	186.459747	17.859224	23.251 ± 0.019	1.48 ± 0.07	0.83 ± 0.03
GC0957	186.460876	18.250711	23.500 ± 0.023	1.20 ± 0.07	0.60 ± 0.03
GC0958	186.461136	18.204613	23.555 ± 0.025	0.90 ± 0.06	0.56 ± 0.04
GC0959	186.461258	18.203613	22.954 ± 0.015	1.10 ± 0.04	0.70 ± 0.02
GC0960	186.461685	18.257790	22.229 ± 0.008	1.28 ± 0.03	0.71 ± 0.01
GC0961	186.461823	18.101183	23.401 ± 0.022	0.87 ± 0.05	0.61 ± 0.03
GC0962	186.463120	18.416977	21.961 ± 0.007	1.05 ± 0.02	0.73 ± 0.01
GC0963	186.463242	18.195196	21.685 ± 0.006	1.35 ± 0.02	0.85 ± 0.01
GC0964	186.463959	17.604162	23.276 ± 0.018	1.45 ± 0.07	0.76 ± 0.03
GC0965	186.464630	18.211830	22.475 ± 0.010	1.24 ± 0.03	0.77 ± 0.01
GC0966	186.468674	17.901711	22.177 ± 0.008	1.17 ± 0.02	0.71 ± 0.01
GC0967	186.468765	18.581978	21.793 ± 0.006	1.50 ± 0.02	0.81 ± 0.01
GC0968	186.468994	18.237629	23.446 ± 0.022	1.54 ± 0.09	0.87 ± 0.03
GC0969	186.469833	18.275715	22.946 ± 0.015	1.19 ± 0.04	0.66 ± 0.02
GC0970	186.470215	17.872749	21.910 ± 0.007	1.63 ± 0.03	1.08 ± 0.01
GC0971	186.470230	18.189514	22.647 ± 0.012	1.08 ± 0.03	0.75 ± 0.02
GC0972	186.470764	18.179298	22.826 ± 0.013	1.05 ± 0.04	0.58 ± 0.02
GC0973	186.470932	18.427269	23.373 ± 0.020	1.17 ± 0.06	0.63 ± 0.03
GC0974	186.472275	17.954842	22.400 ± 0.009	1.15 ± 0.03	0.71 ± 0.01
GC0975	186.472931	17.986509	22.876 ± 0.014	1.09 ± 0.04	0.64 ± 0.02
GC0976	186.476578	18.284246	23.231 ± 0.019	1.61 ± 0.08	0.90 ± 0.02

Table A.1: (cont'd)

ID	α (J2000) (deg)	δ (J2000) (deg)	g (mag)	$u-g$ (mag)	$g-i$ (mag)
GC0977	186.476593	18.279037	23.396 ± 0.022	0.86 ± 0.05	0.69 ± 0.03
GC0978	186.477036	18.433382	23.530 ± 0.023	0.94 ± 0.06	0.90 ± 0.03
GC0979	186.477219	18.262146	23.498 ± 0.023	0.92 ± 0.06	0.58 ± 0.03
GC0980	186.477417	17.947351	22.242 ± 0.008	1.62 ± 0.03	1.14 ± 0.01
GC0981	186.477539	18.190903	22.679 ± 0.012	1.06 ± 0.03	0.65 ± 0.02
GC0982	186.477661	18.176586	23.520 ± 0.024	1.07 ± 0.06	0.67 ± 0.03
GC0983	186.477966	17.600565	23.313 ± 0.019	1.07 ± 0.06	0.62 ± 0.03
GC0984	186.478729	17.896111	20.972 ± 0.004	1.69 ± 0.01	1.11 ± 0.00
GC0985	186.479370	17.788864	21.708 ± 0.006	0.83 ± 0.01	0.57 ± 0.01
GC0986	186.479691	18.109177	23.284 ± 0.020	1.16 ± 0.06	0.66 ± 0.03
GC0987	186.479767	18.326345	20.264 ± 0.002	0.96 ± 0.01	0.64 ± 0.00
GC0988	186.481003	18.159040	23.094 ± 0.017	1.17 ± 0.05	0.76 ± 0.02
GC0989	186.481873	18.150984	21.230 ± 0.004	1.03 ± 0.01	0.57 ± 0.01
GC0990	186.482681	17.936279	21.996 ± 0.007	0.97 ± 0.02	0.56 ± 0.01
GC0991	186.484528	18.146975	23.179 ± 0.018	1.10 ± 0.05	0.69 ± 0.03
GC0992	186.485260	18.217434	21.065 ± 0.004	1.50 ± 0.01	0.99 ± 0.00
GC0993	186.485443	17.791096	22.140 ± 0.008	1.63 ± 0.03	1.05 ± 0.01
GC0994	186.485504	17.731779	21.963 ± 0.007	1.22 ± 0.02	0.93 ± 0.01
GC0995	186.485535	18.309912	22.973 ± 0.015	1.15 ± 0.04	0.77 ± 0.02
GC0996	186.487244	18.265203	23.122 ± 0.017	1.35 ± 0.06	0.75 ± 0.02
GC0997	186.487518	18.464834	23.099 ± 0.016	1.48 ± 0.06	0.78 ± 0.02
GC0998	186.487595	18.125460	21.680 ± 0.006	1.61 ± 0.02	1.06 ± 0.01
GC0999	186.488373	18.107792	22.872 ± 0.014	1.22 ± 0.04	0.76 ± 0.02
GC1000	186.489334	18.533623	23.600 ± 0.025	1.76 ± 0.12	1.02 ± 0.03
GC1001	186.490112	17.921387	20.835 ± 0.003	1.10 ± 0.01	0.76 ± 0.00
GC1002	186.490158	18.056267	22.976 ± 0.015	1.74 ± 0.07	1.16 ± 0.02
GC1003	186.490265	17.612589	22.638 ± 0.011	1.53 ± 0.04	1.09 ± 0.01
GC1004	186.490860	18.229095	23.232 ± 0.019	0.98 ± 0.05	0.62 ± 0.03
GC1005	186.491028	18.483624	23.506 ± 0.023	1.21 ± 0.07	0.61 ± 0.03
GC1006	186.491074	18.253242	23.190 ± 0.018	0.87 ± 0.04	0.66 ± 0.03
GC1007	186.491348	18.179501	22.589 ± 0.011	1.08 ± 0.03	0.68 ± 0.02
GC1008	186.491531	18.239412	22.895 ± 0.014	1.16 ± 0.04	0.84 ± 0.02
GC1009	186.493301	18.268782	23.064 ± 0.016	1.03 ± 0.04	0.68 ± 0.02
GC1010	186.493942	17.819202	22.484 ± 0.010	1.77 ± 0.05	1.17 ± 0.01
GC1011	186.496185	18.218157	20.317 ± 0.002	1.16 ± 0.01	0.82 ± 0.00
GC1012	186.496246	18.285427	23.535 ± 0.025	1.30 ± 0.08	0.80 ± 0.03
GC1013	186.497375	18.198225	23.106 ± 0.017	0.97 ± 0.04	0.76 ± 0.02
GC1014	186.497604	18.136724	22.087 ± 0.008	1.78 ± 0.03	1.12 ± 0.01
GC1015	186.498199	18.141739	23.415 ± 0.022	1.06 ± 0.06	0.70 ± 0.03
GC1016	186.501724	18.293427	22.892 ± 0.014	1.03 ± 0.04	0.61 ± 0.02
GC1017	186.501785	18.139441	23.481 ± 0.023	0.86 ± 0.05	0.57 ± 0.03
GC1018	186.501968	18.196192	23.201 ± 0.018	1.30 ± 0.06	0.97 ± 0.02
GC1019	186.502945	18.254948	22.554 ± 0.011	1.11 ± 0.03	0.65 ± 0.01
GC1020	186.503128	18.286690	23.163 ± 0.018	1.07 ± 0.05	0.61 ± 0.03
GC1021	186.503616	18.197788	23.577 ± 0.025	1.34 ± 0.08	0.72 ± 0.04
GC1022	186.505203	17.735826	22.171 ± 0.008	0.91 ± 0.02	0.59 ± 0.01
GC1023	186.506500	18.229334	22.143 ± 0.008	1.01 ± 0.02	0.69 ± 0.01
GC1024	186.507843	17.693884	22.832 ± 0.013	1.66 ± 0.06	0.98 ± 0.02

Table A.1: (cont'd)

ID	α (J2000) (deg)	δ (J2000) (deg)	g (mag)	$u-g$ (mag)	$g-i$ (mag)
GC1025	186.508179	17.990225	23.228 ± 0.018	1.68 ± 0.08	0.94 ± 0.02
GC1026	186.510620	17.701952	23.571 ± 0.023	1.43 ± 0.09	0.87 ± 0.03
GC1027	186.510757	18.097383	23.176 ± 0.018	1.36 ± 0.06	0.72 ± 0.02
GC1028	186.511230	18.165592	23.153 ± 0.018	1.39 ± 0.06	0.84 ± 0.02
GC1029	186.511826	17.711414	22.697 ± 0.012	1.66 ± 0.05	1.19 ± 0.01
GC1030	186.512543	17.948980	23.312 ± 0.020	1.17 ± 0.06	0.73 ± 0.03
GC1031	186.514618	17.917330	21.129 ± 0.004	1.12 ± 0.01	0.71 ± 0.00
GC1032	186.514664	18.025400	21.147 ± 0.004	1.11 ± 0.01	0.68 ± 0.01
GC1033	186.515228	18.215872	23.314 ± 0.020	1.17 ± 0.06	0.77 ± 0.03
GC1034	186.517349	18.321339	23.248 ± 0.019	1.27 ± 0.06	0.68 ± 0.03
GC1035	186.517563	17.904104	22.122 ± 0.008	1.66 ± 0.03	1.14 ± 0.01
GC1036	186.517746	18.232906	23.400 ± 0.022	1.05 ± 0.06	0.63 ± 0.03
GC1037	186.518005	18.247179	23.400 ± 0.022	1.57 ± 0.09	1.01 ± 0.03
GC1038	186.518036	17.945925	21.523 ± 0.005	1.23 ± 0.01	0.96 ± 0.01
GC1039	186.518906	18.202578	22.424 ± 0.010	1.17 ± 0.03	0.59 ± 0.01
GC1040	186.519531	18.463158	22.844 ± 0.014	1.61 ± 0.06	0.98 ± 0.02
GC1041	186.520416	18.188438	22.344 ± 0.009	1.27 ± 0.03	0.69 ± 0.01
GC1042	186.521667	18.041508	23.357 ± 0.024	1.84 ± 0.12	1.08 ± 0.03
GC1043	186.525330	18.417778	23.444 ± 0.026	1.04 ± 0.07	0.70 ± 0.04
GC1044	186.525513	18.203398	23.070 ± 0.019	0.87 ± 0.05	0.58 ± 0.03
GC1045	186.525558	17.853962	22.573 ± 0.013	1.00 ± 0.03	0.61 ± 0.02
GC1046	186.526123	17.683857	21.658 ± 0.006	1.11 ± 0.02	0.60 ± 0.01
GC1047	186.526535	18.206448	23.255 ± 0.023	1.24 ± 0.07	0.80 ± 0.03
GC1048	186.526962	18.206945	22.255 ± 0.009	1.00 ± 0.02	0.70 ± 0.01
GC1049	186.526993	18.331787	22.424 ± 0.016	1.01 ± 0.04	0.83 ± 0.02
GC1050	186.527786	18.135717	23.324 ± 0.023	1.05 ± 0.06	0.67 ± 0.03
GC1051	186.530548	18.205006	23.176 ± 0.018	1.14 ± 0.05	0.64 ± 0.03
GC1052	186.530823	18.307970	21.992 ± 0.007	1.15 ± 0.02	0.77 ± 0.01
GC1053	186.532578	18.237915	21.785 ± 0.006	1.12 ± 0.02	0.73 ± 0.01
GC1054	186.533249	18.519876	23.160 ± 0.017	1.19 ± 0.05	0.63 ± 0.02
GC1055	186.533676	18.498030	22.549 ± 0.010	1.16 ± 0.03	0.63 ± 0.01
GC1056	186.534866	18.143873	21.362 ± 0.004	1.39 ± 0.01	0.77 ± 0.01
GC1057	186.536530	17.967999	21.796 ± 0.006	1.24 ± 0.02	0.83 ± 0.01
GC1058	186.536667	18.134405	23.297 ± 0.019	0.94 ± 0.05	0.58 ± 0.03
GC1059	186.536789	18.053703	22.612 ± 0.011	1.29 ± 0.03	0.72 ± 0.02
GC1060	186.537231	18.479837	22.028 ± 0.007	0.95 ± 0.02	0.56 ± 0.01
GC1061	186.537994	18.325020	22.109 ± 0.008	0.96 ± 0.02	0.71 ± 0.01
GC1062	186.541473	18.031807	21.039 ± 0.004	1.09 ± 0.01	0.66 ± 0.00
GC1063	186.543610	18.179792	23.037 ± 0.016	1.04 ± 0.04	0.62 ± 0.02
GC1064	186.546402	18.390221	22.625 ± 0.011	0.87 ± 0.03	0.56 ± 0.02
GC1065	186.547272	17.934832	22.697 ± 0.012	1.12 ± 0.03	0.63 ± 0.02
GC1066	186.550156	17.764580	20.971 ± 0.004	0.98 ± 0.01	0.61 ± 0.00
GC1067	186.550949	18.090328	22.547 ± 0.011	1.75 ± 0.05	1.08 ± 0.01
GC1068	186.552002	18.392870	20.634 ± 0.003	0.86 ± 0.01	0.57 ± 0.00
GC1069	186.552673	18.169510	23.041 ± 0.015	1.03 ± 0.04	0.65 ± 0.02
GC1070	186.553238	18.472134	23.513 ± 0.023	1.07 ± 0.06	0.67 ± 0.03
GC1071	186.553421	17.633364	21.464 ± 0.005	1.27 ± 0.01	0.79 ± 0.01
GC1072	186.553635	17.697136	22.837 ± 0.014	1.06 ± 0.03	0.66 ± 0.02

Table A.1: (cont'd)

ID	α (J2000) (deg)	δ (J2000) (deg)	g (mag)	$u-g$ (mag)	$g-i$ (mag)
GC1073	186.554565	18.094284	22.083 ± 0.007	1.07 ± 0.02	0.60 ± 0.01
GC1074	186.555206	18.525051	23.490 ± 0.022	1.17 ± 0.07	0.66 ± 0.03
GC1075	186.556015	18.308714	21.923 ± 0.007	1.88 ± 0.03	1.24 ± 0.01
GC1076	186.557266	18.294901	20.379 ± 0.002	1.46 ± 0.01	0.84 ± 0.00
GC1077	186.557953	18.195946	23.272 ± 0.019	1.23 ± 0.06	0.72 ± 0.03
GC1078	186.558655	18.077478	22.278 ± 0.008	1.32 ± 0.03	0.91 ± 0.01
GC1079	186.560181	17.703356	21.469 ± 0.005	1.06 ± 0.01	0.60 ± 0.01
GC1080	186.561630	18.539429	22.856 ± 0.013	1.24 ± 0.04	0.63 ± 0.02
GC1081	186.562485	18.228304	22.364 ± 0.009	1.10 ± 0.02	0.80 ± 0.01
GC1082	186.562546	18.501846	23.296 ± 0.019	1.00 ± 0.05	0.69 ± 0.03
GC1083	186.562546	18.561739	23.335 ± 0.019	1.31 ± 0.07	0.75 ± 0.03
GC1084	186.563904	18.265446	21.900 ± 0.006	1.52 ± 0.02	0.95 ± 0.01
GC1085	186.564026	18.148020	21.350 ± 0.004	1.84 ± 0.02	1.24 ± 0.01
GC1086	186.566147	17.869427	22.249 ± 0.008	1.05 ± 0.02	0.59 ± 0.01
GC1087	186.566193	18.190681	23.185 ± 0.017	1.19 ± 0.05	0.72 ± 0.02
GC1088	186.567749	18.443127	22.648 ± 0.011	1.55 ± 0.04	0.95 ± 0.01
GC1089	186.567841	18.009369	20.714 ± 0.003	1.31 ± 0.01	0.80 ± 0.00
GC1090	186.568176	18.242140	23.217 ± 0.018	0.95 ± 0.04	0.57 ± 0.03
GC1091	186.569687	18.519770	22.064 ± 0.007	1.45 ± 0.03	0.98 ± 0.01
GC1092	186.570267	18.082716	20.688 ± 0.003	0.86 ± 0.01	0.60 ± 0.00
GC1093	186.570450	18.134844	20.920 ± 0.003	0.99 ± 0.01	0.72 ± 0.00
GC1094	186.570557	18.367836	22.406 ± 0.009	1.91 ± 0.05	1.08 ± 0.01
GC1095	186.571579	18.191843	23.327 ± 0.019	0.97 ± 0.05	0.75 ± 0.03
GC1096	186.573227	18.082048	22.074 ± 0.007	1.21 ± 0.02	0.70 ± 0.01
GC1097	186.574646	17.925171	22.127 ± 0.008	1.09 ± 0.02	0.69 ± 0.01
GC1098	186.576935	17.669714	23.345 ± 0.021	0.93 ± 0.05	0.58 ± 0.03
GC1099	186.577484	18.157955	22.331 ± 0.009	1.67 ± 0.04	0.95 ± 0.01
GC1100	186.579178	18.009647	20.881 ± 0.003	1.23 ± 0.01	0.85 ± 0.00
GC1101	186.579376	18.303230	23.470 ± 0.022	0.92 ± 0.05	0.63 ± 0.03
GC1102	186.582031	17.674490	20.972 ± 0.004	0.91 ± 0.01	0.67 ± 0.00
GC1103	186.582657	18.250280	22.646 ± 0.011	1.11 ± 0.03	0.75 ± 0.02
GC1104	186.582794	17.720867	22.902 ± 0.014	1.04 ± 0.04	0.58 ± 0.02
GC1105	186.584290	18.562576	22.490 ± 0.010	0.96 ± 0.03	0.55 ± 0.01
GC1106	186.585556	18.523678	22.660 ± 0.011	1.55 ± 0.04	0.88 ± 0.01
GC1107	186.588638	17.943106	20.364 ± 0.002	1.04 ± 0.01	0.55 ± 0.00
GC1108	186.589493	18.019365	23.364 ± 0.020	1.60 ± 0.08	1.08 ± 0.02
GC1109	186.591965	18.166372	22.391 ± 0.009	1.85 ± 0.04	1.15 ± 0.01
GC1110	186.592224	18.107084	23.057 ± 0.015	1.01 ± 0.04	0.63 ± 0.02
GC1111	186.593292	18.464270	20.928 ± 0.003	1.67 ± 0.01	1.14 ± 0.00
GC1112	186.594833	18.043074	23.155 ± 0.017	1.20 ± 0.05	0.84 ± 0.02
GC1113	186.594971	18.539196	21.604 ± 0.005	1.59 ± 0.02	1.09 ± 0.01
GC1114	186.596191	18.193604	21.738 ± 0.006	1.00 ± 0.01	0.72 ± 0.01
GC1115	186.596497	18.319632	21.317 ± 0.004	1.49 ± 0.01	0.92 ± 0.01
GC1116	186.596985	18.205563	21.467 ± 0.005	1.51 ± 0.02	0.98 ± 0.01
GC1117	186.597839	18.572090	20.473 ± 0.003	1.04 ± 0.01	0.67 ± 0.00
GC1118	186.598541	18.171110	22.048 ± 0.007	1.24 ± 0.02	0.81 ± 0.01
GC1119	186.599701	18.481447	20.544 ± 0.003	1.35 ± 0.01	0.92 ± 0.00
GC1120	186.601456	18.062712	23.486 ± 0.022	1.44 ± 0.08	0.78 ± 0.03

Table A.1: (cont'd)

ID	α (J2000) (deg)	δ (J2000) (deg)	g (mag)	$u-g$ (mag)	$g-i$ (mag)
GC1121	186.602570	17.987377	20.753 ± 0.003	1.80 ± 0.01	1.22 ± 0.00
GC1122	186.603317	17.687456	21.262 ± 0.004	1.48 ± 0.01	1.13 ± 0.00
GC1123	186.607574	18.189796	22.419 ± 0.009	0.94 ± 0.02	0.58 ± 0.01
GC1124	186.608871	18.306881	22.809 ± 0.013	1.22 ± 0.04	0.69 ± 0.02
GC1125	186.610992	18.469135	23.406 ± 0.021	1.49 ± 0.08	0.84 ± 0.03
GC1126	186.611343	18.276909	21.149 ± 0.004	0.91 ± 0.01	0.58 ± 0.01
GC1127	186.611481	17.907864	22.194 ± 0.008	1.15 ± 0.02	0.70 ± 0.01
GC1128	186.612015	17.753017	21.733 ± 0.006	1.73 ± 0.02	1.23 ± 0.01
GC1129	186.616714	17.807457	20.673 ± 0.003	0.89 ± 0.01	0.64 ± 0.00
GC1130	186.617386	17.935009	21.401 ± 0.005	1.02 ± 0.01	0.73 ± 0.01
GC1131	186.620255	18.293690	20.961 ± 0.004	1.07 ± 0.01	0.72 ± 0.00
GC1132	186.624115	18.420593	21.307 ± 0.004	1.13 ± 0.01	0.82 ± 0.01
GC1133	186.625122	17.749331	23.374 ± 0.021	1.03 ± 0.05	0.63 ± 0.03
GC1134	186.626770	17.950636	22.392 ± 0.009	1.19 ± 0.03	0.65 ± 0.01
GC1135	186.630829	18.130758	21.820 ± 0.006	1.18 ± 0.02	0.75 ± 0.01
GC1136	186.631699	18.472252	21.037 ± 0.004	1.06 ± 0.01	0.71 ± 0.00
GC1137	186.632492	18.329494	22.893 ± 0.017	1.49 ± 0.07	0.88 ± 0.02
GC1138	186.632996	18.131805	21.711 ± 0.006	1.07 ± 0.01	0.65 ± 0.01
GC1139	186.635574	18.354498	23.110 ± 0.019	0.88 ± 0.05	0.76 ± 0.03
GC1140	186.640076	17.610085	21.956 ± 0.008	1.27 ± 0.02	0.93 ± 0.01
GC1141	186.640488	17.973827	22.630 ± 0.014	1.81 ± 0.07	1.08 ± 0.02
GC1142	186.641174	18.366943	23.059 ± 0.018	1.00 ± 0.05	0.75 ± 0.03
GC1143	186.648483	17.778957	21.047 ± 0.004	0.85 ± 0.01	0.60 ± 0.00
GC1144	186.651962	18.049425	23.528 ± 0.023	0.91 ± 0.06	0.65 ± 0.03
GC1145	186.652664	18.177197	22.310 ± 0.009	1.86 ± 0.04	1.16 ± 0.01
GC1146	186.653168	17.998501	22.361 ± 0.009	1.02 ± 0.02	0.65 ± 0.01
GC1147	186.653839	17.665546	21.250 ± 0.004	1.08 ± 0.01	0.58 ± 0.01
GC1148	186.653870	18.225601	22.719 ± 0.012	1.88 ± 0.06	1.21 ± 0.01
GC1149	186.654556	18.274414	21.296 ± 0.004	1.05 ± 0.01	0.82 ± 0.01
GC1150	186.657883	18.144876	23.339 ± 0.020	0.98 ± 0.05	0.58 ± 0.03
GC1151	186.658401	17.905153	23.219 ± 0.018	1.39 ± 0.06	0.89 ± 0.02
GC1152	186.659195	18.252762	20.708 ± 0.003	0.94 ± 0.01	0.63 ± 0.00
GC1153	186.660172	17.956993	21.199 ± 0.004	1.17 ± 0.01	0.66 ± 0.01
GC1154	186.661240	18.356798	22.023 ± 0.007	1.29 ± 0.02	0.90 ± 0.01
GC1155	186.662048	17.750452	22.674 ± 0.012	0.93 ± 0.03	0.64 ± 0.02
GC1156	186.664642	17.641361	21.061 ± 0.004	1.10 ± 0.01	0.71 ± 0.00
GC1157	186.665543	18.133924	23.134 ± 0.017	1.04 ± 0.04	0.57 ± 0.03
GC1158	186.666168	17.934540	23.489 ± 0.023	1.09 ± 0.06	0.62 ± 0.03
GC1159	186.667068	17.891315	22.004 ± 0.007	1.03 ± 0.02	0.66 ± 0.01
GC1160	186.667099	18.297802	22.624 ± 0.011	1.56 ± 0.04	0.86 ± 0.01
GC1161	186.667633	18.389181	23.320 ± 0.019	1.83 ± 0.10	1.09 ± 0.02
GC1162	186.668259	18.371450	22.697 ± 0.011	1.12 ± 0.03	0.66 ± 0.02
GC1163	186.668427	17.917429	22.329 ± 0.009	1.44 ± 0.03	0.87 ± 0.01
GC1164	186.668716	17.709730	23.080 ± 0.016	1.10 ± 0.04	0.69 ± 0.02
GC1165	186.669632	17.952892	21.866 ± 0.007	1.78 ± 0.03	1.17 ± 0.01
GC1166	186.669678	18.265085	22.615 ± 0.011	1.21 ± 0.03	0.79 ± 0.01
GC1167	186.671799	17.980045	21.739 ± 0.006	1.78 ± 0.03	1.10 ± 0.01
GC1168	186.671906	17.691685	20.803 ± 0.003	1.82 ± 0.01	1.15 ± 0.00

Table A.1: (cont'd)

ID	α (J2000) (deg)	δ (J2000) (deg)	g (mag)	$u-g$ (mag)	$g-i$ (mag)
GC1169	186.673813	18.024693	23.507 ± 0.023	0.97 ± 0.06	0.69 ± 0.03
GC1170	186.674454	17.722919	23.470 ± 0.022	1.07 ± 0.06	0.59 ± 0.03
GC1171	186.678680	18.139526	21.945 ± 0.007	1.26 ± 0.02	0.65 ± 0.01
GC1172	186.679123	17.597565	22.799 ± 0.013	1.04 ± 0.03	0.56 ± 0.02
GC1173	186.679367	17.880215	21.932 ± 0.007	1.12 ± 0.02	0.63 ± 0.01
GC1174	186.682388	17.600506	23.372 ± 0.021	1.08 ± 0.06	0.58 ± 0.03
GC1175	186.682892	18.433096	21.015 ± 0.004	1.16 ± 0.01	0.72 ± 0.00
GC1176	186.683350	17.730776	21.652 ± 0.005	1.80 ± 0.02	1.13 ± 0.01
GC1177	186.685425	18.105450	22.868 ± 0.014	1.30 ± 0.04	0.75 ± 0.02
GC1178	186.686691	18.032442	21.803 ± 0.006	1.67 ± 0.03	1.11 ± 0.01
GC1179	186.687241	18.532036	21.739 ± 0.006	1.14 ± 0.02	0.89 ± 0.01
GC1180	186.688553	18.554384	22.491 ± 0.010	0.99 ± 0.03	0.69 ± 0.01
GC1181	186.689026	17.970093	23.578 ± 0.025	1.48 ± 0.10	1.11 ± 0.03
GC1182	186.689392	17.617208	21.749 ± 0.006	1.22 ± 0.02	0.71 ± 0.01
GC1183	186.689682	17.805992	21.245 ± 0.004	1.07 ± 0.01	0.77 ± 0.01
GC1184	186.690720	17.706425	22.383 ± 0.009	1.79 ± 0.04	1.17 ± 0.01
GC1185	186.690857	18.240482	22.057 ± 0.007	1.04 ± 0.02	0.65 ± 0.01
GC1186	186.691025	17.906931	22.788 ± 0.013	1.78 ± 0.06	1.20 ± 0.02
GC1187	186.691177	18.432407	23.259 ± 0.018	0.93 ± 0.05	0.69 ± 0.03
GC1188	186.691223	18.036493	21.916 ± 0.007	1.27 ± 0.02	0.85 ± 0.01
GC1189	186.691940	18.470690	21.599 ± 0.005	1.26 ± 0.02	0.94 ± 0.01
GC1190	186.695023	18.107616	23.488 ± 0.023	1.62 ± 0.09	0.88 ± 0.03
GC1191	186.696487	18.227749	22.386 ± 0.009	1.22 ± 0.03	0.62 ± 0.01
GC1192	186.697983	18.501299	21.049 ± 0.004	1.80 ± 0.02	1.22 ± 0.00
GC1193	186.701706	18.311314	22.851 ± 0.013	1.52 ± 0.05	0.83 ± 0.02
GC1194	186.701843	17.875248	21.117 ± 0.004	1.27 ± 0.01	0.79 ± 0.00
GC1195	186.703430	18.518103	22.647 ± 0.011	0.83 ± 0.03	0.63 ± 0.02
GC1196	186.703918	17.592466	21.338 ± 0.005	1.22 ± 0.01	0.65 ± 0.01
GC1197	186.704178	18.325214	21.660 ± 0.006	1.55 ± 0.02	0.94 ± 0.01
GC1198	186.705307	17.996572	22.460 ± 0.010	1.33 ± 0.03	0.79 ± 0.01
GC1199	186.705826	18.463526	22.627 ± 0.011	1.59 ± 0.05	1.15 ± 0.01
GC1200	186.706604	17.696272	22.914 ± 0.014	1.23 ± 0.04	0.65 ± 0.02
GC1201	186.708542	18.049170	22.202 ± 0.008	1.37 ± 0.03	0.79 ± 0.01
GC1202	186.709473	17.986015	22.714 ± 0.012	1.74 ± 0.06	1.09 ± 0.01
GC1203	186.712860	18.455263	22.535 ± 0.010	1.87 ± 0.05	1.22 ± 0.01
GC1204	186.713928	18.460135	23.422 ± 0.020	1.37 ± 0.07	0.78 ± 0.03
GC1205	186.715485	17.783478	23.356 ± 0.020	0.89 ± 0.05	0.68 ± 0.03
GC1206	186.716629	18.437683	21.993 ± 0.007	0.88 ± 0.02	0.60 ± 0.01
GC1207	186.718369	17.785284	23.329 ± 0.020	1.15 ± 0.06	0.66 ± 0.03
GC1208	186.719086	17.715090	22.741 ± 0.012	1.00 ± 0.03	0.55 ± 0.02
GC1209	186.719559	17.875240	23.493 ± 0.023	1.36 ± 0.08	0.87 ± 0.03
GC1210	186.720108	18.037567	20.795 ± 0.003	1.12 ± 0.01	0.67 ± 0.00
GC1211	186.720139	17.677298	22.942 ± 0.014	0.93 ± 0.04	0.75 ± 0.02
GC1212	186.721588	18.477892	23.543 ± 0.023	1.05 ± 0.06	0.68 ± 0.03
GC1213	186.722397	18.026894	21.094 ± 0.004	0.91 ± 0.01	0.59 ± 0.01
GC1214	186.723984	17.993128	22.875 ± 0.014	1.17 ± 0.04	0.68 ± 0.02
GC1215	186.727295	18.571186	20.563 ± 0.003	1.65 ± 0.01	1.24 ± 0.00
GC1216	186.727524	17.743113	22.275 ± 0.009	0.95 ± 0.02	0.56 ± 0.01

Table A.1: (cont'd)

ID	α (J2000) (deg)	δ (J2000) (deg)	g (mag)	$u-g$ (mag)	$g-i$ (mag)
GC1217	186.727951	17.859459	20.453 ± 0.003	1.05 ± 0.01	0.66 ± 0.00
GC1218	186.730042	18.090088	21.751 ± 0.006	0.94 ± 0.02	0.70 ± 0.01
GC1219	186.732803	18.312447	22.105 ± 0.008	1.33 ± 0.02	0.78 ± 0.01
GC1220	186.732910	18.497265	20.901 ± 0.003	1.57 ± 0.01	1.13 ± 0.00
GC1221	186.737045	18.176632	22.899 ± 0.014	1.12 ± 0.04	0.63 ± 0.02
GC1222	186.739182	18.146914	22.830 ± 0.013	1.35 ± 0.04	0.71 ± 0.02
GC1223	186.739243	18.127340	22.813 ± 0.013	1.12 ± 0.04	0.58 ± 0.02
GC1224	186.740082	18.370474	22.947 ± 0.014	1.24 ± 0.05	0.85 ± 0.02
GC1225	186.743515	18.410070	20.937 ± 0.003	1.18 ± 0.01	0.75 ± 0.00
GC1226	186.743805	17.733877	23.267 ± 0.019	1.57 ± 0.07	0.98 ± 0.02
GC1227	186.755783	18.534094	22.633 ± 0.013	0.88 ± 0.03	0.56 ± 0.02
GC1228	186.756622	18.468281	22.637 ± 0.013	0.83 ± 0.03	0.65 ± 0.02
GC1229	186.758987	18.013193	23.563 ± 0.025	1.25 ± 0.08	0.67 ± 0.04
GC1230	186.760803	18.540121	22.692 ± 0.011	1.01 ± 0.03	0.60 ± 0.02
GC1231	186.761276	18.175879	21.471 ± 0.005	0.93 ± 0.01	0.59 ± 0.01
GC1232	186.762512	18.229874	21.512 ± 0.005	1.02 ± 0.01	0.62 ± 0.01
GC1233	186.765106	18.398874	21.961 ± 0.007	1.67 ± 0.03	1.03 ± 0.01
GC1234	186.768173	18.409340	23.235 ± 0.017	0.98 ± 0.04	0.72 ± 0.03
GC1235	186.768494	17.914871	21.714 ± 0.006	0.90 ± 0.01	0.58 ± 0.01
GC1236	186.768997	17.853781	22.089 ± 0.007	1.50 ± 0.03	0.85 ± 0.01
GC1237	186.772369	18.450064	23.085 ± 0.015	1.07 ± 0.04	0.64 ± 0.02
GC1238	186.772568	18.245413	23.132 ± 0.017	1.29 ± 0.05	0.75 ± 0.02
GC1239	186.772598	17.660084	21.500 ± 0.005	1.50 ± 0.02	1.08 ± 0.01
GC1240	186.772964	18.067513	21.671 ± 0.006	1.24 ± 0.02	0.74 ± 0.01
GC1241	186.773972	17.994383	21.137 ± 0.004	1.26 ± 0.01	0.82 ± 0.00
GC1242	186.774948	17.859894	20.845 ± 0.003	0.98 ± 0.01	0.56 ± 0.00
GC1243	186.775665	18.063763	23.330 ± 0.020	0.98 ± 0.05	0.83 ± 0.03
GC1244	186.777298	18.390579	23.305 ± 0.018	1.41 ± 0.07	0.92 ± 0.02
GC1245	186.779175	18.458683	22.551 ± 0.010	1.08 ± 0.03	0.76 ± 0.01
GC1246	186.782043	18.289982	22.475 ± 0.010	1.00 ± 0.03	0.68 ± 0.01
GC1247	186.782120	18.304462	20.781 ± 0.003	1.67 ± 0.01	1.05 ± 0.00
GC1248	186.782120	18.492270	21.967 ± 0.007	0.87 ± 0.02	0.57 ± 0.01
GC1249	186.782730	18.399548	21.296 ± 0.004	1.01 ± 0.01	0.73 ± 0.01
GC1250	186.782898	18.575066	21.694 ± 0.005	1.14 ± 0.02	0.78 ± 0.01
GC1251	186.785995	18.410990	21.507 ± 0.005	1.75 ± 0.02	1.18 ± 0.01
GC1252	186.786011	17.973274	22.858 ± 0.013	1.07 ± 0.04	0.62 ± 0.02
GC1253	186.786789	18.469021	23.070 ± 0.015	1.07 ± 0.04	0.71 ± 0.02
GC1254	186.787247	17.909302	22.739 ± 0.012	1.15 ± 0.04	0.77 ± 0.02
GC1255	186.791473	18.163555	22.181 ± 0.008	1.11 ± 0.02	0.76 ± 0.01
GC1256	186.791992	18.403400	22.877 ± 0.013	1.38 ± 0.04	0.96 ± 0.02
GC1257	186.792221	18.178720	23.585 ± 0.024	1.60 ± 0.10	1.01 ± 0.03
GC1258	186.794250	17.927475	22.510 ± 0.010	1.07 ± 0.03	0.65 ± 0.01
GC1259	186.795074	18.418264	22.935 ± 0.014	1.79 ± 0.06	1.20 ± 0.02
GC1260	186.795166	17.968782	21.794 ± 0.006	1.46 ± 0.02	1.02 ± 0.01
GC1261	186.795761	17.850885	22.520 ± 0.010	1.43 ± 0.04	0.77 ± 0.01
GC1262	186.798447	18.398794	22.914 ± 0.014	1.41 ± 0.05	0.83 ± 0.02
GC1263	186.798950	18.011440	22.688 ± 0.012	1.17 ± 0.03	0.74 ± 0.02
GC1264	186.804596	18.396557	23.166 ± 0.017	1.04 ± 0.04	0.67 ± 0.03

Table A.1: (cont'd)

ID	α (J2000) (deg)	δ (J2000) (deg)	g (mag)	$u-g$ (mag)	$g-i$ (mag)
GC1265	186.804672	18.111612	20.747 ± 0.003	0.90 ± 0.01	0.61 ± 0.00
GC1266	186.805756	17.952137	22.259 ± 0.008	1.01 ± 0.02	0.62 ± 0.01
GC1267	186.807129	17.897427	22.219 ± 0.008	0.98 ± 0.02	0.66 ± 0.01
GC1268	186.808762	18.015795	21.914 ± 0.007	1.61 ± 0.03	1.21 ± 0.01
GC1269	186.809006	17.757652	20.762 ± 0.003	1.34 ± 0.01	0.73 ± 0.00
GC1270	186.809189	18.385592	22.090 ± 0.007	1.21 ± 0.02	0.85 ± 0.01
GC1271	186.809418	17.789562	23.041 ± 0.016	1.63 ± 0.07	0.94 ± 0.02
GC1272	186.809647	18.180969	22.403 ± 0.009	1.36 ± 0.03	0.87 ± 0.01
GC1273	186.812027	17.907091	20.637 ± 0.003	1.38 ± 0.01	1.08 ± 0.00
GC1274	186.813522	18.067936	22.908 ± 0.014	1.33 ± 0.05	0.80 ± 0.02
GC1275	186.814453	17.911343	22.600 ± 0.011	1.45 ± 0.04	0.93 ± 0.01
GC1276	186.814713	18.370832	23.524 ± 0.022	1.22 ± 0.07	0.66 ± 0.03
GC1277	186.820465	18.451956	22.871 ± 0.013	1.03 ± 0.04	0.74 ± 0.02
GC1278	186.822876	18.155327	22.694 ± 0.012	1.18 ± 0.03	0.71 ± 0.02
GC1279	186.823700	18.126530	21.943 ± 0.007	1.21 ± 0.02	0.80 ± 0.01
GC1280	186.824234	18.187031	22.186 ± 0.008	1.38 ± 0.03	0.79 ± 0.01
GC1281	186.825684	18.161016	21.262 ± 0.004	1.07 ± 0.01	0.63 ± 0.01
GC1282	186.826065	18.519146	20.160 ± 0.002	1.64 ± 0.01	1.09 ± 0.00
GC1283	186.826462	18.299479	21.294 ± 0.004	1.10 ± 0.01	0.77 ± 0.01
GC1284	186.826813	18.448339	22.817 ± 0.014	1.64 ± 0.06	1.09 ± 0.02
GC1285	186.827881	18.293285	20.266 ± 0.002	1.09 ± 0.01	0.73 ± 0.00
GC1286	186.829803	17.746670	22.113 ± 0.008	1.67 ± 0.03	0.92 ± 0.01
GC1287	186.830048	18.078939	21.835 ± 0.006	1.07 ± 0.02	0.68 ± 0.01
GC1288	186.830734	17.797390	21.222 ± 0.004	1.11 ± 0.01	0.75 ± 0.01
GC1289	186.835388	17.587574	22.786 ± 0.019	1.70 ± 0.10	1.16 ± 0.02
GC1290	186.835693	18.033039	22.172 ± 0.008	0.92 ± 0.02	0.64 ± 0.01
GC1291	186.835754	18.121576	21.932 ± 0.007	0.88 ± 0.02	0.57 ± 0.01
GC1292	186.836319	18.152273	22.807 ± 0.013	0.99 ± 0.03	0.56 ± 0.02
GC1293	186.836639	18.205160	23.085 ± 0.016	1.53 ± 0.06	0.92 ± 0.02
GC1294	186.838089	18.289968	22.243 ± 0.008	1.27 ± 0.02	0.69 ± 0.01
GC1295	186.841232	18.237436	20.631 ± 0.003	1.16 ± 0.01	0.74 ± 0.00
GC1296	186.844742	18.050741	21.136 ± 0.004	1.07 ± 0.01	0.79 ± 0.00
GC1297	186.845169	18.041046	23.205 ± 0.018	1.06 ± 0.05	0.72 ± 0.02
GC1298	186.847168	18.170343	21.490 ± 0.005	0.84 ± 0.01	0.61 ± 0.01
GC1299	186.848465	18.408520	22.400 ± 0.009	0.95 ± 0.02	0.77 ± 0.01
GC1300	186.848480	18.186607	23.122 ± 0.016	1.48 ± 0.06	1.00 ± 0.02
GC1301	186.849243	17.781591	21.362 ± 0.005	1.50 ± 0.02	0.80 ± 0.01
GC1302	186.849655	18.267473	21.856 ± 0.006	1.24 ± 0.02	0.87 ± 0.01
GC1303	186.850800	18.513407	23.519 ± 0.022	1.31 ± 0.07	0.99 ± 0.03
GC1304	186.850952	18.218571	23.144 ± 0.017	0.98 ± 0.04	0.59 ± 0.02
GC1305	186.851883	18.278088	22.151 ± 0.008	1.06 ± 0.02	0.71 ± 0.01
GC1306	186.852081	18.457487	23.329 ± 0.019	1.00 ± 0.05	0.62 ± 0.03
GC1307	186.852264	18.148077	22.647 ± 0.011	1.52 ± 0.04	0.95 ± 0.01
GC1308	186.852936	18.262205	21.316 ± 0.004	1.11 ± 0.01	0.75 ± 0.01
GC1309	186.853088	18.106298	23.512 ± 0.023	1.13 ± 0.06	0.65 ± 0.03
GC1310	186.857529	17.957178	22.196 ± 0.008	1.40 ± 0.03	0.85 ± 0.01
GC1311	186.857574	18.232792	21.371 ± 0.004	1.06 ± 0.01	0.73 ± 0.01
GC1312	186.858658	18.547276	21.902 ± 0.006	1.55 ± 0.02	0.94 ± 0.01

Table A.1: (cont'd)

ID	α (J2000) (deg)	δ (J2000) (deg)	g (mag)	$u-g$ (mag)	$g-i$ (mag)
GC1313	186.859161	18.007404	23.167 ± 0.017	1.53 ± 0.07	0.94 ± 0.02
GC1314	186.860031	18.124468	22.796 ± 0.013	1.18 ± 0.04	0.71 ± 0.02
GC1315	186.861038	17.965334	23.264 ± 0.019	1.06 ± 0.05	0.70 ± 0.03
GC1316	186.862411	18.081169	22.334 ± 0.009	1.13 ± 0.03	0.86 ± 0.01
GC1317	186.863800	18.471836	22.950 ± 0.014	1.18 ± 0.04	0.67 ± 0.02
GC1318	186.865402	18.042542	21.453 ± 0.005	1.58 ± 0.02	0.93 ± 0.01

Table A.2. Lick Line Indices from CN_1 to Mg_2 of M85 GCs, M85-HCC1, and M85 Nucleus

ID	CN_1 (mag)	CN_2 (mag)	Ca4227 (Å)	G4300 (Å)	Fe4383 (Å)	Ca4455 (Å)	Fe4531 (Å)	Fe4668 (Å)	Hβ (Å)	Fe5015 (Å)	Mg_1 (mag)	Mg_2 (mag)
M85-GC01	−0.249	−0.250	−5.135	1.928	6.233	2.572	−0.671	8.623	1.270	3.517	0.149	0.273
M85-GC02	0.027	0.094	−0.298	1.888	4.607	4.489	5.904	−4.517	1.712	2.954	−0.028	0.118
M85-GC03	−0.077	0.086	−9.722	6.679	8.137	6.090	−3.703	2.300	3.295	0.555	0.096	0.204
M85-GC04	−0.280	−0.253	−1.815	−0.027	7.378	−0.033	1.548	−8.970	3.561	−0.051	−0.033	0.106
M85-GC05	−0.263	−0.209	−1.256	3.491	3.057	−1.011	0.544	1.648	1.958	7.707	0.092	0.131
M85-GC06	−0.061	−0.018	0.942	−5.269	6.957	−1.214	3.114	2.448	2.003	1.796	0.017	0.185
M85-GC07	−0.192	−0.101	1.814	−4.453	3.963	1.635	5.419	−3.850	2.868	−1.710	0.029	0.137
M85-GC08	−0.040	0.011	0.058	1.518	4.268	−0.002	3.139	7.686	3.284	4.144	0.043	0.199
M85-GC09	−0.292	0.009	−0.628	−2.134	6.875	−0.257	−3.265	−3.062	4.006	−0.892	0.045	0.093
M85-GC10	−0.027	0.002	−0.034	−1.019	5.193	0.853	2.266	2.745	3.533	4.095	0.015	0.179
M85-GC11	−0.146	−0.083	−0.992	2.358	2.144	1.036	1.929	−0.479	1.316	1.107	0.083	0.243
M85-GC12	−0.176	−0.132	−1.858	−4.666	1.925	−0.837	−1.261	2.216	3.872	−0.549	0.034	0.056
M85-GC13	−0.197	−0.186	0.676	4.288	10.231	0.652	0.269	−5.248	1.215	1.326	0.005	0.126
M85-GC14	−0.216	−0.193	1.747	−11.399	8.937	2.793	3.549	3.401	3.421	2.069	−0.026	0.131
M85-GC15	−0.054	0.007	−0.735	−1.218	5.873	1.215	3.323	−0.917	2.591	1.066	−0.028	0.065
M85-GC16	−0.110	−0.086	2.140	0.947	9.335	2.356	−0.712	2.650	3.023	4.261	0.048	0.191
M85-GC17	−0.183	−0.029	−1.074	−3.661	14.303	0.752	−0.955	−1.526	0.804	7.140	0.014	0.186
M85-GC18	0.106	−0.134	−2.860	5.219	−11.919	−1.031	7.300	−7.450	4.953	4.965	0.027	0.186
M85-GC19	−0.158	−0.086	0.759	−1.563	−5.579	−1.455	0.180	−2.475	2.669	4.452	−0.019	0.073
M85-GC20	0.049	−0.047	1.096	−0.764	3.346	0.259	−0.370	−2.884	1.721	6.478	0.034	0.125
M85-HCC1	−0.078	−0.029	0.695	0.114	4.077	0.723	2.729	3.964	3.694	4.110	0.040	0.188
M85-Nucleus	−0.029	0.013	0.852	2.011	5.237	0.873	3.052	5.390	3.078	4.863	0.083	0.262

Table A.3. Lick Line Indices from Mgb to Hγ_F of M85 GCs, M85-HCC1, and M85 Nucleus

ID	Mgb (Å)	Fe5270 (Å)	Fe5335 (Å)	Fe5406 (Å)	Fe5709 (Å)	Fe5782 (Å)	NaD (Å)	TiO_1 (mag)	TiO_2 (mag)	Hδ_A (Å)	Hγ_A (Å)	Hδ_F (Å)	Hγ_F (Å)
M85-GC01	3.334	4.108	1.595	2.690	0.536	−0.303	3.689	···	···	3.992	−11.067	8.445	−1.280
M85-GC02	2.286	1.204	1.134	0.766	−0.195	−0.067	0.128	0.053	−0.014	−0.007	−1.052	3.385	1.415
M85-GC03	1.012	0.937	1.638	0.526	0.237	0.537	3.319	···	···	1.086	−6.473	−1.641	3.157
M85-GC04	2.071	1.471	1.140	1.116	0.298	−0.714	−0.336	0.043	−0.010	6.157	−1.684	1.622	2.032
M85-GC05	−0.223	3.494	2.395	1.958	0.632	0.330	3.967	···	···	6.081	−8.541	4.952	0.665
M85-GC06	2.650	1.973	1.621	1.154	−0.243	0.188	0.776	0.056	−0.037	−3.951	−4.094	−0.054	−0.463
M85-GC07	1.008	0.991	−0.239	1.074	0.945	0.061	2.850	0.057	−0.048	10.821	0.334	7.102	0.549
M85-GC08	3.314	3.121	1.891	1.762	0.733	0.524	3.885	0.095	0.006	3.663	−3.612	3.889	2.481
M85-GC09	0.267	1.055	0.724	0.876	1.124	0.163	2.517	0.095	···	15.933	−3.571	5.639	2.706
M85-GC10	3.058	2.927	1.416	0.649	−0.155	0.548	3.666	0.055	0.028	2.364	−2.826	2.412	2.342
M85-GC11	3.262	2.468	1.079	1.046	0.251	0.690	3.009	0.074	0.227	7.681	−5.570	0.115	0.768
M85-GC12	0.204	−1.105	0.313	−0.677	−0.268	−0.389	2.388	0.013	···	2.083	−0.266	−1.327	0.952
M85-GC13	3.274	2.799	0.967	−0.166	0.666	0.278	−0.952	−0.010	−0.032	2.514	−8.107	0.408	1.867
M85-GC14	1.968	3.059	1.778	0.601	0.457	0.494	2.436	0.076	0.037	9.644	2.037	4.477	2.578
M85-GC15	1.154	0.734	−0.452	0.210	−0.187	−0.211	0.961	0.044	−0.044	1.372	−1.425	2.787	2.451
M85-GC16	4.172	2.981	3.054	0.697	0.869	1.391	3.631	0.042	−0.004	8.107	−3.131	4.787	3.288
M85-GC17	3.132	0.987	1.423	1.805	0.627	1.106	3.198	0.033	0.031	8.861	−6.556	6.243	1.043
M85-GC18	4.394	2.539	2.759	0.681	0.395	0.782	0.566	0.050	0.029	−8.259	−5.567	−1.949	−0.837
M85-GC19	1.409	−0.205	1.499	−0.257	−0.442	0.285	−0.249	0.050	−0.051	10.788	−6.749	5.132	−5.471
M85-GC20	2.794	2.099	1.287	1.257	0.402	−0.571	4.108	0.066	···	−11.910	4.212	−8.028	6.782
M85-HCC1	2.700	2.653	1.975	1.344	0.445	0.730	4.151	0.060	0.056	3.262	−2.431	2.751	1.786
M85-Nucleus	3.726	3.056	2.222	1.504	0.542	0.818	4.419	0.061	0.064	1.910	−5.441	2.122	0.473

Table A.4. Lick Line Index Errors from CN_1 to Mg_2 of M85 GCs, M85-HCC1, and M85 Nucleus

ID	CN_1 (mag)	CN_2 (mag)	Ca4227 (Å)	G4300 (Å)	Fe4383 (Å)	Ca4455 (Å)	Fe4531 (Å)	Fe4668 (Å)	Hβ (Å)	Fe5015 (Å)	Mg_1 (mag)	Mg_2 (mag)
M85-GC01	0.049	0.063	1.540	1.446	1.653	0.833	1.371	1.533	0.579	1.024	0.010	0.011
M85-GC02	0.044	0.053	0.809	1.197	1.842	0.760	1.290	1.794	0.536	0.937	0.010	0.011
M85-GC03	0.046	0.055	1.642	1.217	1.643	0.831	1.640	1.703	0.545	1.066	0.010	0.011
M85-GC04	0.031	0.040	0.717	1.023	1.291	0.662	1.090	1.582	0.464	0.892	0.009	0.009
M85-GC05	0.028	0.036	0.572	0.784	1.187	0.678	0.948	1.238	0.433	0.714	0.008	0.008
M85-GC06	0.025	0.031	0.455	0.895	1.077	0.627	0.788	1.004	0.351	0.647	0.006	0.007
M85-GC07	0.031	0.038	0.520	1.117	1.292	0.667	0.860	1.341	0.404	0.811	0.008	0.008
M85-GC08	0.021	0.025	0.370	0.619	0.843	0.461	0.602	0.746	0.270	0.491	0.005	0.006
M85-GC09	0.049	0.055	0.679	1.224	1.297	0.796	1.143	1.474	0.431	0.939	0.009	0.009
M85-GC10	0.013	0.016	0.246	0.416	0.521	0.281	0.401	0.543	0.187	0.353	0.004	0.004
M85-GC11	0.035	0.043	0.643	0.982	1.250	0.569	0.832	1.125	0.382	0.701	0.007	0.008
M85-GC12	0.022	0.027	0.474	0.752	1.005	0.524	0.789	0.994	0.318	0.655	0.006	0.007
M85-GC13	0.026	0.033	0.492	0.803	0.918	0.555	0.869	1.256	0.373	0.674	0.007	0.007
M85-GC14	0.031	0.039	0.518	1.380	1.014	0.553	0.787	1.106	0.365	0.715	0.007	0.008
M85-GC15	0.017	0.020	0.339	0.536	0.712	0.379	0.525	0.777	0.262	0.489	0.005	0.005
M85-GC16	0.029	0.037	0.467	0.875	0.968	0.536	0.934	1.099	0.376	0.669	0.007	0.008
M85-GC17	0.052	0.063	0.952	1.585	1.570	0.982	1.380	1.693	0.559	0.868	0.009	0.011
M85-GC18	0.055	0.075	1.315	1.356	2.798	1.133	1.165	2.009	0.545	1.039	0.010	0.012
M85-GC19	0.037	0.046	0.696	1.322	2.205	0.973	1.271	1.727	0.509	0.902	0.009	0.010
M85-GC20	0.050	0.064	1.148	1.708	2.296	1.361	1.749	2.258	0.726	1.119	0.012	0.013
M85-HCC1	0.006	0.008	0.116	0.200	0.276	0.144	0.206	0.281	0.098	0.189	0.002	0.002
M85-Nucleus	0.001	0.001	0.015	0.025	0.035	0.019	0.027	0.037	0.013	0.025	< 0.001	< 0.001

Table A.5. Lick Line Index Errors from Mgb to Hγ_F of M85 GCs, M85-HCC1, and M85 Nucleus

ID	Mgb (Å)	Fe5270 (Å)	Fe5335 (Å)	Fe5406 (Å)	Fe5709 (Å)	Fe5782 (Å)	NaD (Å)	TiO_1 (mag)	TiO_2 (mag)	Hδ_A (Å)	Hγ_A (Å)	Hδ_F (Å)	Hγ_F (Å)
M85-GC01	0.428	0.420	0.464	0.318	0.231	0.228	0.252	···	···	1.785	1.574	0.971	0.916
M85-GC02	0.423	0.448	0.493	0.348	0.246	0.236	0.309	0.006	0.005	1.734	1.329	1.100	0.843
M85-GC03	0.464	0.452	0.484	0.363	0.252	0.240	0.277	···	···	1.632	1.595	1.302	0.878
M85-GC04	0.375	0.409	0.437	0.311	0.214	0.221	0.276	0.006	0.005	1.040	1.027	0.834	0.667
M85-GC05	0.360	0.328	0.360	0.261	0.195	0.186	0.209	···	···	0.991	0.926	0.709	0.523
M85-GC06	0.283	0.299	0.325	0.232	0.171	0.163	0.211	0.004	0.004	1.105	0.792	0.712	0.496
M85-GC07	0.349	0.363	0.404	0.279	0.193	0.196	0.237	0.005	0.004	0.874	0.918	0.624	0.632
M85-GC08	0.224	0.241	0.262	0.188	0.136	0.133	0.158	0.004	0.003	0.707	0.646	0.474	0.378
M85-GC09	0.394	0.395	0.443	0.307	0.212	0.215	0.255	0.006	···	1.463	1.087	1.505	0.595
M85-GC10	0.161	0.174	0.191	0.140	0.097	0.091	0.112	0.003	0.002	0.468	0.395	0.325	0.234
M85-GC11	0.299	0.307	0.340	0.242	0.176	0.167	0.207	0.005	0.003	1.105	0.995	1.009	0.579
M85-GC12	0.286	0.315	0.331	0.248	0.170	0.164	0.191	0.004	···	0.854	0.638	0.687	0.420
M85-GC13	0.281	0.304	0.343	0.250	0.164	0.164	0.210	0.005	0.004	0.958	0.954	0.743	0.523
M85-GC14	0.313	0.313	0.352	0.260	0.178	0.167	0.209	0.005	0.004	0.913	0.838	0.717	0.544
M85-GC15	0.215	0.233	0.264	0.187	0.130	0.126	0.159	0.003	0.003	0.611	0.523	0.404	0.319
M85-GC16	0.285	0.312	0.330	0.254	0.174	0.162	0.199	0.005	0.004	0.895	0.881	0.663	0.488
M85-GC17	0.407	0.447	0.472	0.320	0.226	0.207	0.261	0.006	0.005	1.580	1.547	1.085	0.921
M85-GC18	0.427	0.460	0.483	0.374	0.250	0.238	0.303	0.007	0.005	2.403	1.550	1.480	0.999
M85-GC19	0.415	0.463	0.482	0.356	0.240	0.228	0.294	0.006	0.005	1.050	1.281	0.835	0.907
M85-GC20	0.507	0.535	0.568	0.413	0.288	0.286	0.314	0.007	···	2.493	1.569	1.790	0.947
M85-HCC1	0.087	0.091	0.099	0.073	0.053	0.050	0.061	0.001	0.001	0.224	0.200	0.157	0.123
M85-Nucleus	0.012	0.012	0.013	0.010	0.007	0.007	0.008	< 0.001	< 0.001	0.030	0.028	0.020	0.017

Table A.6: Spectroscopic and photometric properties of foreground stars and background galaxies

ID	α (J2000) (deg)	δ (J2000) (deg)	i^a (mag)	$(g-i)^a$ (mag)	v_r (km s^{-1})
Star001	185.835114	18.226645	20.423 ± 0.004	0.689 ± 0.006	-121 ± 40
Star002	185.835785	18.116449	20.406 ± 0.004	0.849 ± 0.006	0 ± 22
Star003	185.839340	18.155159	20.080 ± 0.002	1.005 ± 0.004	105 ± 20
Star004	185.849579	18.077505	20.706 ± 0.004	0.789 ± 0.006	154 ± 37
Star005	185.860168	17.903006	20.527 ± 0.003	1.140 ± 0.006	58 ± 28
Star006	185.863434	18.273386	20.033 ± 0.002	0.608 ± 0.004	149 ± 21
Star007	185.868011	18.082602	20.542 ± 0.004	1.110 ± 0.007	165 ± 27
Star008	185.886322	18.108820	20.847 ± 0.004	0.816 ± 0.007	4 ± 36
Star009	185.890579	18.215181	20.552 ± 0.003	0.624 ± 0.005	-139 ± 48
Star010	185.892273	18.367609	19.594 ± 0.002	0.670 ± 0.003	81 ± 13
Star011	185.892609	18.149979	19.429 ± 0.002	0.822 ± 0.003	396 ± 14
Star012	185.900223	18.316135	21.519 ± 0.007	1.159 ± 0.014	91 ± 60
Star013	185.902802	18.223606	18.539 ± 0.001	0.662 ± 0.002	-23 ± 9
Star014	185.911682	18.111792	20.155 ± 0.002	0.802 ± 0.004	99 ± 24
Star015	185.916626	17.791079	19.989 ± 0.002	0.878 ± 0.004	212 ± 40
Star016	185.922150	17.887087	18.846 ± 0.001	0.800 ± 0.002	3 ± 10
Star017	185.926453	18.298052	19.484 ± 0.002	0.629 ± 0.003	100 ± 19
Star018	185.931595	17.857603	21.711 ± 0.009	1.114 ± 0.016	0 ± 61
Star019	185.939957	18.230825	21.184 ± 0.006	0.718 ± 0.009	-119 ± 40
Star020	185.940125	18.146074	20.859 ± 0.004	0.751 ± 0.007	-228 ± 23
Star021	185.950790	18.130808	18.225 ± 0.001	1.048 ± 0.002	96 ± 10
Star022	185.955856	18.486605	18.856 ± 0.001	0.758 ± 0.002	-13 ± 6
Star023	185.969986	17.948118	20.447 ± 0.003	0.979 ± 0.006	-50 ± 34
Star024	185.970352	17.918602	19.683 ± 0.002	0.602 ± 0.003	53 ± 12
Star025	185.970840	18.042912	19.303 ± 0.001	0.900 ± 0.003	82 ± 10
Star026	185.973541	18.257473	20.720 ± 0.004	1.152 ± 0.007	-17 ± 29
Star027	185.976898	18.271927	19.735 ± 0.002	0.890 ± 0.003	-80 ± 14
Star028	185.987503	18.313053	20.193 ± 0.002	1.159 ± 0.005	-115 ± 37
Star029	185.990311	18.463867	20.214 ± 0.003	0.671 ± 0.004	139 ± 23
Star030	185.991684	17.967123	18.969 ± 0.001	1.021 ± 0.002	2 ± 10
Star031	185.993088	18.278391	20.673 ± 0.004	0.903 ± 0.006	281 ± 27
Star032	186.001465	18.433458	18.772 ± 0.001	0.884 ± 0.002	56 ± 11
Star033	186.002411	18.246712	19.733 ± 0.002	0.838 ± 0.003	40 ± 18
Star034	186.006088	17.872530	20.575 ± 0.004	0.800 ± 0.006	102 ± 19
Star035	186.009415	18.271671	20.938 ± 0.005	0.645 ± 0.007	156 ± 42
Star036	186.012085	17.912750	21.557 ± 0.008	0.695 ± 0.011	-32 ± 63
Star037	186.012360	18.421362	20.924 ± 0.004	0.814 ± 0.007	-28 ± 32
Star038	186.015060	17.789724	19.772 ± 0.002	0.606 ± 0.003	18 ± 23
Star039	186.016449	18.068935	17.996 ± 0.001	0.626 ± 0.001	18 ± 7
Star040	186.017563	18.065155	20.078 ± 0.002	1.102 ± 0.005	78 ± 16
Star041	186.019287	17.747484	18.137 ± 0.001	0.686 ± 0.001	-41 ± 6
Star042	186.021561	18.173914	20.958 ± 0.005	0.747 ± 0.007	-132 ± 26
Star043	186.031403	18.427856	19.256 ± 0.001	0.937 ± 0.003	114 ± 12
Star044	186.033173	17.857197	20.006 ± 0.002	0.789 ± 0.004	72 ± 14
Star045	186.037277	18.243841	19.612 ± 0.002	1.012 ± 0.003	-4 ± 11
Star046	186.047760	18.124245	20.299 ± 0.003	0.714 ± 0.004	138 ± 31

Table A.6: (cont'd)

ID	α (J2000) (deg)	δ (J2000) (deg)	i^a (mag)	$(g-i)^a$ (mag)	v_r (km s^{-1})
Star047	186.054871	18.030945	19.360 ± 0.001	0.727 ± 0.003	-35 ± 15
Star048	186.058350	18.058609	21.835 ± 0.011	0.605 ± 0.015	-207 ± 53
Star049	186.066772	17.781504	20.551 ± 0.004	0.579 ± 0.006	-2 ± 52
Star050	186.071915	18.196117	20.361 ± 0.003	0.837 ± 0.005	41 ± 33
Star051	186.073441	17.760057	18.968 ± 0.001	0.585 ± 0.002	-70 ± 12
Star052	186.075317	17.741087	20.970 ± 0.005	0.705 ± 0.007	21 ± 57
Star053	186.076706	18.590166	19.892 ± 0.004	0.996 ± 0.006	-139 ± 17
Star054	186.083878	18.275703	20.233 ± 0.003	0.842 ± 0.005	114 ± 25
Star055	186.086487	18.185928	19.272 ± 0.001	0.762 ± 0.002	-54 ± 20
Star056	186.090393	18.009836	18.085 ± 0.001	0.856 ± 0.001	63 ± 7
Star057	186.090836	17.737198	19.657 ± 0.002	1.043 ± 0.003	59 ± 16
Star058	186.094086	18.218548	20.802 ± 0.004	0.618 ± 0.006	108 ± 29
Star059	186.095261	17.923819	20.350 ± 0.003	0.664 ± 0.005	-66 ± 26
Star060	186.095535	17.979103	19.122 ± 0.001	1.003 ± 0.002	-11 ± 10
Star061	186.095825	18.405609	18.070 ± 0.001	0.693 ± 0.001	46 ± 5
Star062	186.103561	18.223019	20.787 ± 0.004	0.580 ± 0.006	-97 ± 26
Star063	186.105545	18.518892	19.752 ± 0.002	0.678 ± 0.003	104 ± 16
Star064	186.108093	18.429928	20.544 ± 0.003	0.585 ± 0.005	-15 ± 35
Star065	186.111404	17.760185	20.011 ± 0.002	0.647 ± 0.004	-69 ± 18
Star066	186.112030	17.866674	18.965 ± 0.001	0.615 ± 0.002	67 ± 17
Star067	186.112534	18.484570	20.768 ± 0.004	0.598 ± 0.006	9 ± 41
Star068	186.116608	18.210732	20.242 ± 0.003	0.631 ± 0.004	208 ± 24
Star069	186.117584	18.406212	21.712 ± 0.009	0.646 ± 0.013	88 ± 60
Star070	186.122086	18.436558	21.003 ± 0.005	0.541 ± 0.007	64 ± 24
Star071	186.123703	18.035933	18.449 ± 0.001	0.910 ± 0.002	-11 ± 8
Star072	186.125015	18.084366	20.286 ± 0.003	0.832 ± 0.005	125 ± 25
Star073	186.125870	18.046839	20.378 ± 0.003	0.747 ± 0.005	85 ± 28
Star074	186.130737	18.370806	21.505 ± 0.007	0.654 ± 0.011	79 ± 63
Star075	186.131012	17.691833	20.817 ± 0.004	0.750 ± 0.007	-33 ± 33
Star076	186.134506	18.216639	21.091 ± 0.005	0.698 ± 0.008	80 ± 75
Star077	186.134811	18.118006	18.359 ± 0.001	0.747 ± 0.001	58 ± 9
Star078	186.137512	18.094959	20.527 ± 0.003	1.174 ± 0.006	-156 ± 28
Star079	186.137512	18.208092	20.648 ± 0.004	0.583 ± 0.005	-39 ± 29
Star080	186.137650	18.354206	20.406 ± 0.004	0.859 ± 0.006	93 ± 25
Star081	186.137665	17.990139	20.322 ± 0.003	0.622 ± 0.004	-17 ± 38
Star082	186.140884	18.565172	20.324 ± 0.003	0.602 ± 0.004	-89 ± 29
Star083	186.145782	18.219984	20.362 ± 0.003	0.571 ± 0.004	-190 ± 29
Star084	186.147446	17.881308	18.309 ± 0.001	0.971 ± 0.002	89 ± 10
Star085	186.148804	17.778784	18.177 ± 0.001	0.942 ± 0.001	51 ± 9
Star086	186.149368	18.239405	18.434 ± 0.001	1.145 ± 0.002	-61 ± 13
Star087	186.150314	18.277824	18.672 ± 0.001	0.706 ± 0.002	80 ± 11
Star088	186.150711	18.073536	18.958 ± 0.001	0.990 ± 0.002	79 ± 11
Star089	186.154953	18.120216	20.081 ± 0.002	0.766 ± 0.004	22 ± 17
Star090	186.158432	18.449259	18.607 ± 0.001	0.593 ± 0.002	51 ± 10
Star091	186.164093	18.426901	18.826 ± 0.001	1.102 ± 0.002	37 ± 10
Star092	186.169556	17.977806	18.196 ± 0.001	0.862 ± 0.001	-10 ± 8
Star093	186.179977	18.580847	20.663 ± 0.005	0.572 ± 0.007	-95 ± 27
Star094	186.181061	18.331558	19.542 ± 0.003	0.818 ± 0.004	-67 ± 15

Table A.6: (cont'd)

ID	α (J2000) (deg)	δ (J2000) (deg)	i^a (mag)	$(g-i)^a$ (mag)	v_r (km s^{-1})
Star095	186.183426	17.917242	19.304 ± 0.001	0.818 ± 0.003	-13 ± 13
Star096	186.184326	18.189516	18.465 ± 0.001	0.685 ± 0.002	53 ± 10
Star097	186.188919	17.873173	20.453 ± 0.003	0.632 ± 0.005	-26 ± 27
Star098	186.191452	18.182806	19.946 ± 0.002	0.697 ± 0.003	-40 ± 20
Star099	186.191498	18.300644	20.859 ± 0.004	0.632 ± 0.007	-139 ± 35
Star100	186.194244	18.532858	20.693 ± 0.004	0.566 ± 0.006	-124 ± 39
Star101	186.201767	18.078653	18.081 ± 0.001	0.841 ± 0.001	-51 ± 7
Star102	186.204849	18.174356	19.607 ± 0.002	0.796 ± 0.003	-35 ± 15
Star103	186.205429	18.045401	20.461 ± 0.003	0.590 ± 0.005	-109 ± 20
Star104	186.207687	18.150600	20.680 ± 0.004	0.691 ± 0.006	183 ± 30
Star105	186.208801	17.775620	20.689 ± 0.004	0.902 ± 0.006	34 ± 42
Star106	186.210724	18.470188	21.857 ± 0.010	0.642 ± 0.014	309 ± 39
Star107	186.211563	17.621895	18.858 ± 0.001	1.155 ± 0.002	-84 ± 12
Star108	186.213959	18.410166	20.534 ± 0.003	0.731 ± 0.005	248 ± 24
Star109	186.214081	17.698425	18.757 ± 0.001	0.815 ± 0.002	-8 ± 8
Star110	186.214615	17.981247	18.489 ± 0.001	0.606 ± 0.002	102 ± 11
Star111	186.219284	18.465090	20.791 ± 0.004	0.632 ± 0.006	223 ± 27
Star112	186.219666	17.675690	19.330 ± 0.001	0.783 ± 0.003	102 ± 10
Star113	186.221909	18.454256	20.074 ± 0.002	0.851 ± 0.004	324 ± 36
Star114	186.227081	17.983065	19.412 ± 0.001	0.709 ± 0.003	32 ± 14
Star115	186.227783	17.882933	20.274 ± 0.003	0.614 ± 0.004	190 ± 18
Star116	186.228363	18.214205	19.873 ± 0.002	1.081 ± 0.004	-46 ± 20
Star117	186.230576	18.546295	21.120 ± 0.005	1.033 ± 0.009	-69 ± 31
Star118	186.235565	18.464970	20.076 ± 0.002	0.681 ± 0.004	-34 ± 21
Star119	186.244064	17.781054	20.053 ± 0.002	1.017 ± 0.004	96 ± 15
Star120	186.248291	17.902939	20.705 ± 0.004	0.550 ± 0.006	-49 ± 25
Star121	186.250504	18.082481	20.435 ± 0.003	0.687 ± 0.005	-76 ± 19
Star122	186.250534	18.369204	20.343 ± 0.003	0.802 ± 0.005	-113 ± 24
Star123	186.251007	17.716356	18.298 ± 0.001	0.719 ± 0.001	-39 ± 9
Star124	186.251068	17.713539	18.995 ± 0.001	0.672 ± 0.002	-4 ± 9
Star125	186.253052	17.712448	21.296 ± 0.006	0.612 ± 0.009	-107 ± 45
Star126	186.253967	17.691427	19.328 ± 0.001	0.982 ± 0.003	-9 ± 14
Star127	186.258118	18.137899	19.468 ± 0.002	1.141 ± 0.003	50 ± 17
Star128	186.259064	17.827850	18.016 ± 0.001	0.977 ± 0.001	0 ± 8
Star129	186.261200	18.325163	18.376 ± 0.001	0.831 ± 0.002	38 ± 8
Star130	186.262344	17.734337	18.463 ± 0.001	0.663 ± 0.002	-50 ± 9
Star131	186.262466	17.601152	19.202 ± 0.001	0.826 ± 0.002	-118 ± 14
Star132	186.263840	18.555840	21.695 ± 0.009	1.118 ± 0.016	-58 ± 36
Star133	186.266205	18.228367	21.294 ± 0.006	0.919 ± 0.010	-18 ± 39
Star134	186.271057	18.566977	21.085 ± 0.005	0.834 ± 0.008	-93 ± 23
Star135	186.275620	17.611370	20.710 ± 0.004	0.708 ± 0.006	-36 ± 28
Star136	186.275894	17.740608	20.707 ± 0.004	0.958 ± 0.007	-84 ± 34
Star137	186.280441	17.975748	20.143 ± 0.002	0.827 ± 0.004	217 ± 17
Star138	186.280869	17.881037	21.243 ± 0.006	0.923 ± 0.010	-60 ± 39
Star139	186.283875	18.448830	20.065 ± 0.002	0.636 ± 0.004	-58 ± 21
Star140	186.286728	18.531652	21.422 ± 0.007	1.063 ± 0.012	-142 ± 44
Star141	186.297318	18.264208	19.326 ± 0.002	0.661 ± 0.002	235 ± 16
Star142	186.299561	17.620920	20.020 ± 0.002	0.669 ± 0.004	1 ± 30

Table A.6: (cont'd)

ID	α (J2000) (deg)	δ (J2000) (deg)	i^a (mag)	$(g-i)^a$ (mag)	v_r (km s^{-1})
Star143	186.299744	17.863102	20.977 ± 0.005	0.590 ± 0.007	-55 ± 54
Star144	186.300201	18.313126	20.797 ± 0.004	0.601 ± 0.006	-5 ± 37
Star145	186.301682	18.240011	21.542 ± 0.008	0.716 ± 0.012	-96 ± 63
Star146	186.302551	18.184595	19.402 ± 0.001	1.033 ± 0.003	-24 ± 12
Star147	186.303635	17.856287	20.187 ± 0.002	0.752 ± 0.004	44 ± 19
Star148	186.304306	18.360703	20.955 ± 0.005	0.568 ± 0.007	61 ± 39
Star149	186.305695	18.320381	18.498 ± 0.001	0.705 ± 0.002	-43 ± 5
Star150	186.308853	17.656580	18.409 ± 0.001	1.059 ± 0.002	25 ± 10
Star151	186.313141	18.467440	20.970 ± 0.005	0.787 ± 0.007	-78 ± 31
Star152	186.313965	18.530323	20.197 ± 0.002	0.598 ± 0.004	-129 ± 35
Star153	186.314316	18.403135	19.492 ± 0.002	0.587 ± 0.003	-90 ± 18
Star154	186.315506	18.152666	18.087 ± 0.001	0.712 ± 0.001	-35 ± 10
Star155	186.322998	18.304373	18.903 ± 0.001	0.827 ± 0.002	-51 ± 7
Star156	186.325104	17.630995	19.007 ± 0.001	0.761 ± 0.002	-17 ± 9
Star157	186.330887	18.094978	21.590 ± 0.008	0.673 ± 0.012	133 ± 86
Star158	186.333908	18.367588	18.173 ± 0.001	0.661 ± 0.001	63 ± 7
Star159	186.334167	18.053749	18.031 ± 0.001	0.599 ± 0.001	107 ± 8
Star160	186.338089	18.573565	20.966 ± 0.005	0.712 ± 0.007	-137 ± 38
Star161	186.343994	17.872990	20.467 ± 0.003	0.584 ± 0.005	-63 ± 35
Star162	186.346268	17.751183	18.061 ± 0.001	0.697 ± 0.001	53 ± 5
Star163	186.349930	17.918514	18.554 ± 0.001	0.722 ± 0.002	17 ± 8
Star164	186.357971	18.051208	19.009 ± 0.001	0.694 ± 0.002	88 ± 9
Star165	186.358810	17.942965	20.970 ± 0.005	0.989 ± 0.008	-50 ± 35
Star166	186.359482	17.951792	21.019 ± 0.005	0.673 ± 0.007	-126 ± 74
Star167	186.360107	18.052254	20.061 ± 0.002	1.051 ± 0.004	269 ± 33
Star168	186.365845	17.929649	19.531 ± 0.002	0.599 ± 0.003	58 ± 11
Star169	186.367554	18.045042	21.408 ± 0.007	0.830 ± 0.011	-171 ± 58
Star170	186.369278	18.554214	21.336 ± 0.006	0.660 ± 0.009	-133 ± 46
Star171	186.371017	18.383181	19.108 ± 0.001	0.658 ± 0.002	41 ± 32
Star172	186.377197	18.018139	20.839 ± 0.004	0.577 ± 0.006	-64 ± 30
Star173	186.382553	18.062233	19.070 ± 0.001	0.614 ± 0.002	-38 ± 16
Star174	186.383163	18.357386	20.275 ± 0.003	0.703 ± 0.004	-36 ± 27
Star175	186.385406	18.264565	21.982 ± 0.011	0.690 ± 0.016	-106 ± 32
Star176	186.387848	17.795681	20.162 ± 0.002	0.637 ± 0.004	-27 ± 19
Star177	186.390808	17.659901	19.301 ± 0.001	1.181 ± 0.003	131 ± 14
Star178	186.391983	18.419512	21.623 ± 0.008	1.098 ± 0.014	60 ± 44
Star179	186.392807	18.468624	20.808 ± 0.004	0.749 ± 0.006	98 ± 31
Star180	186.393005	18.205725	21.524 ± 0.008	0.970 ± 0.013	-2 ± 40
Star181	186.394089	18.225124	21.066 ± 0.005	0.824 ± 0.008	38 ± 63
Star182	186.396088	17.755241	20.691 ± 0.004	1.151 ± 0.007	-113 ± 40
Star183	186.397141	17.870903	18.055 ± 0.001	0.631 ± 0.001	-61 ± 7
Star184	186.397339	18.302708	21.302 ± 0.006	0.598 ± 0.009	-174 ± 50
Star185	186.397705	18.376612	20.078 ± 0.002	0.909 ± 0.004	125 ± 23
Star186	186.399445	18.576054	18.450 ± 0.001	1.147 ± 0.002	-53 ± 12
Star187	186.401932	18.549938	19.175 ± 0.001	0.638 ± 0.002	56 ± 17
Star188	186.402054	18.199120	21.921 ± 0.011	0.792 ± 0.017	96 ± 62
Star189	186.402954	18.375116	18.432 ± 0.001	0.821 ± 0.002	-83 ± 9
Star190	186.404205	18.260937	21.495 ± 0.008	0.660 ± 0.012	19 ± 67

Table A.6: (cont'd)

ID	α (J2000) (deg)	δ (J2000) (deg)	i^a (mag)	$(g-i)^a$ (mag)	v_r (km s^{-1})
Star191	186.410873	18.564911	20.575 ± 0.004	0.617 ± 0.006	-129 ± 38
Star192	186.414719	17.929035	20.231 ± 0.003	0.594 ± 0.004	254 ± 22
Star193	186.414856	17.758152	19.511 ± 0.002	0.756 ± 0.003	57 ± 11
Star194	186.419647	18.062256	18.801 ± 0.001	0.673 ± 0.002	23 ± 8
Star195	186.421066	18.241087	21.101 ± 0.005	0.916 ± 0.009	6 ± 40
Star196	186.422302	17.891716	20.579 ± 0.004	0.707 ± 0.006	154 ± 40
Star197	186.428284	18.364119	20.922 ± 0.004	0.633 ± 0.007	-82 ± 54
Star198	186.435379	17.790684	20.528 ± 0.003	0.566 ± 0.005	144 ± 18
Star199	186.436203	17.606215	20.659 ± 0.004	0.596 ± 0.005	224 ± 36
Star200	186.437775	18.361656	20.072 ± 0.002	0.633 ± 0.004	242 ± 55
Star201	186.437805	18.396719	18.965 ± 0.001	0.951 ± 0.002	36 ± 9
Star202	186.443100	18.407097	21.619 ± 0.008	1.073 ± 0.014	-61 ± 25
Star203	186.443481	18.558870	21.540 ± 0.008	0.855 ± 0.012	-40 ± 29
Star204	186.446365	18.242987	21.616 ± 0.008	0.914 ± 0.013	-59 ± 51
Star205	186.450775	17.852684	18.463 ± 0.001	0.726 ± 0.002	-77 ± 13
Star206	186.450989	17.891768	18.621 ± 0.001	0.816 ± 0.002	-6 ± 6
Star207	186.453110	18.482006	19.585 ± 0.002	0.874 ± 0.003	-195 ± 16
Star208	186.453247	18.000299	19.830 ± 0.002	0.558 ± 0.003	86 ± 17
Star209	186.454758	17.920366	18.247 ± 0.001	0.774 ± 0.001	12 ± 6
Star210	186.455750	18.239456	20.087 ± 0.002	0.705 ± 0.004	236 ± 24
Star211	186.457047	18.001661	20.431 ± 0.003	0.651 ± 0.005	33 ± 47
Star212	186.457962	18.026220	21.702 ± 0.009	0.682 ± 0.013	-65 ± 94
Star213	186.459473	18.247967	21.246 ± 0.006	0.687 ± 0.009	-26 ± 40
Star214	186.459656	17.629105	20.681 ± 0.004	0.594 ± 0.006	-14 ± 37
Star215	186.463104	18.416977	21.231 ± 0.006	0.730 ± 0.009	-230 ± 64
Star216	186.463242	18.195198	20.838 ± 0.004	0.847 ± 0.007	-240 ± 24
Star217	186.464630	18.211834	21.702 ± 0.009	0.774 ± 0.013	61 ± 77
Star218	186.470215	17.872749	20.828 ± 0.004	1.083 ± 0.008	167 ± 24
Star219	186.476089	18.471931	18.804 ± 0.001	0.706 ± 0.002	-4 ± 7
Star220	186.478729	17.896111	19.860 ± 0.002	1.112 ± 0.004	70 ± 29
Star221	186.479782	18.326347	19.625 ± 0.002	0.638 ± 0.003	100 ± 14
Star222	186.481873	18.150984	20.660 ± 0.004	0.570 ± 0.006	-64 ± 25
Star223	186.485443	17.791094	21.086 ± 0.005	1.054 ± 0.009	-20 ± 32
Star224	186.485504	17.731777	21.032 ± 0.005	0.931 ± 0.008	54 ± 43
Star225	186.487595	18.125458	20.617 ± 0.004	1.063 ± 0.007	90 ± 41
Star226	186.488159	18.226004	19.240 ± 0.001	0.742 ± 0.002	260 ± 16
Star227	186.490112	17.921387	20.080 ± 0.002	0.755 ± 0.004	152 ± 21
Star228	186.496185	18.218161	19.502 ± 0.002	0.815 ± 0.003	-114 ± 32
Star229	186.497589	18.136724	20.970 ± 0.005	1.117 ± 0.009	58 ± 31
Star230	186.498306	17.856455	19.019 ± 0.001	0.703 ± 0.002	-107 ± 9
Star231	186.503052	18.372944	18.405 ± 0.001	0.617 ± 0.001	130 ± 7
Star232	186.506561	18.131683	18.100 ± 0.001	0.929 ± 0.001	-1 ± 8
Star233	186.508057	17.679562	17.979 ± 0.001	0.599 ± 0.001	22 ± 4
Star234	186.514618	17.917330	20.424 ± 0.003	0.705 ± 0.005	12 ± 30
Star235	186.514664	18.025400	20.462 ± 0.003	0.684 ± 0.005	-93 ± 52
Star236	186.517563	17.904106	20.981 ± 0.005	1.140 ± 0.009	-242 ± 48
Star237	186.518036	17.945929	20.564 ± 0.003	0.959 ± 0.006	-118 ± 81
Star238	186.526962	18.206947	21.552 ± 0.009	0.704 ± 0.013	-67 ± 44

Table A.6: (cont'd)

ID	α (J2000) (deg)	δ (J2000) (deg)	i^a (mag)	$(g-i)^a$ (mag)	v_r (km s^{-1})
Star239	186.532578	18.237913	21.053 ± 0.005	0.732 ± 0.008	-43 ± 43
Star240	186.532852	18.221842	22.016 ± 0.011	0.777 ± 0.017	-54 ± 59
Star241	186.534866	18.143871	20.592 ± 0.004	0.770 ± 0.006	201 ± 28
Star242	186.536545	17.968000	20.961 ± 0.005	0.835 ± 0.008	134 ± 40
Star243	186.536728	17.870220	18.737 ± 0.001	0.728 ± 0.002	-28 ± 9
Star244	186.541473	18.031805	20.383 ± 0.003	0.656 ± 0.005	7 ± 24
Star245	186.550156	17.764580	20.361 ± 0.003	0.609 ± 0.005	-17 ± 22
Star246	186.550949	18.090324	21.467 ± 0.008	1.080 ± 0.013	264 ± 91
Star247	186.553589	18.183186	18.619 ± 0.001	0.683 ± 0.002	213 ± 10
Star248	186.560181	17.703358	20.864 ± 0.004	0.604 ± 0.007	213 ± 20
Star249	186.563889	18.265444	20.954 ± 0.005	0.946 ± 0.008	-59 ± 25
Star250	186.567841	18.009367	19.919 ± 0.002	0.795 ± 0.004	150 ± 11
Star251	186.569672	18.519770	21.080 ± 0.005	0.983 ± 0.009	-4 ± 61
Star252	186.570267	18.082718	20.084 ± 0.002	0.604 ± 0.004	28 ± 42
Star253	186.570450	18.134842	20.201 ± 0.003	0.719 ± 0.004	352 ± 35
Star254	186.573227	18.082047	21.370 ± 0.007	0.704 ± 0.010	-6 ± 30
Star255	186.579178	18.009644	20.030 ± 0.002	0.851 ± 0.004	32 ± 23
Star256	186.581390	17.931847	18.126 ± 0.001	0.728 ± 0.001	21 ± 8
Star257	186.581619	18.395264	21.857 ± 0.010	0.855 ± 0.015	2 ± 42
Star258	186.582031	17.674488	20.304 ± 0.003	0.667 ± 0.005	171 ± 48
Star259	186.593277	18.464266	19.791 ± 0.002	1.137 ± 0.004	102 ± 15
Star260	186.594971	18.539198	20.509 ± 0.003	1.094 ± 0.006	86 ± 30
Star261	186.596481	18.319639	20.401 ± 0.003	0.916 ± 0.005	-167 ± 22
Star262	186.596848	17.868483	20.893 ± 0.004	0.755 ± 0.007	185 ± 25
Star263	186.596985	18.205564	20.491 ± 0.003	0.977 ± 0.006	-84 ± 25
Star264	186.597839	18.572090	19.798 ± 0.002	0.675 ± 0.003	-7 ± 14
Star265	186.598526	18.171112	21.240 ± 0.006	0.808 ± 0.009	-85 ± 37
Star266	186.599609	18.363358	18.069 ± 0.001	0.688 ± 0.001	1 ± 13
Star267	186.599686	18.481447	19.620 ± 0.002	0.925 ± 0.003	-30 ± 14
Star268	186.601395	17.869905	18.731 ± 0.001	0.644 ± 0.002	-20 ± 6
Star269	186.603088	18.144537	18.714 ± 0.001	1.122 ± 0.002	172 ± 12
Star270	186.603317	17.687456	20.136 ± 0.002	1.126 ± 0.005	15 ± 36
Star271	186.609711	17.936506	18.695 ± 0.001	0.820 ± 0.002	5 ± 13
Star272	186.610138	17.784946	22.127 ± 0.013	0.934 ± 0.021	130 ± 35
Star273	186.611481	17.907864	21.491 ± 0.007	0.703 ± 0.011	115 ± 46
Star274	186.613190	18.242550	18.046 ± 0.001	0.981 ± 0.001	-65 ± 8
Star275	186.616714	17.807459	20.031 ± 0.002	0.641 ± 0.004	-12 ± 17
Star276	186.626770	17.950634	21.742 ± 0.009	0.650 ± 0.013	-18 ± 66
Star277	186.631699	18.472252	20.327 ± 0.003	0.711 ± 0.005	-19 ± 19
Star278	186.643311	17.827532	20.396 ± 0.004	0.628 ± 0.006	113 ± 17
Star279	186.647812	18.216608	18.641 ± 0.001	0.630 ± 0.002	156 ± 10
Star280	186.648483	17.778959	20.450 ± 0.003	0.597 ± 0.005	137 ± 32
Star281	186.653290	18.307880	18.321 ± 0.001	0.859 ± 0.001	45 ± 9
Star282	186.659210	18.252762	20.077 ± 0.002	0.630 ± 0.004	-12 ± 29
Star283	186.660080	17.803055	18.942 ± 0.001	0.559 ± 0.002	126 ± 8
Star284	186.660172	17.956991	20.538 ± 0.003	0.661 ± 0.005	22 ± 17
Star285	186.661255	18.356798	21.121 ± 0.005	0.902 ± 0.009	-9 ± 39
Star286	186.664627	18.125406	19.017 ± 0.001	0.555 ± 0.002	54 ± 12

Table A.6: (cont'd)

ID	α (J2000) (deg)	δ (J2000) (deg)	i^a (mag)	$(g-i)^a$ (mag)	v_r (km s^{-1})
Star287	186.671799	17.980045	20.641 ± 0.004	1.098 ± 0.007	160 ± 26
Star288	186.672852	17.781303	18.134 ± 0.001	0.782 ± 0.001	36 ± 7
Star289	186.686691	18.032433	20.695 ± 0.004	1.108 ± 0.007	-18 ± 22
Star290	186.687241	18.532036	20.848 ± 0.004	0.891 ± 0.007	79 ± 25
Star291	186.689484	18.018480	18.178 ± 0.001	0.580 ± 0.001	62 ± 9
Star292	186.689682	17.805992	20.471 ± 0.003	0.774 ± 0.005	115 ± 25
Star293	186.691940	18.470692	20.657 ± 0.004	0.943 ± 0.006	122 ± 45
Star294	186.700577	18.223402	18.063 ± 0.001	1.075 ± 0.001	-31 ± 9
Star295	186.701614	18.290800	18.139 ± 0.001	0.682 ± 0.001	194 ± 10
Star296	186.701843	17.875248	20.330 ± 0.003	0.787 ± 0.005	101 ± 16
Star297	186.704193	18.325214	20.723 ± 0.004	0.937 ± 0.007	-42 ± 28
Star298	186.705307	17.996569	21.672 ± 0.009	0.788 ± 0.013	-85 ± 55
Star299	186.706070	18.394577	19.222 ± 0.001	0.803 ± 0.002	152 ± 13
Star300	186.713364	17.812441	18.703 ± 0.001	0.954 ± 0.002	186 ± 13
Star301	186.717255	17.915987	18.736 ± 0.001	0.604 ± 0.002	-74 ± 14
Star302	186.720108	18.037567	20.130 ± 0.002	0.665 ± 0.004	-39 ± 29
Star303	186.722397	18.026894	20.502 ± 0.003	0.592 ± 0.005	35 ± 39
Star304	186.724396	18.188866	18.847 ± 0.001	0.595 ± 0.002	236 ± 13
Star305	186.727951	17.859459	19.791 ± 0.002	0.662 ± 0.003	292 ± 14
Star306	186.730042	18.090090	21.054 ± 0.006	0.697 ± 0.009	-83 ± 36
Star307	186.732819	18.312447	21.323 ± 0.006	0.783 ± 0.010	-117 ± 29
Star308	186.732910	18.497263	19.774 ± 0.002	1.126 ± 0.004	82 ± 15
Star309	186.742935	17.821636	21.421 ± 0.007	0.912 ± 0.011	3 ± 31
Star310	186.743515	18.410069	20.189 ± 0.003	0.749 ± 0.004	-62 ± 24
Star311	186.747269	18.459204	18.001 ± 0.001	0.769 ± 0.001	7 ± 6
Star312	186.747925	17.949142	21.928 ± 0.011	1.017 ± 0.018	-45 ± 55
Star313	186.762512	18.229876	20.895 ± 0.004	0.616 ± 0.007	362 ± 50
Star314	186.769699	18.109388	18.009 ± 0.001	0.729 ± 0.001	-51 ± 6
Star315	186.772964	18.067514	20.934 ± 0.005	0.737 ± 0.007	223 ± 27
Star316	186.773987	17.994383	20.313 ± 0.003	0.824 ± 0.005	70 ± 26
Star317	186.774948	17.859894	20.288 ± 0.003	0.557 ± 0.004	-25 ± 22
Star318	186.782730	18.399549	20.569 ± 0.004	0.728 ± 0.005	123 ± 28
Star319	186.784470	17.979574	18.555 ± 0.001	0.690 ± 0.002	9 ± 14
Star320	186.785980	18.410990	20.330 ± 0.003	1.177 ± 0.006	45 ± 24
Star321	186.789749	18.082958	17.999 ± 0.001	1.194 ± 0.001	-11 ± 10
Star322	186.791489	18.163553	21.426 ± 0.007	0.755 ± 0.011	13 ± 38
Star323	186.795166	17.968782	20.775 ± 0.004	1.018 ± 0.007	123 ± 38
Star324	186.804352	18.083860	19.013 ± 0.001	0.849 ± 0.002	9 ± 8
Star325	186.804672	18.111610	20.137 ± 0.002	0.610 ± 0.004	-86 ± 27
Star326	186.809647	18.180969	21.535 ± 0.008	0.868 ± 0.012	22 ± 29
Star327	186.812027	17.907089	19.556 ± 0.002	1.081 ± 0.003	116 ± 19
Star328	186.814453	17.911345	21.668 ± 0.009	0.932 ± 0.014	-38 ± 40
Star329	186.825684	18.161016	20.635 ± 0.004	0.627 ± 0.006	175 ± 26
Star330	186.827881	18.293285	19.533 ± 0.002	0.733 ± 0.003	-45 ± 11
Star331	186.830048	18.078939	21.152 ± 0.005	0.683 ± 0.008	-140 ± 46
Star332	186.832123	18.029051	18.945 ± 0.001	0.971 ± 0.002	59 ± 10
Star333	186.838089	18.289967	21.555 ± 0.008	0.687 ± 0.011	-47 ± 37
Star334	186.838516	18.142605	18.704 ± 0.001	0.884 ± 0.002	96 ± 7

Table A.6: (cont'd)

ID	α (J2000) (deg)	δ (J2000) (deg)	i^a (mag)	$(g-i)^a$ (mag)	v_r (km s^{-1})
Star335	186.841232	18.237436	19.886 ± 0.002	0.745 ± 0.004	-8 ± 12
Star336	186.844742	18.050739	20.350 ± 0.003	0.785 ± 0.005	38 ± 32
Star337	186.857574	18.232792	20.638 ± 0.004	0.733 ± 0.006	102 ± 25
Star338	186.862381	18.100967	18.149 ± 0.001	0.975 ± 0.001	107 ± 8
Gal01	185.900116	17.980145	21.834 ± 0.010	0.489 ± 0.013	50373 ± 15
Gal02	185.904617	18.043806	19.892 ± 0.002	0.955 ± 0.004	37263 ± 13
Gal03	185.906403	18.110588	21.971 ± 0.011	0.832 ± 0.017	50311 ± 11
Gal04	185.973541	18.411480	21.354 ± 0.006	0.761 ± 0.010	75329 ± 11
Gal05	185.987747	18.048506	21.319 ± 0.006	0.775 ± 0.010	47322 ± 13
Gal06	185.988388	18.061272	20.892 ± 0.004	0.689 ± 0.007	51004 ± 20
Gal07	186.019913	18.392822	21.382 ± 0.007	1.089 ± 0.012	58357 ± 45
Gal08	186.061127	18.113384	21.767 ± 0.011	0.629 ± 0.015	82108 ± 13
Gal09	186.087433	18.157852	20.186 ± 0.002	0.550 ± 0.004	80084 ± 10
Gal10	186.101013	18.062937	21.716 ± 0.009	0.640 ± 0.013	35950 ± 12
Gal11	186.103683	18.255192	21.160 ± 0.005	0.751 ± 0.008	77032 ± 17
Gal12	186.107788	18.448547	20.602 ± 0.004	0.508 ± 0.005	33281 ± 7
Gal13	186.127213	18.504505	21.654 ± 0.009	0.589 ± 0.012	40253 ± 18
Gal14	186.128876	18.090500	19.558 ± 0.002	0.644 ± 0.003	40614 ± 6
Gal15	186.141830	18.186899	20.013 ± 0.002	0.683 ± 0.004	24612 ± 7
Gal16	186.173904	17.629711	21.003 ± 0.005	0.729 ± 0.008	43171 ± 14
Gal17	186.179214	17.680815	21.433 ± 0.008	1.010 ± 0.014	63215 ± 13
Gal18	186.186264	18.306753	19.723 ± 0.002	0.751 ± 0.003	45710 ± 5
Gal19	186.194885	17.918917	20.081 ± 0.002	0.861 ± 0.004	39277 ± 7
Gal20	186.201874	17.941936	21.763 ± 0.009	0.552 ± 0.013	50472 ± 10
Gal21	186.203415	18.171402	20.661 ± 0.004	1.151 ± 0.007	45875 ± 30
Gal22	186.224869	18.305252	19.943 ± 0.002	0.621 ± 0.003	61842 ± 5
Gal23	186.229202	18.241766	21.401 ± 0.007	0.907 ± 0.011	40017 ± 30
Gal24	186.232605	18.332434	20.765 ± 0.008	85.505 ± 99.000	109397 ± 16
Gal25	186.239304	18.192448	20.977 ± 0.005	0.955 ± 0.008	83717 ± 10
Gal26	186.245468	18.372902	20.848 ± 0.004	0.755 ± 0.007	64255 ± 16
Gal27	186.257339	17.943821	18.570 ± 0.001	1.038 ± 0.002	24397 ± 14
Gal28	186.257416	18.243998	20.593 ± 0.004	0.675 ± 0.005	50347 ± 6
Gal29	186.277512	18.545589	21.015 ± 0.005	0.535 ± 0.007	63771 ± 7
Gal30	186.294037	17.928776	21.018 ± 0.006	0.729 ± 0.009	222214 ± 21
Gal31	186.306808	17.628136	21.929 ± 0.010	0.758 ± 0.016	58660 ± 15
Gal32	186.309433	17.717884	21.915 ± 0.010	0.896 ± 0.016	84162 ± 38
Gal33	186.329559	18.566311	20.904 ± 0.004	0.586 ± 0.007	88478 ± 5
Gal34	186.336273	18.398195	20.891 ± 0.004	0.612 ± 0.007	39840 ± 7
Gal35	186.342590	18.525341	21.640 ± 0.008	0.693 ± 0.012	55480 ± 8
Gal36	186.356186	18.058426	21.967 ± 0.011	0.668 ± 0.016	74952 ± 9
Gal37	186.414337	17.734072	20.679 ± 0.004	0.527 ± 0.006	33491 ± 5
Gal38	186.455551	17.807653	21.892 ± 0.010	0.607 ± 0.014	59624 ± 10
Gal39	186.471130	18.175081	20.933 ± 0.005	0.560 ± 0.007	31269 ± 8
Gal40	186.489624	18.132486	21.451 ± 0.007	0.635 ± 0.010	61856 ± 6
Gal41	186.496521	18.142906	22.015 ± 0.012	0.993 ± 0.020	75393 ± 21
Gal42	186.500183	17.855198	20.902 ± 0.004	0.500 ± 0.006	33002 ± 7
Gal43	186.512283	17.847658	21.633 ± 0.010	0.981 ± 0.017	68271 ± 13
Gal44	186.525406	17.764765	21.490 ± 0.008	0.864 ± 0.013	68469 ± 12

Table A.6: (cont'd)

ID	α (J2000) (deg)	δ (J2000) (deg)	i^a (mag)	$(g-i)^a$ (mag)	v_r (km s^{-1})
Gal45	186.532715	18.535963	21.264 ± 0.006	0.888 ± 0.010	84241 ± 14
Gal46	186.548264	18.422771	20.949 ± 0.005	0.539 ± 0.007	23183 ± 7
Gal47	186.548660	18.534914	20.278 ± 0.003	0.855 ± 0.005	63783 ± 10
Gal48	186.555923	17.742592	20.620 ± 0.004	0.558 ± 0.005	32511 ± 17
Gal49	186.575348	18.579365	21.006 ± 0.005	0.698 ± 0.007	75517 ± 12
Gal50	186.575974	17.871061	20.674 ± 0.004	0.805 ± 0.006	36116 ± 13
Gal51	186.577957	18.386339	19.785 ± 0.002	0.553 ± 0.003	23402 ± 6
Gal52	186.578552	18.188305	19.511 ± 0.002	1.047 ± 0.003	44956 ± 21
Gal53	186.590164	18.061481	21.406 ± 0.007	0.733 ± 0.010	50721 ± 8
Gal54	186.606293	18.239017	21.157 ± 0.005	0.687 ± 0.008	50428 ± 12
Gal55	186.608551	17.992174	21.467 ± 0.007	0.858 ± 0.011	44824 ± 15
Gal56	186.646713	17.972086	19.886 ± 0.002	0.688 ± 0.003	29397 ± 7
Gal57	186.647476	18.322824	19.845 ± 0.002	0.734 ± 0.003	20678 ± 13
Gal58	186.648697	17.959621	19.751 ± 0.002	0.730 ± 0.003	30299 ± 6
Gal59	186.683899	17.819330	19.796 ± 0.002	0.603 ± 0.003	17303 ± 10
Gal60	186.691238	18.220739	21.876 ± 0.010	0.595 ± 0.014	84869 ± 12
Gal61	186.712555	17.819647	21.084 ± 0.005	0.791 ± 0.008	33966 ± 9
Gal62	186.733932	18.387321	21.132 ± 0.005	0.632 ± 0.008	59405 ± 8
Gal63	186.747803	18.375273	22.120 ± 0.013	0.543 ± 0.017	91798 ± 17
Gal64	186.758743	18.443821	19.726 ± 0.002	1.296 ± 0.004	35073 ± 10
Gal65	186.775406	18.368656	21.000 ± 0.005	0.897 ± 0.008	59824 ± 8
Gal66	186.816940	18.226229	20.379 ± 0.003	0.645 ± 0.005	60610 ± 5
Gal67	186.847275	17.963545	21.754 ± 0.009	0.668 ± 0.013	84415 ± 20
Gal68	186.859879	18.150764	21.921 ± 0.011	0.627 ± 0.015	68561 ± 15

[a]CFHT/MegaCam AB magnitudes.

Table A.7: Spectroscopic and photometric properties of the GCs confirmed in this study.

ID	α (J2000) (deg)	δ (J2000) (deg)	g^a (mag)	$(g-i)^a$ (mag)	$v_{\rm r}$ (km s^{-1})	Class
GC01	185.846497	18.014795	20.407 ± 0.003	0.629 ± 0.005	489 ± 46	IGC
GC02	185.973221	17.820648	20.941 ± 0.005	0.840 ± 0.008	714 ± 105	IGC
GC03	186.040955	18.078588	20.691 ± 0.004	0.754 ± 0.006	735 ± 55	M85/BGC
GC04	186.095642	18.139322	20.314 ± 0.003	0.734 ± 0.005	999 ± 39	M85/BGC
GC05	186.153976	18.049810	20.094 ± 0.002	0.783 ± 0.004	921 ± 20	M85/BGC
GC06	186.166245	18.091394	21.026 ± 0.006	0.629 ± 0.008	882 ± 69	M85/BGC
GC07	186.168869	18.325640	21.090 ± 0.007	1.062 ± 0.010	1310 ± 71	IGC
GC08	186.221970	18.089117	20.149 ± 0.002	0.771 ± 0.004	1007 ± 24	M85/BGC
GC09	186.224136	18.133577	19.648 ± 0.002	0.780 ± 0.003	1006 ± 20	M85/BGC
GC10	186.233231	18.007664	20.649 ± 0.004	0.743 ± 0.006	992 ± 36	M85/BGC
GC11	186.236923	18.098547	21.794 ± 0.010	0.629 ± 0.014	1484 ± 71	IGC
GC12	186.254257	18.157011	20.816 ± 0.004	0.827 ± 0.007	854 ± 36	M85/BGC
GC13	186.267181	18.188093	20.861 ± 0.004	0.698 ± 0.007	474 ± 50	M85/BGC
GC14	186.267593	18.186392	20.590 ± 0.004	0.747 ± 0.006	820 ± 36	M85/BGC
GC15	186.275726	18.179281	19.859 ± 0.002	0.988 ± 0.004	994 ± 16	M85/RGC
GC16	186.278961	18.049801	20.981 ± 0.005	0.747 ± 0.007	716 ± 39	M85/BGC
GC17	186.284042	18.127205	20.899 ± 0.004	0.764 ± 0.007	1094 ± 33	M85/BGC
GC18	186.286331	18.156069	20.093 ± 0.002	0.729 ± 0.004	621 ± 21	M85/BGC
GC19	186.288849	18.148579	20.608 ± 0.004	0.754 ± 0.006	1040 ± 27	M85/BGC
GC20	186.289780	18.120619	20.985 ± 0.005	0.734 ± 0.008	846 ± 31	M85/BGC
GC21	186.294983	18.122747	20.869 ± 0.005	0.807 ± 0.008	851 ± 25	M85/BGC
GC22	186.304825	18.235580	20.484 ± 0.003	0.875 ± 0.006	840 ± 18	M85/RGC
GC23	186.311371	17.989689	20.859 ± 0.004	0.712 ± 0.007	491 ± 54	M85/BGC
GC24	186.312546	18.113945	21.986 ± 0.011	0.735 ± 0.017	896 ± 52	M85/BGC
GC25	186.314865	18.164808	19.861 ± 0.002	0.775 ± 0.004	921 ± 20	M85/BGC
GC26	186.319885	18.146456	21.402 ± 0.007	0.684 ± 0.010	954 ± 93	M85/BGC
GC27	186.324387	18.233643	20.914 ± 0.004	0.916 ± 0.008	746 ± 23	M85/RGC
GC28	186.327881	18.143229	19.987 ± 0.002	0.899 ± 0.004	699 ± 11	M85/RGC
GC29	186.329224	18.280996	20.810 ± 0.004	0.755 ± 0.007	558 ± 63	M85/BGC
GC30	186.334122	17.975805	20.959 ± 0.005	0.720 ± 0.007	629 ± 48	M85/BGC
GC31	186.341232	17.802233	21.920 ± 0.010	0.555 ± 0.014	1367 ± 66	IGC
GC32	186.361130	18.140669	21.819 ± 0.010	0.782 ± 0.015	793 ± 38	M85/BGC
GC33	186.377289	18.237936	20.472 ± 0.003	0.998 ± 0.006	649 ± 21	M85/RGC
GC34	186.379929	18.232170	20.466 ± 0.003	1.038 ± 0.006	629 ± 17	M85/RGC
GC35	186.384689	18.114702	20.791 ± 0.004	0.722 ± 0.006	649 ± 38	M85/BGC
GC36	186.397446	18.214993	20.930 ± 0.005	0.826 ± 0.008	619 ± 30	M85/BGC
GC37	186.402267	18.151552	20.743 ± 0.004	0.735 ± 0.006	922 ± 33	M85/BGC
GC38	186.404083	18.172537	20.730 ± 0.004	0.891 ± 0.007	534 ± 26	M85/RGC
GC39	186.420181	18.076006	20.574 ± 0.004	0.687 ± 0.005	799 ± 58	M85/BGC
GC40	186.421295	18.229662	19.760 ± 0.002	0.865 ± 0.003	542 ± 19	M85/RGC
GC41	186.429123	18.190605	20.939 ± 0.005	0.642 ± 0.007	500 ± 64	M85/BGC
GC42	186.432602	17.814720	21.307 ± 0.006	0.698 ± 0.009	1395 ± 65	IGC
GC43	186.435425	18.228134	20.913 ± 0.004	0.967 ± 0.008	471 ± 38	M85/RGC
GC44	186.446564	18.188711	20.565 ± 0.003	0.712 ± 0.005	792 ± 32	M85/BGC
GC45	186.477295	18.189302	20.062 ± 0.002	0.811 ± 0.004	864 ± 21	M85/BGC
GC46	186.489548	18.003197	19.545 ± 0.002	0.740 ± 0.003	677 ± 26	M85/BGC

Table A.7: (cont'd)

ID	α (J2000) (deg)	δ (J2000) (deg)	g^a (mag)	$(g-i)^a$ (mag)	$v_{\rm r}$ (km s^{-1})	Class
GC47	186.492798	18.269644	18.924 ± 0.001	0.772 ± 0.002	611 ± 9	M85/BGC
GC48	186.617386	17.935007	20.670 ± 0.004	0.732 ± 0.006	974 ± 40	IGC
GC49	186.620255	18.293690	20.236 ± 0.003	0.725 ± 0.004	481 ± 32	M85/BGC
GC50	186.624115	18.420595	20.490 ± 0.003	0.817 ± 0.005	753 ± 27	IGC
GC51	186.682892	18.433098	20.295 ± 0.003	0.719 ± 0.005	741 ± 27	IGC
GC52	186.826462	18.299479	20.526 ± 0.003	0.767 ± 0.005	546 ± 35	IGC
GC53	186.851883	18.278090	21.444 ± 0.007	0.707 ± 0.010	1356 ± 93	IGC

[a]CFHT/MegaCam AB magnitudes.

요 약

본 연구에서는 광범위한 측광, 분광 자료를 이용하여 처녀자리은하단과 M85의 구상성단계에 대한 연구를 수행하였다. 구상성단의 측광, 분광학적 특성을 이용함으로써, 그들의 속한 환경인 처녀자리은하단과 병합잔해은하 M85의 형성 및 진화 과정을 추적하였다.

먼저, 처녀자리은하단 중심부에 위치하는 구상성단 후보들에 대해 광시야 분광 탐사를 진행하였다. Multiple-mirror Telescope (MMT)의 Hectospec 분광 기기를 사용하여 총 201개의 구상성단과 55개의 초밀집 왜소은하(ultracompact dwarf; UCD)의 스펙트럼을 얻었고, 그들의 후퇴 속도를 측정하였다. 3차원 가우시안 혼합 모델링을 통해, 201개의 구상성단들 중 46개의 구상성단이 어느 은하에도 속하지 않고 처녀자리은하단을 방랑하는 구상성단(intracluster globular cluster; IGC)임을 확인하였다. 그들은 처녀자리은하단에 속한 가장 무거운 은하인 M87로부터 50 kpc부터 500 kpc까지의 거리에 분포해있다. 처녀자리은하단의 IGC는 후퇴속도 $v_{\rm r} = 400$ km s^{-1}를 기준으로 두 집단으로 나누어진다. 한 집단은 평균 속도가 $v_{\rm r} = 1023$ km s^{-1} 정도로 처녀자리은하단의 본체에 속한 것이고, 다른 집단은 평균 속도가 $v_{\rm r} = 36$ km s^{-1} 근처로 은하단의 바깥에서 안쪽으로 떨어지는 집단이다. 은하단의 본체에 속한 IGC들의 후퇴속도 분산은 $\sigma_{\rm IGC} = 314$ km s^{-1}로, M87에 속한 구상성단의 후퇴속도 분산과 유사하지만 탐사 영역에 위치한 왜소은하들의 후퇴속도 분산에 비해서는 훨씬 작다($\sigma_{\rm dwarf} = 608$ km s^{-1}). 본 연구에서는 측광 연구들에서 예측된 IGC의 대규모 분포를 분광학적으로 확인하였다. 확인된 IGC들의 색지수 분포는 이원 분포를 보이며, 이를 바탕으로 처녀자리은하단의 IGC들은 왜소은하뿐 아니라 무거운 은하들로부터도 빠져나온 것임을 추정할 수 있다.

M85는 수백만 년 전 병합 과정을 겪었을 것으로 추정되는 병합잔해은하 중 하나이다. Canada-French-Hawaii Telescope의 MegaCam 기기를 사용하여 M85 부근의 $1^\circ \times 1^\circ$ 영역의 ugi 영상 자료를 얻었고, 이 자료를 이용하여 구상성단 탐사를 수행하였다. 점광원들 중, 색지수와 등급 기준을 이용하여 총 1318개의 구상성단 후보들을 발견하였다. 그들은 M85 중심부에 잘 모여있으며, 전체 구상성단계의 유효 반경은 $5\farcm54$, 즉 29 kpc 정도로 은하 빛보다 더 바깥 영역까지 분포해 있다. 구상성단 후보들의 색분포는

이중분포이며, $(g-i)_0 = 0.65$ 와 0.87에서 최고점을 이룬다. 그러나 $R < 2'$ 영역에서는 푸른구상성단과 붉은구상성단 외에도 중간 정도의 색을 띠는 성단들이 발견되었다. 푸른구상성단은 붉은구상성단보다 더 바깥 영역까지 분포하며, 각 구상성단계의 유효반경은 7.′41과 2.′31이다. 두 구상성단 후보들의 공간분포는 은하 빛의 공간분포와 마찬가지로 찌그러져 있으며, 이것은 일반적인 조기형 은하의 구상성단들에서 보이는 현상과는 다르다. 중간 정도의 색을 띠는 구상성단들의 존재와, 특정 방향으로 늘어진 푸른구상성단과 붉은구상성단 후보들의 공간분포는 M85가 겪었을 병합의 증거로 제시할 수 있다.

영상 자료를 이용하여 얻은 구상성단 후보들의 목록을 이용하여, M85 구상성단들에 대해 Gemini-North Telescope의 Gemini Multi-Object Spectrograph (GMOS) 기기와 MMT의 Hectospec 기기를 이용하여 분광 관측을 수행하였다. GMOS 기기를 사용해서 20개의 구상성단을 관측하였고, 그들의 후퇴 속도는 396 km s^{-1}에서 1127 km s^{-1} 까지 분포한다. 구상성단들은 M85를 중심으로 회전하는 모습을 보이며, 그들의 후퇴 속도 분산은 154 km s^{-1} 정도이다. 스펙트럼 맞춤 방식을 이용하여 구상성단들의 나이를 측정한 결과, 나이가 많은 구상성단 이외에, 중금속함량이 태양과 비슷하고 4.0 ± 2.0 Gyr의 나이를 갖는 젊은 구상성단들이 존재함을 확인하였다. 이는 M85가 4 Gyr 전에 별형성을 동반하는 병합과정을 겪었음을 의미한다.

Hectospec 기기를 이용하여 53개 구상성단들의 스펙트럼을 얻었고, 그들의 후퇴 속도는 400 km s^{-1}에서 1600 km s^{-1} 까지 분포한다. 53개의 구상성단 중, $R < 20'$와 $v_{\rm r} < 1200$ km s^{-1}의 조건을 만족하는 42개의 성단을 M85에 속한 구상성단으로 분류하였고 그 외의 11개의 성단은 IGC로 분류하였다. M85에 속한 구상성단은 $(g-i)_0 = 0.8$을 기준으로 푸른구상성단과 붉은구상성단으로 분류하였다. M85의 푸른구상성단은 $20'$까지 퍼져있는 반면, 모든 M85의 붉은구상성단은 $6'$ 안쪽에 위치한다. 구상성단계는 GMOS 분광 관측에서도 확인했듯이 전체적으로 회전하고 있으나 그 회전축은 M85 중심부 은하 빛의 회전축과는 전혀 다름을 확인하였다. 붉은구상성단은 적은 숫자임에도 불구하고 강한 회전을 보여준다. 푸른구상성단과 붉은구상성단의 회전 효과를 제거한 후퇴 속도 분산은 각각 149 ± 20 km s^{-1}, 51 ± 14 km s^{-1}로 측정되었다. 구상성단계의

강한 회전과, 중심부 은하 빛으로부터 운동학적으로 분리된 모습은 M85가 이전에 겪었던 병합 과정에 의한 것으로 의심된다. M85에 속한 구상성단과 M85 근처의 IGC들은 운동학적으로 전혀 다른 모습을 보인다. 그들의 평균 후퇴속도는 각각 765 ± 27 km s^{-1}, 1012 ± 108 km s^{-1}로 차이가 있고, IGC의 후퇴 속도 분산은 354 ± 78 km s^{-1}로서 M85에 속한 구상성단에 비해 훨씬 크다. 이는 관측 영역에 위치한 왜소은하들의 후퇴 속도 분산과 유사하며 ($\sigma = 330 \pm 95$ km s^{-1}), 이는 IGC가 은하단의 중력 포텐셜에 속해 있다는 것을 보여준다.

주요어: 은하단, 은하단:Virgo, 은하, 은하:M85, 은하:형성, 구상성단, 탐사, 측광, 분광

학 번: 2010-20386